The Electrocatalytic and Stoichiometric Oxidation Chemistry of Binuclear Ruthenium Complexes Incorporating the Anionic Tripod Ligand $\{(\eta^5\text{-}C_5H_5)Co[P(OCH_3)_2(=O)]_3\}^-$.

Thesis by
Eric P. Kelson

In Partial Fulfillment of the Requirements
for the Degree of
Doctor of Philosophy

Division of Chemistry
and Chemical Engineering

California Institute of Technology
Pasadena, CA

1994
(Submitted September 3, 1993)

For My Parents

Acknowledgments

First, I thank John Bercaw for giving me the opportunity to work in his group. When I was considering which research group to join, I was particularly impressed by the openness of the group and John's approachability. John has been very helpful in helping me focus my career goals and plans. I feel that I have grown intellectually and socially while under his supervision. Though my project required me to use techniques and procedures somewhat unfamiliar to the group, I appreciate John's open-mindedness in allowing me to continue this work.

I also thank the other people who contributed to my work at Caltech. Though not an official group member, Jay Labinger was helpful through his comments, advice, and his assistance in preparing the recent publication of this research. Jim Toth and Bruce Tufts were very patient teachers of the experimental electrochemistry without which this project would not have been possible. I appreciate the efforts of Bill Schaefer, Larry Henling, and Dick Marsh in the solution of the second crystal structure mentioned in Chapter 4 and for their patience as I solved the other structure by myself. I acknowledge John Power and Kaspar Evertz for their pioneering work in the ruthenium project.

I also thank past and present members of the Bercaw group for their help and support during my time at Caltech. Warren Piers and John Power were especially supportive in my first year, both with professional advice and friendship. My many discussions with Gerrit Luinstra were helpful in understanding and focusing my plans for the future. Roger Quan was an excellent classmate who was always friendly and receptive; Tim Herzog tolerated me when we shared a vacuum line and when he taught Ch 154 with me. Bob Blake and Sue Haney shared some of the frustrations of ruthenium.

I thank those who have helped me grow personally as well as professionally at Caltech. Donnie Cotter provided me with my first real taste of backpacking; I will never forget Kawea Gap. Special thanks are due the Hogs (who patiently taught me how to play softball), those group members who encouraged me to ski (especially Roger Quan who learned with me), and to Andy Herring who encouraged me to try rock climbing for the first time. Philosophical discussions with Gerrit Luinstra, Jim Gilchrist, David Antonelli and Shannon Stahl were very enlightening; I have found that ideas need to be discussed to take form. Outside the group, I would also like to thank Jim Gerdy and Sean Plunket for both being good roommates and good friends.

I am also indebted to past teachers and advisors that helped me to recognize my interests and find my way to Caltech. Dr. Doan Sanders and Dr. Harward nurtured my early interest in science (especially chemistry). Ronald Ragsdale gave much-appreciated encouragement; Thomas Richmond and Charles Wight gave me my first academic research experience and certainly helped me reach Caltech.

I especially thank my family for their love and support. Though we varied in views and interests, I always found understanding and support at home. I am especially grateful for my parents' tolerance of my initial interest in chemistry. I am sure that I would not be where I am now without them.

Finally, I thank those whose financial support made my graduate career and this research possible. My first year at Caltech was supported by the Earle C. Anthony Graduate Fellowship, and the subsequent years were supported by the Fannie and John Hertz Foundation Fellowship. Financial support for the laboratory work was provided by the Office of Navel Research.

Abstract:

The anionic tripod ligand NaL_{OMe} (L_{OMe}^- = $[(\eta^5\text{-}C_5H_5)Co\{P(O)(OCH_3)_2\}_3]^-$) reacts with RuO_4 in a biphasic reaction mixture of 1% H_2SO_4 and CCl_4 to afford $[(L_{OMe})(HO)Ru^{IV}\text{-}(\mu\text{-}O)_2Ru^{IV}(OH)(L_{OMe})]$ (**1**), which is treated with aqueous CF_3SO_3H to generate $[(L_{OMe})(H_2O)Ru^{IV}(\mu\text{-}O)_2Ru^{IV}(OH_2)(L_{OMe})][CF_3SO_3]_2$ ($[H_21][CF_3SO_3]_2$). Addition of iodosobenzene to an acetonitrile solution of this salt yields $[(L_{OMe})(O)Ru^{V}(\mu\text{-}O)_2Ru^{V}\text{-}(O)(L_{OMe})]$ (**2**). The dimer **1** can be reduced chemically or electrochemically to the $Ru^{III}\text{-}Ru^{III}$ dimers $[(L_{OMe})(H_2O)Ru^{III}(\mu\text{-}OH)_2Ru^{III}(OH_2)(L_{OMe})]^{2+}$ and $[(L_{OMe})Ru^{III}(\mu\text{-}OH)_2(\mu\text{-}OH_2)\text{-}Ru^{III}(L_{OMe})]^{2+}$ which interconvert in aqueous media. Two electron processes dominate both the bulk chemistry and the electrochemistry of **1**. Among these processes are the quasi-reversible $Ru^{IV}\text{-}Ru^{IV}/Ru^{III}\text{-}Ru^{III}$ and $Ru^{III}\text{-}Ru^{III}/Ru^{II}\text{-}Ru^{II}$ reductions and a largely irreversible $Ru^{V}\text{-}Ru^{V}/Ru^{IV}\text{-}Ru^{IV}$ oxidation. The dioxo dimer **2** oxidizes alcohols and aldehydes in organic media to afford **1** and the corresponding aldehydes and acids. Analogously, the $Ru^{V}\text{-}Ru^{V}/Ru^{IV}\text{-}Ru^{IV}$ redox wave mediates the electrooxidation of alcohols and aldehydes in aqueous buffer. In this system, substrates can be oxidized completely to CO_2. The kinetic behavior of these oxidations was examined by UV-vis and chronoamperometry, respectively, and the chemistry is typical of metal-oxo complexes, indicating that electronic coupling between two metal centers does not dramatically affect the metal-oxo chemistry. Dimer $[H_21]^{2+}$ also reacts with alcohols, aldehydes, and triphenylphosphine in CH_3CN to afford $Ru^{III}\text{-}Ru^{III}$ products including $[(L_{OMe})(CH_3CN)Ru^{III}(\mu\text{-}OH)_2Ru^{III}(NCCH_3)(L_{OMe})][CF_3SO_3]_2$ (characterized by X-ray crystallography) and the corresponding organic products. Reaction of **1** with formaldehyde in aqueous buffer quantitatively affords the triply bridged dimer $[(L_{OMe})Ru^{III}(\mu\text{-}OH)_2\text{-}(\mu\text{-}HCOO)Ru^{III}(L_{OMe})][CF_3SO_3]$ (characterized by X-ray crystallography). This reaction evidently proceeds by two parallel inner-sphere pathways, one of which is autocatalytic. Neither pathway exhibits a primary isotope effect suggesting the rate determining process

could be the formation of an intermediate, perhaps a Ru^{IV}-Ru^{IV} formate adduct. The Ru^{III}-Ru^{III} formate adduct is easily oxidized to the Ru^{IV}-Ru^{IV} analog $[(L_{OMe})Ru^{IV}(\mu\text{-}O)_2(\mu\text{-}HCOO)\text{-}Ru^{IV}(L_{OMe})][CF_3SO_3]$, which, after isolation, reacts slowly with aqueous formaldehyde to generate free formate and the Ru^{III}-Ru^{III} formate adduct. These dimers function as catalysts for the electrooxidation of formaldehyde at low anodic potentials (+0.0 V versus SCE in aqueous buffer, pH 8.5) and enhance the activity of Nafion treated palladium/carbon heterogeneous fuel cell catalysts.

TABLE OF CONTENTS

List of Figures

Chapter 1.

Chapter 2.

Chapter 3.

Chapter 4.

Chapter 5.

LIST OF TABLES

Chapter 1

Introduction: The Quest for Low Potential Homogeneous Oxidation Electrocatalysts

Abstract:

This chapter describes our motivation to search for low potential homogeneous oxidation electrocatalysts. Energy needs are anticipated to create a demand for fuel cells in which organic fuels are converted to CO_2, H_2O, and electrical energy. Fuel cells using H_2 are well known, but the standard heterogeneous electrocatalysts used in these cells have not been adapted for use with organic fuels. A possible solution is the supplementation of these heterogeneous systems with homogeneous catalysts. Though homogeneous catalyst systems are competent for alcohol and alkane oxidation, the high driving potentials utilized by these systems render them undesirable for use in fuel cells. Many of the lower oxidation state catalysts owe their reactivity to metal-oxo groups which are electronically destabilized in octahedral d^4 complexes. This chapter sets forth a strategy for harnessing this destabilization by making complexes with a coordination environment made up completely of oxygen donors. Such coordination would both provide additional π-donating ligands to destabilize further the metal-oxo bond and provide a hard donor ligand environment to stabilize high metal oxidation states, thereby decreasing the oxidation potentials needed to form these species. The oxygen donor tripod ligand $\{(\eta^5\text{-}C_5H_5)Co[P(OR_3)_2(=O)]_3\}^-=(L_{OR})^-$ was chosen for this purpose. The dimeric complexes of this ligand and ruthenium, $(L_{OR})(HO)Ru^{IV}(\mu\text{-}O)_2Ru^{IV}(OH)(L_{OR})$ (where R=Me, Et), manifests unusual oxidation chemistry. This chemistry is explored in following chapters.

Introduction

In recent years, the chemical industry has increasingly focused on developing and understanding oxidation chemistry to prevent unwanted side reactions and eliminate the need for expensive oxidants (Figure 1.1).[1] Furthermore, active competition and increasingly restrictive environmental laws are driving the search for greater reaction specificity. Even small advances in the specific oxidation of substrates can have large financial and environmental impacts on the production of agricultural and pharmaceutical products. Unfortunately, many of these advances are discovered serendipitously and are optimized by tedious variation of reaction conditions. Also many of these industrial catalysts are heterogeneous and not fully understood. Much research has been devoted to modeling or improving on these processes with homogenous catalysts.

Figure 1.1. Industrial conversion of propylene to propylene oxide: problems with existing catalysts.

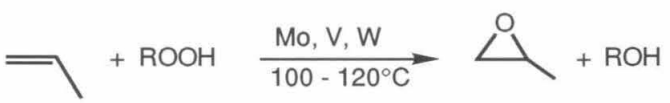

Shell:
R = *tert*-Bu-, $C_6H_5(CH_3)CH$- Must sell ROH to be economical
Enichem:
R = H H_2O_2 is expensive

Another arena of applied oxidation chemistry involves fuel cell technology, a field that has developed in response to a growing interest in alternative (and increasingly portable) energy sources.[2] Fuel cell technology and oxidative synthesis sharply contrast in their goals. Synthetic oxidation chemistry sacrifices excess potential energy for reactivity while fuel cell attempt to capture the chemical potential energy and rapid rate for chemical reactions as electrical power. Often fuel cells couple the complete oxidation of organic substrates to the reduction of dioxygen. While synthetic oxidations often occur at a single catalyst surface or

sites, the conversion of fuel and oxygen to energy requires the oxidation and reduction chemistry to occur at separate sites (Figure 1.2).

Figure 1.2. Catalytic oxidation in synthesis and fuel cell operation.

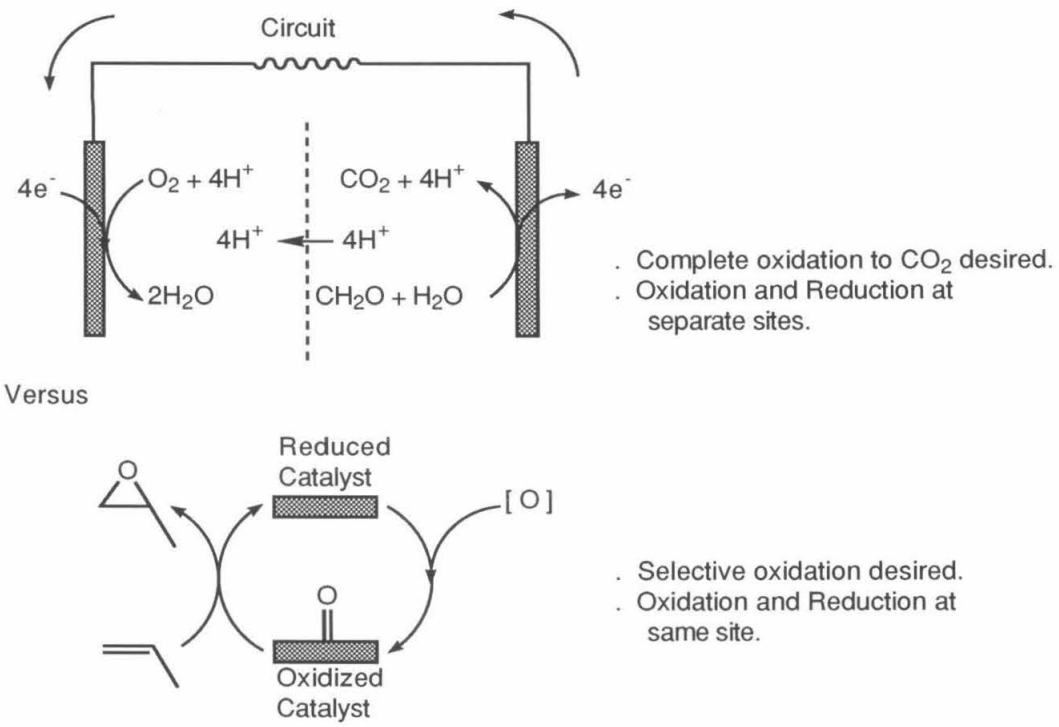

Fuel cell research has been underway for many years, and the development of heterogeneous catalyst electrodes such as high surface area platinum and palladium has been the primary focus.[3] Standard fuel cells use hydrogen for which the mechanism for oxidation is well understood (Figure 1.3).[4] Such fuel cells are currently used in situations such as in the space shuttle fleet, where energy production equipment must be lightweight; however, these catalysts are not as effective for organic fuels. Despite optimization of direct fuel cells using methanol or formaldehyde, their current/voltage performance still falls about 100 times short of analogous H_2-O_2 systems.[5] Low active site densities and catalyst poisoning (by oxidation products such as CO) result in poor catalyst performance (Figure 1.4).[6]

Figure 1.3. Operation of hydrogen/heterogeneous catalyst fuel cell.

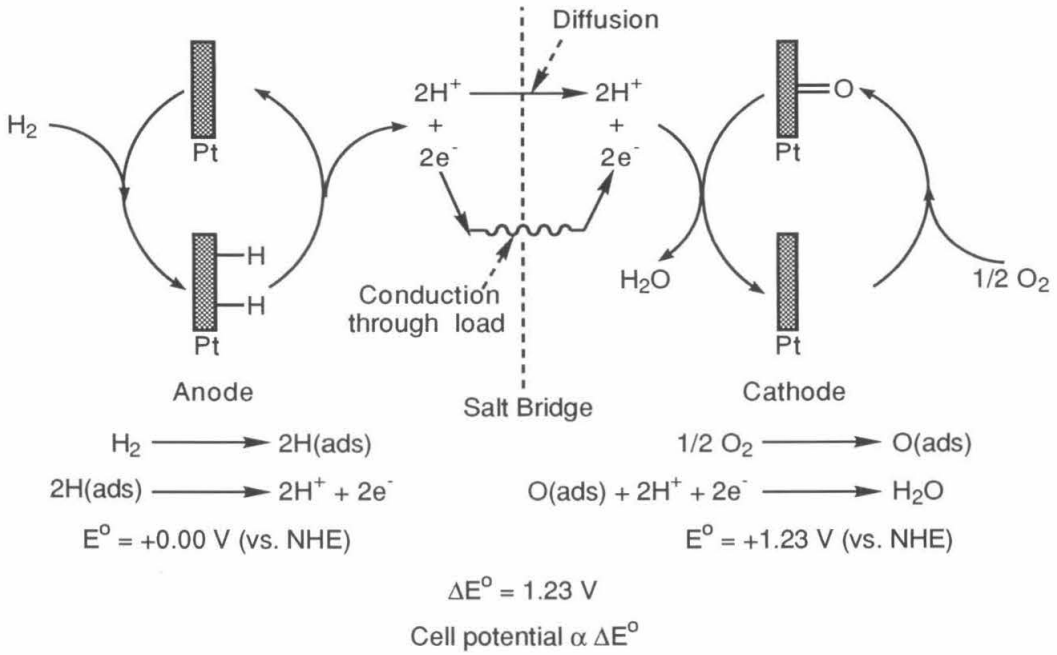

Figure 1.4. Proposed catalytic mechanism for anodic oxidation of HCHO at metallic catalyst.

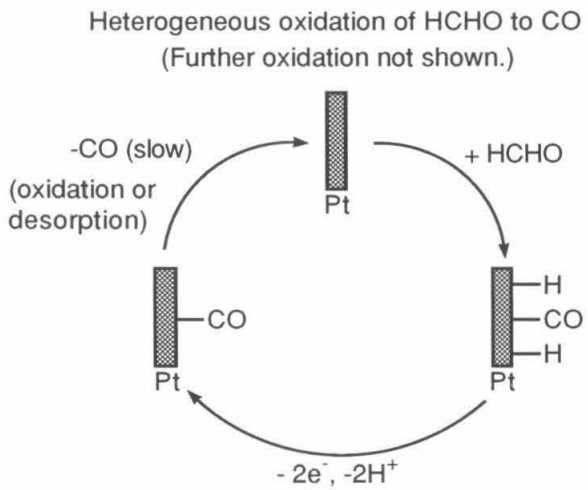

While the effort to investigate and optimize existing heterogeneous catalysts for fuel cell and synthetic applications continue, attempts aimed at designing and synthesizing homogeneous catalysts are also underway.[7] In other industrial applications, homogeneous

systems have provided insight into the activity of existing heterogeneous catalysts and have occasionally found practical use.[7] In fuel-cells, product is easily separated from catalyst. This makes homogeneous catalysts particularly applicable in direct fuel cells (Figure 1.5). Homogeneous catalysts are often less susceptible to poisoning and can improve the performance of existing heterogeneous systems by relieving kinetic barriers and improving product selectivity. Unfortunately, the design of applicable homogeneous fuel cell electrocatalysts has been a serious challenge.

Figure 1.5. Fuel cell with electrocatalyst.

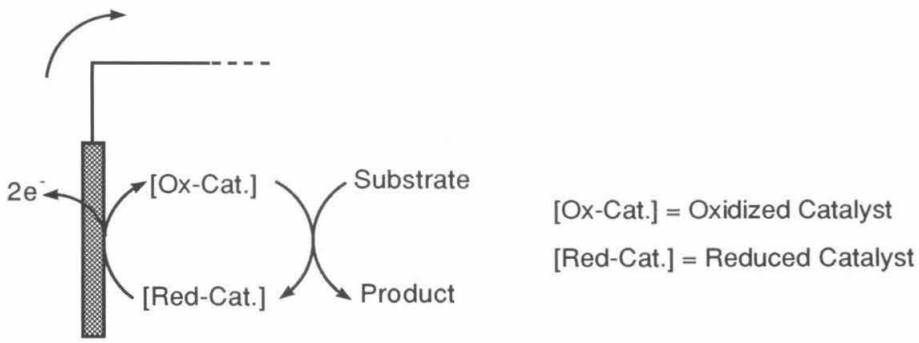

A large majority of homogeneous oxidation catalysts rely on reactive metal-oxo groups. Well-known metal-oxide oxidation reagents and naturally occurring enzymes (particularly Cytochrome P_{450}) with reactive metal-oxo bonds have inspired much of this research.[8] The Sharpless olefin dihydroxylation catalyst is a particularly useful example of a polyoxo catalyst in organic synthesis.[9] Other polyoxo complexes have been examined as catalysts such as $[Ru^{VII}O_4]^-$ studied by Griffith.[10] Many other metal-oxo catalysts aim to mimic Cytochrome P_{450} by supporting metal-oxo bonds with a nitrogen donor coordination environment. Some researchers have attempted to mimic the activity of this enzyme with Mn^{V}-oxo and Ru^{IV}-oxo porphyrins[11] and Fe^{IV}-oxo halogenated porphyrins.[12] Ruthenium complexes have attracted particular interest due in part to the wide range of accessible oxidation states. Indeed, the literature contains many ruthenium-oxo catalysts active via the Ru^{VII} [11], Ru^{VI} [13,14], Ru^{V} [15,16], Ru^{IV} [16,14,17,18], and Ru^{III} [16,17] oxidation states.

The reactivity of the lower oxidation states Ru^{IV} and Ru^{III} have attracted particular attention, especially with the nitrogen based ligand systems illustrated below (Figure 1.6).

Figure 1.6. Reported homogeneous catalysts for alcohol and alkane Oxidation.

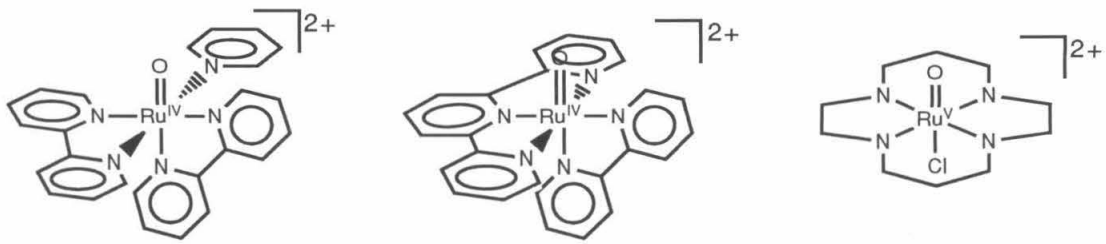

T. J. Meyers
$E_{1/2}(Ru^{IV}/Ru^{III})$ = 0.53 V
(versus SCE, pH=7)

T. J. Meyers
$E_{1/2}(Ru^{IV}/Ru^{III})$ = 0.62 V
(versus SCE, pH=7)

C.-M. Che
$E_{1/2}(Ru^{V}/Ru^{IV})$ = 1.05 V
(versus Cp_2Fe, CH_3CN)

The metal-oxo moieties in these complexes are believed to be intrinsically reactive. While most metal-oxo complexes exhibit strong metal-oxo bonds, these complexes exhibit low metal-oxo vibration frequencies suggesting weakened metal-oxo bonds. Facile oxo-transfer reactions with phosphines and alkenes also imply the metal-oxo bonds are particularly weak.

A possible explanation lies in the destabilization of normal metal-oxo bonding. The metal-oxo bond has two principle resonance forms, one of which involving π-donation from the oxo lone pair yielding a net triple bond (Figure 1.7). The triple bond metal-oxo is the principle resonance contribution in most metal-oxo complexes, especially for those containing high oxidation state metal centers complexes where additional electron density from the oxo group stabilizes the metal center. In contrast, the double bond resonance form seems to be the principle contribution in Ru^{IV} and Ru^{III} oxo complexes.

Figure 1.7. Resonance forms of metal-oxo bond.

A possible explanation for this effect has been proposed by Mayer[19]. The oxo ligand likely interacts with the nonbonding d orbitals of octahedral, square pyramidal, and square planar complexes to form two bonding, one nonbonding, and two antibonding orbitals (Figure 1.8). If the metal has more than two d electrons, the excess electrons would be antibonding. Metal centers such as Ru^{IV} (d^4) would have a $\pi^4n^2\pi^{*2}$ configuration from the d-p interactions resulting in a bond order of only two.

Figure 1.8. Energy levels for d^2 octahedral metal-oxo complex.

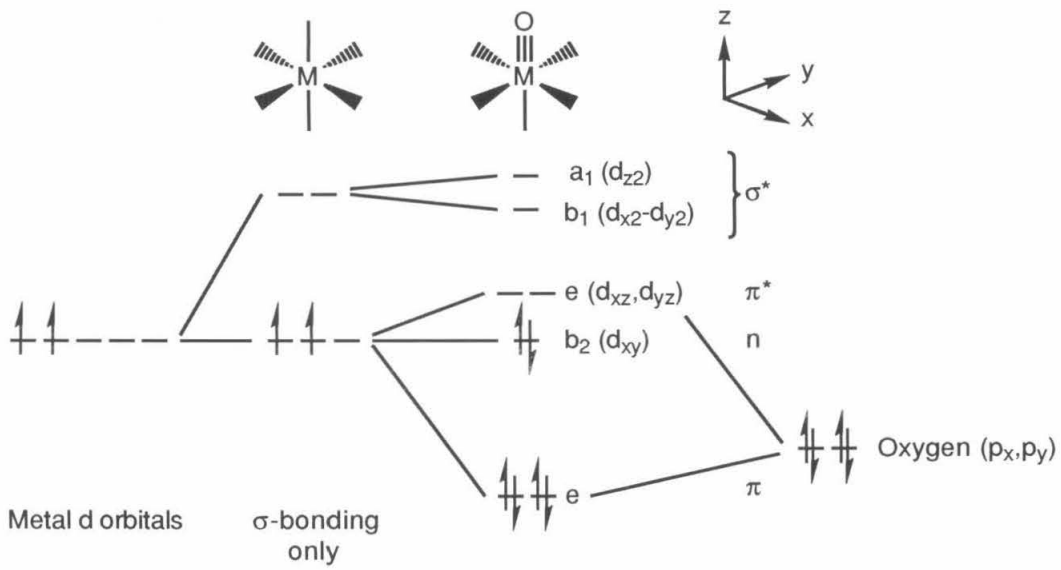

The oxidation chemistry of these complexes has been extensively studied due to their relative stability and well-behaved reactivity. Many of these complexes oxidize and catalyze the oxidation of organic substrates by either oxo-transfer as with alkenes and phosphines (Figure 1.9) or C-H oxidation as with alcohols, aldehydes, and acids (Figure 1.10). As illustrated in the figures, both processes include several mechanistic permutations. Specifically, hydride transfer could occur by initial electron transfer, hydrogen abstraction, or hydride abstraction (Figure 1.10). Unfortunately, both oxo-transfer and C-H oxidation processes involve high energy processes such as electron transfer from σ-bonds and/or cleavage of one or more bonds that require a strong driving potential. This translates into a large

oxidation potential for the active species. However, if the metal-oxo group is further destabilized, lower potentials may be sufficient for oxo-transfer.

Figure 1.9. Intermediates for oxo-transfer.

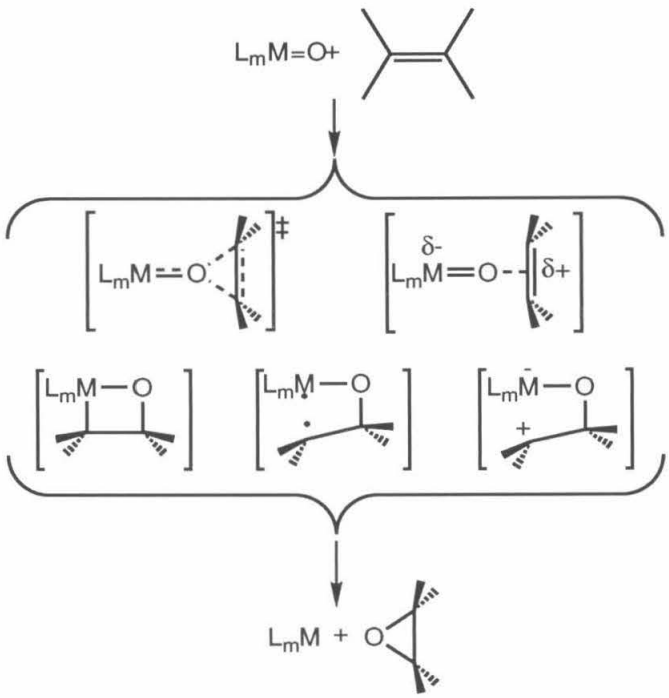

Figure 1.10. Intermediates in C-H oxidation.

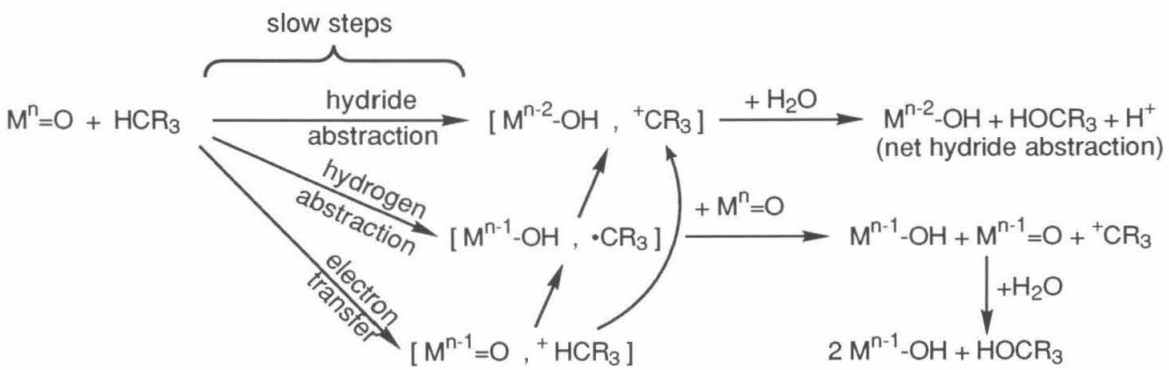

Though the oxidation potentials for the catalysts in Figure 1.6 are too high for application in fuel cells, their reactivity may be achievable at lower potentials. (According to

current estimates in the fuel cell industry, an anodic potential of no higher than 0.0 V versus SCE is required for practical application.[20]) Perhaps the π-interactions from another ligand could further destabilize the metal-oxo moiety.

Such destabilization has been theoretically considered for octahedral dioxo complexes.[21] Two *cis*-oxo groups in an octahedral complex compete for π-overlap with three t_{2g} d-orbitals. In d^0 complexes, a bond order of 2.5 is possible for each metal-oxo group, whereas in d^2 complexes, the nonbonding electrons reside in one of these t_{2g} orbitals allowing a maximum bond order of 2 for each oxo group. Orbital overlaps between *cis*-oxo ligands destabilizes them further. In $d^{n\leq 2}$ *trans*-dioxo complexes, the two oxo groups compete for π-overlap with only two t_{2g} orbitals. This restriction allows only two π-bonds to form, one to each oxo ligand giving a bond order of 2 for each metal-oxo moiety.

This theoretical reasoning is supported by the unusual double oxo-transfer observed for d^2 Os^{IV} dioxo complexes by Meyer et al. (Figure 1.11).[22]

Figure 1.11. Double oxo-transfer by *cis*-$(bpy)_2Os^{VI}O_2$.

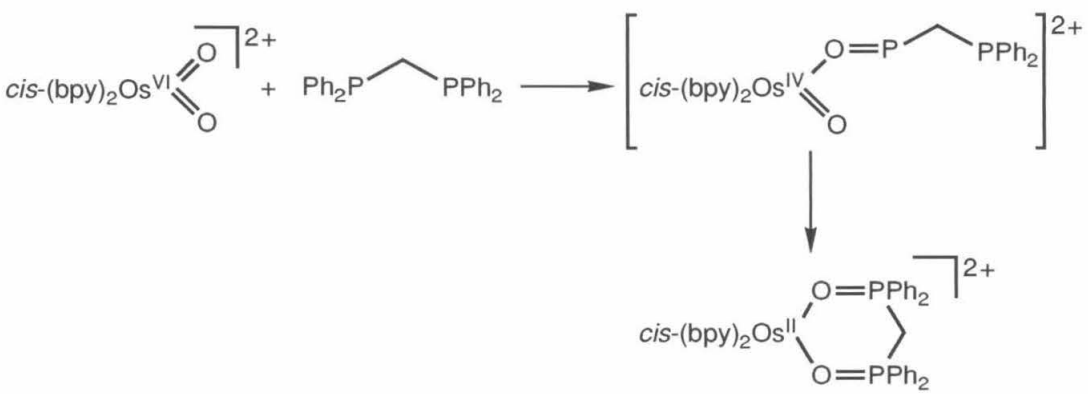

Octahedral d^4 metal-oxo complexes with weakly π-donating bridging oxo groups or other oxygen donors may exhibit similar destabilization. A destabilizing π-interaction could exist though a formal π-bond may not be present. Though such an interaction would not be as strong as that of another oxo bond, the effect could be optimized by a complete oxygen donor

coordination environment. Such a hard donor coordination environment would also stabilize high oxidation states without compromising their electrophilicity. These effects together might allow metal-oxo reactivity such as oxo-transfer at lower potentials.

A large majority of the oxo complexes studied support oxo moieties with soft and/or basic nitrogen ligands. Though these ligands can provide some π-destabilization, they may not stabilize the metal center as efficiently as oxygen donors and they may compromise some of the metal electrophilicity. These factors may be demanding an unnecessarily high driving potential for reactivity.

The anionic tripod ligands $[(\eta^5\text{-}C_5H_5)Co\{P(O)(OR)_2\}_3]^-$ (Figure 1.12), abbreviated as $(L_{OR})^-$, originally reported by Kläui[23] provide such an opportunity to prepare such complexes with entirely oxygen donor ligand environments. These ligands have the additional advantages of being facially coordinating and bulky. This could restrict reactivity to one face of coordinated metal centers and reduce the orbital considerations in exploring and interpreting reactivity. The alkoxy and Cp groups will provide useful NMR spectroscopic handles for characterization and kinetic analysis. Though these complexes possess organic groups, the ligands appear oxidation resistant[23,24].

Figure 1.12. Structure of ligand $(L_{OR})^-$.

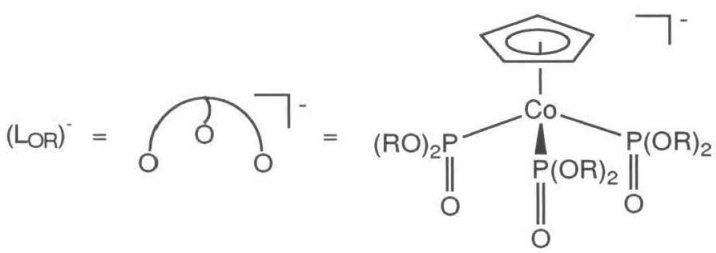

The dimer illustrated in Figure 1.13 with the (L_{OEt}) ligand was prepared in the Bercaw laboratories as reported in the literature.[25] Though monomers are preferable, these dimers apparently represent a thermodynamic product in these systems. Besides having the complete

oxygen donor environment desired, the ruthenium centers appear electronically coupled which could encourage two electron oxidation chemistry better suited for organic oxidation.

Figure 1.13. Structure of $(L_{OEt})(HO)Ru^{IV}(\mu\text{-}O)_2Ru^{IV}(OH)(L_{OEt})$ ($\mathbf{1_{Et}}$).

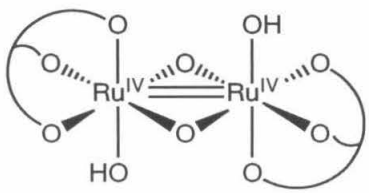

The influence of metal-metal cooperation on metal-oxo chemistry would be of interest. Meyer has reported the chemistry of two octahedral metal-oxo dimers $[(bpy)_2(O)Ru^{IV}(\mu\text{-}O)\text{-}Ru^{V}(O)(bpy)_2]^{3+}$ and $[(bpy)_2(py)Ru^{III}(\mu\text{-}O)Ru^{V}(O)(bpy)_2]^{4+}$ (bpy = 2,2'-bipyridine) in which the metal centers could, in principle, cooperate. However, these dimers did not exhibit unusual reactivity (Figure 1.14)[26]. The mechanism for this reactivity is not understood, and several possible intermolecular electron transfers cloud the effect of electronic metal-metal coupling.

Figure 1.14. Reactivity of ruthenium dimers investigated by Meyer et al.

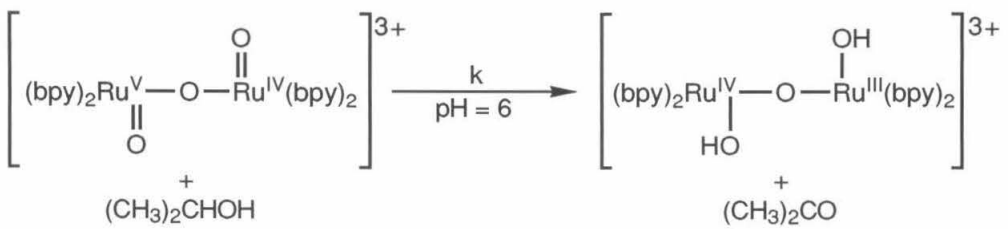

$$-d[Ru^{IV}\text{-}Ru^{V}]/dt = k\,[substrate][Ru^{IV}\text{-}Ru^{V}]$$

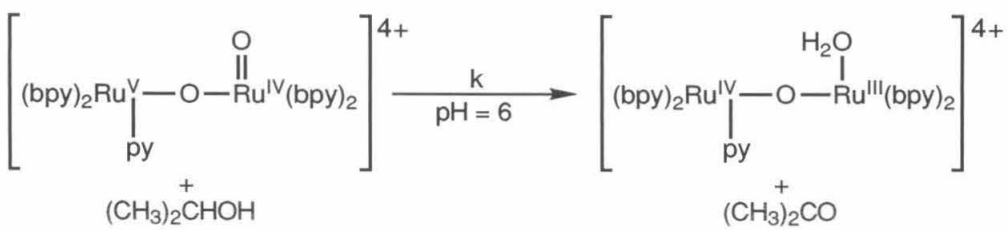

$$-d[Ru^{III}\text{-}Ru^{V}]/dt = k\,[substrate][Ru^{III}\text{-}Ru^{V}]$$

The research described in this thesis explored the effect of an oxygen donor coordination environment on metal-oxo chemistry and the effect of dimer metal-metal cooperation on organic oxidation chemistry. This investigation began with a chemical and electrochemical survey of the accessible oxidation states of this dimer in aqueous systems (Chapter 2). The dimer oxidation chemistry is dominated by two electron processes likely due to the metal-metal cooperation described. Both the Ru^{V}-Ru^{V}/Ru^{IV}-Ru^{IV} and Ru^{IV}-Ru^{IV}/Ru^{III}-Ru^{III} redox couples exhibit interesting oxidation chemistry with various substrates. The former redox couple, being particularly relevant to metal-oxo chemistry, was examined by chemical and electrochemical means and was found to exhibit typical metal-oxo chemistry in both organic and aqueous media (Chapter 3). The latter couple also exhibits oxidation chemistry but at a remarkably mild potential. This reactivity was chemically surveyed, and attempts were made to assess the applicability of this chemistry in fuel cells (Chapter 4). This chemical survey shows that this reactivity is different from known oxidation chemistry and does modestly enhance existing fuel cell catalysts. The mechanistic features of this oxidation chemistry were explored in detail (Chapter 5).

This dimer system offers a unique opportunity to observe two very different kinds of oxidation chemistry from the same system, and the reactivity of the Ru^{V}-Ru^{V}/Ru^{IV}-Ru^{IV} couple makes a significant contribution to the known metal-oxo chemistry. The reactivity of the Ru^{IV}-Ru^{IV}/Ru^{III}-Ru^{III} couple offers a glimpse of new oxidation chemistry that could be important to low-potential oxidation.

References

1. Sheldon, R. A.; Kochi, J. K. *Metal Catalyzed Oxidation of Organic Compounds;* Academic Press: New York, 1981.

2. Bockris, J. O'M.; Srinivasan, S. *Fuel Cells: Their Electrochemistry;* McGraw-Hill: New York, 1969; pp 23-33, 625-627.

3. Young, G. J.; Linden, H. R. *Fuel Cell Systems;* Advances in Chemistry Series 47; American Chemical Society: Washington, DC, 1965.

4. Bockris, J. O'M; Srinivasan, S. *Fuel Cells: Their Electrochemistry;* McGraw-Hill: New York, 1969; pp 126-133.

5. Bockris, J. O'M; Srinivasan, S. *Fuel Cells: Their Electrochemistry;* McGraw-Hill: New York, 1969; pp 619-625.

6. Bagotzky, V. S.; Vasilyev, Yu. B. *Electrochim. Acta,* **1967**, *12*, 1323. Bagotzky, V. S.; Vassiliev, Yu. B.; Khazova, O. A. *J. Electroanal. Chem.*, **1977**, *81*, 229. McNicol, B. D. J. *Electroanal. Chem.*, **1981**, *118*, 71. Goodenough, J. B.; Hamnett, A.; Kennedy, B. J.; Manoharan, R.; Weeks, S. A. *J. Electroanal. Chem.*, **1988**, *240*, 133.

7. Dordrecht; Boston; Reidel; Norwell In *Industrial Applications of Homogeneous Catalysts*, Montreux, A; Petit, F., Ed.; Catalysis by Metal Complexes 10; D. Reidel Publishing: Boston, 1988.

8. Yamazaki, I. In *Molecular Mechanisms of Oxygen Activation;* Hayaishi, O., Ed.; Academic: New York, 1974; p 532.

9. Jacobsen, E. N.; Markó, I.; France, M. B.; Svendsen, J. S.; Sharpless, K. B. *J. Am. Chem. Soc.* **1989**, *111*, 737-739. Wai, J. S. M.; Markó, I.; Svendsen, J. S.; Finn, M. G.; Jacobsen, E. N.; Sharpless, K. B. *J. Am. Chem. Soc.* **1989**, *111*, 1123-1125. Ogino, Y.; Chen, H.; Kwong, H.-L.; Sharpless, K. B. *Tetrahedron Lett.* **1991**, *32(32)*, 3965-3968.

10. Green, G.; Griffith, W. P.; Hollinshead, D. M.; Ley, S. V.; Schröder, M. *J. Chem. Soc., Perkin Trans.* **1984**, 681. Griffith, W. P.; Ley, S. V.; Whitcombe, G. P.; White, A. D. *J. Chem. Soc., Chem. Commun.* **1987**, 1625.

11. a) Groves, J. T.; Quinn, R. *Inorg. Chem.* **1984**, *23*, 3844-3846. Groves, J. T.; Quinn, R. *J. Am. Chem. Soc.* **1985**, *107*, 5790. Llobet, A.; Groves, J. T.; Ahn, K.-H. *Inorg. Chem.* **1987**, *26*, 3831-3832.

12. Lyons, J. E.; Ellis, P. E., Jr. *Coord. Chem. Rev.*, **1990**, *105*, 181-193. Lyons, J. E.; Ellis, P. E., Jr. *Cat. Lett.*, **1991**, *8*, 45-52.

13. a) Che, C.-M.; Leung, W.-H.; Poon, C.-K. *J. Chem. Soc., Chem. Commun.* **1987**, 173. Che, C.-M.; Leung, W. H. *J. Chem. Soc., Chem. Commun.* **1987**, 1376. Che, C.-M.; Lee, W.-O. *J. Chem. Soc., Chem. Commun.* **1988**, 881. Lau, T.-C.; Che, C.-M.; Lee, W.-O.; Poon, C.-K. *J. Chem. Soc., Chem. Commun.* **1988**, 1406. Che, C.-M.; Tang, W.-T.; Lee, W.-O.; Wong, W.-T.; Lai, T.-F. *J. Chem. Soc., Dalton* **1989**, 2011. Che, C.-M.; Wong, K.-Y. *J. Chem. Soc., Dalton* **1989**, 2065. Che, C.-M.; Tang, W.-T.; Wong, W.-T.; Lai, T.-F. *J. Am. Chem. Soc.* **1989**, *111*, 9048. Che, C.-M.; Leung, W.-H.; Li, C.-K.; Poon, C.-K. *J. Chem. Soc., Dalton* **1991**, 379.

b) Bailey, C. L.; Drago, R. S. *J. Chem. Soc., Chem. Commun.* **1987**, 179. Goldstein, A. S.; Drago, R. S. *J. Chem. Soc., Chem. Commun.* **1991**, 21.

c) El-Hendawy, A. M.; Griffith, W. P.; Taha, F. I.; Moussa, M. N. *J. Chem. Soc., Dalton* **1989**, 901. Griffith, W. P.; Jolliffe, J. M.; Ley, S. V.; Willimas, D. J. *J. Chem. Soc., Chem. Commun.* **1990**, 1219.

d) Dovletoglou, A.; Adeyemi, S. A.; Lynn, M. H.; Hodgeson, D. J.; Meyer, T. J. *J. Am. Chem. Soc.* **1990**, *112*, 8989-8990.

14. Leung, W.-H.; Che, C. M. *J. Am. Chem. Soc.* **1989**, *111*, 8812.

15. a) Che, C.-M.; Yam, V. W.-W. *J. Am. Chem. Soc.* **1987**, *109*, 1262. Wong, K.-Y.; Che, C.-M.; Anson, F. C. *Inorg. Chem.* **1987**, *26*, 737. Che, C.-M.; Yam, V. W.-W.; Mak, T. C. *J. Am. Chem. Soc.* **1990**, *112*, 2284. Che, C.-M.; Ho, C.; Lau, T. C. *J. Chem. Soc., Dalton* **1991**, 1259. Che, C.-M.; Ho, C.; Lai, T.-C. *J. Chem. Soc., Dalton* **1991**, 1910.

b) Raven, S. J.; Meyer, T. J. *Inorg. Chem.* **1988**, *27*, 4478-4483.

c) Denggel, A. C.; Griffith, W. P.; O'Mahoney, C. A.; Williams, D. J. *J. Chem. Soc.*, **1989**, 1720.

16. Llobet, A.; Hodgson, D. J.; Meyer, T. J. *Inorg. Chem* **1990**, *29*, 3760-3766.

17. Samuels, G. J.; Meyer, T. J. *J. Am. Chem. Soc.* **1981**, 307-312. Meyer, B. A.; Sipe, B. K.; Meyer, T. J. *Inorg. Chem.* **1981**, *20*, 1475-1480. Binstead, R. A.; Moyer, B. A.; Samuels, G. J.; Meyer, T. J. *J. Am. Chem. Soc.* **1981**, *103*, 2897-2899. Thompson, M. S.; Meyer, T. J. *J. Am. Chem. Soc.* **1982**, *104*, 4106-4115. Thompson, M. S.; Meyer, T. J. *J. Am. Chem. Soc.* **1982**, *104*, 5070-5076. Thompson, M. S.; De Giovani, W. F.; Moyer, B. A.; Meyer, T. J. *J. Org. Chem.* **1984**, *49*, 4972-4977. Dobson, J. C.; Seok, W. K.; Meyer, T. J. *Inorg. Chem.* **1986**, *25(10)*, 1513-1514. Roecker, L.; Meyer, T. J. *J. Am. Chem. Soc.* **1986**, *108*, 4066-4073. Roecker, L.; Meyer, T. J. *J. Am. Chem. Soc.* **1987**, *109*, 746-754. Roecker, L.; Dobson, J. C.; Vining, W. J.; Meyer, T. J. *Inorg. Chem.* **1987**, *26*, 779-781. Seok, W. K.; Dobson, J. C.; Meyer, T. J. *Inorg. Chem.* **1988**, *27*, 3-5.

18. a) Marmion, M. E.; Takauchi, K. J. *J. Am. Chem. Soc.* **1986**, *108*, 510. Marmion, M. E.; Takeuchi, K. J. *J. Chem. Soc., Chem. Commun.* **1987**, 1396. Leising, R. A.; Takeuchi, K. J. *Inorg. Chem.* **1987**, 4391. Marmion, M. E.; Takeuchi, K. J. *J. Chem. Soc., Dalton* **1988**, 2385.

b) Ho, C.; Che, C.-M.; Lau, T.-C. *J. Chem. Soc., Dalton* **1990**, 967. Che, C.-M.; Ho, C.; Lau, T.-C. *J. Chem. Soc., Dalton* **1991**, 1901.

19. Mayer, J. M. *Comments Inorg. Chem.*, **1988**, *8*, 125-135.

20. Breiter, M. W. *Electrochemical Processes in Fuel Cells*, Anorganishe und Allgemeine Chemie in Einzeldarstellungen 9; Springer-Verlag: New York, 1969. Archer, D. H. *et al., Energy Conversion Systems*; Grimes, P. G., Ed.; Chemical Engineering Progress Symposium Series; American Institute of Chemical Engineers: New York, 1967. Bockris, J. O'M.; Srinivasan, S. *Fuel Cells: Their Electrochemistry*; McGraw-Hill: New York, 1969.

21. Griffith, W. P.; Wickins, T. D. *J. Chem. Soc. (A)*, **1968**, 400-404. Brower, D. C.; Templeton, J. L.; Mingos, D. M. P. *J. Am. Chem. Soc.*, **1987**, *109*, 5203-5208. Mingos, D. M. P. *J. Organomet. Chem.*, **1979**, C29-C33.

22. Dobson, J. C.; Meyer, T. J. *Inorg. Chem*, **1989**, *28*, 2013-2016.

23. Kläui, W. *Angew. Chem. Int. Ed. Engl.* **1990**, *29*, 627-637.

24. Banbery, H. J.; Hussain, W.; Evans, I. G.; Hamor, T. A.; Jones, C. J. *Polyhedron*, **1990**, *9*, 2549-2551.

25. Power, J. M.; Evertz, K.; Henling, L.; Marsh, R.; Schaefer, W. P.; Labinger, J. A.; Bercaw, J. E. *Inorg. Chem.* **1990**, *29*, 5058-5065.

26. Raven, S. J.; Meyer, T. J. *Inorg. Chem.*, **1988**, *27*, 4478-4483.

Chapter 2

Synthesis and Electrochemistry of the Ruthenium Dimers Incorporating the Tripod Ligand(L_{OMe})$^-$

Abstract:

The ligand salt $Na(L_{OMe})$, where $(L_{OMe}) = \{(\eta^5\text{-}C_5H_5)Co[P(OCH_3)_2(=O)]_3\}^-$, reacts with RuO_4 to afford the edge sharing ruthenium dimer $(L_{OMe})(HO)Ru^{IV}(\mu\text{-}O)_2\text{-}Ru^{IV}(OH)(L_{OMe})$ (**1**). From **1**, homovalent oxidation states from $Ru^V\text{-}Ru^V$ to $Ru^{II}\text{-}Ru^{II}$ are electrochemically accessible. A $Ru^V\text{-}Ru^V$ dimer, two $Ru^{IV}\text{-}Ru^{IV}$dimers, and two $Ru^{III}\text{-}Ru^{III}$ dimers have been isolated. The $Ru^{III}\text{-}Ru^{III}$ dimers, with edge-sharing and face-sharing coordination geometries, interconvert in water. As in its bulk chemistry, **1** exhibits two electron electrochemistry including quasi-reversible $Ru^{IV}\text{-}Ru^{IV}/Ru^{III}\text{-}Ru^{III}$ and $Ru^{III}\text{-}Ru^{III}/Ru^{II}\text{-}Ru^{II}$ redox couples and an electrocatalytic $Ru^V\text{-}Ru^V/Ru^{IV}\text{-}Ru^{IV}$ couple. The latter implies a reactive $Ru^V\text{-}Ru^V$ species. The potential of the $Ru^V\text{-}Ru^V/Ru^{IV}\text{-}Ru^{IV}$ couple appears surface-dependent, suggesting that electron transfer from **1** can occur by at least two types of electrode interactions. The oxidation/protonation manifold of the dimer system was explored through a potential versus pH dependence survey for each couple; the reactive $Ru^V\text{-}Ru^V$ species appears to be the protonated dioxo complex. Crossover experiments between $(L_{OMe})^-$ and $(L_{OEt})^-$ based dimers produced no evidence for dimer-monomer equilibria with the $Ru^V\text{-}Ru^V$, $Ru^{IV}\text{-}Ru^{IV}$, and $Ru^{III}\text{-}Ru^{III}$ dimers. In addition, the terminal ligands of the edge-sharing $Ru^{III}\text{-}Ru^{III}$ dimer were found to be relatively labile while those of the $Ru^{IV}\text{-}Ru^{IV}$ were found to be inert to exchange.

Introduction

This chapter presents the synthesis and electrochemical survey of the accessible oxidation states of $(L_{OMe})(HO)Ru^{IV}(\mu\text{-}O)_2Ru^{IV}(OH)(L_{OMe})$ (**1**) (where $L_{OMe}^- = [(\eta^5\text{-}C_5H_5)Co\{P(O)(OCH_3)_2\}_3]^-$) (Figure 2.1).

Figure 2.1 . Structure of $(L_{OMe})(HO)Ru^{IV}(\mu\text{-}O)_2Ru^{IV}(OH)(L_{OMe})$ (**1**).

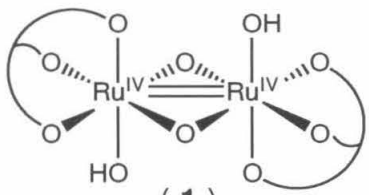

(**1**)

Briefly, the dimer **1** is prepared in the neutral form by the reaction of $Na(L_{OMe})$ and RuO_4. The dimer is then easily protonated to $[(L_{OMe})(H_2O)Ru^{IV}(\mu\text{-}O)_2Ru^{IV}(OH_2)(L_{OMe})]\text{-}[CF_3SO_3]_2$ ($[H_2\mathbf{1}][CF_3SO_3]_2$) with CF_3SO_3H. This protonation is convenient for purification and storage. Oxidation of this salt with iodosobenzene affords $[(L_{OMe})(O)Ru^{V}(\mu\text{-}O)_2\text{-}Ru^{V}(O)(L_{OMe})]$ (**2**) which appears to easily oxidize substrates. The electrochemical reduction of **1** in acidic buffer affords $[(L_{OMe})(H_2O)Ru^{III}(\mu\text{-}OH_2)(\mu\text{-}OH)Ru^{III}(OH_2)(L_{OMe})][CF_3SO_3]_3$ ($[H\mathbf{3}][CF_3SO_3]_3$) and the chemical reduction with zinc/mercury amalgam with precipitation with $CH_3C_6H_4SO_3H$ affords $[(L_{OMe})(H_2O)Ru^{III}(\mu\text{-}OH)_2Ru^{III}(OH_2)(L_{OMe})][CF_3SO_3]\text{-}[4\text{-}CH_3C_6H_4SO_3]$ ($[\mathbf{3}][CF_3SO_3][4\text{-}CH_3C_6H_4SO_3]$). While the $Ru^{V}\text{-}Ru^{V}$ and $Ru^{IV}\text{-}Ru^{IV}$ edge-sharing structures appear stable, the $Ru^{III}\text{-}Ru^{III}$ dimer $[\mathbf{3}]^{2+}$ reversibly rearranges in alkaline buffer to the face sharing dimer $[(L_{OMe})Ru^{III}(\mu\text{-}OH_2)(\mu\text{-}OH)_2Ru^{III}(L_{OMe})]^{2+}$ ($[\mathbf{4}]^{2+}$). All of these complexes are diamagnetic (in spite of d^3 and d^5 ruthenium centers) suggesting a form of electronic coupling between the metal centers. Such coupling may encourage two electron oxidation chemistry.

Indeed, two electron processes dominate the aqueous electrochemistry of **1** which includes two reductions to Ru^{III}-Ru^{III} and Ru^{II}-Ru^{II} oxidation states and an oxidation to the Ru^{V}-Ru^{V} oxidation state (Section 2.2). The absence of one electron electrochemistry and mixed valent complexes suggests that such mixed valent states are unstable to the homovalent states. Mirroring the observations from solutions chemistry, the Ru^{IV}-Ru^{IV}, Ru^{III}-Ru^{III}, and Ru^{II}-Ru^{II} species appear stable on the electrochemical time scale while the Ru^{V}-Ru^{V} appears to electrocatalyze the oxidation of substrates.

Strangely, Ru^{V}-Ru^{V}/Ru^{IV}-Ru^{IV} redox couple can appear at two different potentials depending on the electrode surface. The couple appears at the higher potential at basal-plane graphite electrodes and at the lower potential at edge-plane graphite electrodes. This effect may be due to different electron transfer rates at two different carbon electrode sites. Though the discussion of this effect contributes little to the survey of the oxidation manifold of these dimers, it needs to be addressed to properly interpret the electrochemistry of this couple. This effect will also be of interest to those who study chemical interactions at electrode surfaces.

The pH dependence for the three redox couples of **1** was surveyed from pH 2.3 to 11.7. These data allows the protonation state for each oxidation state to be assigned over the pH range. This reveals a detailed picture of the dimer oxidation manifold. For example, the reaction Ru^{V}-Ru^{V} species in the electrocatalysis is likely the monoprotonated monocation $[H2]^{+}$. This experiment and the chemical and electrochemical surveys above portray the oxidation manifold in water.

Beyond the electrochemistry, two other chemical observations were made. First, the Ru^{V}-Ru^{V}, Ru^{IV}-Ru^{IV}, and Ru^{III}-Ru^{III} dimers do not dissociate into monomers under normal conditions; the dimers represent the actual active species. This becomes an important point in Chapters 3 and 4. Further, the terminal aquo ligands of Ru^{III}-Ru^{III} dimers appear labile to substitution by strong donors while those of the Ru^{IV}-Ru^{IV} dimers appear inert. The rearrangements of the Ru^{III}-Ru^{III} dimers are consistent with the observed lability. This

observation becomes important in interpreting the unusual oxidation chemistry of **1**. Both observations will be important in the mechanistic interpretation of the oxidation chemistry of this system.

Results and Discussion

2.1. Synthesis of Ru^{V}-Ru^{V}, Ru^{IV}-Ru^{IV}, Ru^{III}-Ru^{III} Dimers.

The Ru^{IV}-Ru^{IV} dimer, $[(L_{OMe})(HO)Ru^{IV}(\mu\text{-}O)_2Ru^{IV}(OH)(L_{OMe})]$ (**1**) where $(L_{OMe})^- = \{(\eta^5\text{-}C_5H_5)Co[P(=O)(OMe)_2]_3\}^-$ is readily synthesized, and the analogous Ru^{V}-Ru^{V} and Ru^{III}-Ru^{III} dimers are readily prepared from **1**. The preparation of **1** is similar to that reported for the analog with $(L_{OEt})^- = \{(\eta^5\text{-}C_5H_5)Co[P(=O)(OEt)_2]_3\}^-$ with the primary differences being due to substitution of methoxy groups for ethoxy groups increasing water solubility.[1] Dimer **1** is prepared in a biphasic reaction between RuO_4 in CCl_4 and $Na(L_{OMe})$ in 1% aqueous H_2SO_4 from which **1** is extracted with CH_2Cl_2 (Figure 2.2). Addition of excess acid to yellow-green **1** affords the emerald green $[(L_{OMe})(H_2O)Ru^{IV}(\mu\text{-}O)_2Ru^{IV}(OH_2)(L_{OMe})]^{2+}$ ($[H_21]^{2+}$), which readily precipitates with counterions other than HSO_4^- (Figure 2.3). Both **1** and $[H_21](CF_3SO_3)_2$ are stable in solution under air, but **1** slowly decomposes in the solid state. The dimer $[H_21](CF_3SO_3)_2$ salt is stable indefinitely, and is easily purified by recrystallization from dilute aqueous CF_3SO_3H.

Figure 2.2. Synthesis of **1**.

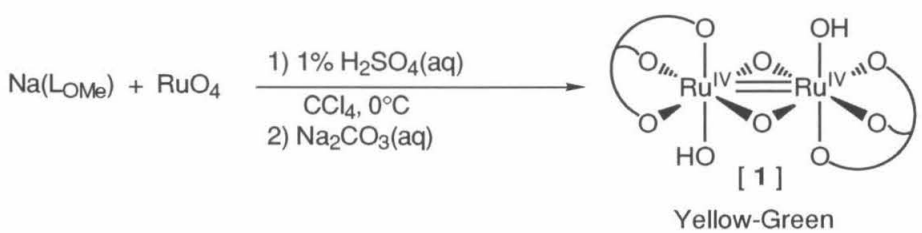

Figure 2.3. Synthesis of $[H_21][CF_3SO_3]_2$.

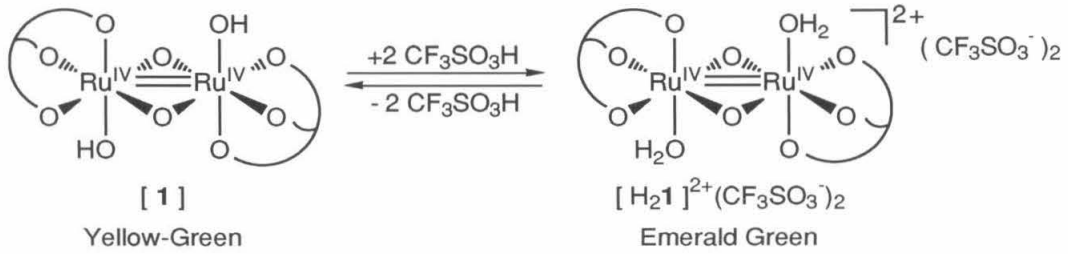

Treatment of an acetonitrile solution of **1** with excess iodosobenzene in acetonitrile and then with an equivalent of base gives the purple Ru^V-Ru^V dimer $[(L_{OMe})(O)Ru^V(\mu\text{-}O)_2\text{-}Ru^V(O)(L_{OMe})]$ (**2**) which crystallizes upon concentration in CH_3CN (Figure 2.4). This crude **2** often contains an unidentified brown impurity that accelerates the decomposition of **2** upon exposure to moisture. While crude **2** reverts to **1** in air, it is stable when stored under argon.[2] A similar situation with $[(L_{OEt})(O)Ru^V(\mu\text{-}O)_2Ru^V(O)(L_{OEt})]$ ($\mathbf{2_{Et}}$) was encountered earlier where the varying instability of different preparations of $\mathbf{2_{Et}}$ implicated an impurity as an agent of decomposition.[3] Fortunately, recrystallization from CH_3CN affords pure and air stable **2**.

Figure 2.4. Synthesis of $(L_{OMe})(O)Ru^V(\mu\text{-}O)_2Ru^V(O)(L_{OMe})$ (**2**).

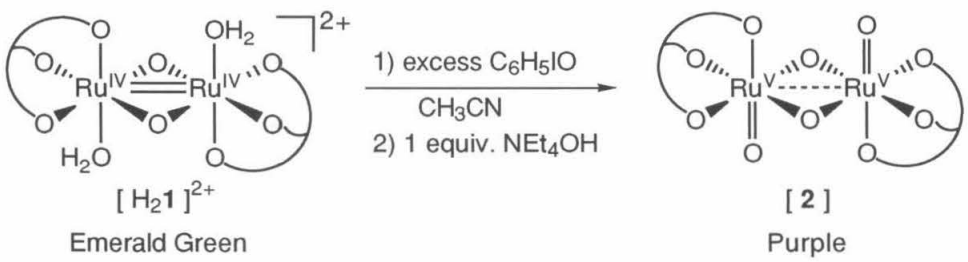

The ^1H NMR spectra and physical appearance of **1**, $[H_21]^{2+}$, and **2** dimers are parallel in all respects to those of the $(L_{OEt})^-$ analogs characterized by X-ray crystallography (see Experimental).[1,4] In particular, the diagnostic triplet (12 H), triplet (12 H), doublet (12 H) ^1H *NMR* splittings for the methoxy groups of the $(L_{OMe})^-$ ligand are indicative of two identical metal centers with mirror plane symmetry. As described in footnote 4, a mirror plane through

the $(L_{OMe})^-$ ligand splits its six methoxy groups into three pairs. The two triplets correspond to methoxy groups associated to a pair of equivalent and virtually coupled phosphorus atoms, and the doublet corresponds to methyl groups on the symmetry independent phosphite. This characteristic splitting pattern indicates that the structures of these dimers are wholly analogous to those of the $(L_{OEt})^-$ analogs.

Chemical and electrochemical reduction of **1** readily affords Ru^{III}-Ru^{III} dimers. The treatment of **1** with excess Zn/Hg amalgam in water affords a yellow solution that grows orange (likely due to excess reduction) with prolonged stirring. After the solutions was decanted from the remaining amalgam, the orange solution again turns yellow upon exposure to air. Addition of 4-$CH_3C_6H_4SO_3H$ precipitates the moderately air-sensitive yellow product. The elemental analysis and ^1H NMR spectrum of this product are consistent with the formulation $[(L_{OMe})(H_2O)Ru^{III}(\mu\text{-}OH)_2Ru^{III}(OH_2)(L_{OMe})][CF_3SO_3][4\text{-}CH_3C_6H_4SO_3]$ ($[\mathbf{3}][CF_3SO_3][4\text{-}CH_3C_6H_4SO_3]$) illustrated in Figure 2.5. Electroreduction (+0.15 V versus SCE) of an aqueous solution (pH 2.5) of **1** affords the protonated Ru^{III}-Ru^{III} complex $[H\mathbf{3}]^+$ illustrated in Figure 2.6.

Electroreduction of **1** (-0.55 V versus SCE) in alkaline (pH~11) buffer still results in the net two electron reduction per equivalent of dimer but affords a different Ru^{III}-Ru^{III} dimer. The ^1H NMR spectrum (D_2O) of this complex exhibits a 1:1:1:1 pseudo-quartet $(L_{OMe})^-$ splitting pattern also observed for the free ligand (at a different shift). This splitting pattern is

Figure 2.5. Synthesis of $[(L_{OMe})(H_2O)Ru^{III}(\mu\text{-}OH)_2Ru^{III}(OH_2)(L_{OMe})]^{2+}$ ($[\mathbf{3}]^{2+}$).

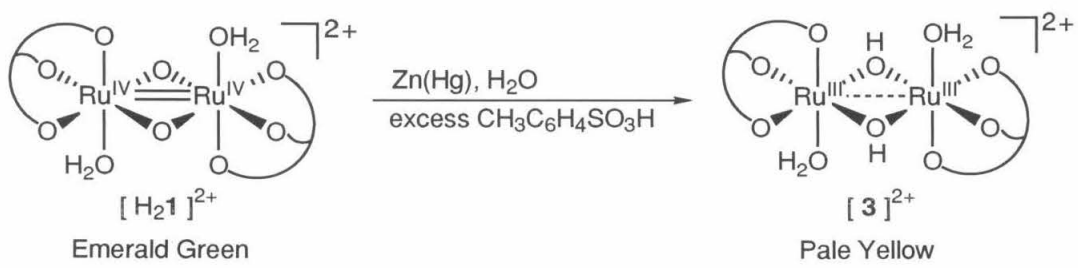

Figure 2.6. Synthesis of $[(L_{OMe})(H_2O)Ru^{III}(\mu\text{-}OH)(\mu\text{-}OH_2)Ru^{III}(OH_2)(L_{OMe})]^{3+}$ ($[H3]^{3+}$).

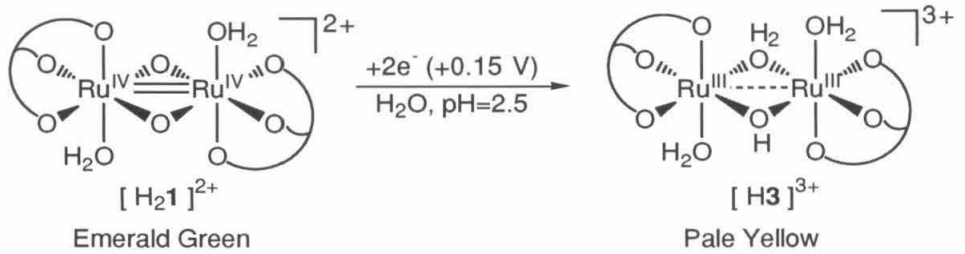

indicative of C_3 ligand symmetry and is due to the equivalent methoxy groups being split by three equivalent and virtually-coupled phosphorous atoms. In addition to the ^1H NMR splitting pattern, the evident diamagnetism of the new Ru^{III}-Ru^{III} product suggests it is a dimer with strongly coupled ruthenium centers. These observations are consistent with three nearly identical bridging ligands with rapid exchange of protons (and deuterons) with D_2O solvent. The analytical data are consistent with the formulation $[(L_{OMe})Ru^{III}(\mu\text{-}OH)_2(\mu\text{-}OH_2)Ru^{III}(L_{OMe})][CF_3SO_3]_2$ ($[\mathbf{4}][CF_3SO_3]_2$) illustrated in Figure 2.7.

Figure 2.7. Synthesis of $[(L_{OMe})Ru^{III}(\mu\text{-}OH)_2(\mu\text{-}OH_2)Ru^{III}(L_{OMe})]^{2+}$ ($[\mathbf{4}]^{2+}$).

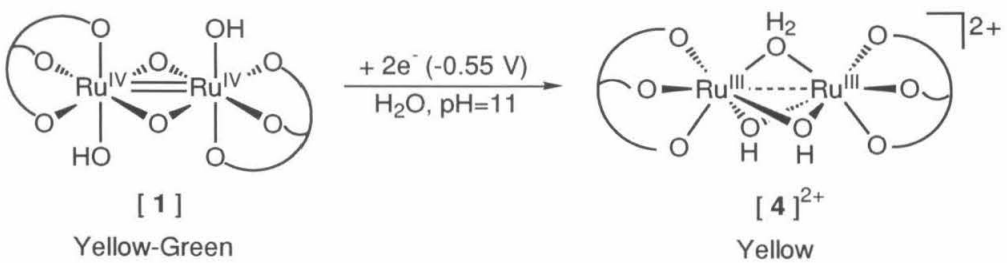

Dimers $[\mathbf{3}]^{2+}$ and $[\mathbf{4}]^{2+}$ interconvert in aqueous solution. The dimer $[\mathbf{3}]^{2+}$ is favored in acidic solutions and $[\mathbf{4}]^{2+}$ is favored in alkaline solutions. As mentioned later in this chapter, $[\mathbf{3}]^{2+}$ is deprotonated at high pH; perhaps under these conditions one terminal ligand is nucleophilic enough to bridge between the ruthenium centers and displace the other terminal ligand. Nevertheless, this equilibrium is relatively slow between pH 2.5 and 7.0 (Figure 2.8).

Figure 2.8. Interconversion of $[3]^{2+}$ and $[4]^{2+}$.

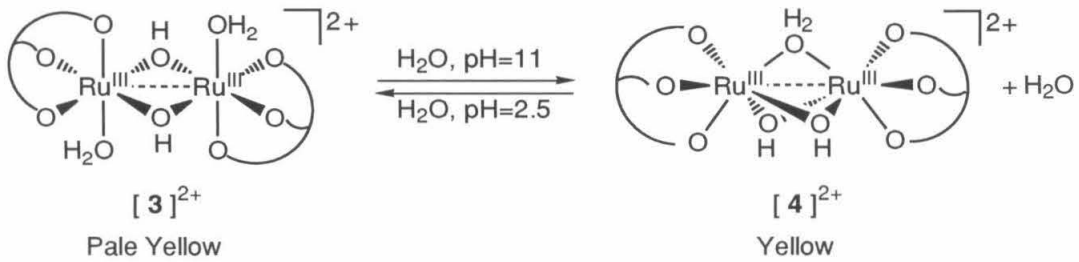

2.2. General Electrochemistry of ***1****.*

Cyclic voltammograms of **1** in pH 7 phosphate buffer (Figure 2.9 and 2.10) exhibit one oxidation (+0.75 V versus SCE) and two reduction waves (+0.10 V and -0.60 V versus SCE). (Figure 2.10 exhibits a similar cyclic voltammogram that does not include the oxidation wave.) The first reduction wave is a reversible two electron wave as measured by coulometry (n=1.95), and thus corresponds to the Ru^{IV}-Ru^{IV}/Ru^{III}-Ru^{III} couple. The reversible nature of this process is consistent with the observed stability of both Ru^{IV}-Ru^{IV} and Ru^{III}-Ru^{III} dimers. At pH 7, the oxidation wave is partially to completely irreversible and the second reduction appears small compared to the reference Ru^{IV}-Ru^{IV}/Ru^{III}-Ru^{III} couple. However, at pH 2.5 (Figure 2.11 and 2.12) both waves exhibit at least partial reversible behavior and oxidation peak currents comparable to that of the Ru^{IV}-Ru^{IV}/Ru^{III}-Ru^{III} couple. This implies the two waves are two electron processes corresponding to the Ru^{V}-Ru^{V}/Ru^{IV}-Ru^{IV} and Ru^{III}-Ru^{III}/Ru^{II}-Ru^{II} couples, respectively, and that both couples are significantly effected by solution chemistry at pH 7.

As mentioned, the enhanced peak currents observed for the Ru^{V}-Ru^{V}/Ru^{IV}-Ru^{IV} redox wave at pH 6.9 suggest electrocatalysis via a reactive Ru^{V}-Ru^{V} species. The peak current of this redox wave increases with the addition of substrates such as methanol. (Compare the Ru^{V}-Ru^{V}/Ru^{IV}-Ru^{IV} redox couple to the Ru^{IV}-Ru^{IV}/Ru^{III}-Ru^{III} couple in Figure 2.13.) This increase in peak current is consistent with the oxidation of substrate by the Ru^{V}-Ru^{V} species to

reform the Ru^{IV}-Ru^{IV} dimer **1** which is reoxidized at the electrode.[5] The smaller electrocatalytic currents without substrate suggest the Ru^{V}-Ru^{V} species is electrooxidizing substrates intrinsic to the buffer such as water or ruthenium dimer itself. In cyclic voltammetry without added substrate, the Ru^{V}-Ru^{V}/Ru^{IV}-Ru^{IV} oxidation does generate secondary redox waves indicative of electroactive fragments from dimer self-attack or degradation (Figure 2.13). This autodegradation seems analogous to the impurity problems noted for the **2** and $\mathbf{2}_{Et}$ dimers. Chapter 3 will address the behavior of this redox couple in greater detail.

In contrast, the behavior of the Ru^{III}-Ru^{III}/Ru^{II}-Ru^{II} redox wave is not as clearly interpreted. Though the Ru^{III}-Ru^{III}/Ru^{II}-Ru^{II} couple appears quasi-reversible, its peak currents decrease with respect to the Ru^{IV}-Ru^{IV}/Ru^{III}-Ru^{III} couple as the pH increases. In principle, the peak currents for the Ru^{III}-Ru^{III}/Ru^{II}-Ru^{II} reduction and the Ru^{IV}-Ru^{IV}/Ru^{III}-Ru^{III} oxidation should be identical since both arise from the same Ru^{III}-Ru^{III} species. The attenuation of the Ru^{III}-Ru^{III} reduction current is consistent with either decreased effective electrode surface area (by incapacitation of electron transfer sites at strong reducing potentials) or decreased effective Ru^{III}-Ru^{III} concentration (or both). The latter explanation is more likely since the observed interconversion of $[\mathbf{3}]^{2+}$ to $[\mathbf{4}]^{2+}$ could deplete the solution of $[\mathbf{3}]^{2+}$. This would result in an apparent decrease in Ru^{III}-Ru^{III} concentration if the potential for the Ru^{III}-Ru^{III}/Ru^{II}-Ru^{II} couple of $[\mathbf{4}]^{2+}$ is significantly lower than that of $[\mathbf{3}]^{2+}$. As mentioned, $[\mathbf{3}]^{2+}$ is the predominant Ru^{III}-Ru^{III} species in acidic conditions. This is consistent with the comparable oxidation peak currents for the Ru^{IV}-Ru^{IV}/Ru^{III}-Ru^{III} and Ru^{III}-Ru^{III}/Ru^{II}-Ru^{II} couples at pH 2.5. (The sharp reduction wave observed at -0.55 V is likely due to reduction of a film of the sparingly soluble $[\mathbf{3}]^{2+}$ formed on the electrode. The small Ru^{III}-Ru^{III}/Ru^{II}-Ru^{II} reduction preceding this wave is probably due to the film inhibiting the reduction of $[\mathbf{3}]^{2+}$ in solution.[6] In alkaline solutions, $[\mathbf{3}]^{2+}$ would rearrange to $[\mathbf{4}]^{2+}$ resulting in attenuation of reduction current from $[\mathbf{3}]^{2+}$ (and no formation of a film). If this is so, the Ru^{IV}-Ru^{IV}/Ru^{III}-Ru^{III} oxidation potentials of $[\mathbf{3}]^{2+}$ and $[\mathbf{4}]^{2+}$ must be nearly equal to explain the insensitivity of this couple to the proposed equilibrium.

Figure 2.9. Cyclic Voltammogram of **1** in pH 6.9 buffer (range: +1.2 V to -0.8 V).

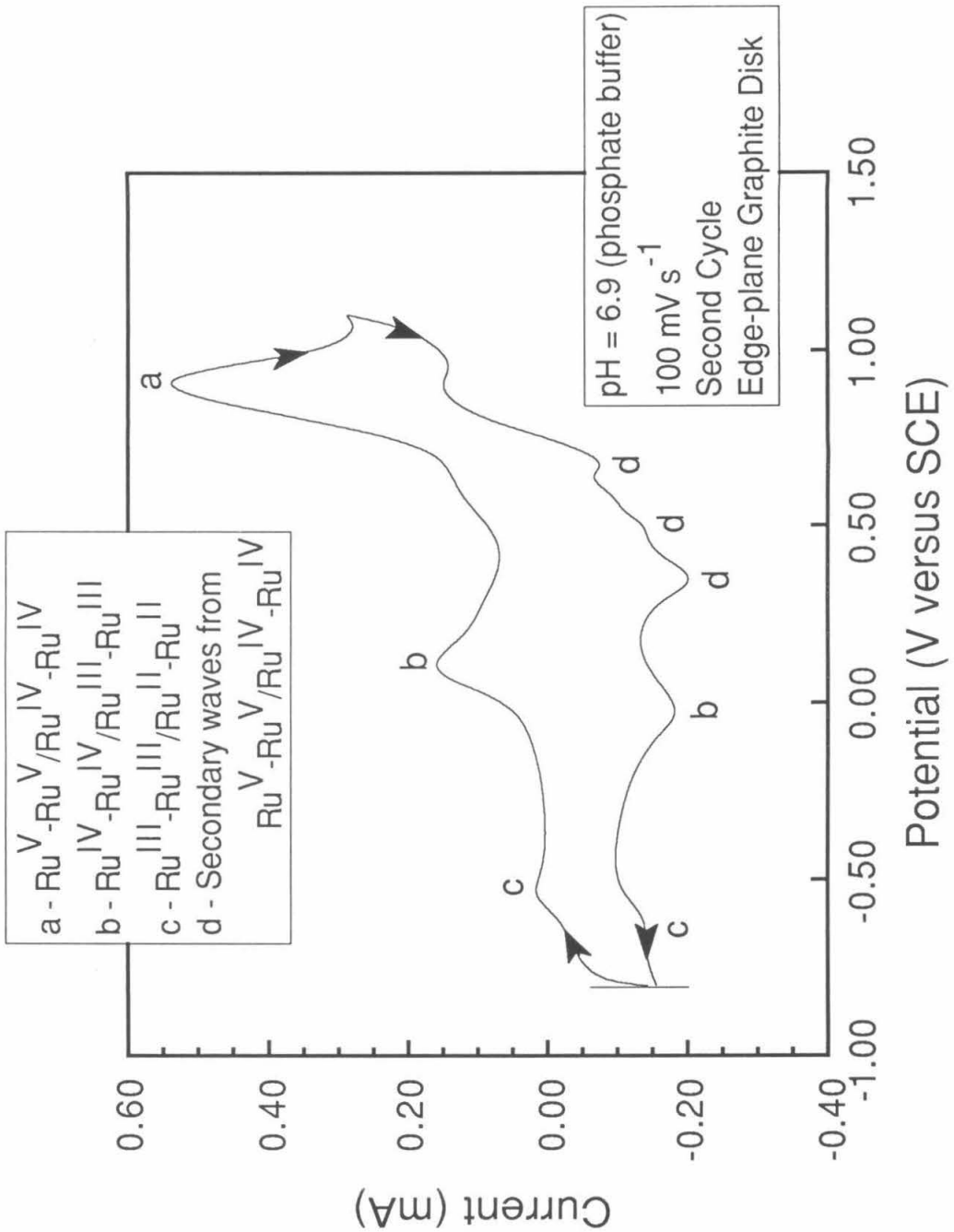

Figure 2.10. Cyclic Voltammogram of **1** in pH 6.9 buffer (range: +0.5 V to -0.9 V).

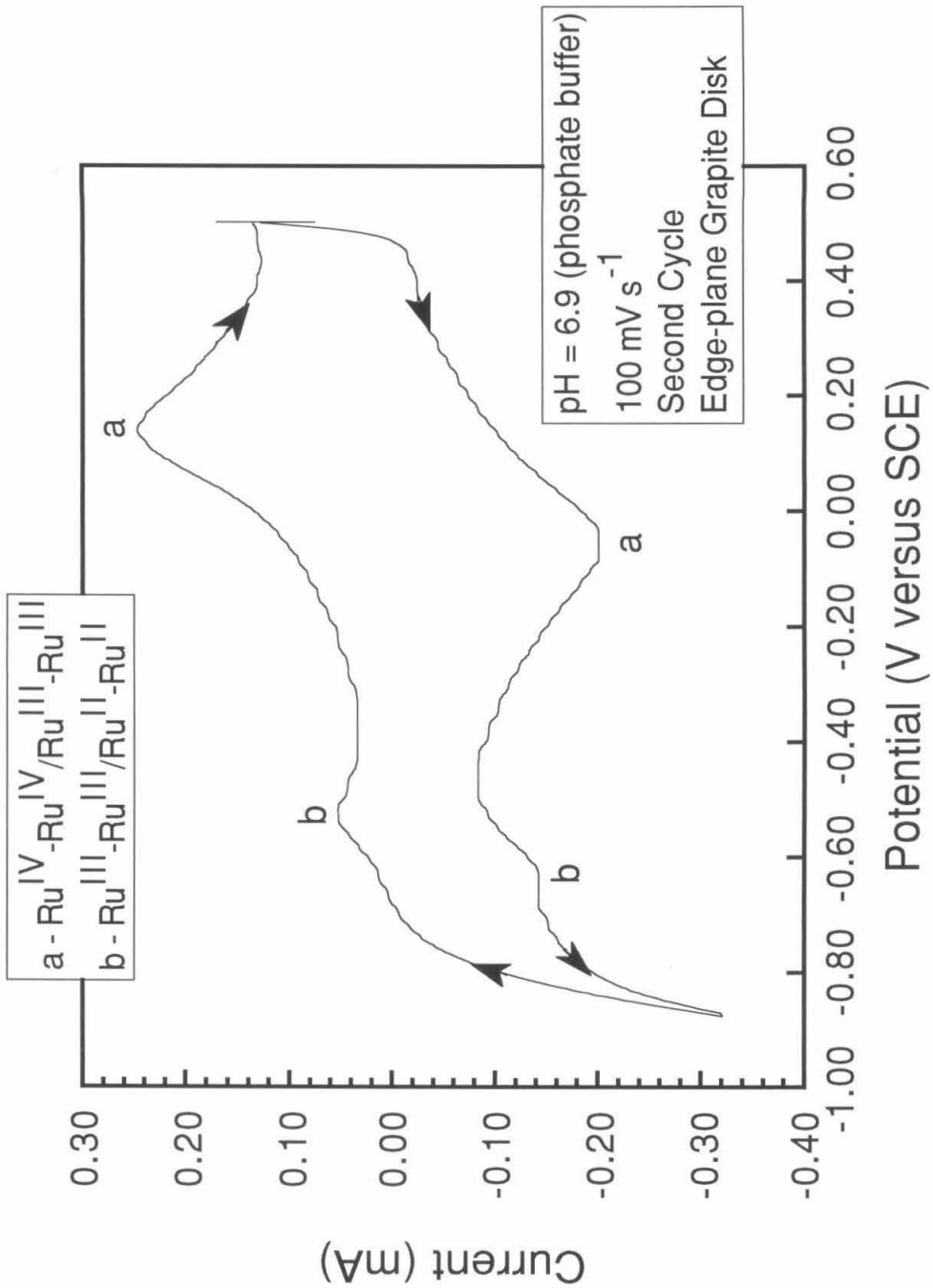

Figure 2.11. Cyclic Voltammogram of **1** in pH 2.5 buffer (range: +1.2 V to -0.8 V).

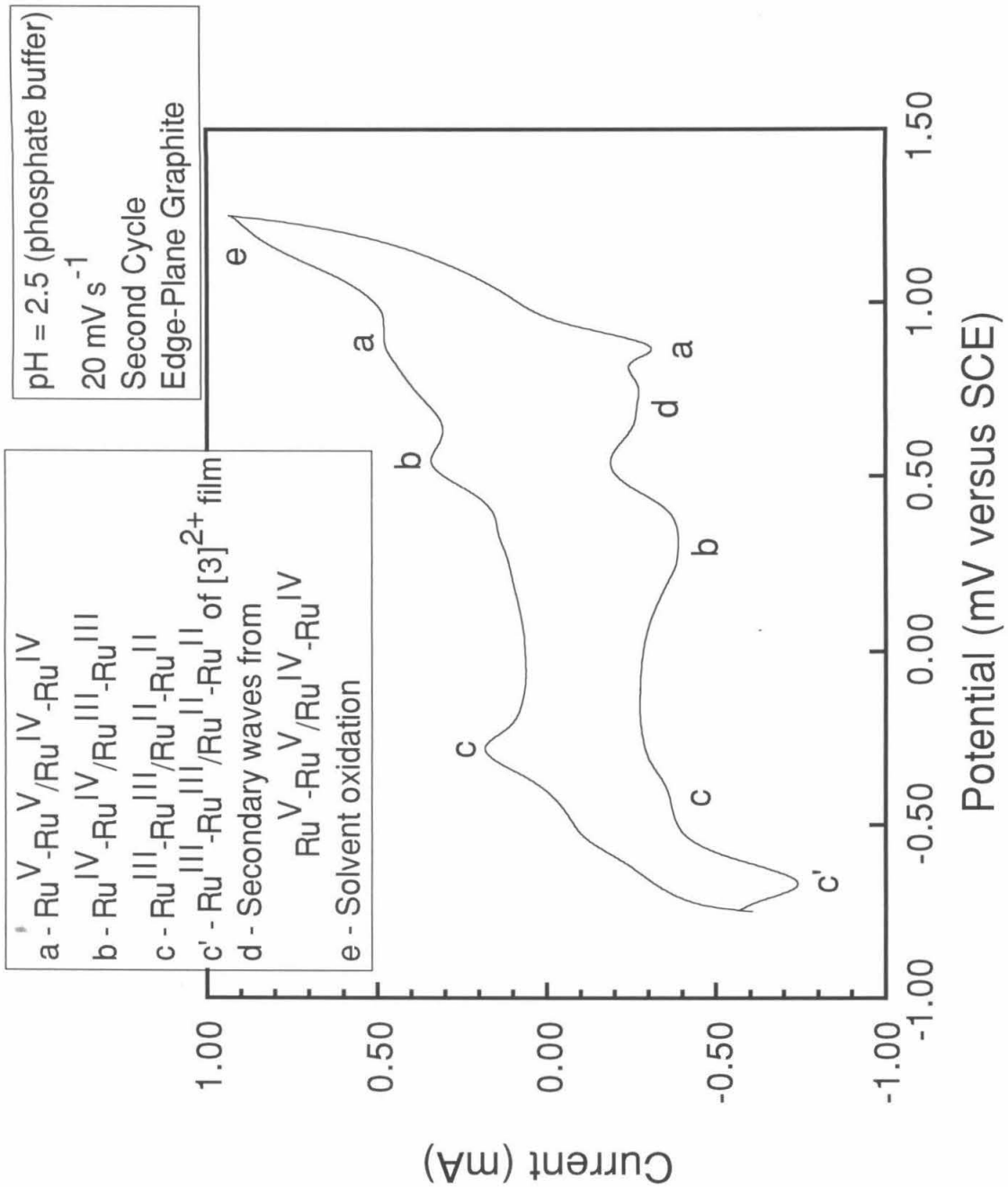

Figure 2.12. Cyclic Voltammogram of 1 in pH 2.5 buffer (range: +0.8 V to -0.8 V).

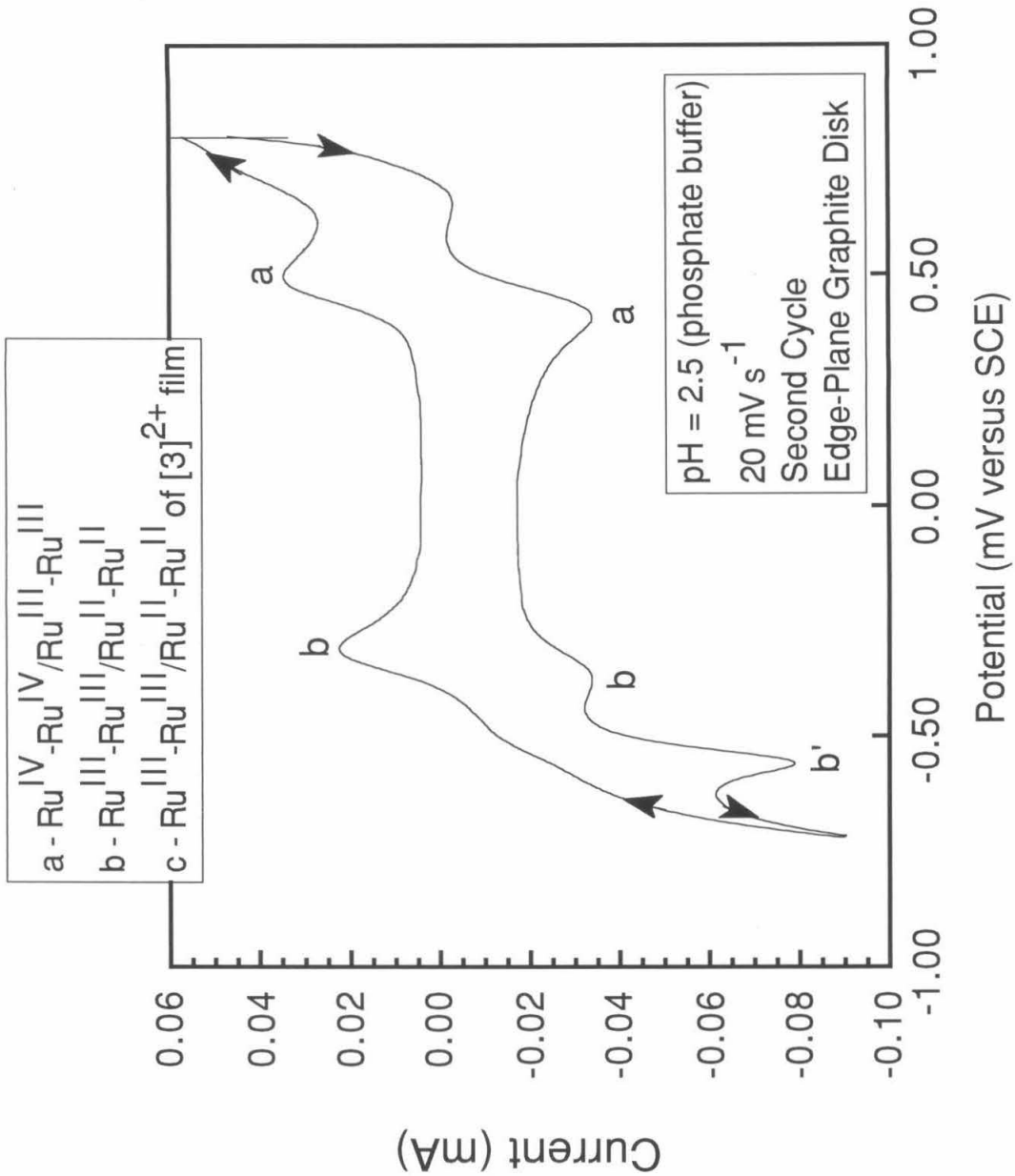

Figure 2.13. Cyclic Voltammogram of **1** in pH 6.9 buffer with and without added methanol.

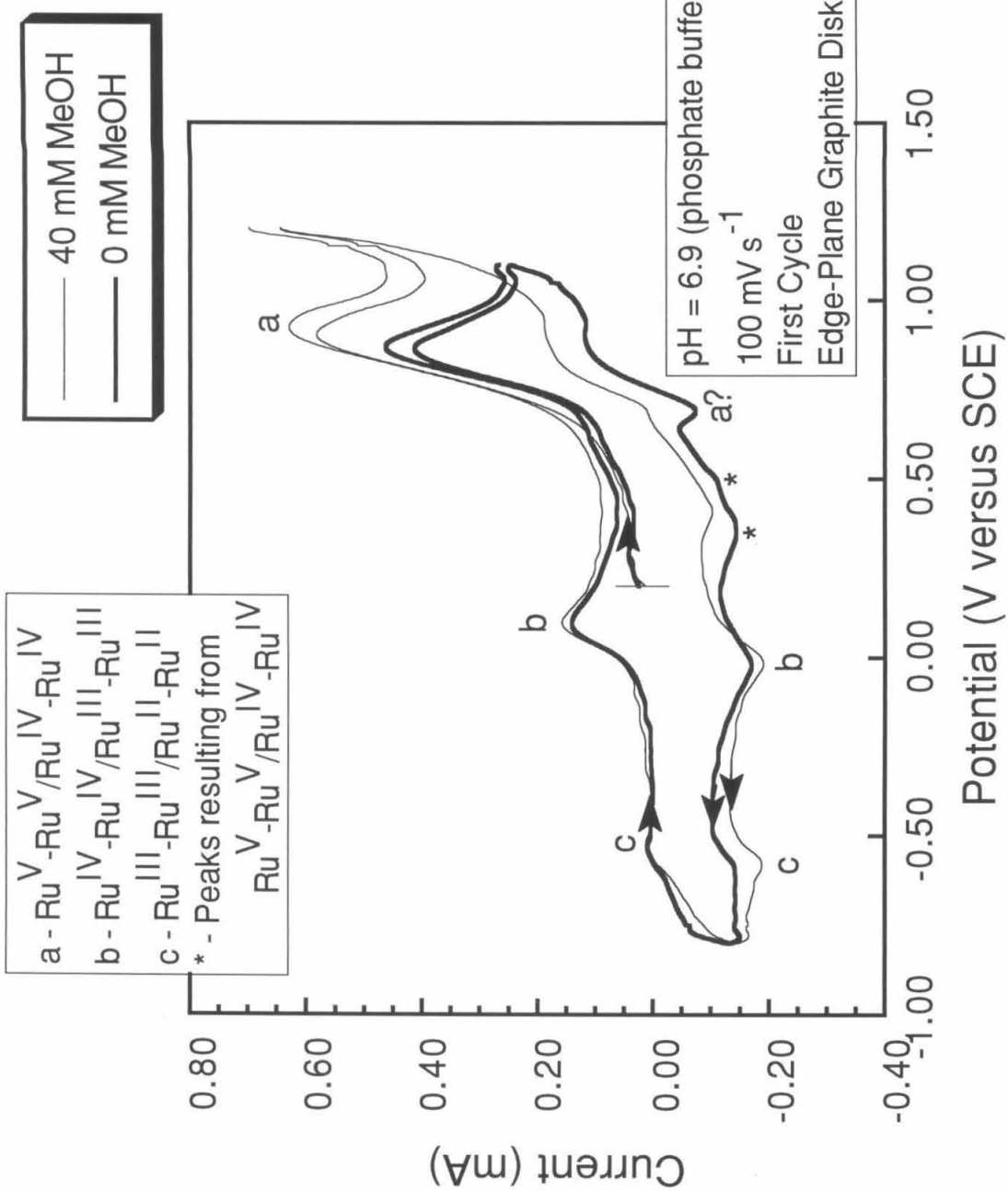

Overall, the aqueous electrochemistry of **1**, like the bulk chemistry, is dominated by two electron processes including two reductions presumably to Ru^{III}-Ru^{III} and Ru^{II}-Ru^{II} species and an oxidation to an Ru^{V}-Ru^{V} species. The electrochemical observation of only homovalent oxidation states suggests that the mixed valent states are unstable with respect to the homovalent states. On the electrochemical time scale the Ru^{IV}-Ru^{IV}, Ru^{III}-Ru^{III}, and Ru^{II}-Ru^{II} species are stable, which is consistent with the isolation of the Ru^{IV}-Ru^{IV} and Ru^{III}-Ru^{III} species described above. The oxidation, however, exhibits enhanced currents indicative of electrocatalytic oxidation of water or dimer itself. This suggests that the Ru^{V}-Ru^{V} species is very reactive in water which is consistent with the described moisture sensitivity of crude Ru^{V}-Ru^{V}.

2.3. *Unusual Electrode Kinetics of Ru^{V}-Ru^{V}/Ru^{IV}-Ru^{IV} Couple.*

Dimer electrochemistry is most clearly observed at graphite electrodes which suppress water oxidation and reduction more prominent on metal electrodes. Strangely, the behavior of the Ru^{V}-Ru^{V}/Ru^{IV}-Ru^{IV} redox couple appears dependent on the type of carbon electrode used. This behavior needed to be addressed to effectively measure and interpret further electrochemistry of the Ru^{V}-Ru^{V}/Ru^{IV}-Ru^{IV} couple.

As shown in the cyclic voltammograms in Figures 2.1 to 2.5, the Ru^{V}-Ru^{V}/Ru^{IV}-Ru^{IV} oxidation appears at +0.80 V at edge plane electrodes in pH 7 buffer. Surprisingly, this oxidation appears at +1.00 V versus SCE at basal-plane graphite electrodes (Figure 2.14). In cyclic voltammetry at glassy carbon electrodes (a mixture of surfaces), the Ru^{V}-Ru^{V}/Ru^{IV}-Ru^{IV} redox couple can appear as two peaks whose relative intensities depend on the potential ranges scanned within the most recent scan cycles (Figure 2.15). At pH 7, the peak at +1.00 V versus SCE is favored when the scan window extends to -0.80 V, and the peak at +0.80 V is favored when the scan window extends to only -0.30 V.

This behavior suggests the peaks correspond to the same oxidation reaction but different heterogeneous electron transfer kinetics. The two redox waves may be due to two electron transfer rates through different interactions with the graphite electrodes. As the electron transfer rate for an oxidation slows, its cyclic voltammetric oxidation wave shifts to higher potentials.[7] This implies that electron transfer at sites predominant on edge-plane graphite is faster than that at sites on basal-plane graphite. This behavior is consistent with basal-plane and edge-plane graphite surfaces possessing different functional groups. The glassy carbon electrode surface likely contains a mixture of surface sites whose proportions depend on the potentials they are subjected to. The faster heterogeneous electron transfer may be attributed to oxygenated sites that are plentiful on reduced edge-plane graphite and glassy carbon surfaces.[8] (Overall, the behavior of the Ru^{V}-Ru^{V}/Ru^{IV}-Ru^{IV} couple suggests that electron transfer occurs by two types of interactions between **1** and carbon surfaces.)

The adhesion of dimer to graphite electrode surfaces further suggests chemical interactions between the dimer and electrode. When a glassy carbon or edge-plane graphite electrode is dipped into a solution of either **1** or $[H_21]^{2+}$ and rinsed, the electrode weakly exhibits electrochemistry of adsorbed dimer. When the Ru^{V}-Ru^{V}/Ru^{IV}-Ru^{IV} couple is scanned, the characteristic electrochemistry rapidly decays suggesting loss of the binding interaction. This behavior suggests that the Ru^{IV}-Ru^{IV} dimer could be either chemically or electrostatically bound to the electrode surface. These binding sites may be the same that allow fast electron transfer from the Ru^{IV}-Ru^{IV} dimer. Perhaps the faster electron transfer is analogous to an "inner sphere" process while the slower electron transfer to the carbon planes of the basal-plane electron is analogous to an "outer sphere" process. The covalent adsorption of complexes to graphite surfaces is precedented. Pentaammineruthenium(II) complexes have been deliberately bound to electrodes through condensation of a dangling organic amine from the complex with oxygenated surface groups.[9] Some organic compounds are also known to spontaneously bind covalently to oxygenated surface functional groups.[10]

Figure 2.14. *Cyclic Voltammogram of* **1** in pH 6.9 buffer at a basal-plane graphite electrode.

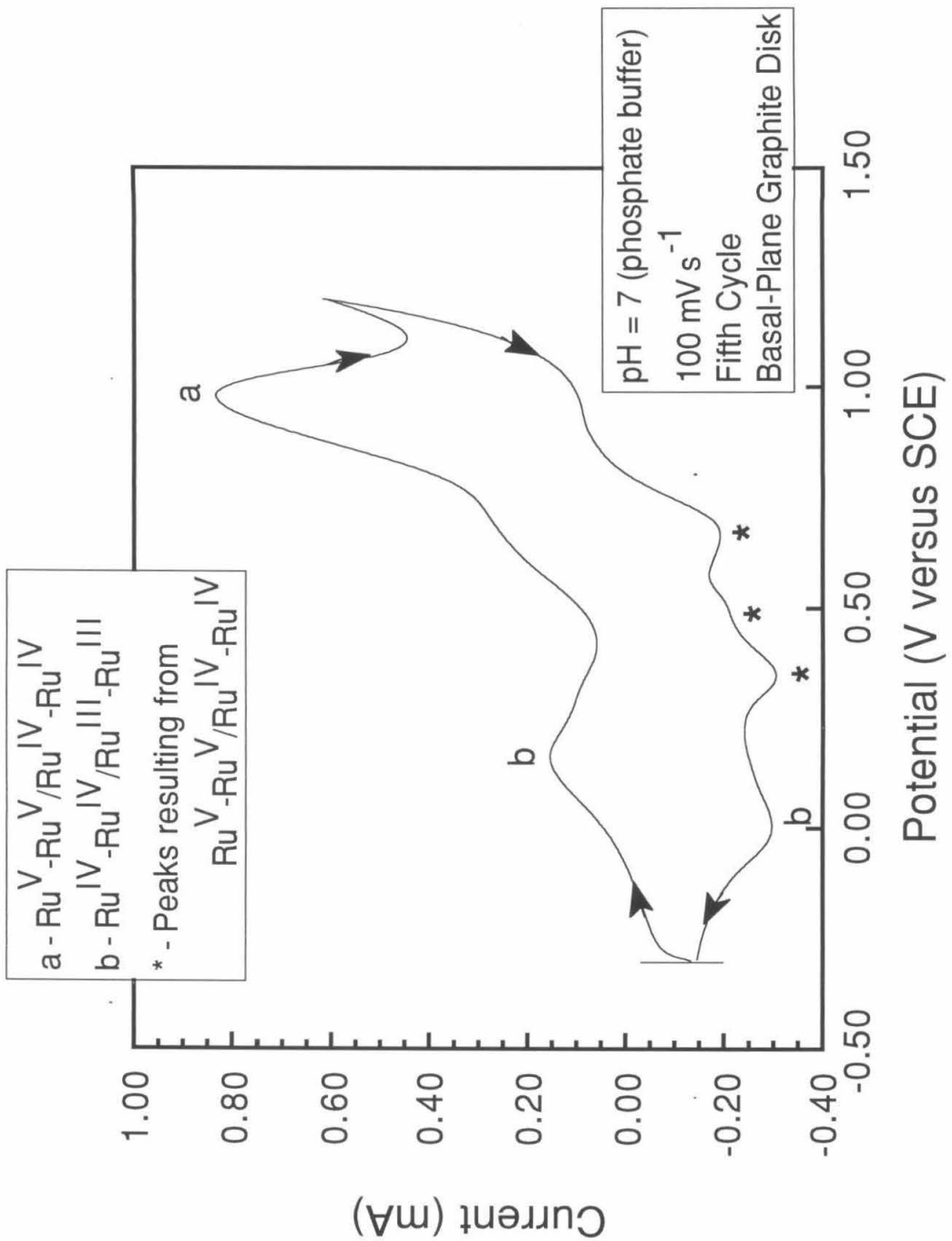

Figure 2.15. Cyclic Voltammogram of 1 in pH 6.9 buffer at a glassy carbon electrode.

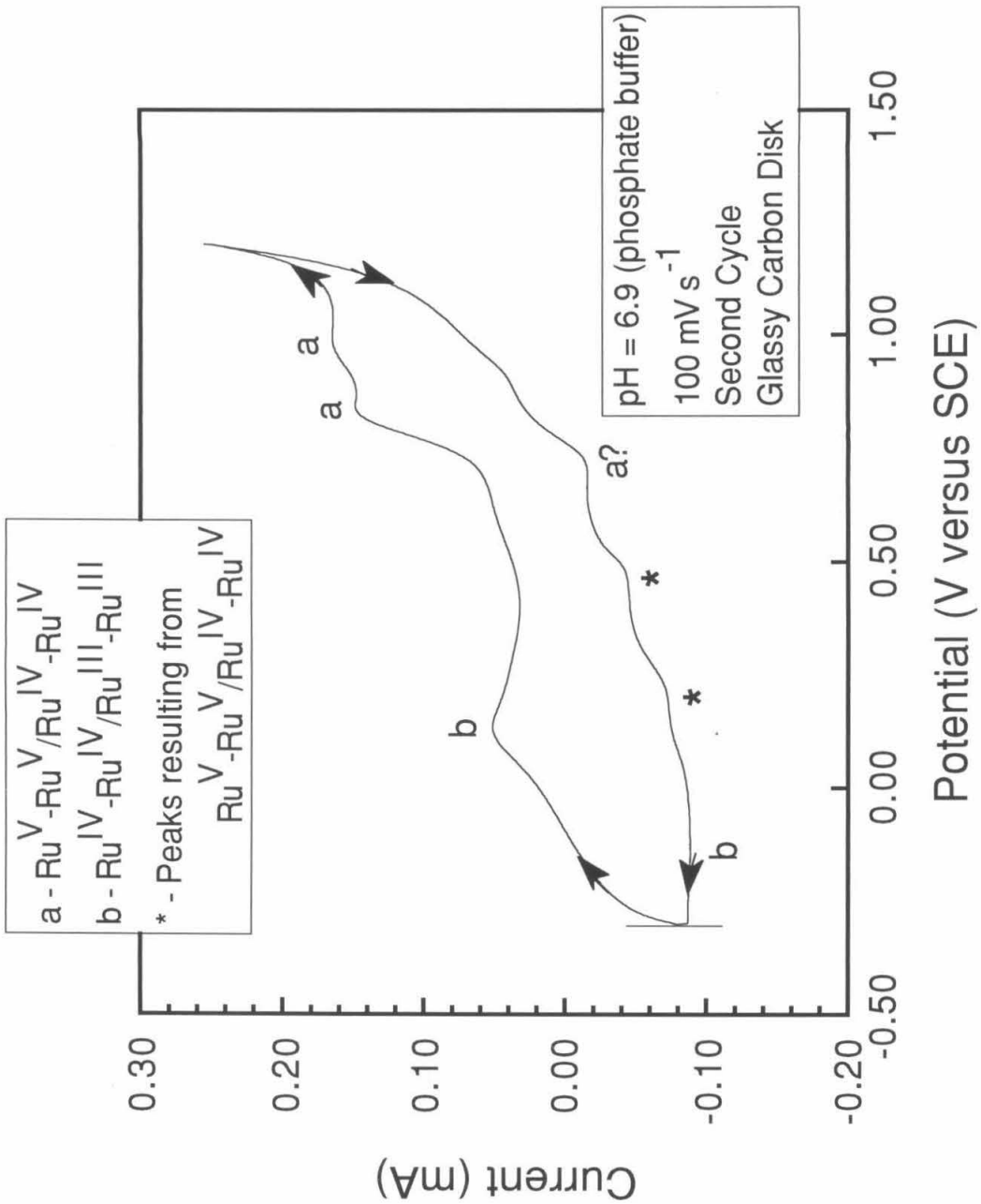

2.4. *Oxidation and Protonation States*

The results from the three previous sections paved the way for a more rigorous analysis of the electrochemistry spanning the accessible oxidation states (the oxidation manifold). The potentials of the three principle redox processes were measured in a buffer as it was titrated from pH 2 to pH 11. Changes in these potentials versus pH are indicative of number of protons involved in each electron transfer. The oxidation and protonation state of each solution species can be deduced from such data. For reversible couples, the Nernst equation relates the change in redox potential versus pH to the number of protons involved in the electron transfer (Figure 2.16).[11] A decrease of 59 mV in the redox potential for every unit increase in pH indicates one proton is added for every electron. A potential versus pH plot of all the redox couples is like an oxidation/protonation state phase diagram. The lines for the redox potentials obviously represent changes in oxidation states. Vertical lines drawn between consecutive couples where they simultaneously change slope represent changes in protonation state. Beginning with the known neutrality of the Ru^{IV}-Ru^{IV} dimer, **1**, this electrochemical survey provides an important overview of the aqueous oxidation chemistry of this system.

Figure 2.16. Example equation and Nernst relation for potential versus pH.

$$O^{x+} + ne^- + mH^+ \rightleftharpoons R^{(x+m-n)+}$$

$$E = E^0 + \frac{RT}{nF}\ln[H^+]^m$$

$$E = E^0 - (0.0591V)\left(\frac{m}{n}\right)(pH)$$

The observed potential versus pH dependencies illustrated in Figure 2.17 offer an overview of the oxidation/protonation manifold for the ruthenium dimers.

Figure 2.17. Plot of Potential versus pH for **1** in aqueous buffer.

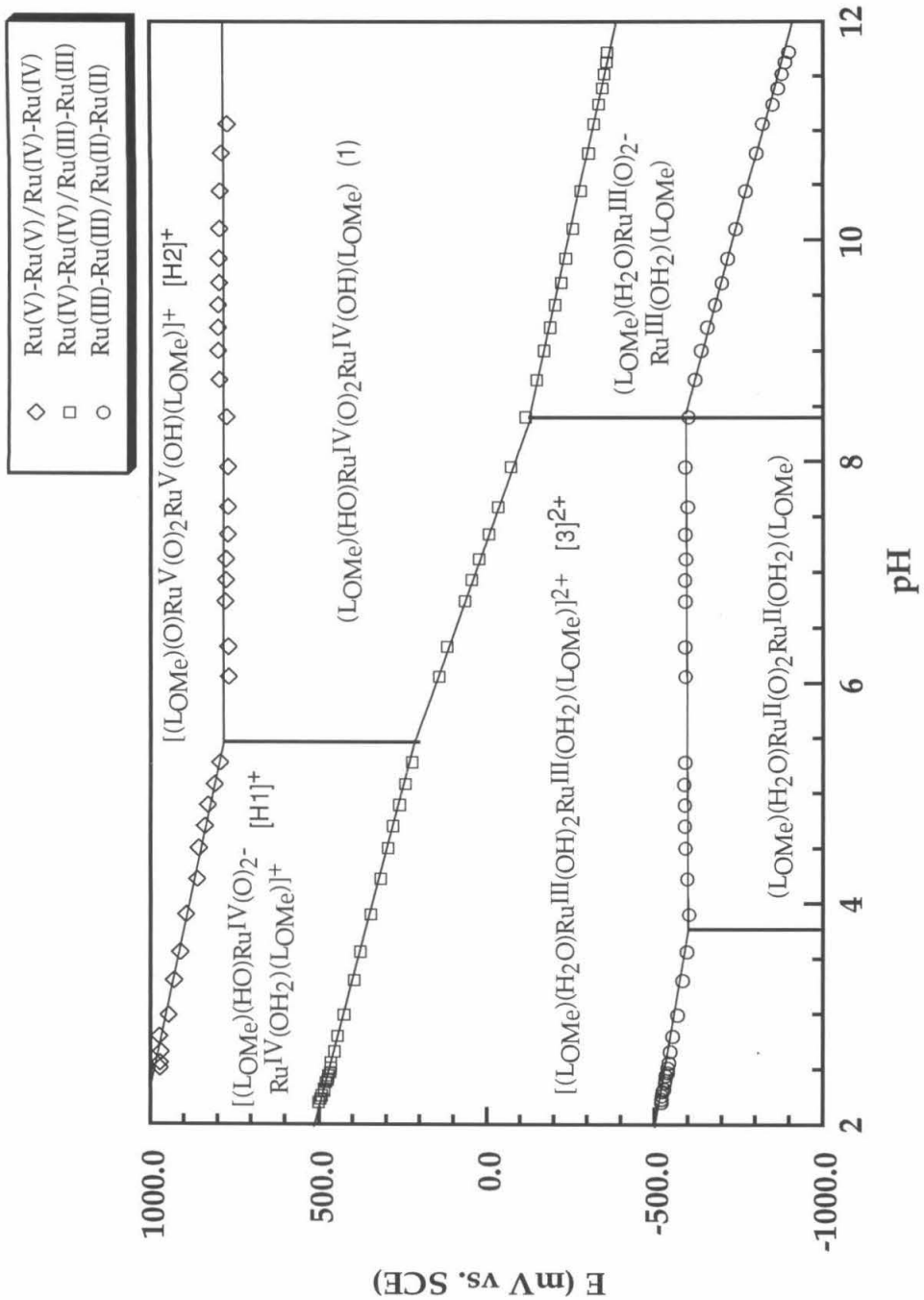

Figure 2.18. Redox processes of **1** in pH 7 buffer.

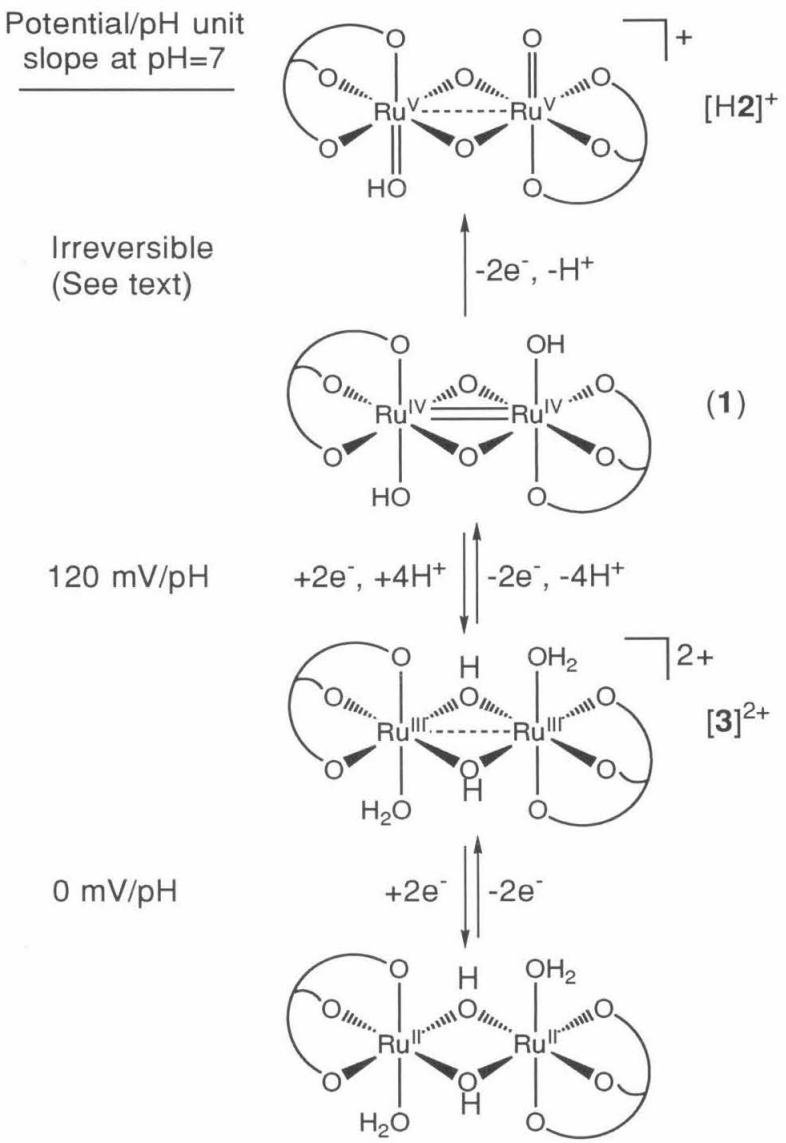

Figure 2.19. Redox processes of **1** in pH 4 buffer.

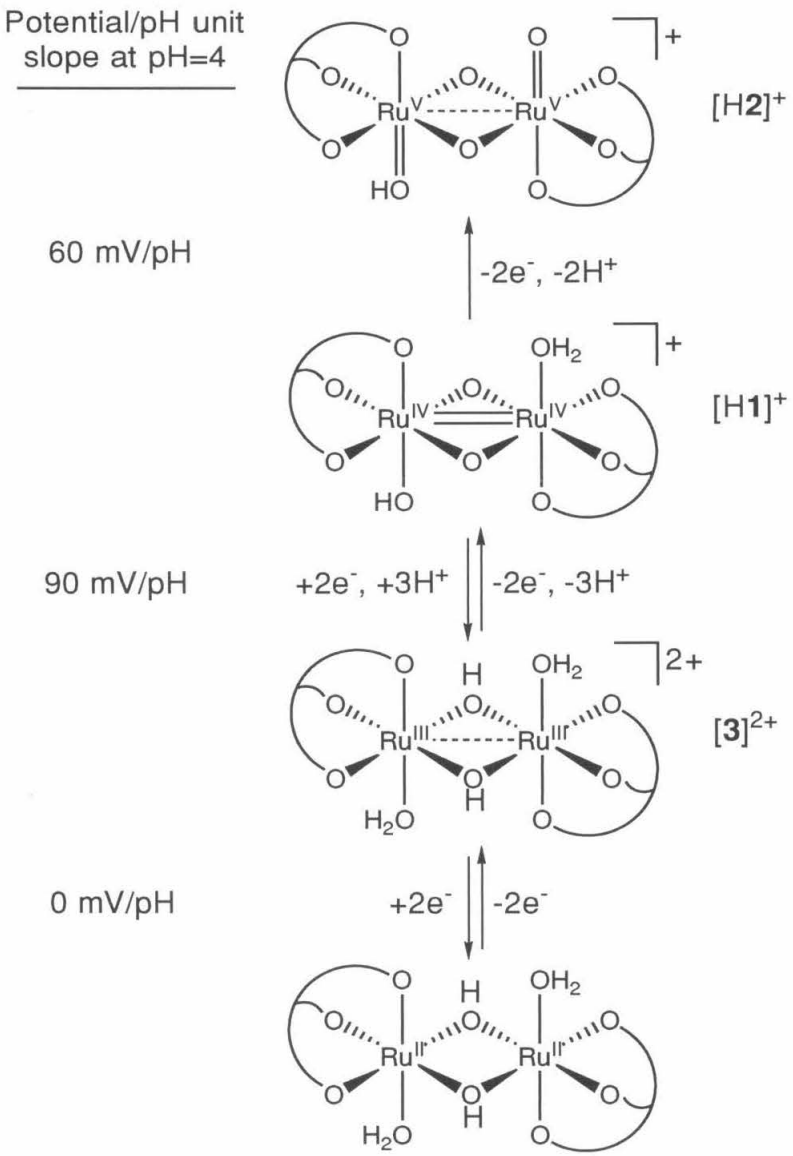

Figure 2.20. Redox processes of **1** in pH 10 buffer.

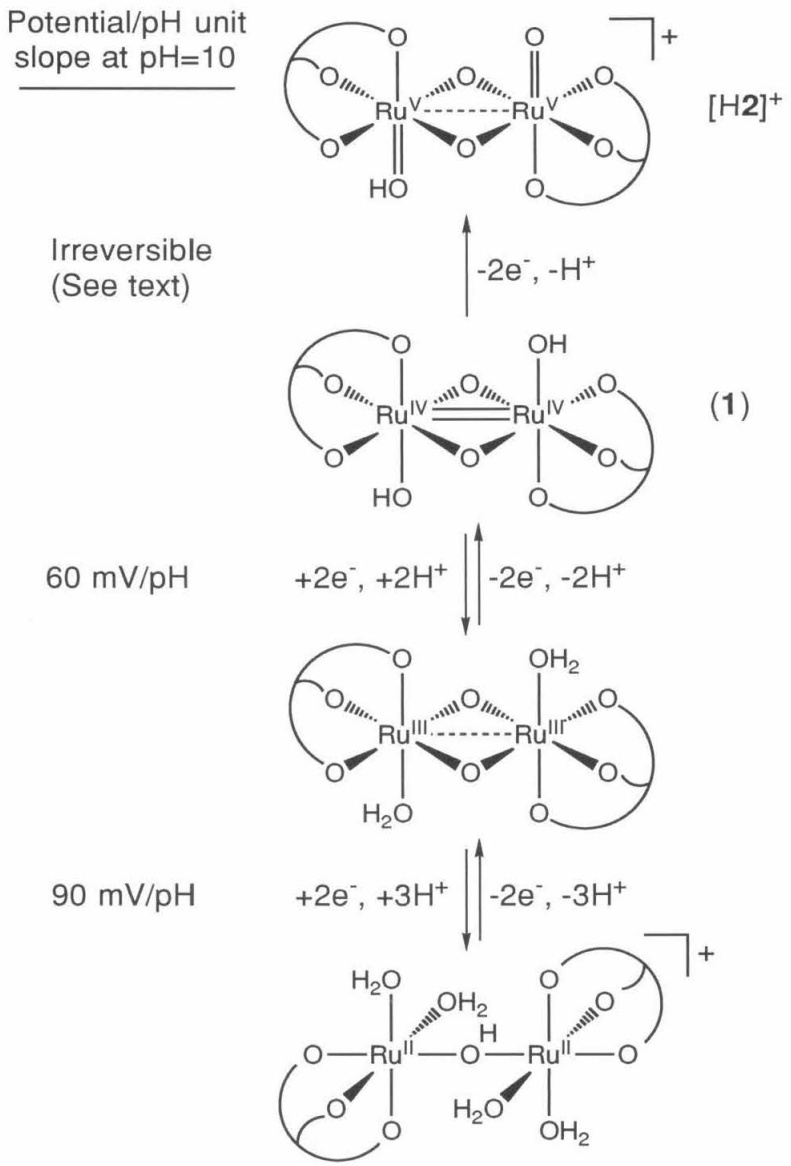

Since **1** is isolated from an alkaline Na_2CO_3 solution as neutral **1** and Figure 2.18 indicates no protonation changes for the Ru^{IV}-Ru^{IV} dimer below pH 5.5, the dimer exists as neutral **1** below pH 5.5. The 120 mV/pH slope of the Ru^{IV}-Ru^{IV}/Ru^{III}-Ru^{III} potential for 5.4<pH<8.4 reflects a two-electron, four-proton reduction from **1** to $[(L_{OMe})(H_2O)Ru^{III}(\mu\text{-}OH)_2\text{-}Ru^{III}(OH_2)(L_{OMe})]^{2+}$ ($[\mathbf{3}]^{2+}$). This is consistent with the formation of $[\mathbf{3}]^{2+}$ from the reduction of **1** by Zn/Hg amalgam. (These reactions approach pH~7 due to H_2 formation.) Similarly, the pH independence of the Ru^{III}-Ru^{III}/Ru^{II}-Ru^{II} couple for 5.4<pH<8.4 suggests Ru^{III}-Ru^{III} dimer is reduced via by a two-electron, no-proton process to a neutral Ru^{II}-Ru^{II} species likely formulated as $(L_{OMe})(H_2O)Ru^{II}(\mu\text{-}OH)_2Ru^{II}(OH_2)(L_{OMe})$.

As expected from section 2.3, the Ru^{V}-Ru^{V}/Ru^{IV}-Ru^{IV} couple is more difficult to interpret. First, the slope of its potential versus pH dependence at pH>5.4 does not reflect the protonation state since this oxidation is completely irreversible within the timescale of these measurements. (The Nernst equation does not apply to irreversible systems.[12]) However, at pH<5.4, the couple exhibits at least partial reversibility. The 60 mV/pH slope in this regime is indicative of a two-electron, two-proton process. As mentioned, the simultaneous slope change in the Ru^{V}-Ru^{V}/Ru^{IV}-Ru^{IV} and Ru^{IV}-Ru^{IV}/Ru^{III}-Ru^{III} couples at pH<5.4 suggest protonation of the Ru^{IV}-Ru^{IV} species. The 90 mV/pH slope for the Ru^{IV}-Ru^{IV}/Ru^{III}-Ru^{III} oxidation at pH≥5.4 indicates a two-electron, three-proton oxidation from $[\mathbf{3}]^{2+}$ suggesting monoprotonation of **1** at pH 5.4 to $[\mathbf{H1}]^{+}$. In turn, this suggests that the two-electron, two-proton Ru^{IV}-Ru^{IV}/Ru^{III}-Ru^{III} oxidation affords the monoprotonated cationic Ru^{V}-Ru^{V} dimer $[(L_{OMe})(O)Ru^{V}(\mu\text{-}O)_2Ru^{V}(OH)(L_{OMe})]^{+}$ ($[\mathbf{H2}]^{+}$). In $(L_{OEt})^{-}$ dimers, protonation appears to preferentially occur at the terminal ligands. This assignment is made by analogy only.

Though the Ru^{V}-Ru^{V} dimer is isolated in the neutral form, **2**, it can be deliberately protonated in organic solvent to a red product with one equivalent of CF_3SO_3H. This compound reverts to **2** upon addition of an equivalent of base. Organic solutions of **2** also immediately change color upon addition to pH 7 buffer suggesting the neutral Ru^{V}-Ru^{V} species rapidly

protonates in aqueous media. This protonated dimer appears to be a more effective oxidizing agent than the neutral species (as will be discussed in Chapter 3). Overall, the general electrochemistry of these dimers at pH 7 and 4 are summarized by figures 2.18 and 2.19 respectively.

The redox manifold in alkaline buffers is slightly different. The changes in the slope at pH 8.4 for the Ru^{IV}-Ru^{IV}/Ru^{III}-Ru^{III} and Ru^{III}-Ru^{III}/Ru^{II}-Ru^{II} couples suggest that the Ru^{III}-Ru^{III} species deprotonates at this pH. The slope of 60 mV/pH for the Ru^{IV}-Ru^{IV}/Ru^{III}-Ru^{III} couple represents a two-electron, two-proton reduction form 1 to the neutral $(L_{OMe})(HO)Ru^{III}(\mu\text{-}OH)_2Ru^{III}(OH)(L_{OMe})$. The slope of the Ru^{III}-Ru^{III}/Ru^{II}-Ru^{II} couple is perplexing in that the 90 mV/pH unit slope indicates a two-electron, three-proton process to a species with seven protons on its terminal and bridging oxygen ligands. This behavior may be explained by the reduction being accompanied by a fast reversible rearrangement to a singly-bridged Ru^{II}-Ru^{II} species such as $[(L_{OMe})(H_2O)_2Ru^{II}(\mu\text{-}OH)\text{-}Ru^{II}(OH_2)_2(L_{OMe})]^+$ (Figure 2.21). Reduction of the two metal centers may dramatically increase the basicity of the bridging and terminal oxygen ligands encouraging their protonation. A bridging aquo ligand may be sufficiently labile to allow the reversible equilibrium between edge sharing and vertex sharing dimers. The oxidation chemistry at pH 10 is summarized by figure 2.20. Overall, the general electrochemistry of these dimers at pH 7 and 4 are summarized by figures 2.19 and 2.20 respectively.

Figure 2.21. Proposed rearrangement of electrogenerated Ru^{II}-Ru^{II} species.

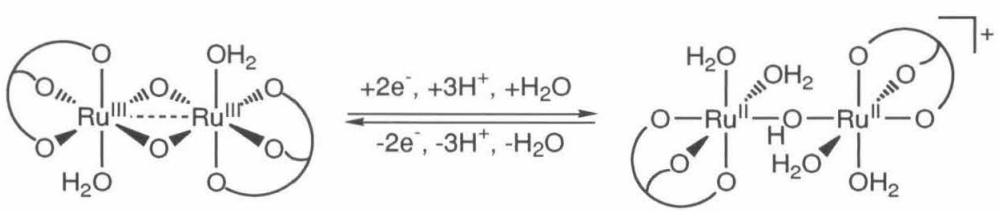

2.5. Crossover Experiments Testing Possible Dimer-Monomer Equilibria.

The unusual tendency for dimer rearrangement in the Ru^{III}-Ru^{III} and Ru^{II}-Ru^{II} oxidation states suggests that dimer-monomer equilibria are also possible. Such equilibria would be particularly important in mechanistic interpretation in Chapters 3 and 5. Clearly if the Ru^{V}-Ru^{V} dimer **2** dissociates into monomers such as illustrated in Figure 2.22, these monomers will need to be considered in interpreting observed reactivity especially since the resulting Ru^{V} and Ru^{VI} monomers would contain *cis*-dioxo moieties.

Figure 2.22. Possible Dimer-Monomer Equilibrium for the Ru^{V}-Ru^{V} dimers.

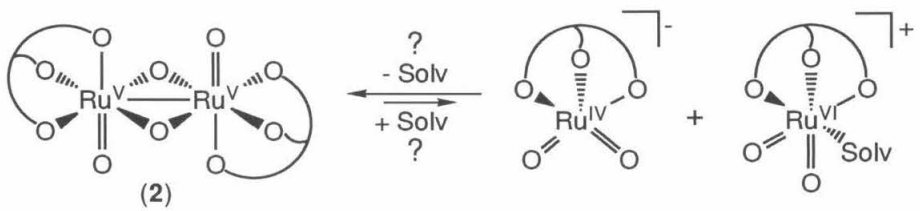

To explore this possibility, mixtures of the (L_{OMe}) and (L_{OEt}) analogs of **2**, **1**, $[H_21]^{2+}$, and $[(L_{OR})(CH_3CN)Ru^{III}(\mu\text{-}OH)_2Ru^{III}(NCCH_3)(L_{OR})]^{2+}$ ($[\mathbf{5}]^{2+}$) (synthesis described in Chapter 4) were prepared in CD_3CN and examined by ^1H NMR spectroscopy. These spectra remained unchanged as the simple sum of constituent spectra giving no evidence for crossover.

2.6. Lability of Terminal Ligands in Ru^{IV}-Ru^{IV} and Ru^{III}-Ru^{III} dimers.

Another important mechanistic process considered in later chapters includes the displacement of terminal ligands for solvent or substrate molecules. Overall, attempts to exchange the hydroxyl ligands of **1** were largely unsuccessful while the aquo ligands of $[\mathbf{3}]^{2+}$ were easily displaced by good donors such as pyridine and nitriles.

The Ru^{IV}-Ru^{IV} dimer, $[H_21]^{2+}$, was refluxed in $H_2{}^{17}O$ in an attempt to exchange the label into the terminal and bridging oxygen ligands. The absence of a signal in the ^{17}O NMR

spectrum implies this exchange did not occur. Terminal aquo ligands in $[H_21]^{2+}$ also resist displacement by nitrogen donors such as CH_3CN and amines. This lack of aquo lability is not surprising; the d^4 electrons at each ruthenium center likely populate nonbonding d_π orbitals leaving the antibonding d_σ-like orbitals empty.[13]

In contrast, the terminal aquo ligands of the Ru^{III}-Ru^{III} dimer, $[3]^{2+}$, readily exchange for other nitrogen ligands though these dimers also should have empty antibonding d_σ-like orbitals. In CH_3CN, $[3]^{2+}$ readily converts to the acetonitrile adduct $[(L_{OMe})(CH_3CN)Ru^{III}(\mu\text{-}OH)_2Ru^{III}(NCCH_3)(L_{OMe})]^{2+}$ ($[5]^{2+}$) discussed in Chapter 4. The dimer $[3]^{2+}$ also reacts with pyridine to afford an adduct.[14] This lability of the Ru^{III}-Ru^{III} oxidation state may be partly responsible for the structural rearrangements of these dimers. One strange feature of this lability is the slow exchange of the aquo ligands for $H_2{}^{17}O$. Evidently a good donor is necessary for ligand displacement suggesting an associative mechanism.

Figure 2.23. Differences in Ligand Lability Between $[H_21]^{2+}$ and $[3]^{2+}$.

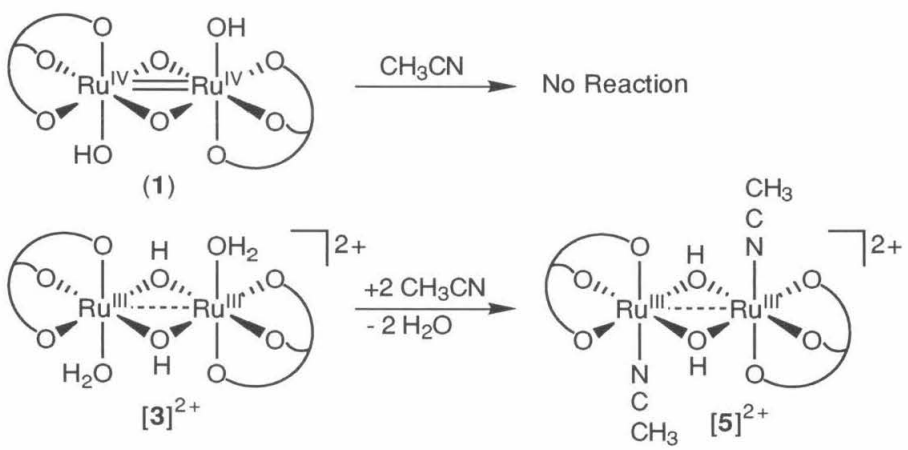

Conclusion

From the $(L_{OMe})^-$ based, edge-sharing ruthenium dimer $(L_{OMe})(HO)Ru^{IV}(\mu\text{-}O)_2$-$Ru^{IV}(OH)(L_{OMe})$ (**1**) homovalent oxidation states from Ru^{V}-Ru^{V} to Ru^{II}-Ru^{II} are

electrochemically accessible of which the Ru^{V}-Ru^{V} and two Ru^{III}-Ru^{III} dimers have been isolated. The Ru^{III}-Ru^{III} dimers, with edge-sharing and face-sharing coordination geometries, interconvert in water. In aqueous buffer, **1** exhibits a quasi-reversible Ru^{IV}-Ru^{IV}/Ru^{III}-Ru^{III} and Ru^{III}-Ru^{III}/Ru^{II}-Ru^{II} redox couples and an electrocatalytic Ru^{V}-Ru^{V}/Ru^{IV}-Ru^{IV} couple implying a reactive Ru^{V}-Ru^{V} species. The potential of the Ru^{V}-Ru^{V}/Ru^{IV}-Ru^{IV} couple is surface dependent suggesting that electron transfer from **1** occurs by two types of substrate-electrode interactions. The oxidation/protonation manifold of the dimer system was explored through a potential versus pH survey; the reactive Ru^{V}-Ru^{V} species appears to be the protonated dioxo complex. A series of crossover experiments between $(L_{OMe})^{-}$ and $(L_{OEt})^{-}$ based dimers exhibited no evidence for dimer-monomer equilibria for the Ru^{V}-Ru^{V}, Ru^{IV}-Ru^{IV}, and Ru^{III}-Ru^{III} dimers. In addition, the terminal ligands of the edge-sharing Ru^{III}-Ru^{III} dimers were found to be relatively labile while those of the Ru^{IV}-Ru^{IV} were found to be inert. These results will be very useful in interpreting the chemistry described in the following three chapters.

Experimental

General Considerations. NMR spectra were recorded on the Bruker AM500 (^{1}H, 500.1 MHz), Jeol JNM-GX400 (^{1}H, 399.65 MHz; ^{13}C, 100.40 MHz; ^{31}P, 161.70 MHz), and General Electric QE 300 (^{1}H, 300.10 MHz; ^{13}C, 75.47 MHz) Fourier transform spectrometers in D_2O (δ 4.63 ppm), CD_2Cl_2 (δ 5.32 ppm), $CDCl_3$ (δ 7.24 ppm), or CD_3CN (δ 1.93 ppm). UV-Vis spectra were recorded on a Hewlett Packard 8452A Diode Array Spectrophotometer equipped with a Hewlett Packard 89090A thermostatted cell holder. The HP8452A was controlled from an IBM compatible Compaq Deskpro computer by Hewlett Packard software. Infrared spectra were recorded as Nujol mulls between KBr plates with a Perkin Elmer 1600 Series FTIR. Elemental analyses for carbon, hydrogen, and nitrogen were carried out in the Caltech Analytical Laboratory by Fenton Harvey.

Most manipulations were carried out in air, except for syntheses of $Na(L_{OMe})$, **2**, $[H3](CF_3SO_3)_2$, and $[4](CF_3SO_3)$ which were carried out under an inert atmosphere with vacuum-line techniques. Water was used as collected from a Barnstead nanopurifier train. Most of the organic solvents including petroleum ether, heptane, and toluene were obtained in the analytical grade and were used after drying with molecular sieves. CH_3CN and CD_3CN were further dried over CaH_2 and then distilled onto, refluxed over, and distilled from P_2O_5. $RuCl_3 \cdot nH_2O$ (Aesar), $Co(acac)_2$ (sublimed) (Alfa), NaC_5H_5 (Aldrich), $HP(O)(OCH_3)_2$ (Aldrich), NaCN (Aldrich), CF_3SO_3H (Aldrich), $C_6H_5I(O_2CCH_3)_2$ (Aldrich), 40% $[N(CH_2CH_3)_4]^+(OH)^-$ (aq) (Thiokol), $P(C_6H_5)_3$ (Aldrich), $OP(C_6H_5)_3$ (Aldrich), $P(CH_3)_3$ (Aldrich), 37% (w/w) HCHO (aq) (Aldrich), 19% (w/w) $H^{13}CHO$ (aq) (CIL), and other reagents and solvents were used as obtained without further purification. The sodium salt $Na\{(\eta^5\text{-}C_5H_5)Co[P(O)(OCH_3)_2]_3\} = Na(L_{OMe})$, the RuO_4 solution in CCl_4, and C_6H_5IO were synthesized by published procedures.[15,16,17]

$(L_{OMe})(HO)Ru^{IV}(\mu\text{-}O)_2Ru^{IV}(OH)(L_{OMe})$ (1). This synthesis is analogous to that reported for $(L_{OEt})(HO)Ru^{IV}(\mu\text{-}O)_2Ru^{IV}(OH)(L_{OEt})$ by Power *et al.*[11] A CCl_4 solution of RuO_4 (86 mL of a 13 g L^{-1} solution, 7.0 mmol) was added dropwise to a solution of $Na(L_{OMe})$ (4.00 g, 8.44 mmol) in 1% H_2SO_4 (78 mL, 7.8 mmol) at 0 °C. During the addition, the solution changed from yellow to dark green-brown. The solution was stirred at 0 °C for 30 minutes and for a further 60 minutes as the solution warmed to room temperature. The dark aqueous layer was carefully separated from the organic layer and filtered through a medium frit to remove an intractable brown residue. A solution of Na_2CO_3 (3.39 g in 10 mL of H_2O, 32.0 mmol) was added, and the resulting suspension was allowed to settle for 5 minutes. The mixture of green and brown solids was collected on a medium frit and then washed with H_2O until the filtrate was no longer green. The combined filtrates were extracted with CH_2Cl_2, and the organic solution was dried with anhydrous $MgSO_4$ and filtered. Petroleum ether (1.5 times the volume of CH_2Cl_2) was added, and the settled precipitate was quickly isolated on a medium frit and washed with

2/3 (v/v) CH_2Cl_2/petroleum ether. The green solid was dried *in vacuo* (0.99 g, 0.85 mmol, 24% based on RuO_4). Anal. Calcd for $C_{22}H_{48}Co_2O_{22}P_6Ru_2$ (mol wt 1170.46): C, 22.58; H, 4.13. Found: C, 22.90; H, 4.02. IR (nujol): 3646(vw), 3599(vw), 3452(w), 3123(vw), 1784(vw), 1646(vw), 1577(vw), 1302(vw), 1207(vw), 1178(w), 1075(s), 1041(s), 845(s), 789(s), 738(s), 693(vw), 600(m), 558(w). ^{1}H NMR (CD_3CN): δ 5.04 (s, C_5H_5, 10H), 3.86 (m, OCH_3, 12H), 3.66 (m, OCH_3, 12H), 3.52 (m, OCH_3, 12H), 2.21 (br-s, OH). (D_2O, pH 7): δ 5.26 (s, C_5H_5, 10H), 3.89 (m, OCH_3, 12H), 3.66 (m, OCH_3, 12H), 3.57 (m, OCH_3, 12H). (CD_2Cl_2): δ 5.11 (s, C_5H_3, 10H), 3.97 (t, J_{HP}=5.7 Hz, OCH_3, 12H), 3.73 (t, J_{HP}=5.7 Hz, OCH_3, 12H), 3.56 (s, J_{HP}=11.4 Hz, OCH_3, 12H). UV-Vis [λ_{max}, nm (ε, $M^{-1}cm^{-1}$), in pH 7 H_2O]: 210 ($2.7 \cdot 10^4$), 240 ($4.1 \cdot 10^4$), 340 ($1.26 \cdot 10^4$), 680 nm ($2.0 \cdot 10^3$).

$[(L_{OMe})(H_2O)Ru^{IV}(\mu\text{-}O)_2Ru^{IV}(OH_2)(L_{OMe})][CF_3SO_3]_2$ ($[H_21][CF_3SO_3]_2$). An excess of concentrated CF_3SO_3H (1 mL, 11.3 mmol) was added dropwise to a suspension of dimer **1** (0.99 g, 0.85 mmol) in H_2O (22 mL). The suspension turned from yellowish-green to bluish-green. The solution was stirred at room temperature for 10 minutes and allowed to settle for 5 minutes. The solid was collected on a medium frit and washed repeatedly with aqueous CF_3SO_3H (1 mL in 22 mL H_2O) until the filtrate was colorless. The solid was then washed with H_2O (3 x 1 mL) and dried *in vacuo* (1.10 g. 0.75 mmol, 88%). To recrystallize the product, $[H_21][CF_3SO_3]_2$ (1.00g, 0.68 mmol) was first dissolved in a minimum of water at room temperature. Concentrated CF_3SO_3H was slowly added dropwise until solid began to emerge, and the slurry was stirred for 15 minutes. The microcrystalline solid was collected on a medium frit and washed repeatedly with dilute aqueous CF_3SO_3H (15 drops concentrated acid/200 mL water) until the filtrate was colorless. This procedure was typically repeated three times after which the solid was washed with water until the filtrate was mildly acidic (pH 5). The microcrystalline solid was dried *in vacuo* (0.91g, 0.62 mmol, 91%). Anal. Calcd for $C_{24}H_{50}Co_2F_6O_{28}P_6Ru_2S_2$ (mol wt 1470.60): C, 19.60; H, 3.43. Found: C, 19.56; H, 3.32. IR(nujol): 3394(br, vw), 3168 (br, w), 3118 (vw), 1805(vw), 1631(vw), 1564(vw), 1296(s), 1239(m), 1225(m), 1180(w), 1170(w), 1159(w), 1147(w), 1063(sh, s), 1043(sh, s), 1027(s), 972(sh, w), 889(vw), 860(m), 800(m), 784(sh, w), 752(m), 722(sh, vw), 701(vw), 638(m), 617(vw), 599(vw). ^{1}H NMR (CD_3CN): δ 5.30 (s, C_5H_5,

10H), 4.00 (t, J_{HP}=5.7 Hz, OCH_3, 12H), 3.70 (t, J_{HP}=5.6 Hz, OCH_3, 12H), 3.49 (d, J_{HP}=12.0 Hz, OCH_3, 12H), 3.0 (br-s, OH). (0.1 M D_2SO_4): δ. ^{31}P NMR (CD_3CN): δ -113.2 [br-t, J_{PP}~150 Hz, 1P], -122.8 [br-d, J_{PP}~150 Hz, 2P]. UV-Vis [λ_{max}, nm (ε, $M^{-1}cm^{-1}$), in 0.1 M H_2SO_4]: 206 ($2.8{\cdot}10^4$), 240 ($4.2{\cdot}10^4$), 334 ($1.17{\cdot}10^4$), 638 ($2.4{\cdot}10^3$). UV-Vis [λ_{max}, nm (ε, $M^{-1}cm^{-1}$), in CH_2Cl_2]: 242 ($4.1{\cdot}10^4$), 336 ($1.18{\cdot}10^4$), 628 ($2.4{\cdot}10^3$).

(L_{OMe})(O)Ru^V(μ-O)$_2Ru^V$(O)(L_{OMe}) (2). Excess C_6H_5IO (0.56 g, 2.5 mmol) was added to [H_2**1**](CF_3SO_3)$_2$ (1.12 g, 0.76 mmol) dissolved in CH_3CN (200 mL) at room temperature, and the suspension was stirred 15 minutes to afford a deep red solution. The solution was filtered through a medium frit. Then 40% (w/w) aqueous NEt_4 OH (0.50 mL, 0.76 mmol) was added slowly, immediately giving a purple solution. The solution was reduced to an oily residue under vacuum, and the residue was extracted with C_6H_6 (200 mL). The solution was filtered and reduced to 50 mL under vacuum. A purple solid precipitated on addition of heptane (100 mL). The solid was isolated upon a medium frit and washed repeatedly with 1 mL portions of CH_3CN until filtrate was purple rather than brown. The solid was dissolved in CH_3CN (350 mL), and the solution was reduced to 10 mL under vacuum. The purple crystals were isolated on a medium frit and washed with 1 mL portions of CH_3CN until the filtrate was purple. Recrystallization from CH_3CN effectively removes impurities (along with significant amounts of product). The solid was dried *in vacuo* and stored under argon (0.12 g, 14%). Anal. Calcd for $C_{22}H_{46}Co_2O_{13}P_6Ru_2$ (Mol wt 1168.44): C, 22.61; H, 3.97. Found: C, 22.90; H, 3.90. IR(KBr): 3123 (w), 2994 (w), 2948 (m), 2901 (m-sh), 2842 (w), 1459 (m), 1425 (m), 1175 (m), 1143 (m-sh), 1104 (s), 1073 (s), 1032 (s), 1008 (s), 850 (s), 836 (m), 784 (m), 734 (s), 617 (s), 599 (s), 472 (m). ^{1}H NMR (CD_3CN): δ 4.937 (s, C_5H_5, 10H), 3.92 (t, J_{HP}=4.6 Hz, OCH_3, 12H), 3.52 (t, J_{HP}=4.6 Hz, OCH_3, 12H), 3.36 (d, J_{HP}=10.5 Hz, OCH_3, 12H). (CD_2Cl_2): δ 4.94 (s, C_5H_5, 10H), 3.98 (t, J_{HP}=5.3 Hz, OCH_3, 12H), 3.58 (t, J_{HP}=5.1 Hz, OCH_3, 12H), 3.43 (d, J_{HP}=10.0 Hz, OCH_3, 12H). UV-Vis [λ_{max}, nm (ε, $M^{-1}cm^{-1}$), in CH_2Cl_2]: 242 ($4.1{\cdot}10^4$), 332 ($9.2{\cdot}10^3$), 564 ($3.1{\cdot}10^3$).

$[(L_{OMe})(H_2O)Ru^{III}(\mu\text{-}OH)_2Ru^{III}(OH_2)(L_{OMe})][CF_3SO_3][4\text{-}CH_3C_6H_4SO_3]$ ($[3][CF_3SO_3][4\text{-}CH_3C_6H_4SO_3]$). A suspension containing dimer $[H_21][CF_3SO_3]_2$ (0.1067 g, 0.0726 mmol) and $CH_3C_6H_4SO_3H$ (0.1249 g, 0.725 mmol) in H_2O (5 mL) was added to Zn amalgam [prepared from a suspension of Zn (0.1016 g, 1.554 mmol) and $HgCl_2$ (0.0222 g, 0.0818 mmol) in H_2O]. This suspension was agitated at room temperature until the solution changed from green to yellow and then to orange. The solution was filtered in air (whereupon the color returned to yellow) and extracted with 5 mL CH_2Cl_2. The CH_2Cl_2 solution was dried with $MgSO_4$ and filtered. A yellow solid was precipitated by the addition of heptane (5 mL) followed by reduction to 5 mL under vacuum. The yellow powder was isolated on a small medium frit and washed with heptane and petroleum ether. The solid was dried *in vacuo* (0.0205 g, 0.0137 mmol, 18.9%). Anal. Calcd for $C_{30}H_{59}Co_2F_3O_{28}P_6Ru_2S_2$ (Mol wt 1494.74): C, 24.11; H, 3.98. Found: C, 23.89; H, 4.00. IR (KBr): 3186(m), 3118(sh, m), 3006(sh, w), 2954(m), 2848(w), 1458(m), 1425(w), 1281(w), 1258(w), 1231(m), 1176(m), 1124(m), 1062(s), 1034(s), 1012(sh, s), 998(sh, s), 847(m), 819(w), 790(m), 773(sh, w), 741(m), 712(w), 682(m), 651(sh, m), 639(m), 612(sh, m), 598(m), 566(m), 455(w). ^1H NMR (CD_2Cl_2): δ 7.62 (d, J_{HH}=7.7 Hz, $CH_3C_6H_4SO_3$, 2H), 7.13 (d, J_{HH}=7.7 Hz, $CH_3C_6H_4SO_3$, 2H), 5.15 (s, C_5H_5, 10H), 4.16 (t, J_{HP}=5.6 Hz, OCH_3, 12H), 4.03 (t, J_{HP}=5.6 Hz, OCH_3, 12H), 2.96 (d, J_{HP}=11.2 Hz, OCH_3, 12H), 2.34 (s, $CH_3C_6H_4SO_3$, 3H), 1.56 (br-s, OH). ^1H NMR (pH 7 D_2O): δ 7.49 (d, J_{HH}=8.1 Hz, $CH_3C_6H_4SO_3$, 2H), 7.17 (d, J_{HH}=8.1 Hz, $CH_3C_6H_4SO_3$, 2H), 5.32 (s, C_5H_5, 10H), 3.97 (q, J_{HP}=3.6 Hz, OCH_3, 12H), 3.87 (q, J_{HP}=3.6 Hz, OCH_3, 12H), 2.94 (m, J_{HP}=3.7 Hz, OCH_3, 12H), 2.20 (s, $CH_3C_6H_4SO_3$, 3H). UV-Vis [λ_{max}, nm (ε, $M^{-1}cm^{-1}$), in CH_2Cl_2]: 242 ($4.2\cdot10^4$), 342 ($1.58\cdot10^4$).

$[(L_{OMe})(H_2O)Ru^{III}(\mu\text{-}OH)(\mu\text{-}OH_2)Ru^{III}(OH_2)(L_{OMe})][CF_3SO_3]_3$ ($[H3][CF_3SO_3]_3$). A solution of $[H_21][CF_3SO_3]_2$ (0.1020 g, 0.0694 mmol), $NaH_2PO_4{\cdot}H_2O$ (0.899 g, 6.51 mmol), and H_3PO_4 (85% w/w) (0.21 mL, 3.07 mmol), dissolved in H_2O (65 mL) was electrolyzed at +0.15 V versus SCE (2.0 C of charge) at a Pt gauze electrode in a two compartment electrochemical cell with stirring. An excess of $NaCF_3SO_3$ (0.42 g, 2.44 mmol) was added, causing a yellow solid to

precipitate. The solid was collected on a medium frit and dissolved in CH_2Cl_2 (50 mL) under argon. The solution was filtered and its volume was reduced under vacuum until solid began to appear. Heptane (30 mL) was added and the solution volume was further reduced under vacuum until the solution was colorless. The yellow powder was isolated on a small medium frit and washed with heptane and dried *in vacuo*. The pad of solid was then washed with 1 mL portions of CH_2Cl_2 until the filtrate was yellow rather than green. The remaining solid was dried *in vacuo* (0.0454 g, 0.0279 mmol, 40%). Anal. Calcd for $C_{25}H_{55}Co_2F_9O_{31}P_6Ru_2S_3$ (Mol wt 1624.71): C, 18.48; H, 3.41. Found: C, 18.68; H, 3.32. IR (KBr): 3313(br, m), 3125(sh, m), 3007(w), 2956(m), 2899(w), 2851(w), 1793(br, w), 1462(m), 1427(m), 1290(sh, w), 1267(s), 1226(sh, m), 1166(s), 1071(s), 1029(s), 1004(sh, s), 944(sh, w), 853(m), 791(s), 745(s), 638(s), 616(s), 599(sh, m), 576(sh, w), 517(w), 482(w), 459(w). ^{1}H NMR (D_2O, pH 7): δ 5.33 (s, C_5H_5, 10H), 3.97 (q, J_{HP}=3.6 Hz, OCH_3, 12H), 3.88 (q, J_{HP}=3.6 Hz, OCH_3, 12H), 2.94 (q, J_{HP}=3.7 Hz, OCH_3, 12H). (CD_2Cl_2): d 5.21 (s, C_5H_3, 10H), 4.20 (t, J_{HP}=5.4 Hz, OCH_3, 12H), 4.04 (t, J_{HP}=5.4 Hz, OCH_3, 12H), 3.11 (d, J_{HP}=10.7 Hz, OCH_3, 12H), 1.55 (br-s, OH). UV-Vis [λ_{max}, nm (ε, $M^{-1}cm^{-1}$), in CH_2Cl_2]: 242 ($3.9 \cdot 10^4$), 342 ($1.75 \cdot 10^4$).

$[(L_{OMe})Ru^{III}(\mu\text{-}OH)_2(\mu\text{-}OH_2)Ru^{III}(L_{OMe})][CF_3SO_3]_2$ ([4][CF_3SO_3]$_2$). A solution of $[H_21][CF_3SO_3]_2$ (0.1032 g, 0.0702 mmol), $Na_2HPO_4 \cdot 7H_2O$ (0.4099 g, 1.529 mmol), and $Na_3PO_4 \cdot 12H_2O$ (0.1279 g, 3.37 mmol) in H_2O (65 mL) was electrolyzed (2.0 C at -0.55 V versus SCE) at a Pt gauze electrode in a two compartment cell (the other compartment also contained phosphate buffer) with stirring. The resulting solution was extracted with CH_2Cl_2 (3 x 20 mL). The extractions were dried with $MgSO_4$ and filtered. The product was precipitated by addition of heptane (120 mL) followed by reduction to 100 mL under vacuum. The solid was isolated on a medium frit and washed with heptane and petroleum ether. The yellow powder was dried *in vacuo* (0.0388 g, 0.030 mmol, 42%). Anal. Calcd for $C_{24}H_{50}Co_2F_6O_{27}P_6Ru_2S_2$ (Mol wt 1454.60): C, 19.82; H, 3.46. Found: C, 20.03; H, 3.56. IR(KBr): 3524(sh, br, m), 3124(w), 3004(w), 2951(m), 2901(br, w), 2844(w), 1439(w), 1425(w), 1284(m), 1262(m), 1253(m), 1224(w), 1174(sh, m), 1157(m), 1070(s), 1039(s), 1032(s), 1009(sh, s), 844(w), 790(m), 740(m), 638(m),

621(m), 518(vw), 485(vw). ^{1}H NMR (pH 7, D_2O): δ 5.37 (s, C_5H_5, 10H), 3.75 (m, OCH_3, 36H). UV-Vis [λ_{max}, nm (ε, $M^{-1}cm^{-1}$), in CH_2Cl_2]: 244 ($4.0 \cdot 10^4$), 342 ($1.46 \cdot 10^4$).

Conversion of $[3]^{2+}$ to $[4]^{2+}$. A small sample of $[H3][CF_3SO_3]_3$ (10 mg, 6 μmol) was slurried into phosphate buffer (10 mL, pH 11.5, I=0.20 M). The solution was stirred at room temperature until the solid dissolved. The solution was stirred an additional hour. The solution was extracted with CH_2Cl_2 (2 x 5 mL). The yellow CH_2Cl_2 solutions were dried with anhydrous $MgSO_4$ and filtered. Heptane (30 mL) was added to precipitate a yellow solid. The solid was collected on a medium frit, air dried, and then dried *in vacuo*. The ^{1}H NMR spectrum of the solid in D_2O phosphate buffer (1 mL, pH 7, I=0.10 M) was indicative of $[4]^{2+}$ with a smaller amount of $[3]^{2+}$. (Note that these two compounds will slowly approach equilibrium in pH 7 buffer.)

Conversion of $[4]^{2+}$ to $[3]^{2+}$. A small sample of $[4][CF_3SO_3]_2$ (10 mg, 7 μmol) was dissolved into phosphate buffer (10 mL, pH 2.5, I=0.10 M). The solution was stirred for several hours. The solution was extracted with CH_2Cl_2 (2 x 5 mL). The yellow CH_2Cl_2 solutions were dried with anhydrous $MgSO_4$ and filtered. Then heptane was added to precipitate a yellow solid. The solid was collected on a medium frit, air dried, and dried *in vacuo*. The ^{1}H NMR spectrum of the solid in buffered D_2O (1 mL, pH 7, I=0.10 M) exhibited a mixture of $[3]^{2+}$ and $[4]^{2+}$.

Protonation of 2 by CF_3SO_3. A solution of **2** (0.00115 g, 0.98 μmol) dissolved in CH_3CN (3.00 mL) was measured into a UV-vis cuvette. Small aliquots (4.4 μL) of CF_3SO_3H in CH_3CN (22.6 mM) were added to the sample, and UV-vis spectra were collected after each addition. The conversion was linear and isosbestic from the spectrum of **2** (λ_{max} = 564 nm) to a spectrum dominated by λ_{max} = 484 nm. Small aliquots (3.5 μL) of NEt_4OH in CH_3CN (27.7 mM) were similarly added. The spectral change from λ_{max} = 484 nm to λ_{max} = 564 nm was linear and isosbestic and returned most of the initial absorptance. An aliquot (0.52 μL) of CF_3SO_3H in

CD_3CN (1.73 M) was added to a solution of **2** (0.0010 g, 0.9 μmol) in CD_3CN (1.0 mL). The resulting ^1H NMR spectrum was very complex.

Dimer crossover experiments. Solutions of the $(L_{OMe})^-$ and $(L_{OEt})^-$ analogs of **1**, $[H_21](CF_3SO_3)_2$, **2**, $[5](CF_3SO_3)_2$ were prepared in CD_3CN (1 mL) with the approximate concentration rations: (2 μmol:1 μmol), (1 μmol:1 μmol), and (1 μmol:2 μmol). The ^1H NMR spectra of these samples were compared with those of the separate compounds. No significant differences were observed in purified CD_3CN.

Attempted ^{17}O labeling of 1. A solution of **1** (0.0214 g, 14.6 μmol) in 10% $H_2{}^{17}O$ (1.0 mL) was stirred for 12 hours under an atmosphere of argon. The solution was degassed by freeze-pump-thaw techniques, and the $H_2{}^{17}O$ was vacuum transferred from the thawed solution. The remaining **1** was dissolved in CD_3CN and examined by ^{17}O NMR internally referenced to added $H_2{}^{17}O$ (0.6 μL, 33.3 μmol). Only the reference signal was observed.

Attempted ^{17}O labeling of $[3]^{2+}$. A suspension of $[3][CF_3SO_3][CH_3C_6H_4SO_3]$ (0.0050 g, 3.35 μmol) in $H_2{}^{17}O$ (1 mL) was stirred at room temperature for 8 hours. Then excess H_2O_2 (20%, 0.05 mL) was added, and the solution was heated to about 60 °C for an hour during which the solution changed from yellow to green. The solution was degassed by freeze-pump-thaw technique, and the $H_2{}^{17}O$ was vacuum transferred from the thawed solution. The remaining solids were extracted with CD_2Cl_2 (1 mL) and examined by ^{17}O NMR. ^{17}O NMR (CD_2Cl_2): δ -63 (br, H_2O or HO).

Electrochemical Measurements. Electrochemical measurements were controlled with the BAS 100A Electrochemical Analyzer using primarily two compartment sample cells. All experiments were performed under inert (argon) atmospheres in aqueous phosphate, pyrophosphate, borate, and acetate buffers. Cyclic voltammetry was carried out on disk electrodes of gold, platinum, glassy carbon, basal-plane graphite, and edge-plane graphite. Gold and platinum electrodes were used as commercially available, and graphite electrodes

were prepared from commercially available plugs mounted to glass rods with shrink-wrap plastic. All electrodes were polished with 0.3 μm alpha alumina and sonicated in water before each experiment. All experiments were referenced either to SCE or $Ag^+/AgCl$ reference electrodes, and large platinum gauzes were used as auxiliary electrodes.

Electrochemistry of 1. The electrochemistry of **1** was surveyed by cyclic voltammetry in phosphate buffer (10 mL, pH 7, I=0.1 M) at electrodes of gold, platinum, glassy carbon, basal-plane graphite, and edge-plane graphite. Experiments at gold and platinum exhibited oxidation adsorption waves that interfered with clear measurement of the Ru^{IV}-Ru^{IV}/Ru^{III}-Ru^{III} couple and solvent oxidation that interfered with measurement of the Ru^{V}-Ru^{V}/Ru^{IV}-Ru^{IV} couple. The differences between the carbon electrodes were primarily in the behavior of the Ru^{V}-Ru^{V}/Ru^{IV}-Ru^{IV} couple as discussed in the text. Best results were obtained with electrodes of glassy carbon or edge-plane graphite. The electrochemistry of **1** was surveyed by cyclic voltammetry (for several scan widths and scan rates) in phosphate/pyrophosphate buffers consisting of the materials in Table 2.1 dissolved in water (100 mL).

Table 2.1. Components for phosphate/pyrophosphate electrolyte-buffers.

pH = 2.5	H_3PO_4 (85%, 0.32 mL, 4.7 mmol) $NaH_2PO_4 \cdot H_2O$ (1.390 g, 10.07 mmol)
pH = 5.5	H_3PO_4 (85%, 0.39 mL, 5.7 mmol) $Na_4P_2O_7 \cdot 10H_2O$ (1.116 g 2.50 mmol)
pH = 6.9	$NaH_2PO_4 \cdot H_2O$ (0.362 g, 2.62 mmol) $Na_2HPO_4 \cdot 7H_2O$ (0.999 g, 3.73 mmol)
pH = 8.5	$NaH_2PO_4 \cdot H_2O$ (0.168 g, 1.22 mmol) $Na_4P_2O_7 \cdot 10H_2O$ (0.978 g, 2.19 mmol)
pH = 11.5	$Na_3PO_4 \cdot 12H_2O$ (1.270 g, 3.34 mmol)

Cyclic voltammagrams were stored on computer and exported in table format by software available from Bioanalytical Systems Inc. This data was easily imported into the Macintosh by Apple File Exchange as text files that were subsequently manipulated in KaleidaGraph.

General potential measurements and redox reversibility assessments were made by cyclic voltammetry. Detailed potential versus pH measurements were made using a rotating disk electrode (RDE) in slow votammetric sweeps from negative to positive potentials. In the experiment reported in the text above, $[H_2\mathbf{1}](CF_3SO_3)_2$ (0.0844 g, 57.4 μmol) was dissolved in a buffer (100 mL) containing $NaHSO_4$ (80 mM), Na_2SO_4 (60 mM), H_3PO_4 (40 mM), CH_3COOH (40 mM), and H_3BO_3 (40 mM). This buffer/electrolyte solution was titrated with 0.25 mL aliquots of NaOH in water (0.52 M) with a voltammogram being collected after each addition. Solution pH was measured with a standard pH probe. The redox potentials were measured from the points of maximum current change.

Affinity of 1 to the edge-plane graphite surface. A clean edge-plane graphite electrode was dipped into a solution of either **1** (1 mM) or $[H_2\mathbf{1}][CF_3SO_3]_2$ (1 mM) in CH_2Cl_2, wicked dry, and rinsed with water. The electrode was immersed into samples of blank pH 7 phosphate buffer and rinsed five times to rinse away residual dimer. The electrode was placed into a one compartment cell with blank phosphate electrolyte. Cyclic voltammetry exhibited redox waves close to those of free **1**. The redox behavior decayed slowly as its electrochemistry continued to be scanned.

In another method, the working, auxiliary, and reference electrodes were placed in a solution of dimer (1 mM) in phosphate buffer (pH 7.0, I=0.1 M), and the working electrode was electrolyzed at 1200 mV versus SCE for 60 seconds. These electrodes were rinsed with blank phosphate buffer as before and electrochemically examined and tested as before. The working electrode indeed exhibited electrochemistry similar to that of **1** that appears stable over time until its oxidation chemistry was scanned.

References

1. Power, J. M.; Evertz, K.; Henling, L.; Marsh, R.; Schaefer, W. P.; Labinger, J. A.; Bercaw, J. E. *Inorg. Chem.*, **1990**, *29*, 5058-5065.

2. The oxidation products that accompany reduction of **2** to **1** are unidentified.

3. Power, J. M.; Blake, R. E.; Bercaw, J. E. *Unpublished results*, California Institute of Technology.

4. The use of NMR splitting patterns to determine dimer symmetry in these compounds has been discussed in the literature.[1] The C_s symmetry of the $(L_{OMe})^-$ with a mirror plane through the two ruthenium centers perpendicular to the $Ru(\mu\text{-}O)_2Ru$ core is evident in ^1H NMR spectra as a triplet, triplet, doublet pattern with 1:1:1 integration for the $(L_{OMe})^-$ methyls. This pattern corresponds to three sets of equivalent methoxy groups as illustrated below (Figure 2.24).

Figure 2.24. Newman projections for $(L_{OMe})^-$.

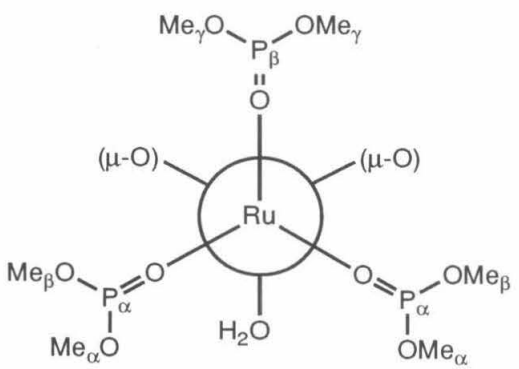

P_α : equivalent, virtually coupled
Me_α : triplet coupling to P_α
Me_β : triplet coupling to P_α
Me_γ : doublet coupling to P_β

The two triplets correspond to methoxy groups associated to a pair of equivalent and virtually coupled phosphorus atoms, and the doublet corresponds to methyl groups on the remaining phosphite. A similar pattern discussed in Chapter 4 consisting of four triplets and two doublets is indicative of two inequivalent ruthenium centers of a C_s symmetric dimer. Another important pattern is the simple looking 1:1:1:1 pseudoquartet indicative of C_3 symmetry where all methoxy groups are equivalent. This pattern is encountered in the ^1H NMR spectra of $Na(L_{OMe})$ and $[3]^{2+}$.

5. Bard, A. J.; Faulkner, L. R. *Electrochemical Methods, Fundamentals and Applications*; John Wiley and Sons: New York, 1980; p 431.

6. Bard, A. J.; Faulkner, L. R. *Electrochemical Methods, Fundamentals and Applications*; John Wiley and Sons: New York, 1980; pp 527-528.

7. Matsuda, H.; Ayabe, Y. *Z. Elektrochem.*, **1955**, *59*, 494. Bard, A. J.; Faulkner, L. R. *Electrochemical Methods, Fundamentals and Applications*; John Wiley and Sons: New York, 1980; pp 224-227.

8. Mattson, J. S.; Mark, H. B., Jr. *Activated Carbon: Surface Chemistry and Adsorption from Solution*; Marcel Dekker: New York, 1971; and references therein.

9. Koval, C.; Anson, F. C. *Anal. Chem.*, **1978**, *55*, 223. Brown, A. P.; Koval, C.; Anson, F. C. *J. Electroanal. Chem.*, **1976**, *72*, 379. Brown, A. P.; Anson, F. C. *J. Electroanal. Chem.*, **1977**, *83*, 203.

10. Brown, A. P.; Anson, F. C. *Anal. Chem.*, **1977**, *49*, 1589. Oyama, N.; Brown, A. P.; Anson, F. C. *J. Electroanal. Chem.*, **1978**, *87*, 435. Mazur, S.; Matusinovic, T.; Cammann, K. *J. Am. Chem. Soc.*, **1977**, *99*, 3888. Armstrong, N. R.; Hawn, D. D. *J. Phys. Chem.*, **1978**, *82*, 1288.

11. Bard, A. J.; Faulkner, L. R. *Electrochemical Methods, Fundamentals and Applications*; John Wiley and Sons: New York, 1980; pp 50-52.

12. Bard, A. J.; Faulkner, L. R. *Electrochemical Methods, Fundamentals and Applications*, John Wiley and Sons: New York, 1980; pp 26-29.

13. Basolo, F.; Johnson, R. C. *Coordination Chemistry*; Science Reviews, 1986, p 104.

14. Haney, S.; Bercaw, J. E. *Unpublished results*, California Insitute of Technology, 1991.

15. Griffith, W. P.; Pawson, D. *J. Chem. Soc., Dalton Trans.*, **1973**, 1315.

16. Saltzman, H.; Sharefkin, J. G. *Organic Syntheses*, *43*, 60-61.

17. Kläui, W. *Z. Naturforsch., B.: Anorg. Chem., Org. Chem.* **1979**, *34B*, 1403. Griffith, W. P.; Pawson, D. *J. Chem. Soc., Dalton Trans.* **1973**, 1315.

Chapter 3

Stoichiometric and Catalytic Oxidation Chemistry by the Ru^{V}-Ru^{V}/Ru^{IV}-Ru^{IV} Redox Couple of $[(L_{OMe})(HO)Ru^{IV}(\mu\text{-}O)_2Ru^{IV}(OH)(L_{OMe})]$

Abstract:

The oxidation chemistry of the Ru^{V}-Ru^{V}/Ru^{IV}-Ru^{IV} couple dimers is similar to that manifested by other high oxidation state metal-oxo complexes. In organic solvents, the neutral Ru^{V}-Ru^{V} dimers **2** and $\mathbf{2}_{Et}$ slowly react with substrates to form the Ru^{IV}-Ru^{IV} dimers **1** and $\mathbf{1}_{Et}$ respectively. In aqueous phosphate buffer, pH 7, the Ru^{V}-Ru^{V}/Ru^{IV}-Ru^{IV} oxidation wave exhibits electrocatalytic behavior. Protonation or electrophile association appears to enhance the metal-oxo reactivity of **2** and $\mathbf{2}_{Et}$. The electrocatalytic oxidation of methanol as measured by chronoamperometry appears to consist of parallel processes, one of which is methanol-dependent. The methanol-dependent process is first order in both dimer and substrate concentrations, and the system exhibits a primary kinetic deuterium isotope effect typical of hydrogen or hydride abstraction by metal-oxo complexes. The parallel process likely involves oxidative ligand degradation. Interestingly, the Ru^{V}-Ru^{V} complex exhibits typical metal-oxo chemistry in the electron transfer from substrate despite the electronic coupling of the metal centers. Unfortunately, the complete oxygen donor coordination environment of this dimer did not effect the desired reduction in the driving potential for the metal-oxo chemistry.

Introduction

The dimer $(L_{OMe})(O)Ru^{V}(\mu\text{-}O)_2Ru^{V}(O)(L_{OMe})$ (**2**) is a strong oxidizing agent. As mentioned in the previous chapter, the Ru^{V}-Ru^{V}/Ru^{IV}-Ru^{IV} redox couple appears electrocatalytic via a reactive Ru^{V}-Ru^{V} species. In addition, previous work by Power and Bercaw found the (L_{OEt}) analog $(L_{OEt})(O)Ru^{V}(\mu\text{-}O)_2Ru^{V}(O)(L_{OEt})$ ($\mathbf{2_{Et}}$) oxidizes alcohols (methanol, isopropanol, and *sec*-phenethyl alcohol) to give $(L_{OEt})(HO)Ru^{IV}(\mu\text{-}O)_2$-$Ru^{IV}(OH)(L_{OEt})$ ($\mathbf{1_{Et}}$), the (L_{OEt}) analog of **1**, and the corresponding aldehyde or ketone products (Figure 3.1).[1] Aldehydes likely undergo further oxidation by $\mathbf{2_{Et}}$ in CH_3CN to the carboxylic acids (Figure 3.2).

Figure 3.1. Oxidation of alcohols by **2**.

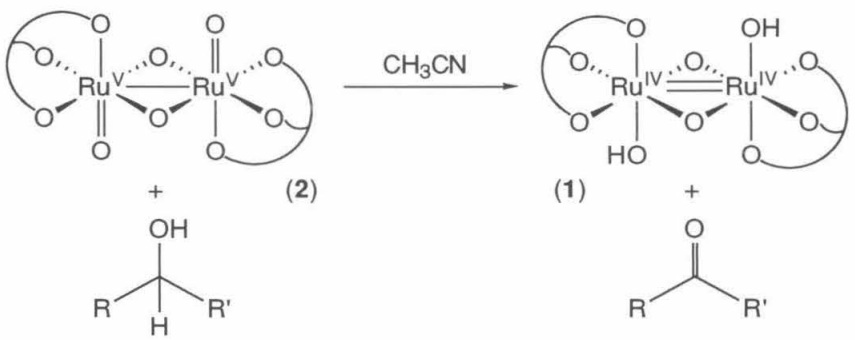

Figure 3.2. Oxidation of aldehydes by **2**.

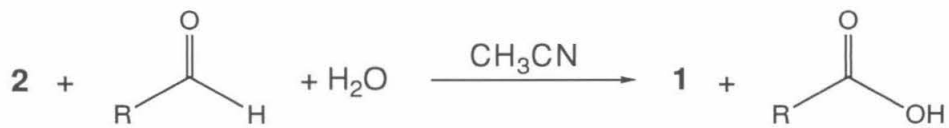

This is no surprise in the context of the metal-oxo literature where Ru^{V}-oxo and other ruthenium complexes with potentials of +0.70 V or greater are known to oxidize organic substrates.[2]

This dimer is somewhat unique in possessing two Ru^{V}-oxo groups that appear electronically coupled. This dimer is diamagnetic despite two d^3 centers, and its electrochemistry is dominated by two electron processes. This electronic cooperation could influence the specifics of two-electron oxidation, the process key to organic oxidation. This may facilitate oxidation and justify attempts to observe reactivity at lower potentials.

The neutral Ru^{V}-Ru^{V} dimers **2** and $\mathbf{2_{Et}}$ easily oxidize primary alcohols, secondary alcohols, and aldehydes to form the neutral Ru^{IV}-Ru^{IV} dimers **1** and $\mathbf{1_{Et}}$ and the corresponding aldehydes, ketones, and acids respectively. The dimer **2** also reacts with formaldehyde and formate suggesting that the complete oxidation of substrates such as methanol to CO_2 and water is possible. The kinetics of *sec*-phenethyl alcohol oxidation by $\mathbf{2_{Et}}$ appears typical of metal-oxo chemistry. On the surface, metal-metal cooperation exhibits no significant effect on the mechanism of metal-oxo chemistry by these dimers.

The Ru^{V}-Ru^{V}/Ru^{IV}-Ru^{IV} couple of **1** electrocatalyzes the oxidation of alcohols and aldehydes. Specifically, the electrocatalytic oxidation of methanol, formaldehyde, and formate indicates that the complete oxidation of substrates to CO_2 and water is possible as was the case for the neutral Ru^{V}-Ru^{V} dimers. This reactivity, via the monoprotonated $[H2]^{+}$, is faster than that of the neutral **2**. This may be due to protonation making the metal-oxo moieties more electrophilic. The kinetics of the electrocatalysis, measured by chronoamperometry, consists of two parallel processes: one is indicative of hydrogen or hydride transfer familiar in metal-oxo chemistry and the other is indicative of water oxidation and/or dimer electrodegradation. Again, the electronic cooperation of the metal centers in the Ru^{V}-Ru^{V} species does not significantly alter the general features of the metal-oxo chemistry.

Results and Discussion

3.1. Bulk Oxidation of substrates by (L_{OMe}) and (L_{OEt}) analogs of [(L_{OR})(O)Ru^{V}(μ-O)$_2$$Ru^{V}$(O)($L_{OR}$)].

The oxidation of *sec*-phenethyl alcohol by (L_{OEt})(O)Ru^{V}(μ-O)$_2$$Ru^{V}$(O)($L_{OEt}$) (**2$_{Et}$**) has been investigated by Blake and Bercaw.[3] In this reaction, the Ru^{V}-Ru^{V} dimer reacts with *sec*-phenethyl alcohol in benzonitrile to form the neutral dimer (L_{OEt})(HO)Ru^{IV}(μ-O)$_2$-Ru^{IV}(OH)(L_{OEt}) (**1$_{Et}$**) and acetophenone (Figure 3.3). The reaction, monitored by UV-vis spectroscopy, exhibited good isosbestic behavior for three half-lives. The reaction exhibits first order behavior for both dimer and alcohol. Overall, this reaction appears typical of metal-oxo chemistry. Strangely, this reaction requires several hours to complete while oxidation in the electrocatalysis observed for the Ru^{V}-Ru^{V}/Ru^{IV}-Ru^{IV} couple of the (L_{OMe})$^{-}$-based dimers (Chapter 2) occurs on the order of seconds (Figure 3.4).

Figure 3.3. Reaction of **2$_{Et}$** with *sec*-phenethyl alcohol.

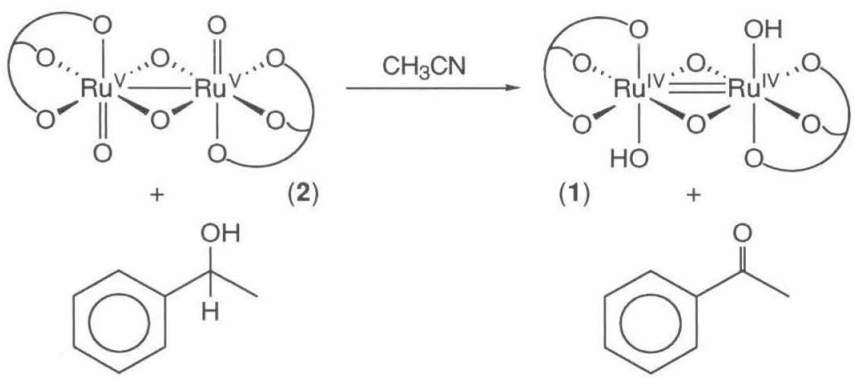

In bulk oxidations with **2** the rate difference in buffered water versus organic solvents is striking. Reactions between **2** and methanol in CH_3CN require about an hour, and the dimer is visibly stable in neat methanol for several minutes. When such a methanol solution is promptly added to aqueous buffer, the solution immediately changes to a brown color followed

Figure 3.4. Relative rates of oxidations by **2** in CH_3CN and water.

$$(\mathbf{2}) + CH_3OH \xrightarrow[CH_3CN]{\text{Slow (hours)}} (\mathbf{1}) + CH_2O$$

$$(\mathbf{2}) + CH_3OH \xrightarrow[pH=7,\ H_2O]{\text{Fast (seconds)}} (\mathbf{1}) + CH_2O$$

by a green color characteristic of the Ru^{IV}-Ru^{IV} dimer. This suggests the dimer assumes a more active form in buffered water. The electrochemical experiments in Chapter 2 suggest this is the result of protonation to $[(L_{OMe})(O)Ru^{V}(\mu\text{-}O)_2Ru^{V}(OH)(L_{OMe})]^+$ ($[\mathbf{H2}]^+$) in pH 7 buffer. Protonation of one Ru^{V}-oxo group could draw electron density from the other and thereby enhance its reactivity over that of the neutral species (Figure 3.5).

Figure 3.5. Oxidation of substrates by protonated **2**.

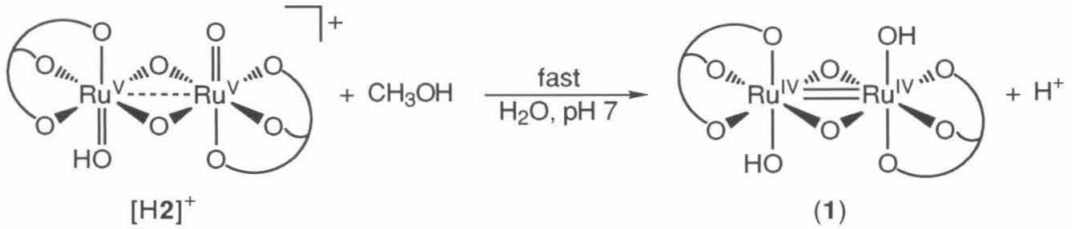

$[\mathbf{H2}]^+$ (**1**)

Blake et al. indeed observed the reactions of $\mathbf{2}_{Et}$ with *sec*-phenethyl alcohol proceed faster upon the addition of acid.[3] Strangely, $\mathbf{2}_{Et}$ slowly changed to $\mathbf{1}_{Et}$ in the absence of substrate. This could be analogous to the catalytic currents observed in the aqueous electrochemistry of (L_{OMe}) analogs without added substrate and the subsequent appearance of new redox waves. The isolation of $(L_{OEt})_2Co$ from the synthesis of $\mathbf{1}_{Et}$ demonstrates ligand degradation. Similarly, small amounts of $(L_{OEt})_2Co$ are believed to be formed in reactions with $\mathbf{2}_{Et}$. The enhanced reactivity of the Ru^{V}-Ru^{V} species in either water or organic solvents may be sufficient to attack the $(L_{OR})^-$ ligands.

Surprisingly, the addition of alkali salts to $\mathbf{2_{Et}}$ in benzonitrile also modestly accelerates substrate oxidation.[3] The association of an alkali metal to one Ru^{V}-oxo group could be accelerating the reaction in a manner like that proposed for acid. In an alternative explanation, the salts could promote a dimer-monomer equilibrium with Ru^{VI} and Ru^{IV} monomers. The Ru^{VI} could react with substrate and Ru^{IV} monomers might form $\mathbf{1_{Et}}$ dimer (Figure 3.6). Though this mechanism is not easily discounted, the dimer-monomer equilibrium is not evident in the absence of alkali salts; mixtures of **2** and $\mathbf{2_{Et}}$ do not exhibit evidence of the cross-over dimer $(L_{OMe})(O)Ru^{V}(\mu\text{-}O)_2Ru^{V}(O)(L_{OEt})$ behavior by ^1H NMR spectroscopy (Chapter 2).

Figure 3.6. Possible mechanism for substrate oxidation by **2** via hypothetical dimer-monomer equilibrium.

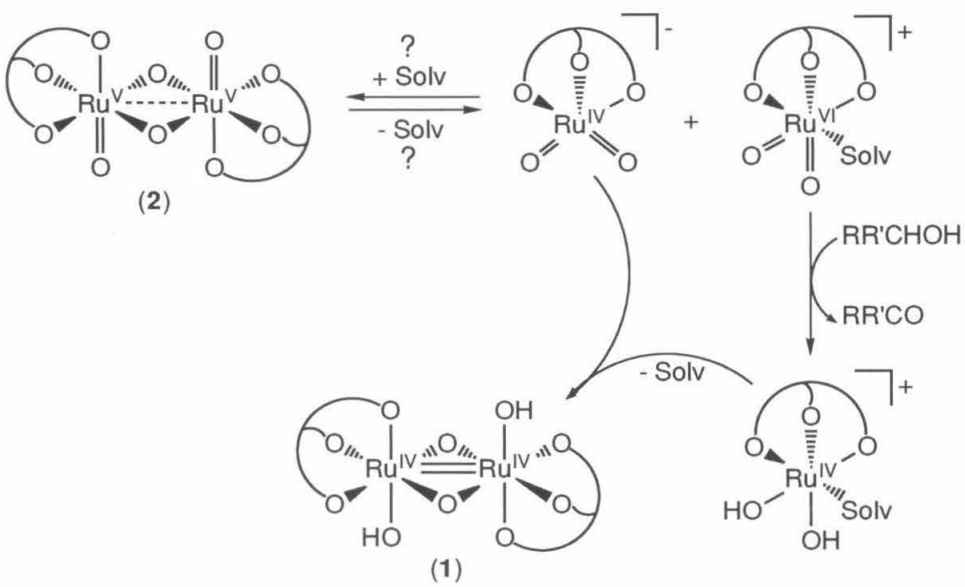

3.2. Electrocatalytic Oxidation by Ru^{V}-Ru^{V}/Ru^{IV}-Ru^{IV} couple in water.

To better understand the oxidation chemistry of the enhanced Ru^{V}-Ru^{V} dimers, aqueous electrocatalysis by the Ru^{V}-Ru^{V}/Ru^{IV}-Ru^{IV} couple was investigated in greater detail. The addition of methanol to buffered **1** enhanced electrocatalytic currents and attenuated the

Figure 3.7. Cyclic Voltammogram of **1** with and without added methanol.

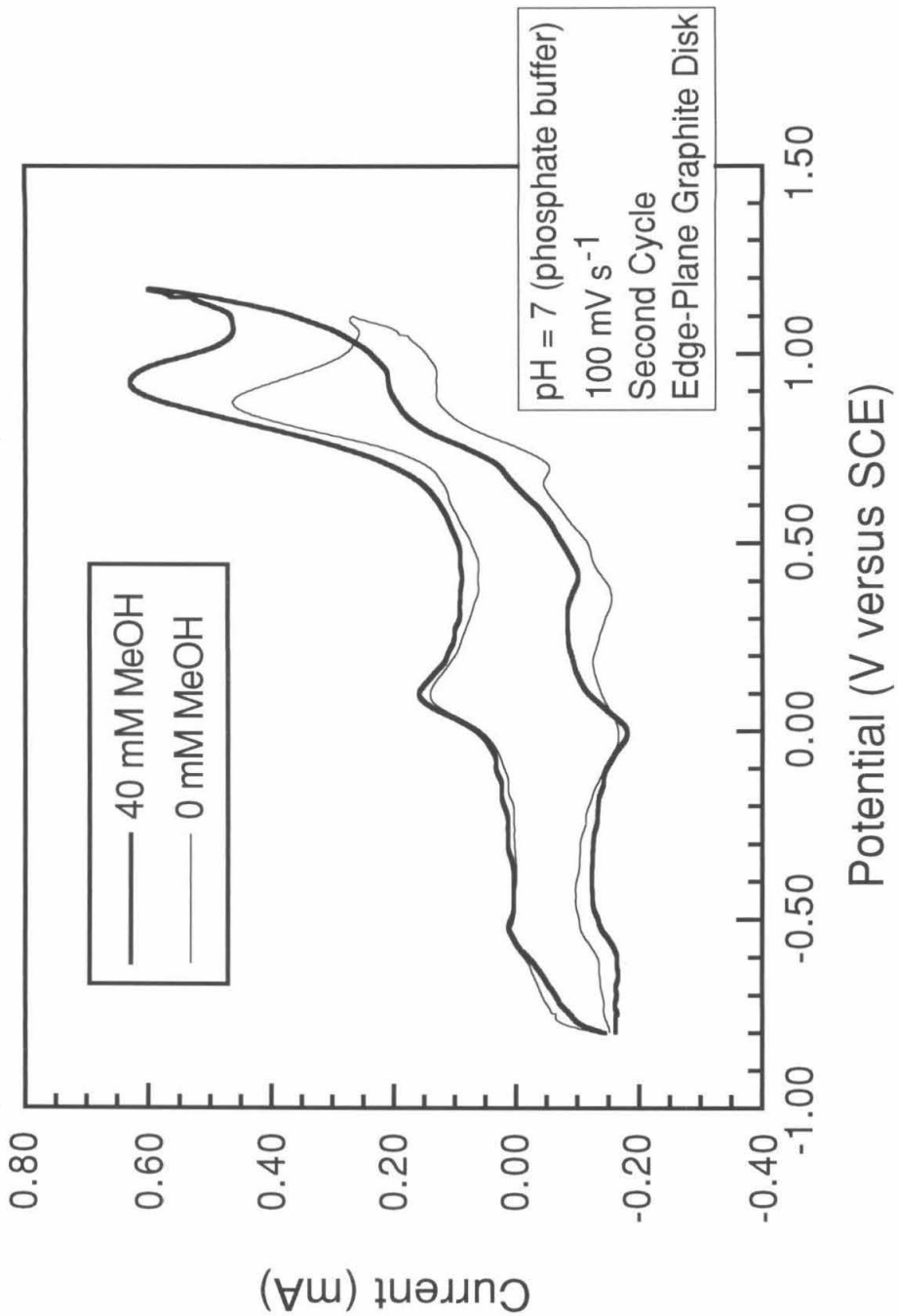

formation of secondary redox waves discussed in Chapter 2 (Figure 3.7). The reaction with methanol is evidently preferred over the side reactions resulting in a cleaner electrocatalytic cycle. Similar behavior is observed for other alcohols (ethanol, isopropanol, and benzyl alcohol), formaldehyde, and formate. The oxidation of the latter two suggests methanol can be electrocatalytically oxidized completely to carbon dioxide or carbonate (a desirable feature in fuel cell electrocatalysts).

The dimer electrocatalysis was examined by chronoamperometry at a large edge-plane graphite electrode.[4] For kinetic analysis of electrocatalysis, this method was easier to interpret than cyclic voltammetry and required less specialized equipment than rotating ring-disk electrode (RRDE) experiments.[5,6] In chronoamperometric measurements, a potential is applied to an electrode and the current is measured at times between 100 ms to 20 s after the beginning of the experiment.[7] Comparing current with and without catalysis allows the catalytic rate to be measured. Since the Ru^{V}-Ru^{V}/Ru^{IV}-Ru^{IV} wave showed electrocatalysis in absence of substrate, currents from similar measurements of the Ru^{IV}-Ru^{IV}/Ru^{III}-Ru^{III} reduction were used. This is reasonable since both redox waves originate from the same Ru^{IV}-Ru^{IV} species. Unfortunately, as suggested in Chapter 2, the Ru^{V}-Ru^{V}/Ru^{IV}-Ru^{IV} oxidation wave is not ideally behaved due to a dependence on the electrode surface. Chronoamperometric measurements were irreproducible unless the electrode was electrochemically stripped between experiments. Even with this rigorous treatment, the electrode required 500 ms before approaching Cottrell behavior (current versus time behavior characteristic of solution electrochemistry at a planar electrode).[8] This is likely due to changes in the electrode surface at short experiment times that manifest themselves through rate changes in heterogeneous electron transfer with dimer. Reasonable Cottrell behavior was approached for the Ru^{V}-Ru^{V}/Ru^{IV}-Ru^{IV} oxidation between 500 ms and 1 s suggesting the electrode was approaching a steady state. Though long current sampling times are not recommended for chronoamperometric measurements, the dimer system appears to exhibit good Cottrell

behavior to current sampling times as long as 20 seconds suggesting that times of 1, 2, and 3 seconds may be acceptable at least in this rough kinetic survey. With this exception, the chronoamperometric measurements were carried out in a standard fashion with 1.0 mM solutions of **1**.[9]

For straightforward data analysis, the simple catalytic cycle illustrated in Figure 3.8 was assumed with the substrate dependencies included in the first order rate constant k'_{obs}.

Figure 3.8. Electrocatalytic cycle and rate law for methanol electrooxidation with Ru^{V}-Ru^{V}/Ru^{IV}-Ru^{IV} couple of **1**.

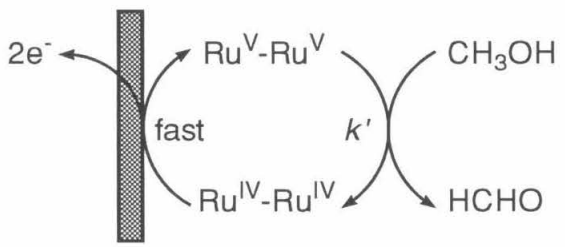

$$k'_{obs} = k'\left([CH_3OH]\text{dependence}\right)$$

$$k'_{obs} = \frac{1}{\pi t}\left(\frac{i}{i_d}\right)^2 \qquad \text{if } \left(\frac{i}{i_d}\right) \geq 2.2$$

i = current at time t with electrocatalysis

i_d = current at time t without electrocatalysis

The side reactions were neglected in the initial analysis, but were reintroduced when interpreting the methanol dependence. The values obtained for k'_{obs} at each current sampling time are tabulated below (Table 3.1). Plots of k'_{obs} versus concentration of methanol are linear with positive intercepts (Figure 3.9). This indicates that the catalytic cycle really consists of two parallel components with one being first order in methanol and the other being independent of methanol (Figure 3.10). This is supported by similar experiments with CD_3OD intended to measure the isotope effect. As observed for CH_3OH, the plot of k'_{obs} versus CD_3OD concentration afforded linear plots in Figure 3.11. The intercepts for the 1, 2, and 3 second data

Figure 3.9. Plot of k'_{obs} versus methanol concentration.

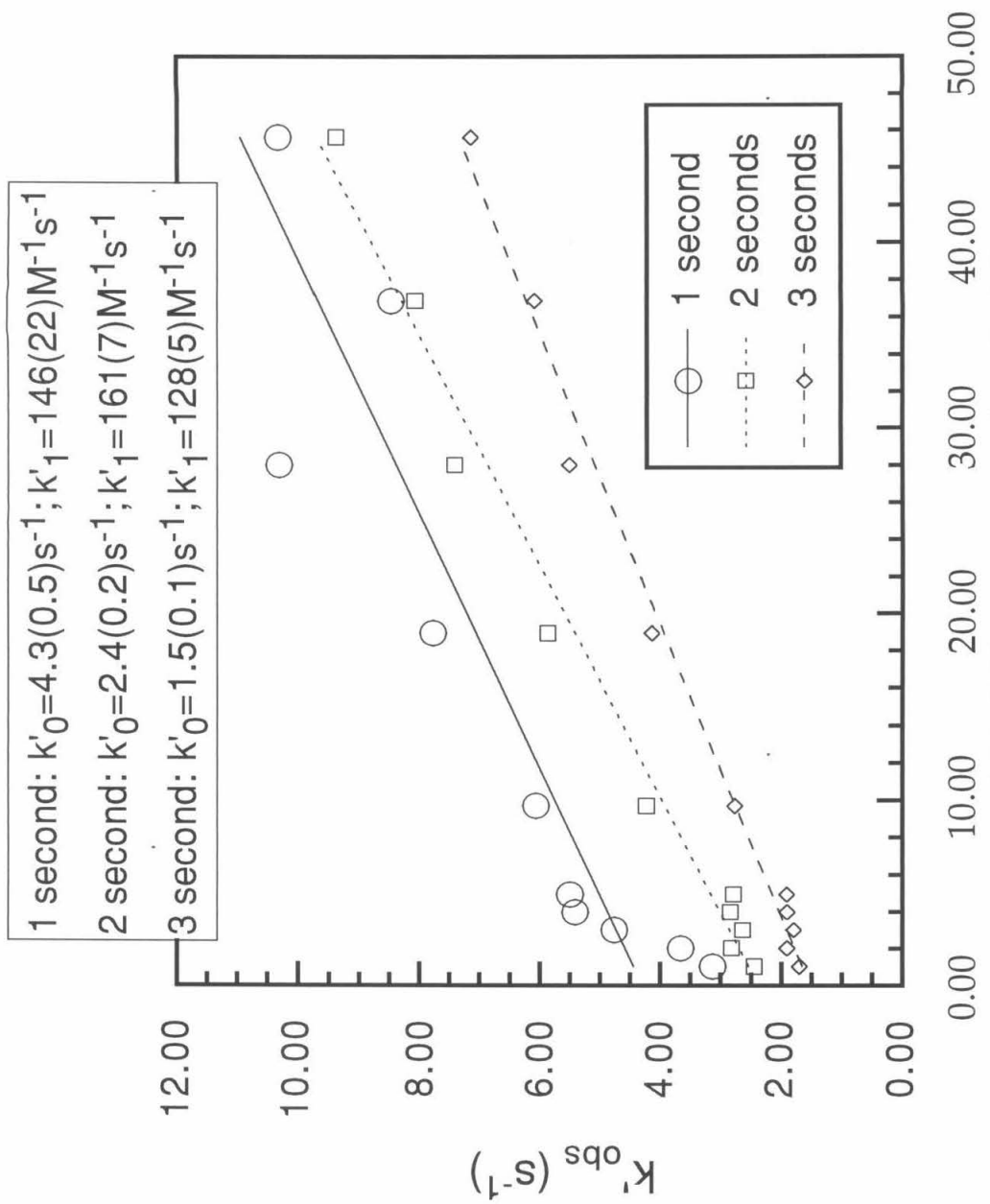

Figure 3.10. Rate law and parallel cycles for methanol electrooxidation by **1**.

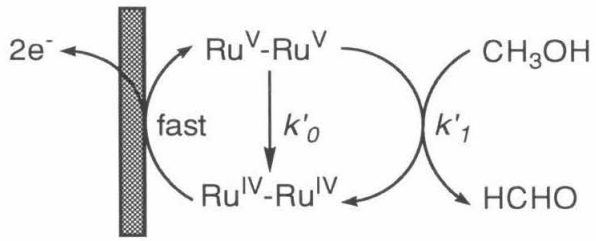

$$k'_{obs} = k'_0 + k'_1[CH_3OH]$$

Table 3.1. k'_{obs} for chronoamperometric measurements with methanol electrooxidation by **1**.

$[CH_3OH]$ (mM)	k'_{obs} (1 second) s^{-1}	k'_{obs} (2 seconds) s^{-1}	k'_{obs} (3 seconds) s^{-1}
1.03	3.14	2.45	1.71
2.04	3.67	2.83	1.92
3.03	4.77	2.65	1.81
4.00	5.42	2.85	1.92
4.95	5.51	2.80	1.93
9.81	6.08	4.24	2.78
19.44	7.79	5.87	4.15
28.89	10.32	7.42	5.52
38.16	8.48	8.08	6.10
47.25	10.34	9.38	7.15

Table 3.2. k'_{obs} for chronoamperometric measurements with d_4-methanol.

$[CD_3OD]$ (mM)	k'_{obs} (1 second) s^{-1}	k'_{obs} (2 seconds) s^{-1}	k'_{obs} (3 seconds) s^{-1}
9.75	3.75	2.40	1.57
19.32	5.08	2.57	1.62
28.71	4.15	3.14	2.00
37.92	5.88	3.17	2.12
47.00	4.74	4.64	3.08
93.10	5.23	3.79	2.70
185.60	9.14	7.03	4.24

Figure 3.11. Plot of k'_{obs} versus d_4-methanol concentration.

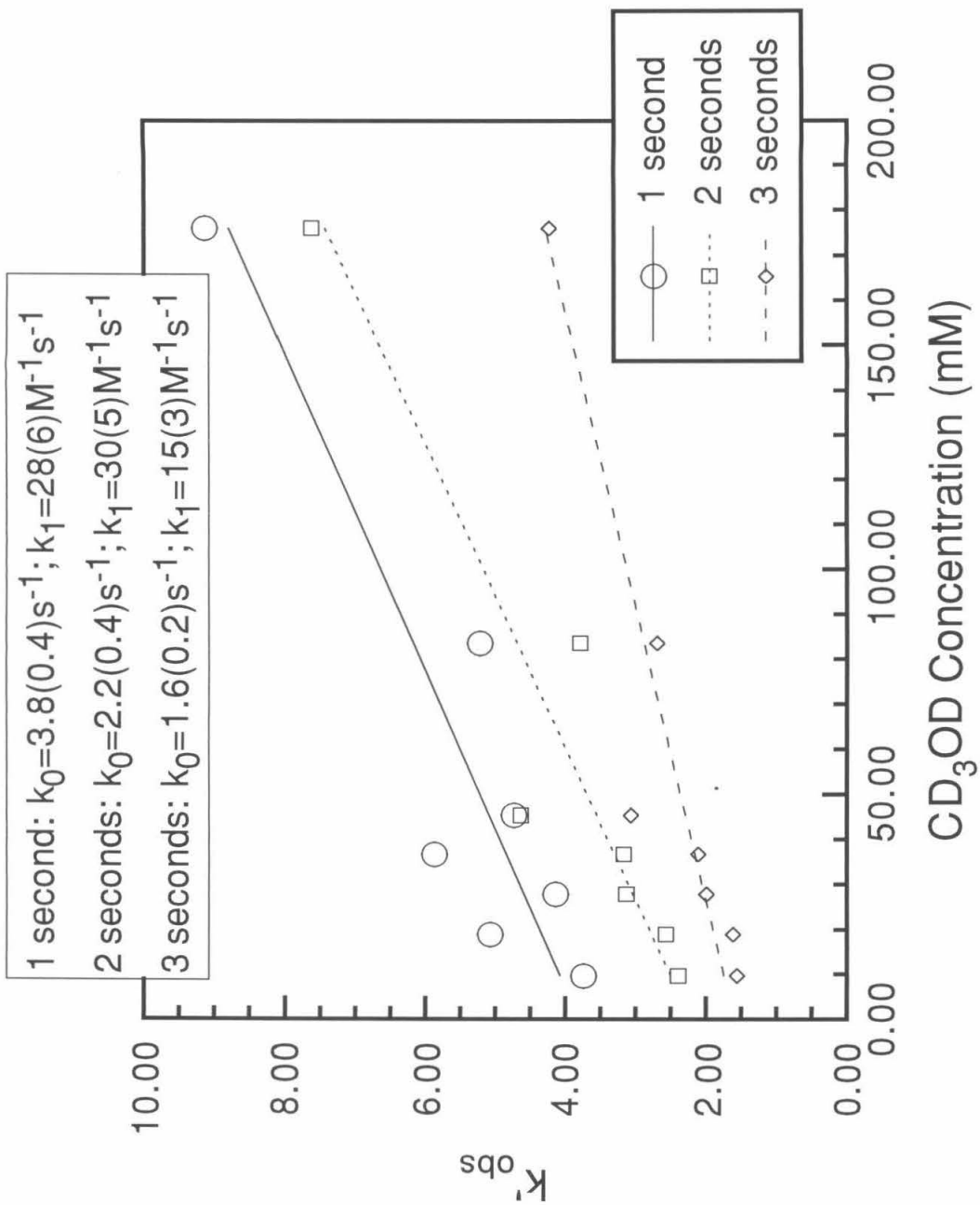

appears within experimental error of the corresponding measurements with CH_3OH. The k'_{obs} versus alcohol concentration slopes indicate a significant primary kinetic deuterium isotope effect ($k'_{1H}/k'_{1D} \sim 5$) in the methanol-dependent process.[10] Evidently, this oxidation involves hydrogen or hydride abstraction similar to known metal-oxo chemistry.[2]

The primary kinetic deuterium isotope effect, first order dependence in dimer and methanol, and the predominance of two electron processes in the dimer oxidation chemistry suggest the first order component of this reactivity is likely methanol oxidation by hydride abstraction from a methyl C-H bond. This process could also occur by hydrogen abstraction followed by a subsequent electron transfer, but this process would generate Ru^V-Ru^{IV} intermediates which are stronger oxidants than the Ru^V-Ru^V species as implied by the two electron nature of the Ru^V-Ru^V/Ru^{IV}-Ru^{IV} redox couple. This process appears to be a simultaneous two electron, one proton abstraction analogous to the oxidation of **1** to $[H2]^+$.

The methanol-independent process is likely a combination of water oxidation and oxidative degradation of the dimer itself. The oxidation of water is suggested by the vicinity of the Ru^V-Ru^V/Ru^{IV}-Ru^{IV} dimer to the water oxidation potential at graphite electrodes. The oxidative degradation of dimer is implied by the appearance of secondary redox waves in cyclic voltammetry and the isolation of $(L_{OMe})_2Co$ from the synthesis of **2**. Each equivalent of dimer could provide many equivalents of oxidizable substrates upon activation and fragmentation.

This ligand degradation could account for peculiarities in Figures 3.9 and 3.11. In these figures, the intercept of each line decreases with increasing current sampling times. This could be attributed to the loss of catalyst through the duration of the experiment. This is also consistent with values of k'_0 for each of the three sampling times with CH_3OH being within experimental error of the corresponding values with CD_3OD. This decomposition of catalyst also accounts for decreasing values of $k'_{1,obs}$ with increasing current sampling times. (This is

most evident in the data with CD_3OD in Figure 3.11.) The effect on $k'_{0,obs}$ is more pronounced than on $k'_{1,obs}$ since the former is likely greater than first order in dimer.

Overall, chronoamperometric data suggests the electrocatalysis by the Ru^V-Ru^V/Ru^{IV}-Ru^{IV} couple consists of two parallel cycles with one oxidizing methanol and the other oxidizing water and/or dimer. In retrospect, RRDE experiments would have been better suited for this study; however, this system is not worthy of further investigation due to the water and/or dimer oxidation.

Conclusion

The oxidation chemistry of the Ru^V-Ru^V dimers is similar to that observed in other high oxidation state metal-oxo complexes described in the literature.[2] In organic solvents, the neutral Ru^V-Ru^V dimers **2** and $\mathbf{2_{Et}}$ slowly react with substrates to form the Ru^{IV}-Ru^{IV} dimers **1** and $\mathbf{1_{Et}}$ respectively. In pH 7 phosphate buffer, the reactivity of **2** is evidently enhanced by protonation such that the Ru^V-Ru^V/Ru^{IV}-Ru^{IV} wave appears electrocatalytic. Protonation or association of an electrophile to **2** and $\mathbf{2_{Et}}$ may enhance the metal-oxo reactivity. The electrocatalytic oxidation of methanol appears to consist of parallel methanol dependent and independent processes. The methanol-dependent process appears first order in both dimer and substrate and exhibits a primary kinetic deuterium isotope effect typical of a hydrogen or hydride abstraction process. This reactivity is troubled by a parallel process that likely oxidizes water and/or ligand. The Kläui ligands, $(L_{OR})^-$, may not be as resistant to oxidation as previously believed. Nevertheless, the completely oxygen donor coordination environment of this dimer did not reduce the potential of the metal-oxo chemistry to applicable values as expected. Interestingly, the Ru^V-Ru^V dimer does exhibit substrate oxidation chemistry typical of metal-oxo complexes though the metal centers likely cooperate in the electron transfer.

Experimental

General experimental considerations for bulk chemistry and electrochemistry were identical to those described in the Experimental section of Chapter 2.

Qualitative rate comparison of methanol oxidation in aqueous and organic media. An excess of CH_3OH (50 μL, 1.23 mmol) was added to a solution of **2** (2 mg, 1.7 μmol) in CH_3CN (1 mL). This reaction turned from the purple of **2** to the green of **1** over a few hours. A sample of **2** (2 mg, 1.7 μmol) was dissolved in neat CH_3OH (1 mL). This solution changed from purple to green over 15 minutes. A freshly prepared sample of **2** (2 mg, 1.7 μmol) in neat CH_3OH (1 mL) was quickly added to phosphate buffer (1 mL, pH 6.9, I=0.1 M). This solution changed from purple to gray within 4 seconds and proceeded to turn yellow-green in 15 seconds. The presence of aqueous buffer apparently enhances the reactivity of **2**. For contrast, a freshly prepared sample of **2** (2mg, 1.7 μmol) in CH_3CN (1 mL) was quickly added to phosphate buffer (1 mL, pH 6.9, I=0.1 M). This solution changed from purple to gray in 7 seconds, bluish-green after 20 seconds. This reaction did not return to the green color of **1**.

Cyclic Voltammetry of 1 with added substrates. A solution of **1** (typically 0.0148g, 10.1 μmol, 1.01 mM) dissolved in phosphate buffer (10 mL, pH 6.9, I=0.1 M) was examined by cyclic voltammetry at an edge-plane graphite electrode. An aliquot (0.40 mL) of CH_3OH (1.04 M) in phosphate buffer (2.00 mL, pH 6.9, I=0.1 M) was prepared and added to the working dimer solution to provide a final CH_3OH concentration of 40 mM. This resulted in enhanced peak currents for the Ru^V-Ru^V/Ru^{IV}-Ru^{IV} couple as illustrated in Figure 3.7. Similar experiments were carried out with formaldehyde, formate, ethanol, and isopropanol which all resulted in enhanced currents for the Ru^V-Ru^V/Ru^{IV}-Ru^{IV} couple.

Chronoamperometric kinetic measurements of methanol electrooxidation by 1. A solution of **1** (typically 1.0 mM) in phosphate buffer (10.0 mL, pH 6.9, I=0.1 M) was examined by chronoamperometry for potential steps of +0.94 V versus SCE at an edge-plane graphite

electrode. Cottrell behavior was confirmed for experiment durations from 500 ms to 1000 ms, 500 ms to 5000 ms, and 1 s to 50 s. Plots of current versus the square root of time were nonlinear before 500 ms indicating that data needed to be collected at experimental times of one second and greater to avoid non-Cottrell processes.

Currents were then sampled for the potential steps of +0.94 V at 1, 2, and 3 second current sampling times. To obtain reproducible data, each measurement needed to be preceded by an electrode preparation consisting of a potential step to +1.00 V for 10 s, -0.80 V for 10 s, and +0.20 V for 30 s followed by solution stirring. This electrode preparation is presumably necessary to remove residual compounds from previous experiments from the electrode surface. Each measurement was repeated twice. Then a sample of CH_3OH in phosphate buffer (2.00 mL, pH 6.9, I=0.1 M) was added to both the working and auxiliary solutions according to the schedule below and the chronoamperometric measurements were repeated. This was repeated through the substrate addition schedule.

Substrate addition schedule.

a. Five additions (0.10 mL) of CH_3OH (10.4 μmol) in buffer.
b. One addition (0.10 mL) of CH_3OH (51 μmol) in buffer.
c. Four additions (0.10 mL) of CH_3OH (100 μmol) in buffer.
d. One addition (0.10 mL) of CH_3OH (0.43 mmol) in buffer.

To obtain blank measurements of methanol oxidation under the same conditions, the experiment was repeated as before without addition of **1**. The electrocatalytic data were corrected with these measurements.

The data analysis requires analogous measurements in the absence of catalysis. Since the Ru^{V}-Ru^{V}/Ru^{IV}-Ru^{IV} couple exhibits electrocatalysis in absence of added substrate, these measurements were made on the Ru^{IV}-Ru^{IV}/Ru^{III}-Ru^{III} couple with a potential step of -0.20 V versus SCE. Fortunately, both Ru^{V}-Ru^{V}/Ru^{IV}-Ru^{IV} oxidation and Ru^{IV}-Ru^{IV}/Ru^{III}-Ru^{III} reduction currents arise from identical species making these measurements compatible. Since

the reduction is independent of methanol, only a few chronoamperometric measurements were made for **1** (1 mM) with and without methanol (40 mM). These measurements were corrected with chronoamperometric data from blank solutions. The remainder of the data analysis was performed as discussed in the text.

To measure isotope effects, an identical set of measurements was made using CD_3OD in place of CH_3OH. The CD_3OD was added to the experiment according to the modified schedule below.

Substrate addition schedule.

a. Five additions (0.10 mL) of CD_3OD (10.4 μmol) in buffer.
b. One addition (0.10 mL) of CD_3OD (51 μmol) in buffer.
c. Four additions (0.10 mL) of CD_3OD (100 μmol) in buffer.
d. One addition (0.10 mL) of CD_3OD (0.43 mmol) in buffer.
e. One addition (42.0 μL) of neat CD_3OD.

Chronoamperometric experiments without background corrections were carried out with added ethanol, isopropanol, formaldehyde and formate. All of these substrates give enhanced currents.

References

1. Power, J. M.; Evertz, K.; Henling, L.; Marsh, R.; Schaefer, W. P.; Labinger, J. A.; Bercaw, J. E. *Inorg. Chem.*, **1990**, *29*, 5058-5065.

2. See references 11 and 13-18 in Chapter 1.

3. Blake, R. E.; Bercaw, J. E. *Unpublished Results*, California Institute of Technology.

4. Delahay, P.; Steihl, G. L. *J. Am. Chem. Soc.*, **1952**, *74*, 3500. Miller, S. L., *ibid.*, **1952**, *74*, 4130.

5. Saveant, J. M.; Vianello, E. *Electrochim. Acta.*, **1963**, *8*, 905. Saveant, J. M.; Vianello, E. *ibid,*, **1967**, *12*, 629.

6. Prater, K. B.; Bard, A. J. *J. Electrochem. Soc.*, **1970**, *117*, 1517. Beran, P.; Bruckenstein, S. *J. Phys. Chem.*, **1968**, *72*, 3630. Kermiche-Aouanouk, F.; Daguenet, M. *Electrochim. Acta.*, **1972**, *17*, 723.

7. Laitinen, H. A.; Kolthoff, I. M. *J. Am. Chem. Soc.*, **1939**, *61*, 3344. Laitinen, H. A. *Trans. Electrochem. Soc.*, **1942**, *82*, 289.

8. Cottrell, F. G. *Z. Physik. Chem.*, **1902**, *42*, 385.

9. Bard, A. J.; Faulkner, L. R. *Electrochemical Methods, Fundamentals and Applications*; John Wiley and Sons: New York, 1980; p 138.

10. Lowry, T. H.; Richardson, K. S. *Mechanism and Theory in Organic Chemistry*; third ed.; Harper and Row: New York, 1987; pp 233-238.

Chapter 4

Stoichiometric and Catalytic Oxidation Chemistry by the Ru^{IV}-Ru^{IV}/Ru^{III}-Ru^{III} Redox Couple of $[(L_{OMe})(HO)Ru^{IV}(\mu\text{-}O)_2Ru^{IV}(OH)(L_{OMe})]$

Abstract:

Despite a relatively low driving potential, **1** oxidizes alcohols, aldehydes, and triphenylphosphine in acetonitrile to afford Ru^{III}-Ru^{III} products such as $[(L_{OMe})(CH_3CN)Ru^{III}(\mu\text{-}OH)_2Ru^{III}(NCCH_3)(L_{OMe})](CF_3SO_3)_2$ (**[5]**$(CF_3SO_3)_2$). These reactions exhibit an unusual rate behavior that suggests an autocatalytic reaction pathway. The mechanism appears to differ fundamentally from known metal-oxo chemistry.

The dimer **1** undergoes a quantitative, inner sphere reaction with formaldehyde in aqueous buffer to afford $[(L_{OMe})Ru^{III}(\mu\text{-}OH)_2(\mu\text{-}HCOO)Ru^{III}(L_{OMe})](CF_3SO_3)$ (**[6]**(CF_3SO_3)), which was characterized by X-ray crystallography. Dimer **[6]**(CF_3SO_3) was easily oxidized by $AgCF_3SO_3$ to $[(L_{OMe})Ru^{IV}(\mu\text{-}O)_2(\mu\text{-}HCOO)Ru^{IV}(L_{OMe})](CF_3SO_3)$ (**[7]**(CF_3SO_3)), which reacts with formaldehyde to generate free formate, $[\mathbf{6}]^+$, and a small amount of $[(L_{OMe})(H_2O)Ru^{III}(\mu\text{-}OH)_2Ru^{III}(OH_2)(L_{OMe})]^{2+}$, ($[\mathbf{3}]^{2+}$). Labeling experiments with $[(L_{OMe})Ru^{IV}(\mu\text{-}O)_2(\mu\text{-}H^{13}COO)Ru^{IV}(L_{OMe})](CF_3SO_3)$ ($(\mu\text{-}H^{13}COO)$-**[7]**(CF_3SO_3)) and $H^{13}CHO$ estabilished that dimer bound formate did not dissociate in the formation of $[\mathbf{6}]^+$ and that a symmetrical dimer with two bound formates does not form as an intermeditate.

The dimer **1** acts as a catalyst for the bulk electrooxidation of formaldehyde in aqueous buffers. Formaldehyde oxidation occurs through two catalytic cycles driven by the Ru^{IV}-Ru^{IV}/Ru^{III}-Ru^{III} couples of $[\mathbf{7}]^+$ and **1**. This catalytic activity is limited by the buildup of free formate, but the catalyst lifetime can be extended by addition of palladium/carbon, a known electrocatalyst for the oxidation of formate.

Palladium/carbon catalysts pretreated with Nafion and loaded with **1** exhibit significant improvement over catalysts pretreated with Nafion alone. This finding demonstrates the feasibility of using homogenous catalysts to compliment existing heterogeneous catalysts.

Introduction

Though the metal-oxo chemistry of the Ru^{V}-Ru^{V}/Ru^{IV}-Ru^{IV} chemistry is driven by a potential too high for application in fuel cells, the dimer $(L_{OMe})(HO)Ru^{IV}(\mu\text{-}O)_2$-$Ru^{IV}(OH)(L_{OMe})$ (**1**) oxidizes substrates through the mild Ru^{IV}-Ru^{IV}/Ru^{III}-Ru^{III} couple. This chemistry is of academic interest in that organic oxidation at such low potentials is unusual for homogeneous catalysts; the mechanism of this reactivity appears very different from familiar metal-oxo chemistry and could contain important mechanistic information. This chemistry is also of practical interest in that these complexes could be used as co-catalysts to enhance the activity of existing heterogeneous catalysts.

The dimer **1** oxidizes primary alcohols, secondary alcohols, aldehydes, and triphenylphosphine in acetonitrile to afford Ru^{III}-Ru^{III} products and the corresponding aldehydes, ketones, acids, and triphenylphosphine oxide. The Ru^{III}-Ru^{III} product from reaction with triphenylphosphine is $[(L_{OMe})(CH_3CN)Ru^{III}(\mu\text{-}OH)_2Ru^{III}(NCCH_3)(L_{OMe})]$-$(CF_3SO_3)_2$ (**[5]**$(CF_3SO_3)_2$). These reactions exhibit unusual rate behavior including a slow initial reaction which rapidly accelerates through the course of the reaction. This rate behavior suggested autocatalytic behavior where an intermediate or the product catalyzed the reaction. The mechanism appears fundamentally different from known metal-oxo chemistry.

The dimer **1** similarly reacts with aldehydes in aqueous buffers. The reaction with formaldehyde cleanly affords $[(L_{OMe})Ru^{III}(\mu\text{-}OH)_2(\mu\text{-}HCOO)Ru^{III}(L_{OMe})](CF_3SO_3)$ (**[6]**(CF_3SO_3)) which was characterized by X-ray crystallography. Since $[(L_{OMe})(H_2O)Ru^{III}$-$(\mu\text{-}OH)_2Ru^{III}(OH_2)(L_{OMe})]^{2+}$ (**[3]**$^{2+}$) failed to react with free $HCOO^-$ in aqueous buffer, the isolated product is likely formed by the inner-sphere oxidation of formaldehyde. The Ru^{III}-Ru^{III} dimer is easily oxidized to $[(L_{OMe})Ru^{IV}(\mu\text{-}O)_2(\mu\text{-}HCOO)Ru^{IV}(L_{OMe})](CF_3SO_3)$ (**[7]**(CF_3SO_3)) which also oxidizes formaldehyde to afford free formate and a mixture of **[6]**$^+$ and a small amount of **[3]**$^{2+}$. Labeling experiments with $[(L_{OMe})Ru^{IV}(\mu\text{-}O)_2(\mu\text{-}H^{13}COO)$-

$Ru^{IV}(L_{OMe})](CF_3SO_3)$ ($(\mu\text{-}H^{13}COO)$-**[7]**(CF_3SO_3)) and $H^{13}CHO$ estabilished that dimer bound formate did not dissociate or exchange for product formate in formaldehyde oxidation by $[\mathbf{7}]^+$.

The dimer **1** acts as a catalyst for the bulk electrooxidation of formaldehyde in aqueous buffers. This activity appears to occur by two catalytic cycles: one of which relies on the Ru^{IV}-Ru^{IV}/Ru^{III}-Ru^{III} couple of $[\mathbf{6}]^+$ and $[\mathbf{7}]^+$ while the other relies on the same couple of $[\mathbf{3}]^{2+}$ and **1**. This catalytic activity was limited by buffer failure due to the generation of acid equivalents from formaldehyde oxidation and the buildup of free formate. The catalyst lifetime was extended using higher buffer strengths and added palladium/carbon, a known electrocatalyst for the oxidation of formate.

Attempts were made to test **1** as a co-catalyst in fuel cells. The dimer is irreversibly bound in Nafion films on electrodes. Palladium/carbon catalysts pretreated with Nafion and loaded with **1** exhibited significant improvement over catalysts simply pretreated with Nafion. This demonstrated that such a strategy using homogenous catalysts to compliment the activity of existing heterogeneous catalysts is feasible. In the longer-term, principles learned from this homogeneous system may assist in understanding and optimizing existing heterogeneous catalysts.

Results and Discussion

*4.1. General Oxidation chemistry of $[H_2\mathbf{1}]^{2+}$ and **1** in organic solvents.*

Surprisingly, **1** is capable of oxidizing organic substrates though its Ru^{IV}-Ru^{IV}/Ru^{III}-Ru^{III} redox potential is modest. In CD_3CN, $(L_{OMe})(HO)Ru^{IV}(\mu\text{-}O)_2Ru^{IV}(OH)(L_{OMe})$ (**1**) is observed by ^1H NMR spectroscopy to react with alcohols (methanol, ethanol, 2-propanol, and benzyl alcohol) to form the corresponding aldehydes or ketones as observed by ^1H NMR spectrometry. Similarly, aldehydes (benzaldehyde, acetaldehyde, and formaldehyde) are oxidized by **1** to the corresponding acids. Dimer **1** also participates in oxo-transfer chemistry in

converting triphenylphosphine to triphenylphosphine oxide (as observed by ^{1}H and ^{31}P NMR spectroscopy). Dimer **1** reacts with anilines (2,6-di-*tert*-butylaniline and aniline) and olefins (cyclohexene) though the organic products were not evident by ^{1}H NMR spectroscopy (Table 4.1).

Table 4.1. Reactivity of **1**: substrates and products.

Substrate	Product
CH_3OH	HCHO
CH_3CH_2OH	CH_3CHO
$(CH_3)_2CHOH$	$(CH_3)_2CO$
$C_6H_5CH_2OH$	C_6H_5CHO
HCHO	HCOOH
CH_3CHO	CH_3COOH
C_6H_5CHO	C_6H_5COOH
$(C_6H_5)_3P$	$(C_6H_5)_3PO$
$C_6H_5NH_2$	uncharacterized
2,6-(t-Bu)$_2C_6H_3NH_2$	uncharacterized
c-C_6H_{10}	uncharacterized

These reactions often generate more than one ruthenium containing product, but in the reactions with aniline and triphenylphosphine, one principle product was isolated as an analytically pure solid. The yellow product was characterized by X-ray crystallography to have the formula $[(L_{OMe})(CH_3CN)Ru^{III}(\mu\text{-}OH)_2Ru^{III}(NCCH_3)(L_{OMe})][CF_3SO_3]_2$ (**[5]**$(CF_3SO_3)_2$). Details of this structure are discussed later in this chapter. This dimer may be from the exchange of acetonitrile for the terminal ligand in a Ru^{III}-Ru^{III} intermediate during substrate oxidation. Figure 4.1 illustrates a hypothetical reaction for triphenylphosphine. The lability of terminal ligands in these Ru^{III}-Ru^{III} intermediates is evident in the conversion of $[(L_{OMe})(H_2O)Ru^{III}(\mu\text{-}OH)_2Ru^{III}(OH_2)(L_{OMe})][CF_3SO_3]_2$ (**[3]**$(CF_3SO_3)_2$) to $[(L_{OMe})(CH_3CN)$-$Ru^{III}(\mu\text{-}OH)_2Ru^{III}(NCCH_3)(L_{OMe})][CF_3SO_3]_2$ (**[5]**$(CF_3SO_3)_2$) in CH_3CN (Equation 2.6).

Figure 4.1. Possible mechanism for mechanism for triphenylphosphine oxidation by 1.

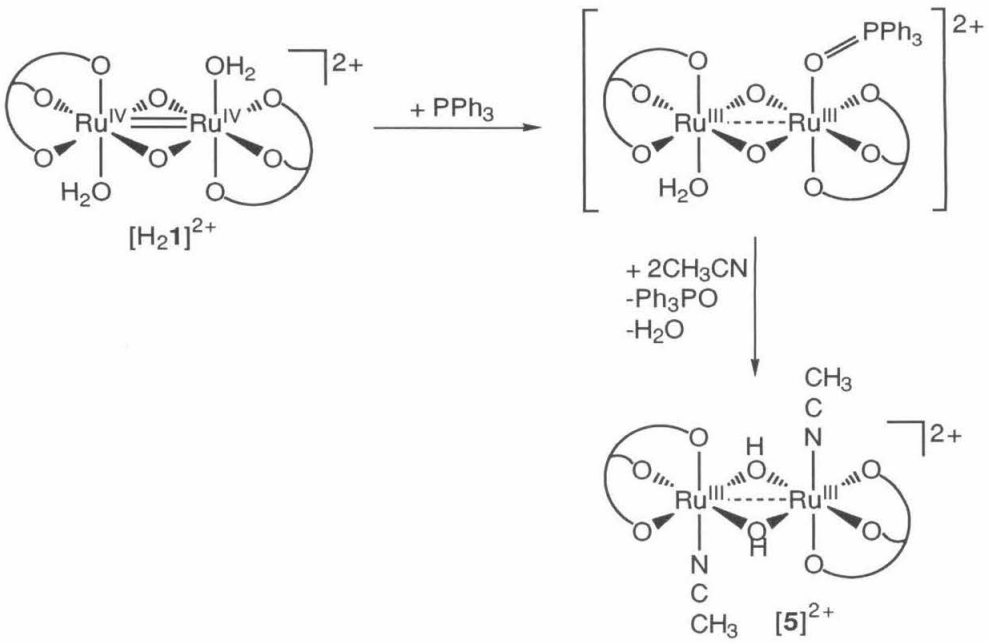

Strangely, reactions of substrates with **1** appear to accelerate as the reaction proceeds. This effect was qualitatively observed in all reactions as the solution changed from the green of $[H_2\mathbf{1}]^{2+}$ or **1** to the yellow of Ru^{III}-Ru^{III} products. The reaction of **1** with triphenylphosphine was monitored by ^1H NMR spectroscopy with particular attention to the C_5H_5 resonances. The reaction begins with the apparent conversion of **1** (5.30 ppm) to an intermediate (5.28 ppm). This intermediate then decays to two new intermediates (5.22 ppm) and (5.20 ppm) which subsequently decay to the products (5.20 ppm of $[\mathbf{5}]^{2+}$) and (5.17 ppm) respectively. The key step in this reaction appears to be formation of the first intermediate which begins slowly and rapidly accelerates. This rate acceleration suggests that the intermediate generated from the initial reaction could be a catalyst for its own formation. The formation of such an autocatalytic intermediate may be key to the reactivity of **1**. A possible mechanism for this effect will be discussed in detail in Chapter 5.

*4.2. General oxidation chemistry of $[H_2\mathbf{1}]^{2+}$ and **1** in aqueous media.*

In pH 7 phosphate buffer, an obvious color change occurs when **1** reacts with aldehydes (acetaldehyde, benzaldehyde, and formaldehyde) and more slowly with alcohols (methanol, ethanol, and benzyl alcohol) and formate. The reactions with aldehydes were particularly clean. The Ru^{III}-Ru^{III} product from formaldehyde was isolated and characterized as the C_s symmetric $[(L_{OMe})Ru^{III}(\mu\text{-}OH)_2(\mu\text{-}HCOO)Ru^{III}(L_{OMe})][CF_3SO_3]$ ($[\mathbf{6}](CF_3SO_3)$) by X-ray crystallography (Figure 4.2). The details of this structure are discussed later in this chapter. The bridging moiety is indeed a formate ligand; the product from $H^{13}CHO$ exhibits a doublet for the formate carbon in ^{13}C NMR spectroscopy. Evidently, the formate from formaldehyde oxidation remains bound to the product Ru^{III}-Ru^{III} dimer. The Ru^{III}-Ru^{III} products from the oxidation of other aldehydes are expected to be analogous.

Figure 4.2. Reaction of **1** with formaldehyde in pH 7 buffer.

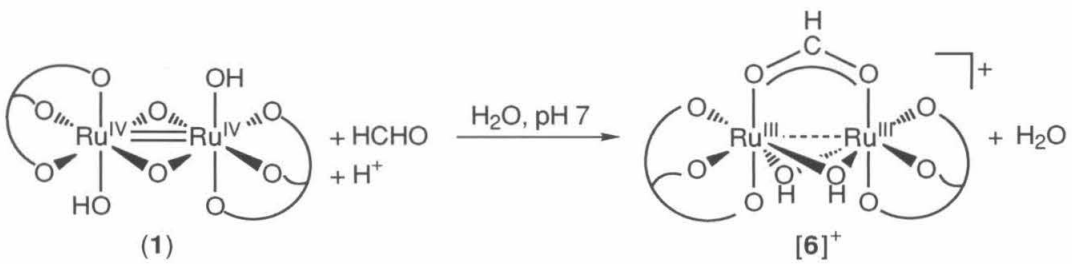

The coordinated formate suggests that either formaldehyde needs to coordinate to the dimer before its oxidation or that product formate rapidly coordinates to a Ru^{III}-Ru^{III} intermediate. The latter explanation is not likely since $[\mathbf{3}]^{2+}$, the product expected for electron transfer to **1**, fails to react with formate in pH 7 phosphate buffer. Compound $[\mathbf{3}]^{2+}$ actually rearranges to the triply bridged dimer $[(L_{OMe})Ru^{III}(\mu\text{-}OH)_2(\mu\text{-}OH_2)Ru^{III}(L_{OMe})]^{2+}$ ($[\mathbf{4}]^{2+}$) discussed in Chapter 2. The absence of $[\mathbf{4}]^{2+}$ in the reaction with formaldehyde suggests that $[\mathbf{3}]^{2+}$ is not involved in the reaction and the oxidation likely occurs by an inner-sphere mechanism.

In order for this reaction to be useful in a fuel cell, it must be possible to regenerate **1**. Unfortunately, the simple oxidation of $[\mathbf{6}]^+$ with silver trifluoromethanesulfonate afforded $[(L_{OMe})Ru^{IV}(\mu\text{-}O)_2(\mu\text{-}HCOO)Ru^{IV}(L_{OMe})]^+$ ($[\mathbf{7}]^+$) (Figure 4.3) as indicated by ^1H NMR spectroscopy. Indeed, the Ru^{IV}-Ru^{IV} product from oxidation of $[(L_{OMe})Ru^{III}(\mu\text{-}OH)_2(\mu\text{-}H^{13}COO)Ru^{III}(L_{OMe})][CF_3SO_3]$ ($(H^{13}COO)$-$[\mathbf{6}]^+$) exhibited a doublet for the formate carbon in ^{13}C NMR spectroscopy.

Figure 4.3. Oxidation of $[\mathbf{6}]^+$ with silver trifluoromethanesulfonate.

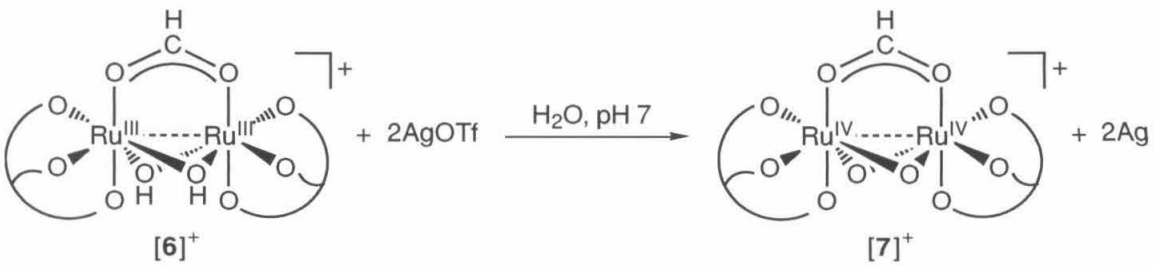

Figure 4.4. $H^{13}CHO$ oxidation by $[\mathbf{7}]^+$.

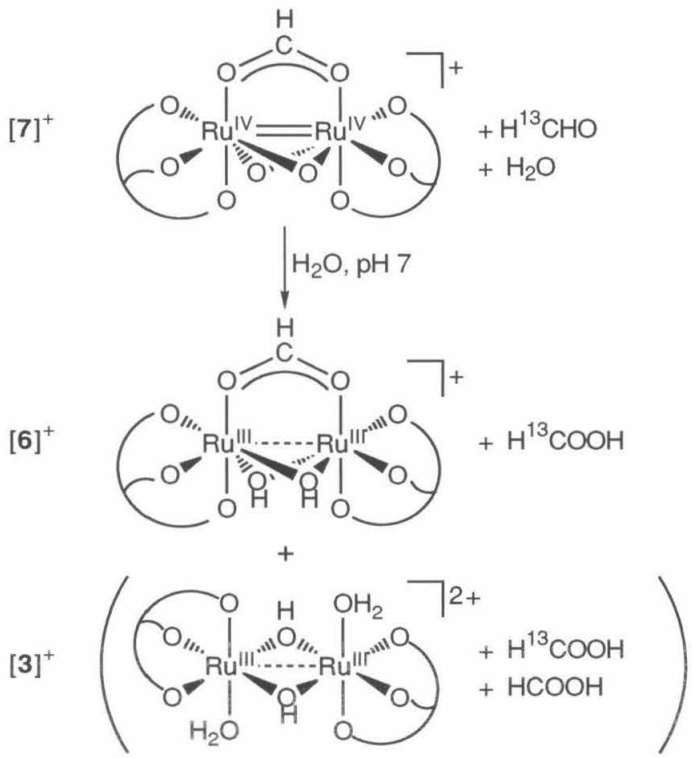

Compound $[7]^+$ also oxidizes formaldehyde, albeit more slowly than **1** does. The reaction of $[7]^+$ with HCHO in pH 7 buffered D_2O afforded $[6]^+$ and a small amount of $[4]^{2+}$ based on ^1H NMR spectroscopy (Figure 4.4). The label from substrate $H^{13}CHO$ used in this reaction appears entirely as free $H^{13}COO^-$ (by comparison to an authentic sample). Similarly, the label from the oxidation of HCHO by $(H^{13}COO)$-$[7]^+$ appeared predominantly in $(H^{13}COO)$-$[6]^+$ with a trace of free $H^{13}COO^-$. The bound formate remains so during the oxidation of formaldehyde by $[7]^+$ to form $[6]^+$. The label retention of $[7]^+$ also indicates that a symmetric dimer with two bound formates does not form as an intermediate. Since $[6]^+$ appears indefinitely stable in pH 7 buffered D_2O, $[4]^{2+}$ likely forms from $[3]^{2+}$ generated during oxidation of HCHO by $[7]^+$. This also explains the observed trace of free $H^{13}COO^-$ from $(H^{13}COO)$-$[7]^+$.

4.3. *Electrocatalytic oxidation of formaldehyde in buffered water.*

Since Ru^{III}-Ru^{III} products from the oxidation of substrates can be reoxidized to Ru^{IV}-Ru^{IV} dimers, these dimers may act as catalysts for the bulk electrooxidation of substrates. Indeed, **1** assists the electrooxidation of methanol and formaldehyde at low potentials (Table 4.2). Total catalyst turnovers were calculated from the total charges assuming two electrons were collected from each Ru^{IV}-Ru^{IV}/Ru^{III}-Ru^{III} cycle. The relatively small number of turnovers observed with methanol are likely due to a side reaction in its reaction with **1**. Bulk reactions of methanol with **1** indeed suggest a prominent side reaction to form a dark product. In contrast, the practically quantitative reaction of formaldehyde with **1** allows a larger number of turnovers.

The reactivity of formaldehyde with the dimer system as described above suggests that the bulk electrooxidation of formaldehyde is occurring by a mechanism like that illustrated in Figure 4.5. Overall, the electrooxidation of formaldehyde is likely occurring by two catalytic cycles: one of which relies on the Ru^{IV}-Ru^{IV}/Ru^{III}-Ru^{III} couple of $[6]^+$ and $[7]^+$ while the other relies on the same couple of $[3]^{2+}$ and **1**.

Table 4.2. Turnovers for bulk formaldehyde electrooxidation with **1** catalyst.

Substrate	Catalyst	pH	E (V)[g]	T (°C)	Buffer I (M)[h]	Turnovers[i]
CH_3OH[a]	**1**[d]	2.5	+0.50	60	2.55	3.0
CH_3OH[a]	**1**[d]	5.5	+0.25	71	2.55	2.6
HCHO[b]	**1**[d]	6.9	+0.30	86	0.10	12
HCHO[b]	**1**[d]	8.5	-0.04	23	0.10	10
HCHO[b]	**1**,(Pd/C)[f]	6.9	+0.10	86	0.10	12
HCHO[b]	**1**[d]	6.9	+0.10	86	0.50	36
HCHO[b]	(Pd/C)[e]	6.9	+0.10	86	0.50	42
HCHO[b]	**1**,(Pd/C)[f]	6.9	+0.10	86	0.50	108

[a] CH_3OH (50% v/v). [b] HCHO (108 mM). [c] HCHO (130 mM).[d] Dimer **1** (1.0 mM). [e] 5% Pd/C ("1 mM" w.r.t. Pd). [f] Dimer **1** (1.0 mM) and 5% Pd/C ("1 mM" w.r.t. Pd). [g] In V versus SCE. [h] Buffer ionic strength in M. [i] Effective turnovers of catalyst assuming two electrons collected for each turnover of **1**.

Figure 4.5. Two part catalytic cycle for bulk formaldehyde electrooxidation with **1** catalyst.

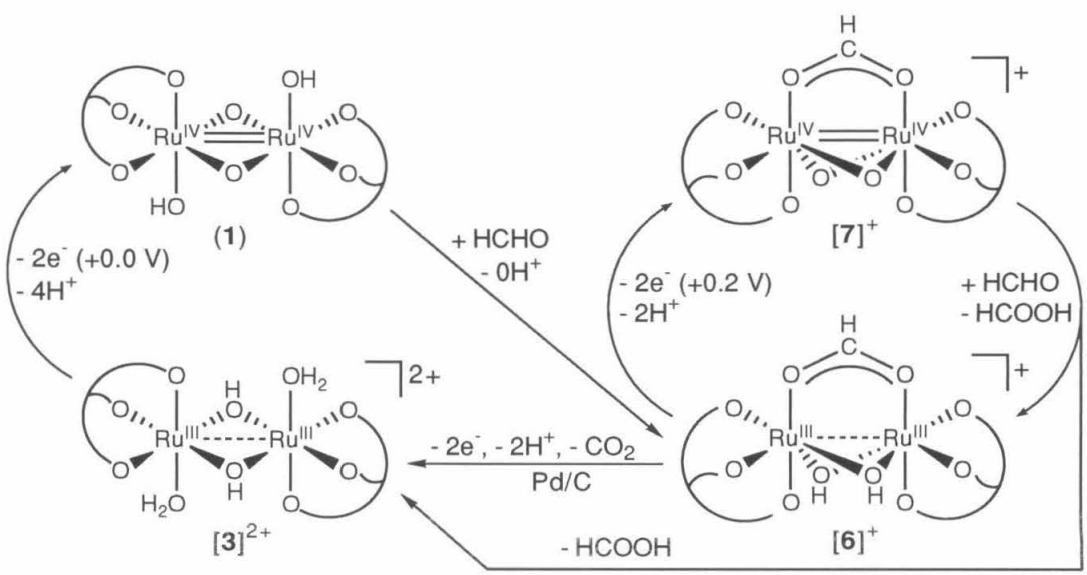

In this catalytic reaction, **1** first reacts with formaldehyde to generate $[\mathbf{6}]^{+}$. Dimer $[\mathbf{6}]^{+}$ can be directly oxidized to $[\mathbf{7}]^{+}$ which subsequently reacts with formaldehyde to regenerate $[\mathbf{6}]^{+}$ and a small amount of $[\mathbf{3}]^{2+}$. The latter dimer is oxidized to **1** which rejoins the catalytic reaction. (The dimer $[\mathbf{3}]^{2+}$ is in equilibrium with $[\mathbf{4}]^{2+}$ which is also oxidized to **1** at 0.00 V at pH 7 as discussed in Chapter 2. This equilibrium likely has little effect on the observations below and is implied throughout the remainder of this discussion though $[\mathbf{4}]^{2+}$ is not explicitly mentioned.) The indefinite oxidation of formaldehyde seems, in principle, possible as long as an oxidation source sufficiently strong to reoxidize $[\mathbf{3}]^{2+}$ and $[\mathbf{6}]^{+}$ is supplied to this system. This oxidation source is conveniently supplied electrochemically. As shown in Figure 4.5, $[\mathbf{3}]^{2+}$ is oxidized to **1** by a potential of 0.00 V versus SCE while $[\mathbf{6}]^{2+}$ is oxidized to $[\mathbf{7}]^{+}$ by a potential of +0.20 V. An applied potential of +0.10 V would drive only the left cycle of the catalytic process while an applied potential of +0.30 V versus SCE would be sufficient to drive both cycles of the catalytic manifold.

As expected, several turnovers are observed with an applied potential of +0.30 V. When formaldehyde is added to the dimer electrolyte solution, the solution quickly changes from green to yellow and the oxidation current rapidly increases to a maximum. This initial color change is clearly the formation of $[\mathbf{6}]^{+}$ which forms faster than the heterogeneous electrooxidation to $[\mathbf{7}]^{+}$. As the experiment proceeds, the electrolyte solution returns to the green color characteristic of the Ru^{IV}-Ru^{IV} oxidation state of $[\mathbf{7}]^{+}$, and the current decreases with the concentration of $[\mathbf{6}]^{+}$. Evidently the heterogeneous electrooxidation of $[\mathbf{6}]^{+}$ proceeds faster than the reaction of formaldehyde with $[\mathbf{7}]^{+}$. After several catalytic cycles, the electrolyte solution becomes red and the oxidation current decays to near zero. This is likely the result of the dimer system degrading to inactive and unidentified ruthenium products. The reaction of formaldehyde with $[\mathbf{7}]^{+}$ does generate dark side products which could be slowly depleting the system of active catalyst.

The solutions from the early experiments in 0.1 M ionic strength buffers were found to be acidic (pH<4) at the end of the experiments indicating buffer failure. The oxidation of formaldehyde to formate releases three equivalents of acid (Figure 4.6) which eventually overwhelms the buffer capacity. The drop in solution pH likely encourages the formation of inactive side products that eventually deplete the system of catalyst. Higher buffer strengths indeed result in larger turnover numbers (Table 4.2).

Figure 4.6. Half-cell reaction for formaldehyde oxidation to formate.

$$HCHO + H_2O \longrightarrow HCOO^- + 3H^+ + 2e^-$$

Surprisingly, experiments at +0.10 V also successfully oxidized formaldehyde though the oxidation of $[\mathbf{6}]^+$ to $[\mathbf{7}]^+$ required an applied potential of at least +0.20 V. Cyclic voltammetry of the electrolyte solution during the course of the experiment exhibited a +0.2 V redox wave expected for the Ru^{IV}-Ru^{IV}/Ru^{III}-Ru^{III} couple of $[\mathbf{6}]^+$ and $[\mathbf{7}]^+$ and a smaller wave near +0.0 V which is the potential for the same couple of **1** and $[\mathbf{3}]^{2+}$. Though the reaction of **1** with formaldehyde quantitatively forms $[\mathbf{6}]^+$ by ^{1}H NMR spectroscopy, $[\mathbf{3}]^{2+}$ seems to appear in the electrochemical experiment.

Cyclic voltammetry of analytically pure $[\mathbf{6}](CF_3SO_3)$ exhibits a quasi-reversible redox wave at +0.18 V for the Ru^{IV}-Ru^{IV}/Ru^{III}-Ru^{III} couple and a reduction wave at about 0.0 V not observed in returning oxidation scans (Figure 4.7). Though the peak current versus scan rate dependence for this 0.0 V reduction was consistent with the reduction of a solution species, the peak current for this redox wave was strongly dependent on the electrode: glassy carbon exhibited the largest current while platinum exhibited the smallest relative to the principal +0.18 V redox couple.

Figure 4.7. Cyclic voltammogram of $[6]^+$ in pH 7 buffer.

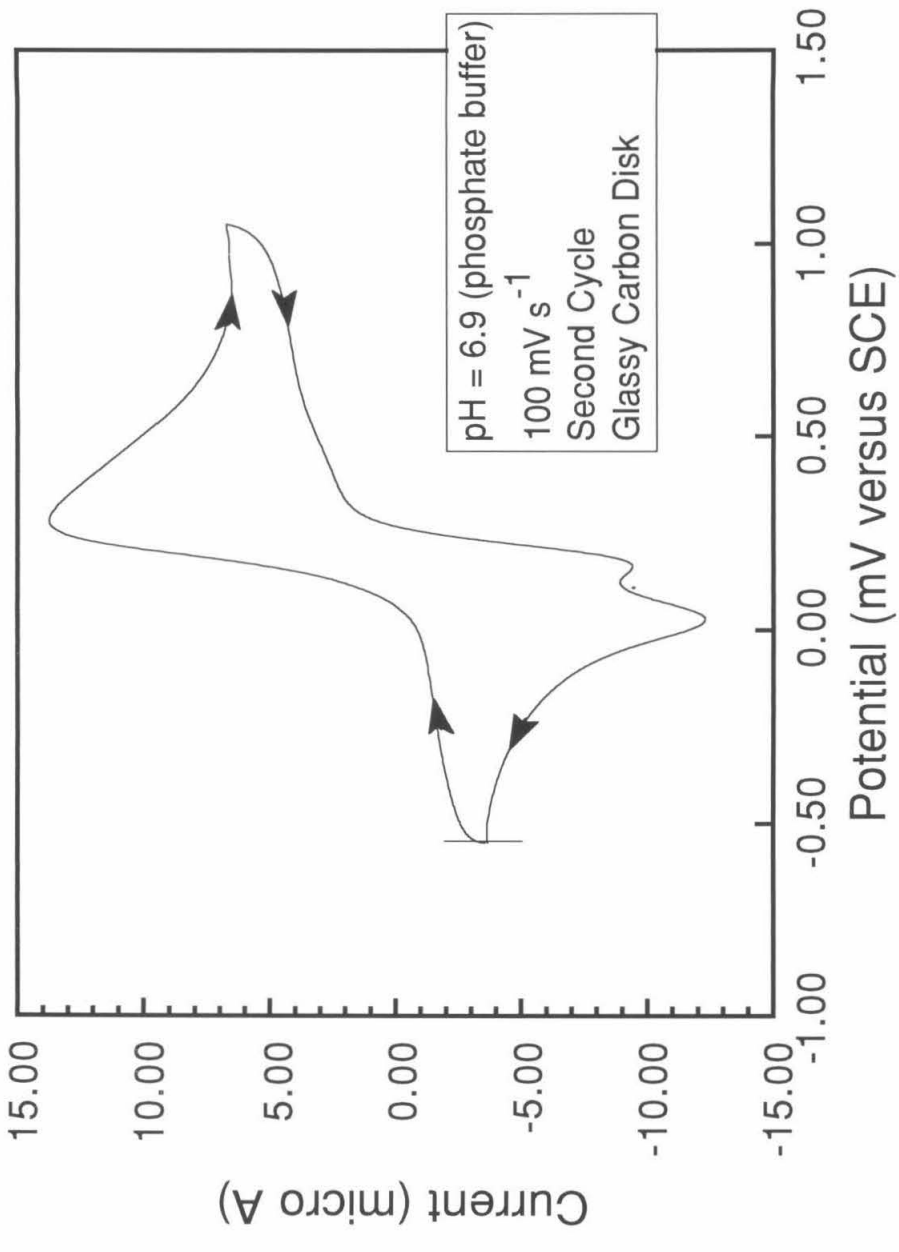

The electrode surfaces may be assisting the dissociation of formate from $[6]^+$ at potentials positive of 0.0 V. This could afford $[3]^{2+}$ and subsequently $[4]^{2+}$ which are then oxidized to **1**. Though this process is localized at the electrode, the formate free dimers could deeply saturate the diffusion layer around the electrode resulting in the observed peak current versus scan rate behavior. Below 0.0 V, this conversion likely halts and allows the formate free dimers to diffuse from the electrode. The interaction of $[6]^+$ with electrode surfaces is further indicated by a broad absorption oxidation wave at +0.42 V observed only with platinum and gold electrodes. The conversion of $[6]^+$ to $[3]^{2+}$ or $[4]^{2+}$ in the presence of large electrode surfaces would allow the catalytic manifold to function even with a driving potential of +0.10 V. The activity at this lower driving potential not only provides a system more attractive for application in fuel cells, but also allows the oxidation of formaldehyde by $[7]^+$ and its suspected side reaction to be avoided.

Though experiments conducted at +0.10 V and high buffer strengths exhibited significant improvement over those at higher potentials and lower buffer strengths, catalyst activity was still limited. This was suspected to be due to the accumulation of free formate that could inhibit the conversion of $[6]^+$ to $[3]^+$. A means of consuming formate was needed. The electrons from formate oxidation would also improve the apparent performance of the catalyst.

In answer to this problem, several bulk electrooxidation experiments were repeated with a stirred suspension of palladium/carbon. In addition to alleviating the accumulation of free formate, palladium/carbon also likely accelerates the conversion of $[6]^+$ to $[3]^+$ and increases the effective surface area of the working electrode. First, palladium/carbon is a known electrocatalyst for the decomposition[1] and electrooxidation[2] of formate. In fact, palladium/carbon and added formate is used as hydrogen sources in organic synthesis and biological research. Second, the palladium was intended to assist the conversion of $[6]^+$ to $[3]^{2+}$. Though the conversion of $[6]^+$ to $[3]^{2+}$ at palladium is somewhat speculative, providing a large metal surface area would accelerate activity at the lower potentials (+0.10 V). As mentioned,

use of the lower driving potential would also extend the lifetime of the catalyst by shifting the catalytic activity away from the formate adduct cycle. Third, the suspended palladium would increase the effective surface area of the electrode, a familiar technique in electrochemistry. This would accelerate the experiment and may allow heterogeneous oxidation of $[3]^{2+}$ to better keep pace with the homogeneous oxidation of formaldehyde. Lower steady state concentrations of Ru^{III}-Ru^{III} species would also reduce possible side reactions from these relatively labile species. As Table 4.2 shows, the use of palladium indeed results in larger initial currents, but its stabilizing effect is not clearly demonstrated at low buffer strength.

The last entry shows that, by providing sufficient buffer and adding Pd/C co-catalyst, electrocatalysis can be continued for over 100 turnovers. The dimer/palladium catalyst system outperforms the sum of the two individual systems, suggesting the activity is indeed cooperative. In principle, such a system could remain active for longer duration times in an actual fuel cell where protons liberated by oxidation are consumed by oxygen reduction. Crude experiments in which base was periodically added to compensate for acid generation also resulted in increased turnover numbers. Unfortunately these experiments still slowly decayed, perhaps by unavoidable side reactions, in this dimer system. In spite of this, these experiments illustrated that such bulk electrooxidation is possible at low potentials and this dimer system is worthy of preliminary testing under fuel cell conditions.

4.4. Binding of ***1*** *to heterogeneous supports and performance testing of dimer/palladium fuel cell electrodes.*

This dimer/palladium system had sufficient promise to warrant preliminary tests in actual fuel cell systems. Current fuel cell technology is engineered for heterogeneous catalysts, which requires that the dimer co-catalyst be bound to the heterogeneous catalyst.[3] One well known method for binding metal complexes to heterogeneous supports is electrostatic binding in Nafion.[4] Nafion is a perfluoronated sulfonate cation exchange resin commonly used in fuel cells

to encourage wetting of electrode surfaces.[5] Indeed, **1** is absorbed from solutions of either its neutral or protonated forms into Nafion films on electrodes. In blank electrolyte solutions, cyclic voltammetry of treated electrodes exhibit the characteristic Ru^{IV}-Ru^{IV}/Ru^{III}-Ru^{III} redox couple as in bulk solution (Figure 4.8). No dimer was measurably lost from these films when immersed in buffers at temperatures up to 90 °C.

With this demonstrated, several attempts were made to prepare fuel-cell electrodes. In the first attempt, the dimer was allowed to absorb from solution into a Nafion film painted on a Pd/C pad on carbon cloth.[6] Though the electrochemistry of the dimer was observable, very little was actually absorbed. This resulted in an insignificant improvement in voltage-current characteristics for the electrooxidation of formaldehyde (Figure 4.9).

The problem with this first attempt was that the dimer likely only penetrated the outer layer of the Nafion film. In order to increase the Nafion surface area exposed to the dimer solution, the Pd/C powder was wetted with diluted Nafion solution and air dried to leave a thin film on the individual co-catalyst particles. These powders absorbed a very large amount of dimer when stirred in dimer solutions. The quantity of ruthenium absorbed was actually larger than expected for the amount of Nafion used suggesting that most of the dimer was absorbed into the Pd/C particles themselves rather than the resin. The Nafion likely enhanced particle-solvent contact making this possible. Pads of this catalyst bound to carbon paper did exhibit electrocatalytic activity at 60°C and were modestly improved over that of palladium catalyst similarly prepared without dimer treatment (Figure 4.10). In the bulk electrooxidation of formaldehyde described above, combined dimer and palladium catalysts performed far better at 80°C than 60°C. A comparable improvement is expected at higher temperatures. (Unfortunately the Jet Propulsion Laboratories did not have their equipment configured for temperatures above 60 °C at the time.)

The actual mechanism for this improvement may be more complex than that illustrated in Figure 4.5 with the additional $[\mathbf{6}]^{+}$ to $[\mathbf{3}]^{2+}$ conversion and $[\mathbf{3}]^{2+}$ and $[\mathbf{4}]^{2+}$ interconversion. The

Figure 4.8. Cyclic voltammogram of 1 bound in Nafion electrode coating.

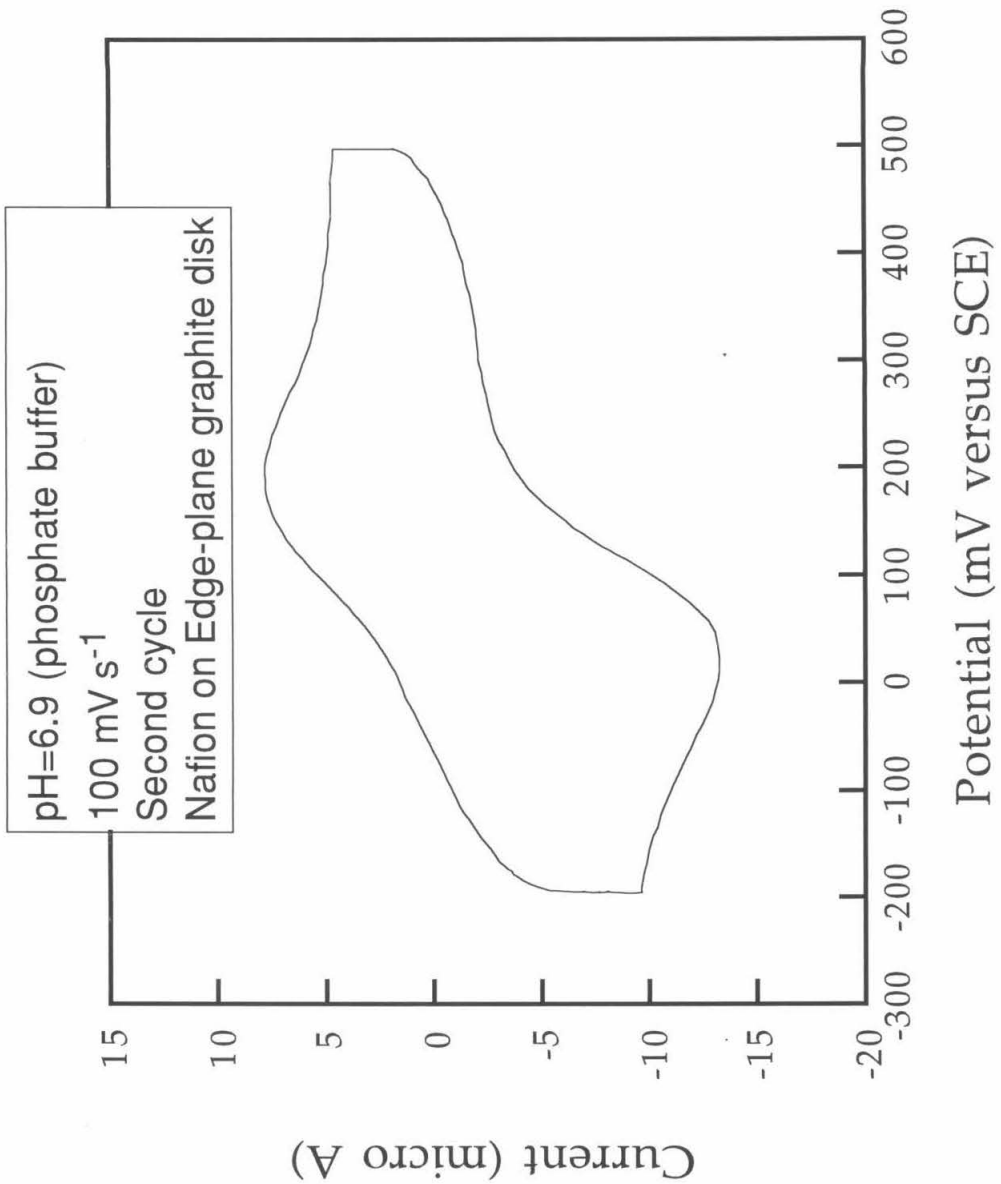

Figure 4.9. Voltage versus current characteristics of electrodes prepared from Pd/C catalysts with and without dimer treatment.

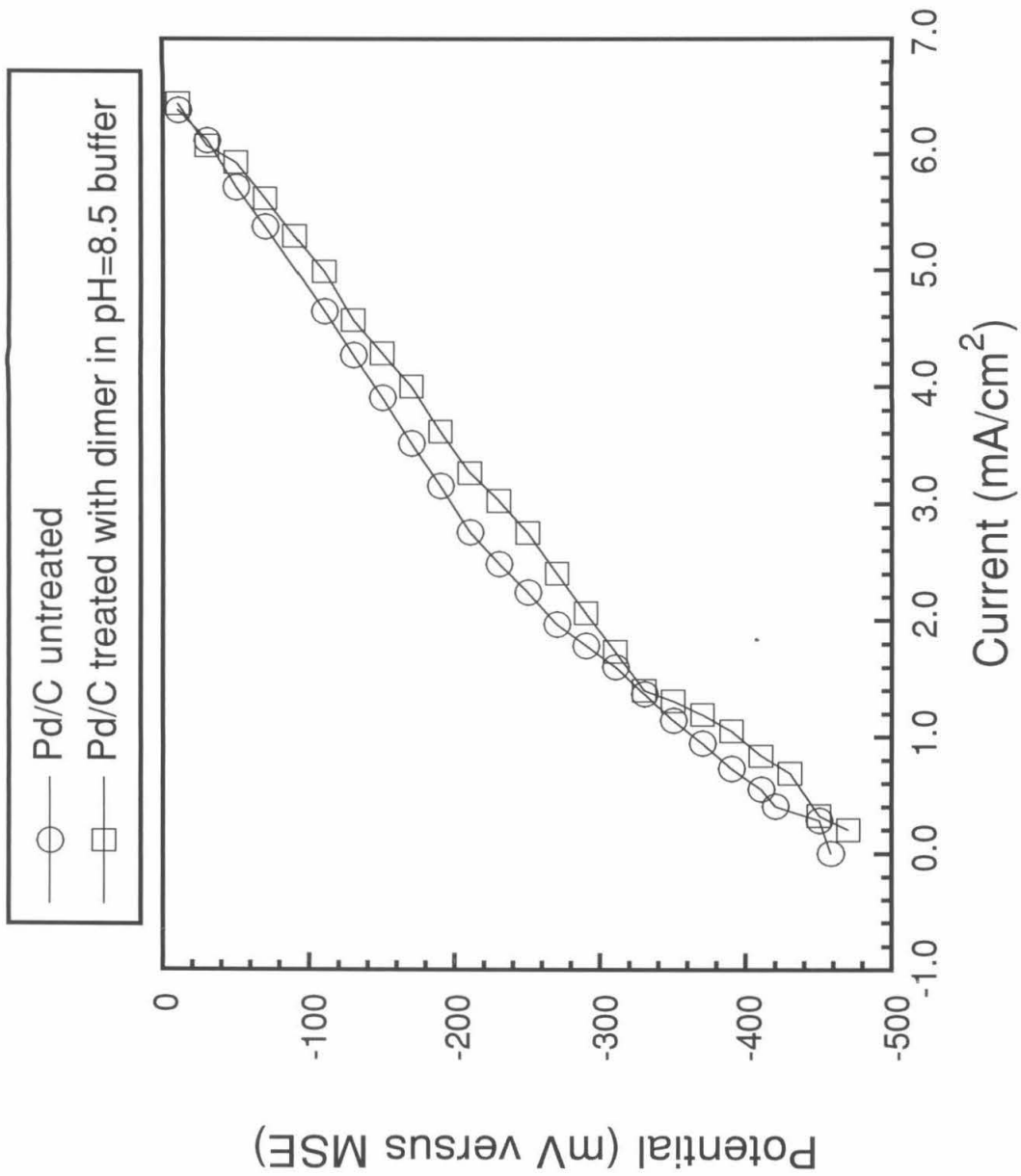

Figure 4.10. Voltage versus current characteristics of electrodes prepared from Pd/C/Nafion with and without dimer treatment.

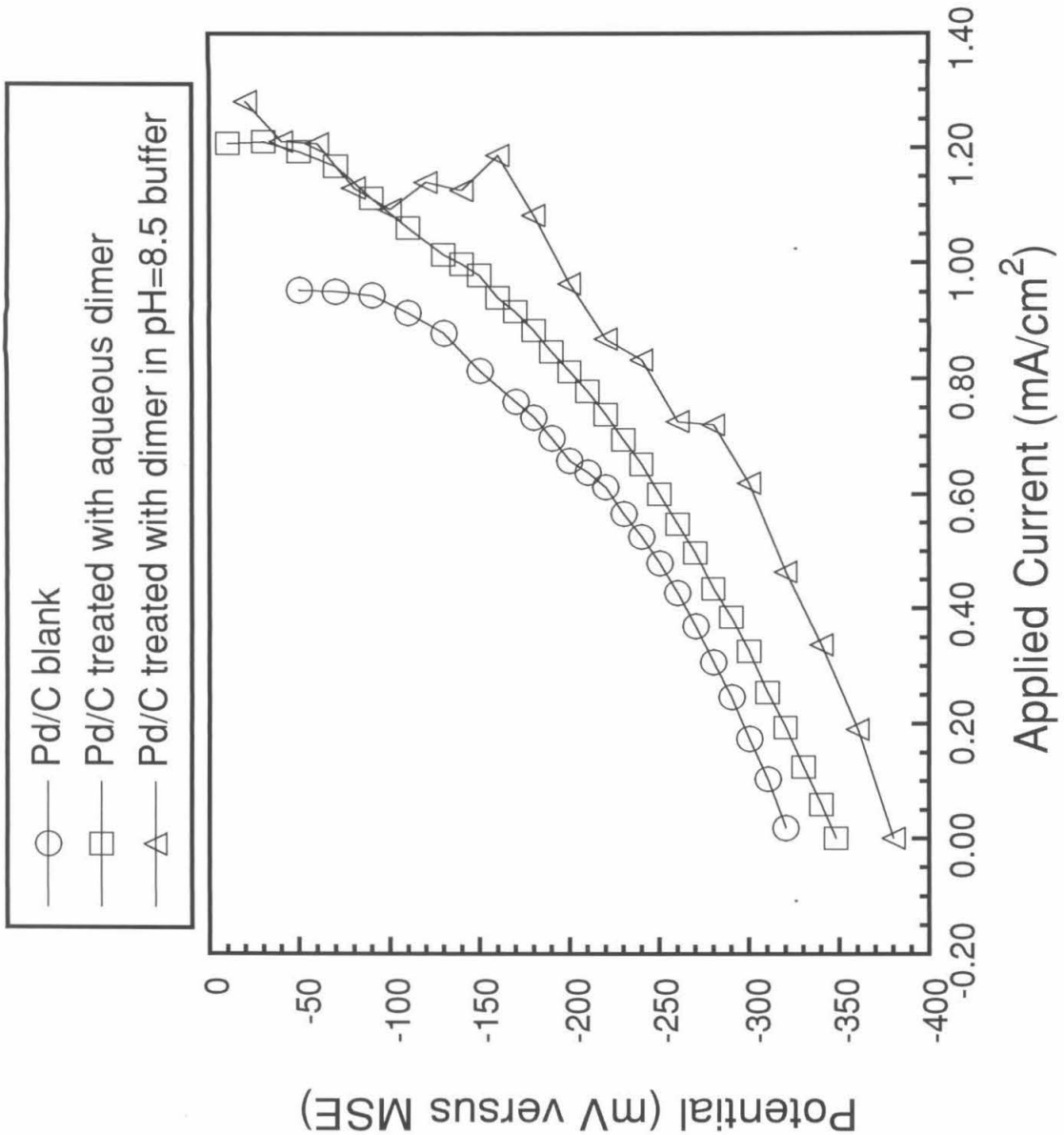

dimer also could also be acting as a hydrogen transfer agent to and from palladium particles thus facilitating the heterogeneous electrooxidation of formaldehyde and formate. Examination of this behavior would be complex and beyond the scope of the research described here.

4.5. Structures of Ru^{III}-Ru^{III} Dimers.

The structure of the Ru^{III}-Ru^{III} dimer $[(L_{OMe})(CH_3CN)Ru^{III}(\mu\text{-}OH)_2Ru^{III}(NCCH_3)(L_{OMe})][CF_3SO_3]_2$ **[3]**$[CF_3SO_3]_2$, is shown in ORTEP representation in Figure 4.11, and selected bond lengths and angles are listed in Table 4.4. (Appendix 1 contains comprehensive tables of bond lengths and angles.) The two halves of the edge sharing bioctahedral dimer are related by an inversion center between the two ruthenium atoms. Each ruthenium center has a pseudooctahedral environment with a facially bound $(L_{OMe})^-$ ligand. In contrast to the previously reported oxo-bridged structures,[7] the ruthenium atoms here are bridged by two hydroxy groups as evidenced by the longer Ru-(μ-O) distances and the easily located hydroxy hydrogen atoms (difference Fourier map). This bridging gives a planar $Ru_2(O)_2$ metallocycle. A terminally bound CH_3CN nitrogen occupies the remaining coordination site at each ruthenium. The Ru-Ru distance [2.622 (1) Å] (Table 4.4) is longer than that observed in the reported structures of the $(L_{OEt})^-$ analogs of **1** and $[H_21]^{2+}$, $[(L_{OEt})(H_2O)Ru^{IV}(\mu\text{-}O)_2Ru^{IV}(OH_2)(L_{OEt})](CF_3SO_3)_2$ $([H_2\mathbf{1}_{Et}](CF_3SO_3)_2)$ [2.505 (1) Å] and $[(L_{OEt})(HO)Ru^{IV}(\mu\text{-}O)_2Ru^{IV}(OH)(L_{OEt})]$ $(\mathbf{1}_{Et})$ [2.452 (1) Å].[8] This is consistent with the qualitative molecular orbital representation of the metal-metal interaction in edge sharing dimers depicted in Figure 4.12 which predicts a $\sigma^2\pi^2\delta^{*2}\delta^2\sigma^{*2}$ configuration for the Ru^{III}-Ru^{III} dimers and a $\sigma^2\pi^2\delta^{*2}\delta^2$ configuration for the Ru^{IV}-Ru^{IV} dimers.[8] The Ru^{III}-Ru^{III} bond distance is consistent with a net Ru-Ru single bond. It is considerably shorter than that in the Ru^{V}-Ru^{V} dimer $[(L_{OEt})(O)Ru^{V}(\mu\text{-}O)_2Ru^{V}(O)(L_{OEt})]$ $(\mathbf{2}_{Et})$ [2.912 (1) Å] which is considered to have no metal-metal bond at all.[8] Since $[\mathbf{3}]^{2+}$ (like all the dimeric complexes obtained in this work) is diamagnetic, the odd spins on the two d^5 centers are

Table 4.3 General Crystallographic Data for $[(L_{OMe})(CH_3CN)Ru^{III}(\mu\text{-}OH)_2Ru^{III}(NCCH_3)(L_{OMe})][CF_3SO_3]_2$ (**[3]**$[CF_3SO_3]_2$) and $[(L_{OMe})Ru^{III}(\mu\text{-}OH)_2Ru^{III}(L_{OMe})][CF_3SO_3]\cdot 2H_2O$ (**[5]**$[CF_3SO_3]\cdot 2H_2O$).

	(**[3]**$[CF_3SO_3]_2$)	(**[5]**$[CF_3SO_3]\cdot 2H_2O$)
formula weight	759.34 g mol^{-1} [a]	1368.57 g mol^{-1}
crystal system	triclinic	monoclinic
space group	P$\underline{1}$ (#2)	P2_1/n (#14)
a	8.626(3) Å	14.356(2) Å
b	12.275(2) Å	23.839(6) Å
c	13.457(3) Å	15.284(3) Å
α	71.32(2)°	90.00°
β	85.35(2)°	115.44(1)°
γ	80.01(3)°	90.00°
V	1328.9(6) Å^3	4723.5(18) Å^3
Z	2	4
T	298° K	225° K
D_{calcd}	1.90 g cm^{-3}	1.92 g cm^{-3}
μ_{calcd}	15.46 cm^{-1}	16.42 cm^{-1}
λ(MoKα) = 0.71073 Å with graphite monochromator		
R(F_o) [reflections with $F_o^2 > 0$]	0.040 [4451]	0.033 [7044]
R(F_o) [reflections with $F_o^2 > 3\sigma(F_o^2)$]	0.031 [3731]	0.027 [6256]
$R_w(F_o^2)$ [all reflections]	0.004 [4669]	0.004 [7402]
$R_w(F_o^2)$ [reflections with $F_o^2 > 3\sigma(F_o^2)$]	0.004 [3731]	0.003 [6256]
Goodness of Fit (S)	1.57 [4669 data, 416 parameters]	1.72 [7402 data, 790 parameters]

[a] Molecular weight of one asymmetric unit. Dimer consists of two asymmetric units.

Figure 4.11. ORTEP of $[(L_{OMe})(CH_3CN)Ru^{III}(\mu\text{-}OH)_2Ru^{III}(NCCH_3)(L_{OMe})]^{2+}$ $([5]^{2+})$.

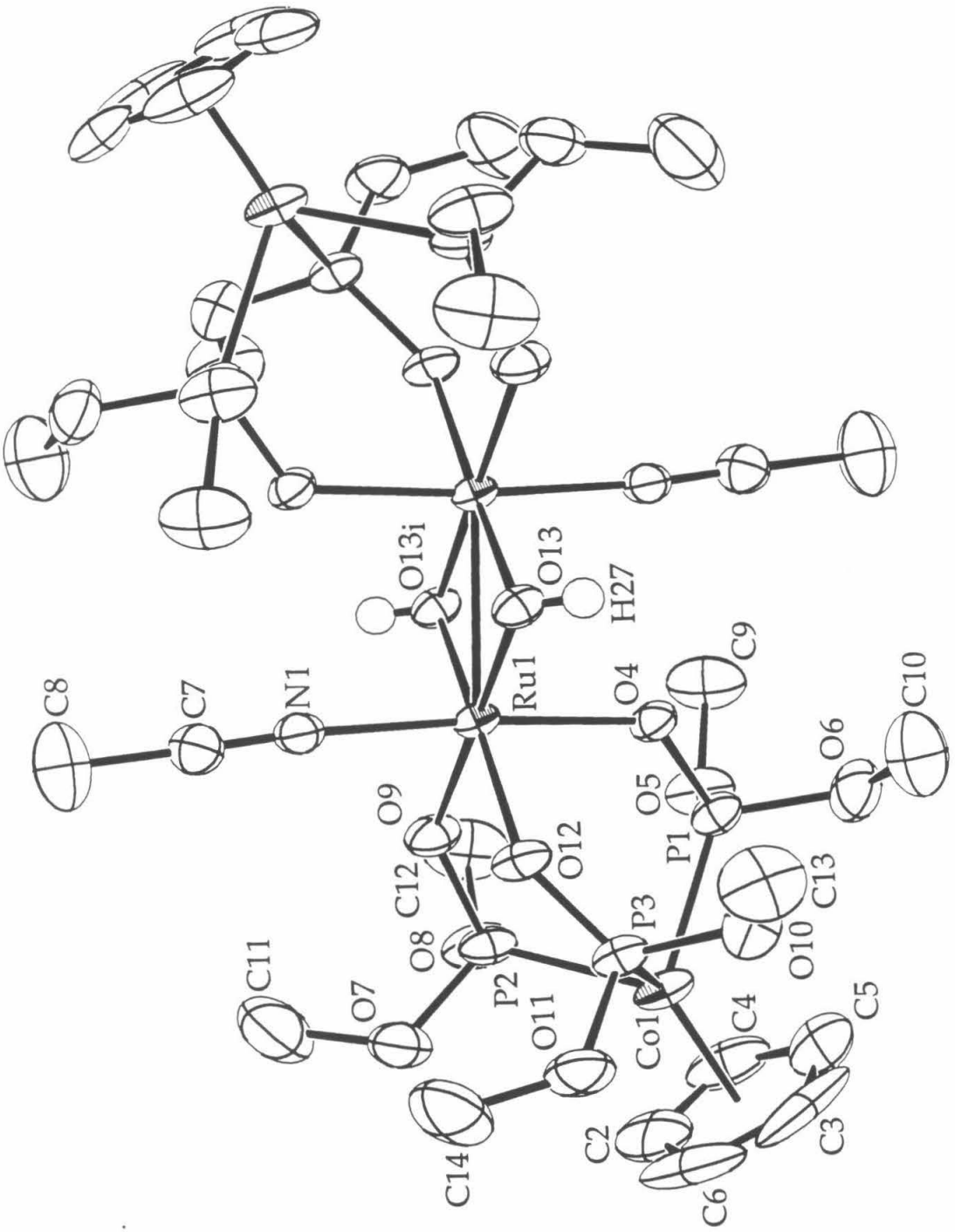

Table 4.4. Selected bond lengths and angles of $[(L_{OMe})(CH_3CN)Ru^{III}(\mu\text{-}OH)_2Ru^{III}(NCCH_3)(L_{OMe})][CF_3SO_3]_2$ ($[\mathbf{5}](CF_3SO_3)_2$).

Ru-Ru$_i$	2.622	(1)
Ru-O4	2.054	(2)
Ru-O9	2.021	(3)
Ru-O12	2.044	(2)
Ru-O13	2.013	(3)
Ru-O13$_i$	2.009	(3)
Ru-N1	2.010	(3)
O4-Ru-O13	90.1	(1)
O4-Ru-O13$_i$	90.6	(1)
O4-Ru-N1	175.4	(1)
O4-Ru-O9	91.4	(1)
O4-Ru-O12	87.5	(1)
O9-Ru-O13	84.8	(1)
O9-Ru-O13$_i$	176.2	(1)
O9-Ru-N1	85.9	(1)
O9-Ru-O12	87.1	(1)
O12-Ru-O13	171.4	(1)
O12-Ru-O13$_i$	89.8	(1)
O12-Ru-N1	88.7	(1)
O13-Ru-O13$_i$	98.4	(1)
O13-Ru-N1	91.9	(1)

paired, perhaps by superexchange through the bridging hydroxy groups or by through-space interaction.

The structure of the formate complex $[\mathbf{6}]^+$ is shown in Figure 4.13, and selected bond lengths and angles are listed in Table 4.5. (Appendix 2 contains comprehensive tables of bonds and angles.) This structure is different in that the dimer is not edge sharing but face sharing, with the two ruthenium centers bridged by two hydroxy groups and a formate group. Overall,

Figure 4.12. Molecular orbital representation for edge sharing dimers.

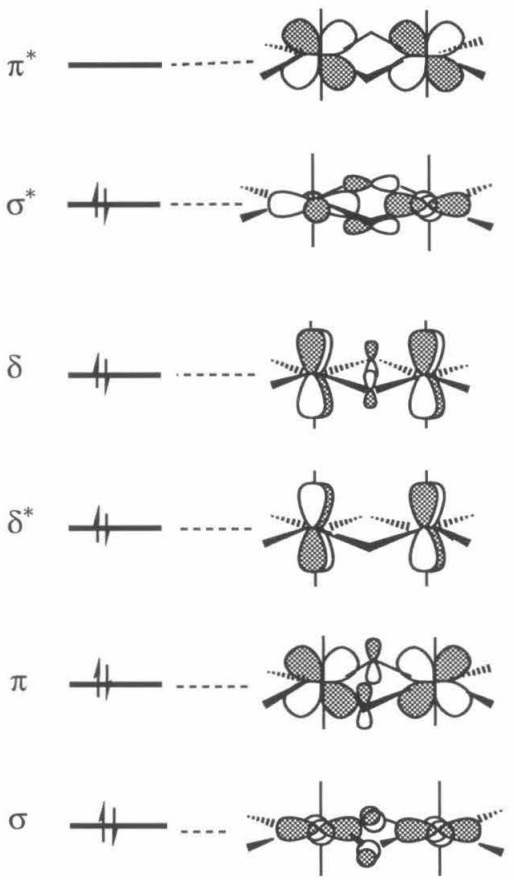

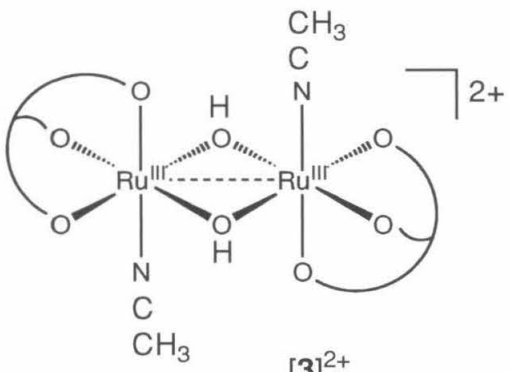

$[\mathbf{3}]^{2+}$

$\mathbf{d^5 - d^5}$

Figure 4.13. ORTEP of $[(L_{OMe})Ru^{III}(\mu\text{-}OH)_2(\mu\text{-}HCOO)Ru^{III}(L_{OMe})]^+$ ($[6]^+$).

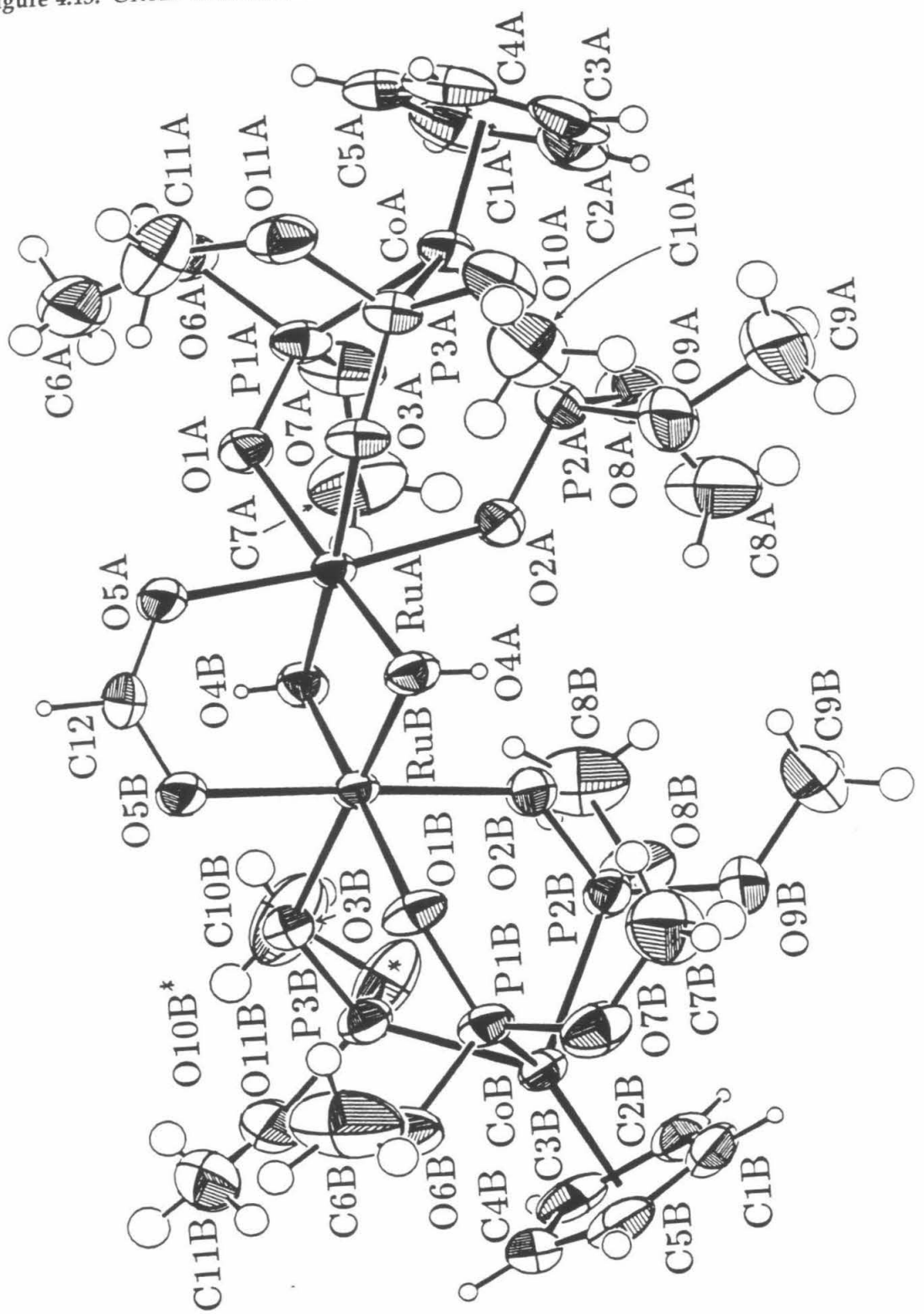

Table 4.5. Selected bond lengths and angles of $[(L_{OMe})Ru^{III}(\mu\text{-}OH)_2(\mu\text{-}HCOO)Ru^{III}(L_{OMe})]^+$ ($[6]^+$).

RuA-RuB	2.548	(1)
RuA-O1A	2.032	(2)
RuB-O1B	2.042	(2)
RuA-O2A	2.079	(2)
RuB-O2B	2.073	(2)
RuA-O3A	2.052	(2)
RuB-O3B	2.051	(2)
RuA-O4A	1.988	(3)
RuA-O4B	1.995	(3)
RuB-O4B	1.989	(3)
RuB-O4A	1.985	(3)
RuA-O5A	2.056	(2)
RuB-O5B	2.058	(2)
O5A-C12	1.247	(5)
O5B-C12	1.263	(5)

O1A-RuA-O2A	88.5	(1)
O1B-RuB-O2B	89.0	(1)
O1A-RuA-O3A	86.8	(1)
O1B-RuB-O3B	85.3	(1)
O1A-RuA-O4A	172.3	(1)
O1B-RuB-O4B	173.1	(1)
O1A-RuA-O4B	87.5	(1)
O1B-RuB-O4A	86.5	(1)
O1A-RuA-O5A	87.0	(1)
O1B-RuB-O5B	89.2	(1)
O2A-RuA-O3A	88.8	(1)
O2B-RuB-O3B	95.4	(1)
O2A-RuA-O4A	94.5	(1)
O2B-RuB-O4B	88.1	(1)
O2A-RuA-O4B	90.2	(1)
O2B-RuB-O4A	90.5	(1)

Table 4.5. (Continued)

O2A-RuA-O5A	174.6	(1)
O2B-RuB-O5B	177.8	(1)
O3A-RuA-O4A	86.1	(1)
O3B-RuB-O4B	88.7	(1)
O3A-RuA-O4B	174.3	(1)
O3B-RuB-O4A	99.8	(1)
O3A-RuA-O5A	87.9	(1)
O3B-RuB-O5B	83.1	(1)
O4A-RuA-O4B	99.6	(1)
O4B-RuB-O5A	92.7	(1)
O4A-RuA-O5A	89.6	(1)
O4B-RuB-O5B	93.6	(1)
O4B-RuA-O5A	92.7	(1)
O4A-RuB-O5B	90.6	(1)
O5A-C12-O5B	127.4	(4)
RuA-O5A-C12	121.4	(2)
RuB-O5B-C12	119.3	(2)

the dimer has a pseudo-C_2 axis passing through the formate ligand perpendicular to the Ru-Ru segment. Most structural parameters for the two halves correspond to each other within experimental error. However, the Ru-O-C angles with the formate [121.4 (2)°, 119.3 (2)°] exhibit a significant difference in spite of their similarity. Again the ruthenium centers each have a pseudooctahedral environment with a facially coordinated $(L_{OMe})^-$ ligand. The hydrogen on the formate group was easily located in a difference Fourier map, and the identity of the formate group was further confirmed by coupled ^{13}C NMR spectroscopy of an enriched sample prepared from labeled formaldehyde. Like the Ru^{III}-Ru^{III} dimer, $[5]^{2+}$, described above, both the Ru-Ru distance [2.548 (1) Å] and the complex's diamagnetism are consistent with a Ru-Ru single bond. Direct comparison of the Ru-Ru distances in $[5]^{2+}$ and $[6]^{+}$ may not be particularly meaningful, as both the number and nature of bridging ligands differ.

Conclusion

The dimer **1** oxidizes alcohols, aldehydes, and triphenylphosphine in acetonitrile to afford Ru^{III}-Ru^{III} products such as $[(L_{OMe})(CH_3CN)Ru^{III}(\mu\text{-}OH)_2Ru^{III}(NCCH_3)(L_{OMe})](CF_3SO_3)_2$ (**[5]**$(CF_3SO_3)_2$) and the corresponding organic products. These reactions exhibit unusual rate behavior suggesting autocatalysis that will be explored further in the following chapter. The mechanism appears fundamentally different from known metal-oxo chemistry in being autocatalytic and exhibiting no definite primary isotope effect.

The dimer **1** reacts with formaldehyde in aqueous buffer to afford $[(L_{OMe})Ru^{III}(\mu\text{-}OH)_2(\mu\text{-}HCOO)Ru^{III}(L_{OMe})](CF_3SO_3)$ (**[6]**(CF_3SO_3)) which was characterized by X-ray crystallography. This product appears to be formed by the inner-sphere oxidation of formaldehyde. The (**[6]**(CF_3SO_3)) was easily oxidized to $[(L_{OMe})Ru^{IV}(\mu\text{-}O)_2(\mu\text{-}HCOO)Ru^{IV}(L_{OMe})](CF_3SO_3)$ (**[7]**(CF_3SO_3)) which also oxidized formaldehyde to afford free formate and a mixture of $[\mathbf{6}]^+$ and a small amount of $[\mathbf{3}]^{2+}$. Labeling experiments with $[(L_{OMe})Ru^{IV}(\mu\text{-}O)_2(\mu\text{-}H^{13}COO)Ru^{IV}(L_{OMe})](CF_3SO_3)$ ((μ-H^{13}COO)-**[7]**(CF_3SO_3)) estabilished that dimer bound formate does not dissociate and that a symmetric dimer with two bridging formates does not form as an intermeditate.

The dimer **1** acts as a catalyst for the bulk electrooxidation of formaldehyde in aqueous buffers. This activity appears to occur by two catalytic cycles driven by the Ru^{IV}-Ru^{IV}/Ru^{III}-Ru^{III} couple of $[\mathbf{6}]^+$ and $[\mathbf{7}]^+$ and the same couple of $[\mathbf{3}]^{2+}$ and **1**. This catalytic activity was limited by buffer failure from the generation of acid during formaldehyde oxidation and the buildup of free formate. The catalyst lifetime was extended with higher buffer strengths and added palladium/carbon, a known electrocatalyst for the oxidation of formate.

Palladium/carbon catalysts pretreated with Nafion and loaded with **1** exhibit significant improvement over catalysts simply pretreated with Nafion. This demonstrated that the use of homogenous catalysts to compliment the activity of existing heterogeneous

catalysts is feasible. In the longer-term, principles learned from this homogeneous system may assist in understanding and optimizing existing heterogeneous catalysts.

Experimental

General experimental considerations for bulk chemistry and electrochemistry were identical to those described in the Experimental section of Chapter 2.

$[(L_{OMe})(CH_3CN)Ru^{III}(\mu\text{-}OH)_2Ru^{III}(NCCH_3)(L_{OMe})][CF_3SO_3]_2$ ([5][$CF_3SO_3]_2$). CH_3CN (40 mL) was added to a mixture of Ph_3P (0.0557 g, 0.212 mmol) and $[H_21][CF_3SO_3]_2$ (0.1498 g, 0.1019 mmol), and the solution was stirred for 18 hours at room temperature. The solution was then evaporated to dryness. The residue was suspended in CH_2Cl_2 (10 mL), and the yellow powder was isolated on a small medium frit. The solid was washed with CH_2Cl_2 and dried *in vacuo* (0.124 g, 0.082 mmol, 80%). Anal. Calcd for $C_{28}H_{54}Co_2F_6N_2O_{26}P_6Ru_2S_2$ (Mol wt 1518.69): C, 22.14; H, 3.58; N, 1.84. Found: C, 21.95; H, 3.62; N, 1.92. IR(nujol): 3311(w), 3122(vw), 3094(vw), 1791(vw), 1461(s), 1426(sh, m), 1276(s), 1261(s), 1224(m), 1170(s), 1158(s), 1082(s), 1031(s), 998(s), 917(w), 845(m), 791(s), 744(s), 635(s), 611(s), 595(s), 574(w). ^1H NMR (CD_3CN): δ 5.20 (s, C_5H_5, 10H), 4.06 (t, J_{HP}=5.4 Hz, OCH_3, 12H), 3.91 (t, J_{HP}=5.2 Hz, OCH_3, 12H), 3.17 (d, J_{HP}=10.8 Hz, OCH_3, 12H), 2.14 (s, CH_3CN, 6H). UV-Vis [λ_{max}, nm (ε, $M^{-1}cm^{-1}$), in CH_2Cl_2]: 242 ($3.9\cdot10^4$), 344 ($1.68\cdot10^4$).

$[(L_{OMe})Ru^{III}(\mu\text{-}OH)_2(\mu\text{-}HCOO)Ru^{III}(L_{OMe})][CF_3SO_3]\cdot2H_2O$ ([6][$CF_3SO_3]\cdot2H_2O$). An excess of 37% aqueous HCHO was added to a solution of $[H_21][CF_3SO_3]_2$ (0.1095 g, 0.0745 mmol), $NaH_2PO_4\cdot H_2O$ (0.0512 g, 0.371 mmol), and $Na_2HPO_4\cdot7H_2O$ (0.0595 g, 0.222 mmol) in H_2O (15 mL). This solution was heated to 80 °C with stirring until the solution became yellow (15 minutes). The reaction was extracted with CH_2Cl_2 (2 x 7.5 mL), and the extracts were dried with $MgSO_4$ and filtered. The product was precipitated by addition of heptane (45 mL). The yellow microcrystalline solid was isolated on a medium frit and washed sequentially with CH_2Cl_2/heptane (1:3), heptane, and petroleum ether. The solid was dried *in vacuo* (0.0739 g,

0.0499 mmol, 72.5%). Anal. Calcd for $C_{24}H_{53}Co_2F_3O_{27}P_6Ru_2S$ (Mol wt 1368.57): C, 21.06; H, 3.90. Found: C, 21.07; H, 3.52. IR (KBr): 3527(s), 3451(s), 3172(sh-w), 3120(m), 3001(m), 2951(s), 2902(sh, m), 2845(m), 2050(br, w), 1774(br, w), 1636(w), 1570(s), 1460(m), 1427(m), 1376(w), 1348(m), 1281(s), 1260(s), 1224(m), 1174(sh, s), 1158(s), 1107(sh, s), 1080(s), 1036(s), 1010(vs), 875(sh, w), 853(m), 838(sh, w), 789(s), 772(sh, s), 739(s), 657(sh, m), 638(s), 614(sh, s), 601(s). ^{1}H NMR (D_2O, pH 7, I=0.1 M): δ 5.29 (s, C_5H_5, 10H), 3.86 (q, J_{HP}=5.4 Hz, OCH_3, 24H), 3.09 (d, J_{HP}=11.1 Hz, OCH_3, 12H). (CD_2Cl_2): δ 12.27 (s, μ-*H*COO, 1H), 5.23 (s, C_5H_5, 10H), 4.04 (m, OCH_3, 24H), 3.21 (m, OCH_3, 12H), 1.62 (br-s, O*H*). UV-Vis [λ_{max}, nm (ε, $M^{-1}cm^{-1}$), in CH_2Cl_2]: 242 ($3.8 \cdot 10^4$), 342 ($1.46 \cdot 10^4$), 694 ($8.4 \cdot 10$).

[(L_{OMe})Ru^{IV}(μ-O)$_2$(μ-HCOO)Ru^{IV}(L_{OMe})][CF_3SO_3] ([7][CF_3SO_3]). Solid $AgCF_3SO_3$ (0.0265 g, 0.103 mmol) was added to a solution of **[6]**(CF_3SO_3) (0.0506 g, 0.0344 mmol), $NaH_2PO_4 \cdot H_2O$ (0.0480 g, 0.348 mmol), and $Na_2HPO_4 \cdot 7H_2O$ (0.0590 g, 0.220 mmol) in H_2O (15 mL). The resulting pale yellow suspension was sonicated until the suspension became a dark green (30 minutes). The suspension was filtered and extracted three times with 15 mL, 10 mL, and 5 mL of CH_2Cl_2 respectively. The combined CH_2Cl_2 solutions were dried with $MgSO_4$ and filtered. The product was precipitated by addition of heptane (120 mL) followed by reduction to 75 mL under vacuum. The green powder was isolated on a medium frit and washed with heptane and petroleum ether. The green powder was dried *in vacuo* (0.0431 g, 0.0323 mmol, 93.9%). Anal. Calcd for $C_{24}H_{47}Co_2F_3O_{25}P_6Ru_2S$ (Mol wt 1330.52): C, 21.67; H, 3.56. Found: C, 21.66; H, 3.52. IR(KBr): 3591(br,sh, m), 3116(w), 3000(w), 2952(m), 2904(sh, w), 2846(w), 1995(br, vw), 1790(br, vw), 1541(m), 1460(m), 1427(w), 1353(m), 1277(m), 1224(m), 1174(sh, m), 1156(m), 1066(sh, s), 1031(s), 850(w), 793(m), 743(m), 696(w), 638(m), 619(sh, m), 604(m), 518(w), 496(w). ^{1}H NMR (pH 7, D_2O): d 5.21 (s, C_5H_5, 10H), 3.75 (m, OCH_3, 12H), 3.48 (m, OCH_3, 12H), 3.34 (m, OCH_3, 12H). (CD_2Cl_2): d 5.20 (s, C_5H_3, 10H), 3.93 (pseudo t, J_{HP}= 5.6 Hz, OCH_3, 12H), 3.62 (pseudo t, J_{HP}=5.6 Hz, OCH_3, 12H); 3.42 (d, J_{HP}=11.1 Hz, OCH_3, 12H). UV-Vis [λ_{max}, nm (ε, $M^{-1}cm^{-1}$), in CH_2Cl_2)]: 242 ($4.0 \cdot 10^4$), 336 ($1.21 \cdot 10^4$), 672 ($1.91 \cdot 10^3$).

$[(L_{OMe})(HO)Ru^{III}(\mu\text{-}OH)_2Ru^{III}(NCCH_3)(L_{OMe})][CF_3SO_3]\cdot H_2O$ ([8][CF_3SO_3]·H_2O). An excess of Me_3CNH_2 (90μL, 0.86 mmol) was added to a suspension of $[H_21][CF_3SO_3]_2$ (0.2003 g, 0.1362 μmol) in CH_3CN (20 mL). The resulting yellowish green solution was quickly degassed and refluxed under an atmosphere of argon for 1 hour. The orange solution was pumped to dryness under vacuum. The residue was extracted with CH_2Cl_2 (60 mL). The CH_2Cl_2 solution was then extracted with water (10 x 30 mL). The CH_2Cl_2 solution was dried with anhydrous $MgSO_4$. A flocculent yellow-green solid precipitated upon addition of petroleum ether (400 mL). The solid was allowed to settle. The solid was isolated on a medium frit, washed with 1:4 CH_2Cl_2: petroleum ether (3 x 3 mL), and dried *in vacuo* (0.0665 g, 0.0488 mmol, 35.8 %). Anal. Calcd for $C_{25}H_{54}Co_2P_6O_{25}Ru_2NF_3S$ (Mol wt 1363.60): C, 22.02; H, 3.99; N, 1.03. Found: C, 21.75; H, 3.74; N, 1.08. IR(nujol): 4328(vw), 4257(vw), 3616(m), 3519(w), 3283(m), 3118(w), 2677(vw), 2615(vw), 1786(vw), 1626(vw), 1571(vw), 1549(vw), 1428(m), 1282(s), 1262(s), 1224(m), 1176(m), 1159(m), 1098(s), 1070(s), 1036(s), 1002(s), 847(m), 837(m), 791(s), 740(s), 694(m), 638(s), 618(s), 600(s), 572(w). ^{1}H NMR (CD_3CN): d 5.18 (s, C_5H_5, 5H), 5.16 (s, C_5H_5, 5H), 3.86 (t, J_{HP}=5.2 Hz, OCH_3, 6H), 3.83 (t, J_{HP}=5.5 Hz, OCH_3, 6H), 3.61 (t ,J_{HP}=5.6 Hz, OCH_3, 6H), 3.57 (t, J_{HP}=5.1 Hz, OCH_3, 6H), 3.46 (d, J_{HP}=11.2 Hz, OCH_3, 6H), 3.41 (d, J_{HP}=11.2 Hz, OCH_3, 6H), 2.30 (br-s, O*H*), 1.98 (s, $NCCH_3$, 3H). UV-Vis (λ_{max}, nm (ε, $M^{-1}cm^{-1}$), in CH_2Cl_2): 242 ($3.2\cdot10^4$), 330 ($1.26\cdot10^4$), 738 ($1.07\cdot10^3$).

$[(L_{OMe})Ru^{III}(\mu\text{-}OH)_2(\mu\text{-}H^{13}COO)Ru^{III}(L_{OMe})][CF_3SO_3]\cdot 2H_2O$ ($(H^{13}COO)$-[6][CF_3SO_3]·$2H_2O$). An excess of 19% $H^{13}CHO$ (aq) (10 equivalents) was added to a suspension of **1** in phosphate buffer (pH 7, I=0.1M) to afford $(H^{13}COO)$-$[6]^+$, which was isolated as the $CF_3SO_3^-$ salt as described above for the synthesis of [6](CF_3SO_3). ^{13}C NMR (CD_2Cl_2, δ 53.5): δ 179.5 (d, J_{CH}=214 Hz, μ-$H^{13}COO$). (pH 7 D_2O): δ 180.7 (d, J_{CH}=217 Hz, μ-$H^{13}COO$).

$[(L_{OMe})Ru^{IV}(\mu\text{-}O)_2(\mu\text{-}H^{13}COO)Ru^{IV}(L_{OMe})][CF_3SO_3]$ ($(H^{13}COO)$-[7][CF_3SO_3]). $(H^{13}COO)$-[7][CF_3SO_3] was prepared by the reaction of excess $AgCF_3SO_3$ with

$(H^{13}COO)$-**[6]**$[CF_3SO_3]\cdot 2H_2O$ in phosphate buffer as described above for the synthesis of **[7]**$[CF_3SO_3]$. ^{13}C NMR (pH 7 D_2O): δ 167.2 (d, J_{CH}=167.1 Hz, μ-$H^{13}COO$).

Reaction of [7][CF_3SO_3] with $H^{13}CHO$. An excess of $H^{13}CHO$ (aq) (7.1 μL, 19%, 50 μmol) was added to a suspension of **[7]**$[CF_3SO_3]$ (7.7 mg, 5.2 μmol) and **[6]**$[CF_3SO_3]\cdot 2H_2O$ (promoter for autocatalysis, 1.9 mg, 1.3 μmol) in D_2O phosphate buffer (0.5 mL, pH 7, I=0.1 M). This mixture was heated to 75°C until the reaction became a yellow-brown solution (30 minutes). ^{13}C NMR (pH 7 D_2O): δ 171.3 (d, J_{CH}=195 Hz, free $H^{13}COO^-$), 82.0 (t, J_{CH}=164 Hz, excess free $H^{13}CHO$).

Reaction of (μ-$H^{13}COO$)-[7][CF_3SO_3] with HCHO. An excess of HCHO (aq) (3.75 μL, 37%, 5.0 μmol) was added to a suspension of $(H^{13}COO)$-**[7]**$[CF_3SO_3]$ (7.4 mg, 5.0 μmol) and $(H^{13}COO)$-**[6]**$[CF_3SO_3]\cdot 2H_2O$ (2.5 mg, 1.7 μmol) in D_2O phosphate buffer (0.5 mL, pH 7, I=0.1M). This mixture was heated to 75°C until the reaction became a yellow-brown solution (30 minutes). ^{13}C NMR (pH 7 D_2O): δ 180.9 (d, 217 Hz, μ-$H^{13}COO$) {This signal characteristic of $(H^{13}COO)$-$[\mathbf{6}]^+$}, trace 171.3 (free $H^{13}COO^-$).

Reaction of [H3][CF_3SO_3]$_3$ with CD_3CN. [H3]$[CF_3SO_3]_3$ (5.0 mg, 3.52 μmol) was suspended in CD_3CN (0.7 mL) in an NMR tube. The ^1H NMR spectrum was collected immediately, and indicated a mixture of soluble $[H3]^+$ and $[\mathbf{5}]^{2+}$. The NMR tube was heated to 40°C for 20 minutes during which time all of the suspended solid dissolved. The ^1H NMR spectrum then showed only $[\mathbf{5}]^{2+}$.

Reaction of [H3][CF_3SO_3]$_3$ with HCOONa. [H3]$[CF_3SO_3]_3$ (5.2 mg, 3.66 μmol) and HCOONa (1.2 mg, 18 μmol) were dissolved/suspended in D_2O phosphate buffer (0.7 mL, pH 7, I=0.1 M). This solution was agitated at room temperature for 1 hour. The ^1H NMR spectrum of this sample exhibited the dimer signals for $[\mathbf{3}]^{2+}$ and $[\mathbf{4}]^{2+}$. No reaction with HCOONa was evident.

Reaction of $[H_21][CF_3SO_3]_2$ with substrates in CD_3CN. A solution of $[H_21][CF_3SO_3]_2$ (0.0751 g, 0.0517 mmol) in CD_3CN (10 mL) was divided into ten portions (1.0 mL). Then a substrate was added to each portion: $C_6H_5CH_2OH$ (1.6 μL, 16 μmol), CH_3CH_2OH (0.9 μL, 15 μmol), C_6H_5CHO (1.5 μL, 15 μmol), CH_3OH (0.6 μL, 15 μmol), cyclohexene (1.5 μL, 15 μmol), $(CH_3)_2CHOH$ (1.2 μL, 16 μmol), CH_3COOH (0.9 μL, 16 μmol), C_6H_5COOH (0.0018 g, 15 μmol), $C_5H_5NH_2$ (1.4 μL, 15 μmol), 2,6-$(CH_3)_2C_6H_3NH_2$ (0.0018 g, 15 μmol). Each solution was heated in a closed vial at 76 °C for one hour, transferred to an NMR tube, and examined by ^1H NMR spectroscopy. These spectra were compared to those prepared from authentic samples of expected organic oxidation products.

Kinetics of Ph_3P oxidation by $[H_21][CF_3SO_3]_2$ monitored by ^1H NMR spectroscopy. A small amount of degassed water (1.57 μL, 87 μmol) was added under argon to a solution of $[H_21][CF_3SO_3]_2$ (6.4 mg, 4.4 μmol) in purified CD_3CN (1.28 mL). A portion (0.70 mL) of this solution was added to Ph_3P (0.0064 g, 24 μmol) in a sealable NMR tube. The sample was cooled to -78 °C , evacuated for 1 minute, and sealed by flame. The sample was thawed and immediately examined by ^1H NMR spectroscopy (at 23.2 °C) after which the sample was alternatively stored at room temperature and reexamined by ^1H NMR spectroscopy over 18 hours. The position and integration of six $(L_{OMe})^-$ Cp peaks were measured. The reaction proceeded as discussed in the text.

Cyclic Voltammetry of $[6]^+$ in pH 7 buffer. A solution of $[6][CF_3SO_3]$ (0.0147 g, 11.0 μmol) in phosphate buffer (10.0mL, pH 6.9, I=0.1 M) was examined by cyclic voltammetry in a one compartment cell at commercially available platinum, gold, and glassy carbon disk electrodes. These experiments used a (Ag/AgCl/3 M KCl) reference electrode and a platinum wire coil auxiliary electrode. A typical cyclic voltammogram at the glassy carbon disk is illustrated in Figure 4.7 and discussed in the text.

Bulk electrooxidation of formaldehyde using 1. In a typical experiment, an electrochemical cell was prepared with its working compartment charged with a solution of $[H_21](CF_3SO_3)_2$ (10 μmol) in phosphate or pyrophosphate buffer (10 mL, see Table A). The auxiliary compartment was charged with a suspension of silica gel (approximately 1 g) in buffer (10 mL); the silica gel was intended to impede diffusion between the cell compartments. Some experiments included 10% palladium carbon (0.0108g, 10.2 μmol Pd) in the working solution (See Table 4.2). The working compartment was equipped with a platinum gauze working electrode, an SCE electrode, and a small stirbar. The auxiliary compartment was equipped with a large platinum gauze auxiliary electrode. To optimize currents the working electrode gauze (sheet) was arranged perpendicularly to the salt bridge with the reference electrode oriented as close as possible.

Table 4.6. Salt composition of buffers used in electrooxidation of formaldehyde.

These salts were volumetrically dissolved into water (100 mL) to prepare the corresponding buffers:

pH 6.9	I=0.10 M	$NaH_2PO_4{\cdot}H_2O$ (0.584 g, 2.18 mmol)
		$Na_2HPO_4{\cdot}7H_2O$ (0.482 g, 3.49 mmol)
pH 6.9	I=0.50 M	$NaH_2PO_4{\cdot}H_2O$ (2.913g, 10.87 mmol)
		$Na_2HPO_4{\cdot}7H_2O$ (2.409g, 17.46 mmol)
pH 8.5	I=0.10 M	$NaH_2PO_4{\cdot}H_2O$ (0.0517g, 0.375 mmol)
		$Na_4P_2O_7{\cdot}10H_2O$ (0.4617g, 1.035 mmol)

After the cell was degassed with argon (sparging), it was immersed as much as possible in a temperature controlled oil bath and warmed to the experimental temperature. Actual cell temperatures were measured in representative experiments with a thermometer immersed in the working compartment. (Oil bath temperatures of 100°C were necessary to achieve 86°C within the cell.) After the oil bath temperature stabilized, formaldehyde (37%, see Table 4.2) was injected into both compartments through septa. Bulk electrolysis began immediately with

current sampling every 1 to 15 seconds. Currents typically reached their maxima within five minutes at which the experiment was halted, saved, and restarted with current sampling every 10 to 30 seconds. This restart is necessary to avoid detector problems with the BAS 100A. Experiments continued until currents decayed to a low, constant level. Total charge passed in each segment of the experiment was summed and reported in Table 4.2 without correction.

Bulk electrooxidation of methanol using 1. These experiments were conducted much as those for electrooxidation of formaldehyde with the single modification that the working and auxiliary solutions were prepared as follows. For the pH 2.5 experiment, $NaH_2PO_4 \cdot H_2O$ (21.35g, 154.7 mmol) and H_3PO_4 (85%, 7.47 mL, 109.2 mmol) were dissolved in water (35.6 mL). Methanol (35.6 mL) was slowly added with stirring to form a clear solution (100 mL). In the pH 5.5 experiment, $Na_4P_2O_7 \cdot 10H_2O$ (2.708 g, 6.07 mmol) and H_3PO_4 (85%, 0.70 mL, 10.2 mmol) were dissolved in water (50 mL). Methanol (50 mL) was slowly added with mixing to form a clear solution.

In both experiments, the fuel-buffer solution (10 mL) was added to the two compartments of the electrolysis cell and $[H_2\mathbf{1}](CF_3SO_3)_2$ (for pH 2.5: 0.0155 g, 10.5 mmol) (for pH 5.5: 0.0151 g, 10.3 mmol) was added to the working compartment, and the cell was briefly degassed with argon. The remainder of the experiments were executed as described for formaldehyde experiments above.

Binding of 1 in Nafion. An edge plane graphite electrode was dipped into a solution of Nafion (0.05%) in isopropanol. After drying, the electrode was soaked in either a solution of **1** (0.80 mM) or $[H_2\mathbf{1}][CF_3SO_3]_2$ (0.80mM) in nano-pure water for several hours. The electrochemistry of the electrode coating was examined in a one compartment cell with either Na_2SO_4 (0.025 M) or $HClO_4$ (0.10 M) electrolyte and a SCE reference electrode. Cyclic voltammetry of electrode coatings loaded in solutions of **1** or $[H_2\mathbf{1}][CF_3SO_3]_2$ were nearly identical except for the larger currents exhibited by the former. This may be due to higher loading encouraged by the additional acid-base driving force for binding **1**.

Fuel cell testing of Nafion bound 1. Electrodes were prepared by a method used by the JPL fuel cell testing team. A paste of palladium/carbon (5%) and binder (1% polymer w/w in cyclohexane) was spread thinly on carbon/Teflon paper. (The experimental catalyst pad measured 1.3 cm x 0.7 cm on a 3.4 cm x 0.7 cm electrode strip. The control catalyst pad measured 1.1 cm x 0.7 cm on a 3.4 cm x 0.7 cm electrode strip.) Nafion solution (2% w/w) in isopropanol was painted on both electrodes and allowed to dry. The quantities of palladium/carbon and Nafion bound to the electrodes was measured by weight differences. (The experimental electrode contained 0.0196 g of palladium/carbon and 0.0032 g of Nafion. The control electrode contained 0.0200 g of palladium/carbon and 0.0032 g of Nafion.) The experimental electrode was immersed in a solution of **1** (0.0295 g, 20.1 μmol) in water (40 mL) for 75 minutes. Each electrode was attached to a wire via an alligator clip, and the untreated portion of the electrode was wrapped (along with the alligator clip) with shrink wrap tubing and Teflon tape.

The working compartment of a large two compartment cell was filled with a solution of formaldehyde (37%, 2.00 mL, 26.7 mmol), $NaH_2PO_4 \cdot H_2O$ (1.2947 g, 9.382 mmol), and $Na_4P_2O_7 \cdot 10H_2O$ (11.5371 g, 25.865 mmol) in nano-pure water (250 mL). A platinum gauze was used as the auxiliary electrode, and a closed-stopcock glass contact MSE (mercury sulfate electrode) was used as the reference electrode. The cell was maintained at 60 °C and was stirred. Both experiments were executed similarly. The working electrode was lowered into the cell and allowed to equilibrate with the electrolyte for several minutes. After the resting potential was measured, currents from 0.1 mA to 5.0 mA were applied in gradual steps allowing for stabilization of resulting potentials and their measurement. Figure 4.9 presents the measured data as a plot of potential versus current-per-unit-area.

Production of modified palladium/carbon catalysts for fuel cell testing: Pd/C control. Palladium/carbon (10%, 1.0g) was suspended in a solution of Nafion (5% w/w) in isopropanol (10 mL). The suspension was stirred for 15 minutes and the black solid was collected on a 15 mL medium frit. The solid was air dried and then dried *in vacuo*. **Pd/C treated-1.** A sample of

Pd/C control catalyst (0.20 g) was suspended in a solution of **1** (0.0294 g, 25.2 μmol) in water (20 mL). This suspension was stirred until the solution (when the solid was allowed to settle) became colorless. The solid was collected on a 15 mL frit and air dried. **Pd/C treated-2.** A sample of **Pd/C control** catalyst (0.20 g) was suspended in a solution of **1** (0.0300 g, 25.6 μmol) in phosphate buffer (20 mL, pH 6.9, I=0.1 M). This suspension was stirred until the solution (when the solid was allowed to settle) became colorless. The solid was collected on a 15 mL frit and air dried.

Fuel cell testing of modified palladium/carbon catalysts. Electrodes were prepared with the modified catalysts as described in "Fuel cell testing of Nafion bound 1" above. The "control" electrode consisted of 0.0196 g of **Pd/C control** in a 1.2 cm x 0.64 cm pad on carbon/Teflon paper. The first experimental electrode consisted of 0.0225 g of **Pd/C treated-1** in a 1.35 cm x 0.75 cm pad. The second experimental electrode consisted of 0.0180 g of **Pd/C treated-2** in a 1.20 cm x 0.70 cm pad. Figure 4.10 presents the measured data as a plot of potential versus current-per-unit-area.

Crystal Structure Determination of $[(L_{OMe})(CH_3CN)Ru^{III}(\mu\text{-}OH)_2Ru^{III}(NCCH_3)\text{-}(L_{OMe})][CF_3SO_3]_2$ ([5][CF_3SO_3]$_2$). X-ray quality crystals were grown by room temperature vapor diffusion of petroleum ether into a CH_2Cl_2 solution of the dimer. A yellow tabular crystal (0.3 mm x 0.4 mm x 0.7 mm) was mounted on a glass fiber with epoxy. A data set of 9449 reflections was collected at 298 °K on an Enraf-Nonius Cad-4 diffractometer over the range of $2°<2\theta<50°$ over all of the ±h, ±k, ±l octants by an ω-scan method. These data were merged with a goodness of fit of 1.02 to give 4669 independent reflections. General crystallographic data are listed in Table 4.3. Computations were done with the CRYM Crystallographic Computing System[9] and the drawings were made with ORTEP.[10] Published values were used for the scattering factors f_o and f'.[11] No corrections for extinction were made. The Ru, Co, and P atoms were located from a Patterson map and the remaining non-hydrogen atoms were located in successive structure factor-Fourier calculations. The atom positions and temperature factors

were then refined by least squares, minimizing $\Sigma\omega(F_o^2-F_c^2)^2$, where $\omega=1/\sigma^2(F_o^2)$ using F_o^2. The H atoms were then placed either in calculated positions (for the Cp rings) or in idealized positions based on difference maps calculated in the expected planes (for the methyl groups). The H atoms on the bridging oxygen atoms were located in a difference Fourier map. Positional and anisotropic displacement parameters of all atoms were refined in a full matrix, with the H atom thermal parameters treated isotropically. Atomic coordinates and displacement parameters are given in Appendix 1.

Crystal Structure Determination of $[(L_{OMe})Ru^{III}(\mu\text{-}OH)_2(\mu\text{-}HCOO)Ru^{III}(L_{OMe})]\text{-}[CF_3SO_3]\cdot 2H_2O$ ([6][CF_3SO_3]·2H_2O). X-ray quality crystals were grown by the slow cooling of a CH_2Cl_2/toluene/heptane (1:2:4 respectively) dimer solution. A yellow-green wedge-shaped lozenge crystal (0.12 mm x 0.29 mm x 0.32 mm) was mounted on a glass fiber with epoxy. The monoclinic lattice parameters were determined by least-squares fit of 25 accurately centered reflections with $22°<2\theta<30°$. A data set of 15660 reflections was collected at 225 °K on an Enraf-Nonius Cad-4 diffractometer over the range $2°<2\theta<48°$ over the octants ±h, ±k, +l by an ω-scan method. Absorption corrections were made analytically by Gaussian integrations using the program CRYM.[17] The 15660 reflections measured were merged to give 7402 independent reflections with a goodness of fit of 0.96 for the 7204 multiple reflections. General crystallographic data are given in Table 4.3. This structure was solved using the same programs and structure factors referenced above. The Ru positions were determined from a Patterson map and the remaining non-H atoms were located from repeated structure factor-Fourier cycles. The H atoms were located at peaks in a difference map in calculated planes. All atoms were refined with the H atom thermal parameters treated isotropically (except those on water molecule one which were fixed at peaks in a difference map). Least-squares refinement was used as for [5][CF_3SO_3]$_2$ performed on F^2, $w = 1/s^2(F_o^2)$, using one full matrix. Atomic coordinates and displacement parameters are given in Appendix 2.

References

1. Ram, S.; Ehrenkaufer, R. E. *Synthesis*,**1988**, 91 and references therein.

2. Nishimura, K.; Yamaguti, K.; Machinda, K.-I.; Enyo, M. *J. Appl. Electrochem.* **1988**, *18*, 183-187.

3. Young, G. J.; Linden, H. R. *Fuel Cell Systems*, Advances in Chemistry Series 47; American Chemical Society: Washington, DC, 1965; pp 1-8.

4. Xie, Y. Q.; Anson, F. C. *J. Elec. Chem.*, **1993**, *349*, 325-340 and references therein. Murray, R. W. *Electroanalytical Chemistry*; Bard, A. J., Ed.; Dekker: New York, 1984; pp 191-368. Hillman, A. R. *Electrochemical Science and Technology of Polymers*; Lindford, R. G., Ed.; Elsevier Applied Science: New York, 1987; Chapters 5 and 6. Kaneka, M.; Woerhle, D. *Adv. Polym. Sci.*, **1988**, *14*, 142.

5. Nandan, D.; Mohan, H.; Iyer, R. M. *Journal of Membrane Science*, **1992**, *71*, 69-80 and references therein.

6. This is the typical procedure used by the JPL fuel-cell team for testing homogeneous catalysts. The methods are described in detail within the Experimental section of this chapter.

7. Power, J. M.; Evertz, K.; Henling, L.; Marsh, R.; Schaefer, W. P.; Labinger, J. A.; Bercaw, J. E. *Inorg. Chem.*, **1990**, *29*, 5058-5065.

8. Shaik, S.; Hoffmann, R.; Fisel, C. R.; Summerville, R. H. *J. Am. Chem. Soc.*, **1980**, *102*, 4555. Cotton, F. A. *Polyhedron*, **1987**, *6*, 667.

9. Duchamp, D. J. *Am. Crystallogr. Assoc. Meet.*, Bozeman, Montana, **1964**, Paper B14; p. 29-30.

10. Johnson, C. K. *ORTEPII. Report ORNL-3794* Oak Ridge National Laboratory: Oak Ridge, Tennessee, USA, **1976**.

11. Cromer, D. T.; Waber, J. T. *International Tables for X-ray Crystallography*; Vol. IV; Kynoch: Birmingham, 1974; pp 99-101, 149-151. (Present distributor Kluwer Academic: Dordrecht.)

Chapter 5

Mechanistic Investigation of Formaldehyde Oxidation by the Ru^{IV}-Ru^{IV}/Ru^{III}-Ru^{III} Redox Couple of $[(L_{OMe})(HO)Ru^{IV}(\mu\text{-}O)_2Ru^{IV}(OH)(L_{OMe})]$

Abstract:

Though the mechanism of formaldehyde oxidation by the mild Ru^{IV}-Ru^{IV}/Ru^{III}-Ru^{III} redox couples of $[(L_{OMe})(HO)Ru^{IV}(\mu\text{-}O)_2Ru^{IV}(OH)(L_{OMe})]$ (**1**) is not completely elucidated, the kinetic survey presented here illustrates important features of the mechanism. The oxidation of formaldehyde appears to be an inner-sphere reaction that proceeds by two pathways, one of which is autocatalytic. Isomerization of **1** appears necessary for productive interaction with formaldehyde. This isomerization seems to occur either spontaneously or with the assistance by product $[\mathbf{6}]^+$. The pH dependence of the rate behavior suggests that this step is accompanied or followed by deprotonation. The reaction displays a primary kinetic deuterium isotope effect near unity, suggesting that the activation of **1** or the coordination of substrate (or both) constitute the rate-determining steps. Overall, this study reveals the mechanistic features of organic oxidation by a redox couple of moderate potential.

Introduction

Though formaldehyde and methanol have intrinsic oxidation potentials of about -0.2 V (SCE, pH 0) and -0.7 (SCE, pH 7)[1] respectively, the only reported homogeneous metal-oxo complexes that could effect the oxidation of substrates had reduction potentials greater than 0.5 V.[2] These potentials are apparently necessary to overcome large kinetic barriers to C-H cleavage by electron, hydrogen, or hydride transfer. As stated in the previous chapter, the ruthenium dimer $(L_{OMe})(HO)Ru^{IV}(\mu\text{-}O)_2Ru^{IV}(OH)(L_{OMe})$ (**1**) oxidizes substrates including alcohols and aldehydes despite its relatively moderate redox potential. Qualitatively, these reactions begin slowly and then accelerate during the course of the reaction. The low driving force and unusual rate behavior indicate that this system differs significantly from known oxidation chemistry and merits further investigation.

In order to examine the mechanism for the oxidation of substrates by the Ru^{IV}-Ru^{IV}/Ru^{III}-Ru^{III} couple, the kinetics of the reaction of **1** with formaldehyde was chosen. Formaldehyde is well-suited for a kinetic investigation since its reaction with **1** quantitatively affords a well-characterized product ($[\mathbf{6}]^+$, Figure 5.1). This reaction also occurs in water allowing facile control of pH and ionic strength, which is particularly important since the oxidation reaction generates protons.

Figure 5.1. Reaction of **1** with formaldehyde.

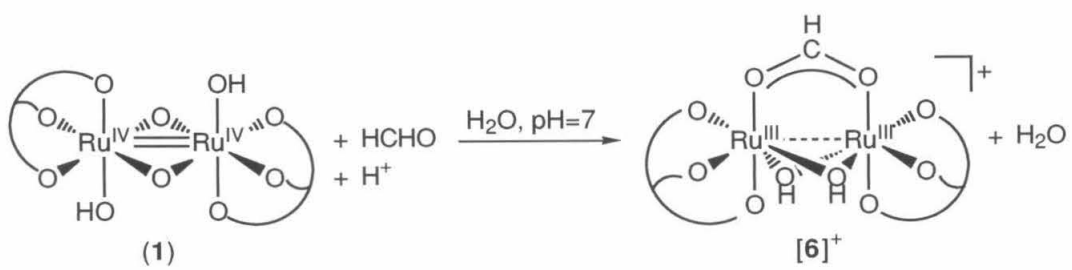

The rate behavior of this reaction is extremely complicated, but the opportunity to examine a system with unusually low kinetic barriers of C-H oxidation justifies the effort. The data analysis did not support reaction via a unique pathway, but Occam's razor was used to pare the proposed mechanism to the simplest form that can account for all observations.

Results

5.1. Kinetic measurements of formaldehyde oxidation by **1**.

In a typical kinetic experiment, formaldehyde was injected into a stirred sample of **1**, which was buffered and kept at constant temperature. Visible spectra from 400 nm to 820 nm were recorded at each time interval. Although atmospheric oxygen did not appear to affect significantly reaction rates, the kinetic measurements were performed under argon. To achieve pseudofirst-order conditions for the ruthenium species, the measurements were carried out with excess formaldehyde. Each experiment had the general appearance in Figure 5.2. Since no intermediate was evident from 400 nm to 820 nm, the kinetics were measured using the absorptance at 680 nm, λ_{max} for **1**. The product $[(L_{OMe})Ru^{III}(\mu\text{-}OH)(\mu\text{-}HCOO)Ru^{III}(L_{OMe})]^+$ ($[\mathbf{6}]^+$) which exhibits a very weak adsorption at 740 nm (Figure 7) did not interfere with these measurements at this wavelength. The raw absorption data were converted to dimer concentrations by standard means to give curves like that in Figure 5.3.

The typical reaction curve in Figure 5.3 exhibits a shape that indicates autocatalysis. Each experiment was initiated without an induction period and accelerated until the reaction rate reached a maximum around 50% completion.

Ru^{III}-Ru^{III} dimer $[\mathbf{6}]^+$ was confirmed as the catalytic species. Reactions beginning with mixtures of **1** and $[\mathbf{6}]^+$ prepared to simulate 5% to 50% completion proceeded as though the parent reaction was being monitored from that degree of completion. In Figure 5.4, the

Figure 5.2. Overlaid UV-vis spectra of progressing reaction. (Spectra were taken at equal time intervals.)

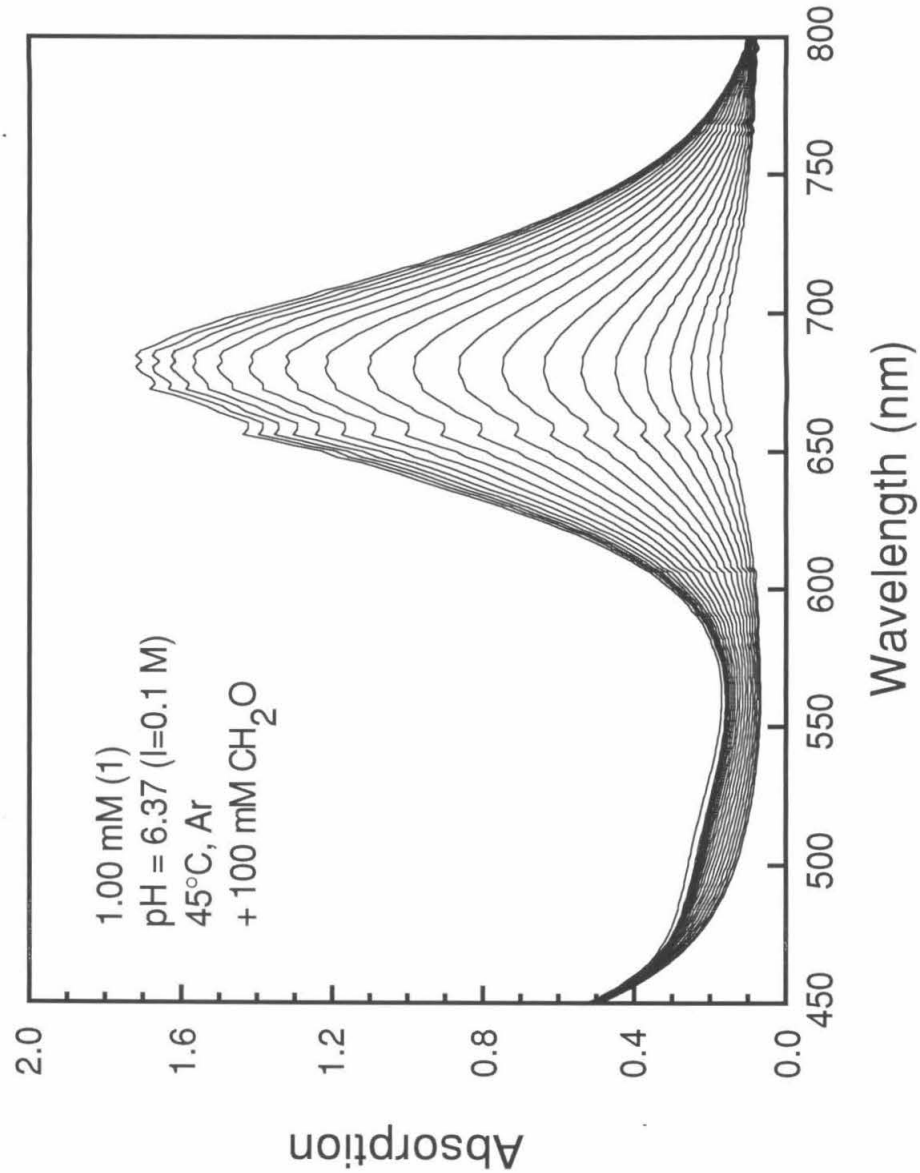

Figure 5.3. Concentration of 1 versus time in reaction with formaldehyde.

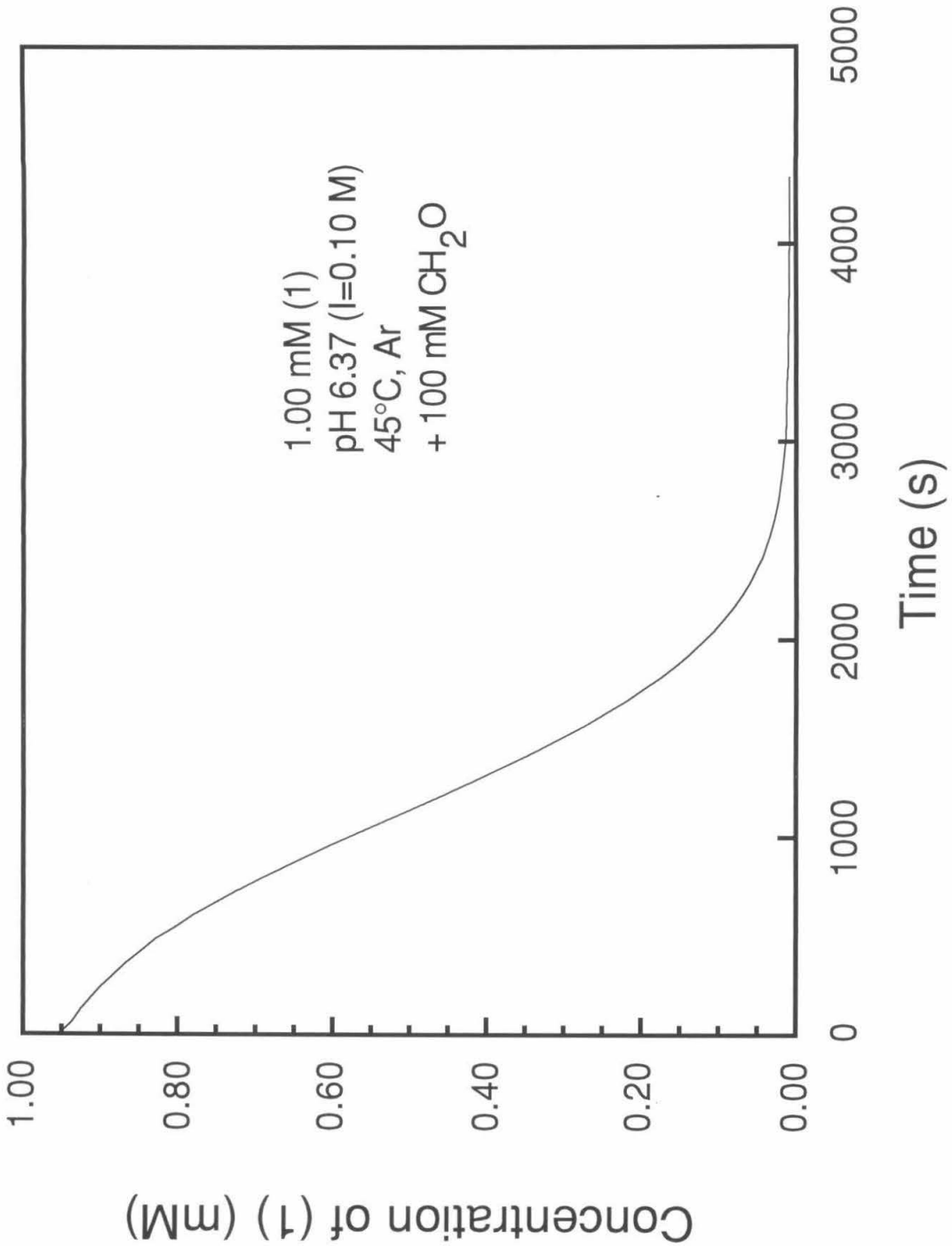

Figure 5.4. Overlaid concentration of **1** versus time curves for formaldehyde oxidations with varying initial ratios of **1** and $[\mathbf{6}]^+$.

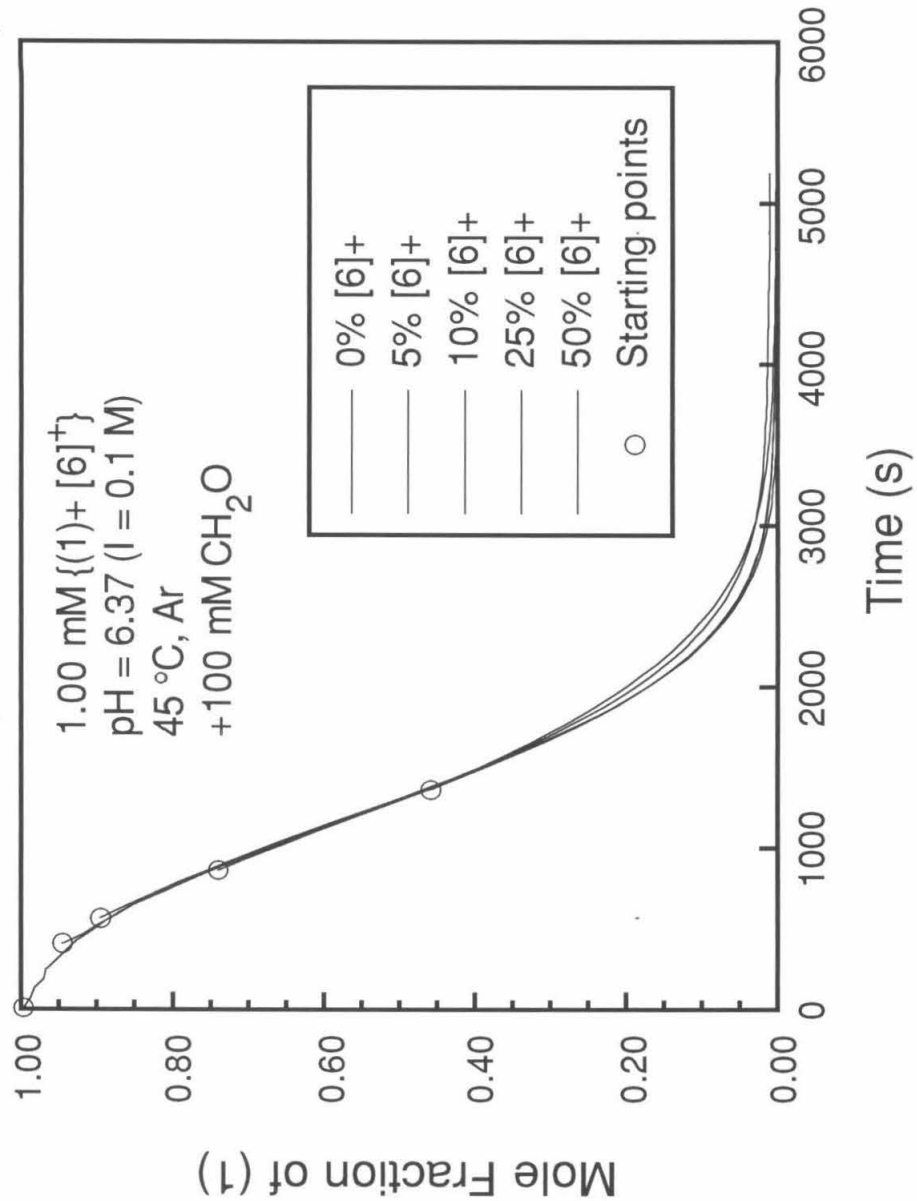

concentration versus time curves were plotted together with each curve offset along the time coordinate such that its initial Ru^{IV}-Ru^{IV} mole ratio corresponded to that degree of completion in the parent reaction. These reaction curves are superimposable until the reaction is nearly complete (deviations near completion are likely measurement errors).

5.2. Curve fitting to minimal rate laws.

Two features of the reaction curves, the initial slope and the autocatalytic rate acceleration, suggest that the reaction consists of at least two pathways. The simple rate law in Equation 5.1 is consistent with the overall features of the observed rate behavior.

Equation 5.1. The minimal rate law for rate behavior of formaldehyde oxidation by **1**.

$$\text{Rate} = k_{1,obs}[\mathbf{1}] + k_{2,obs}[\mathbf{1}][(\mathbf{6})^{+}]$$

Since excess formaldehyde and different pH conditions were used, the formaldehyde and proton dependencies are incorporated into k_{1obs} and k_{2obs}. The first term of this rate law is consistent with the initial rate observed in each experiment and the linearity of early data in log plots (Figure 5.5). The second, autocatalytic term is dictated by the overall features of the reaction curves: the reaction is slow in the early and late reactions where [**1**] and [(**6**)$^+$] are low, respectively, and the reaction is fast where the concentrations of both species are large.

Autocatalytic reactions are known. In reports of simple autocatalytic reactions (where the reactivity was strongly dominated by the autocatalytic component), the single term rate law was integrated, and the curve was fit to the resulting expression.[3] This method is limited to very simple second order autocatalytic mechanisms. The rigorous integration of a rate law containing a first order term and a second order autocatalytic term is a formidable mathematical exercise. In such cases, the rate expressions were fit to hypothetical mechanisms

Figure 5.5. Logarithmic plot of concentration of **1** versus time data for reaction with formaldehyde.

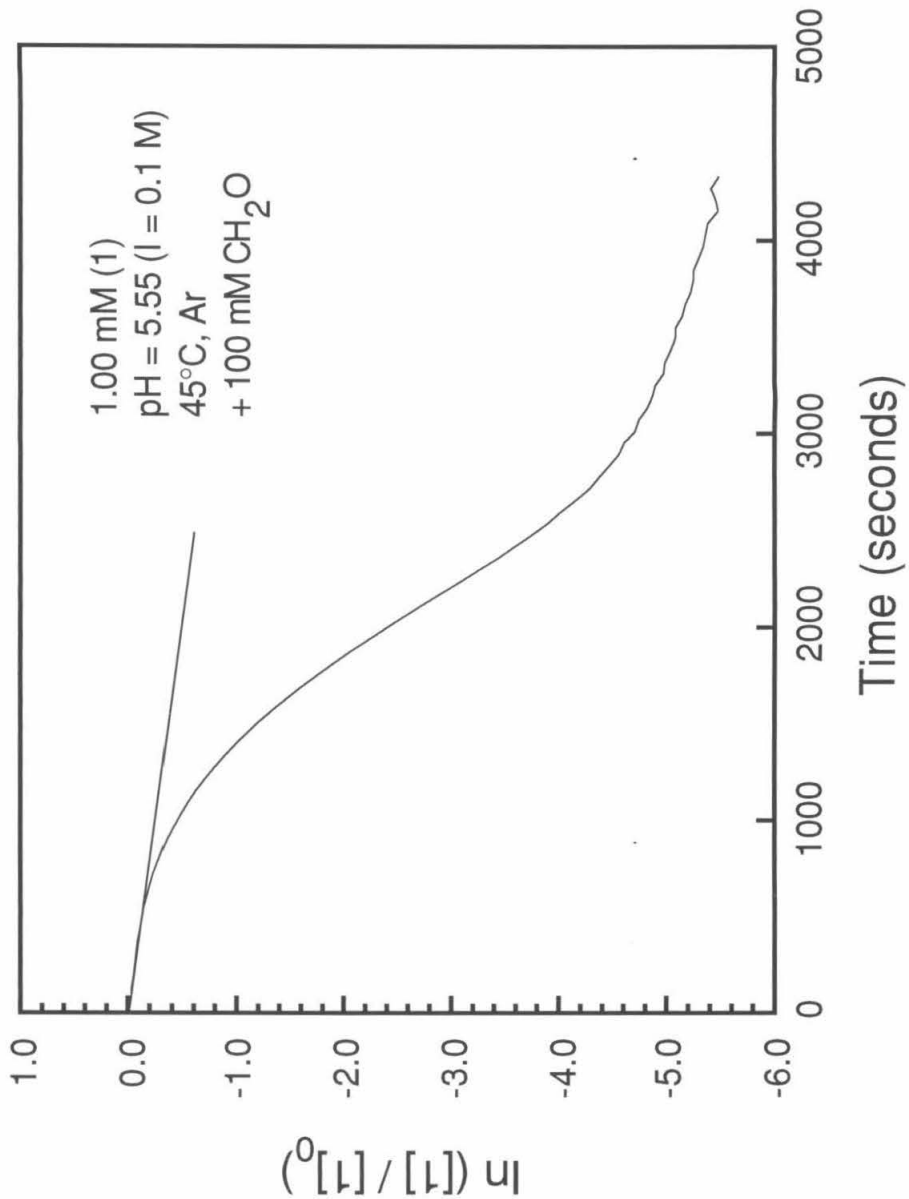

by trial-and-error digital simulation of the data.[4] Unfortunately, the latter method requires many iterations to extract the rate constants from the data.

A more powerful and intuitive approach converts the concentration versus time curves into rate versus concentration curves and then fits this data to the rate expression directly. This could be accomplished by either of two methods. In the first, the rate and concentration data for each point is entered into the rate law to give a series of linear equations with k_{1obs} and k_{2obs} as variables. Then, the least-squares solution for these constants is calculated using matrix least squares methods.[5] This method returns one unique solution for the constants after a single iteration. The source code for a computer program written for this task is provided in Appendix 3. Unfortunately, this first method only applies to rate laws consisting of a sum of "simple" terms (those not containing sums in their denominators).

The second, more general method uses a standard iterative least-squares curve fitting routine. This method is occasionally plagued by convergence and the delivery of false minima. Therefore, the first method was used whenever possible. Finally, rate constants derived by either method were confirmed by digital simulation of the reaction curve with the program listed in Appendix 4.

The simple curve-fitting rate law in Equation 5.1 models rate behavior well for many kinetic experiments, especially those with high concentrations of formaldehyde (Figure 5.6). Unfortunately the simulated curves in slow reactions, especially those with low concentrations of formaldehyde, deviate significantly from the data. While reasonable fits can be obtained for the early reactions where the data best represents differences between k_{1obs} and k_{2obs}, the simulated curves always exhibit a strong deviation from the data curve near completion. Qualitatively, this effect suggests that the reaction order in ruthenium species decreases as the reaction approaches completion. This effect is successfully modeled with the $[6]^+$ dependence illustrated in the second term of Equation 5.2; this dependence is reminiscent of saturation

Figure 5.6. Least-squares fit for simple rate law.

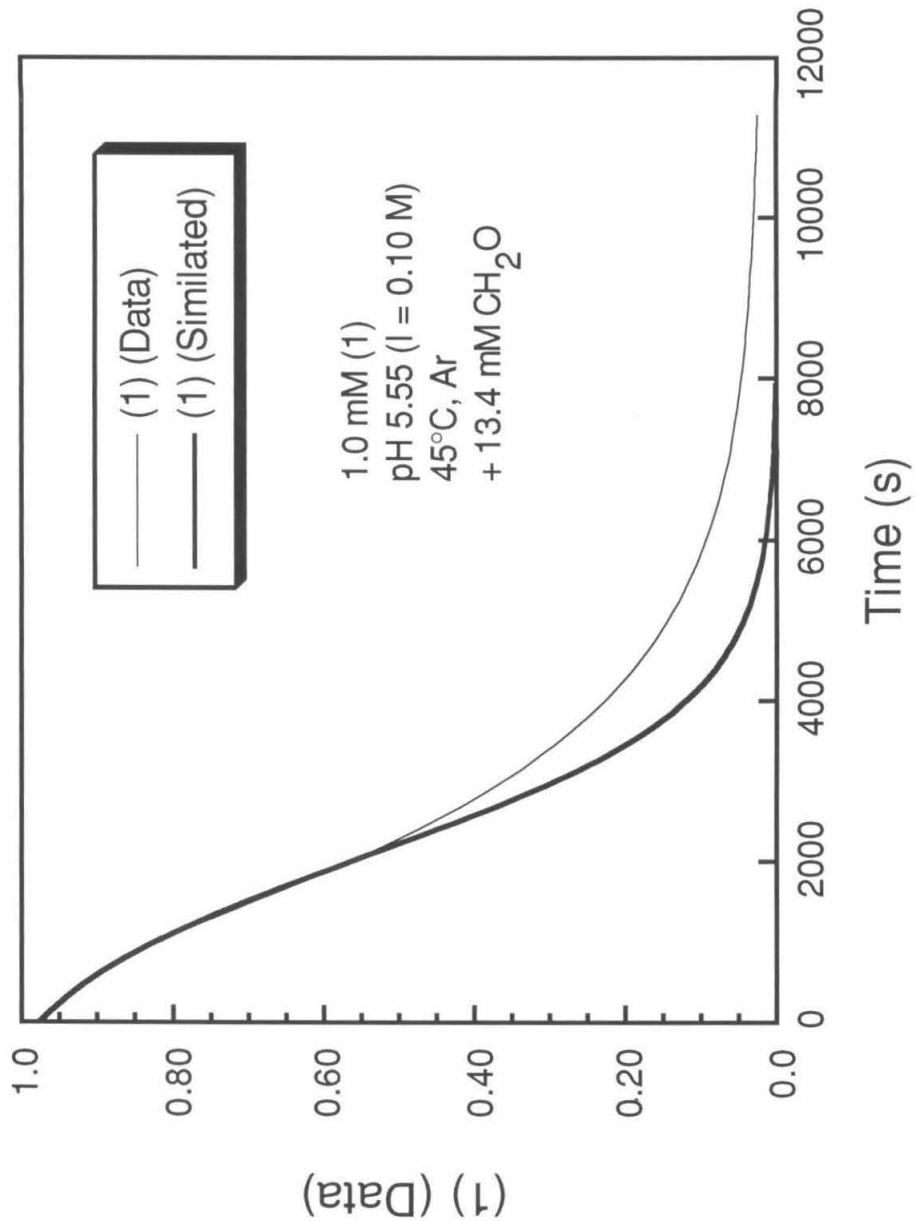

conditions in product. This rate law effectively models the rate behavior of all experiments, and though this rate law appears complex, it is the simplest rate law that fits all of the data.

Equation 5.2. Curve-fitting rate law with correction for observed $[\mathbf{6}]^+$ saturation behavior.

$$\text{Rate} = k_{1,obs}[\mathbf{1}] + \frac{[\mathbf{1}][(\mathbf{6})^+]}{a + b[(\mathbf{6})^+]}$$

5.3. Chemical interpretation of rate law.

The formaldehyde dependence of each of the three parameters were determined. Kinetic data was collected over a range of formaldehyde concentrations, and the rate law was fit to each experimental curve. The formaldehyde dependence was then identified from plots of each curve-fitting parameter versus the corresponding formaldehyde concentration. Each curve-fitting parameter was then written in terms of formaldehyde concentration and a new set of curve fitting constants (Equations 5.3). (See the Experimental for a detailed description of this analysis.) These equations were substituted into the original curve-fitting equation to give the following formaldehyde-dependent rate law (Equation 5.4). The individual terms of this rate law are easily correlated to hypothetical chemical mechanisms. The mechanisms proposed are the simplest cases consistent with this rate law.

Equations 5.3. Formaldehyde dependencies in each curve-fitting rate constant.

$$k_{1,obs} = \frac{[\text{HCHO}]}{A[\text{HCHO}] + B}$$

$$a = \frac{C[\text{HCHO}] + D}{[\text{HCHO}]}$$

$$b = \frac{E}{[\text{HCHO}]}$$

Figure 5.7. *Curve-fit for* concentration of 1 versus time data with improved rate law.

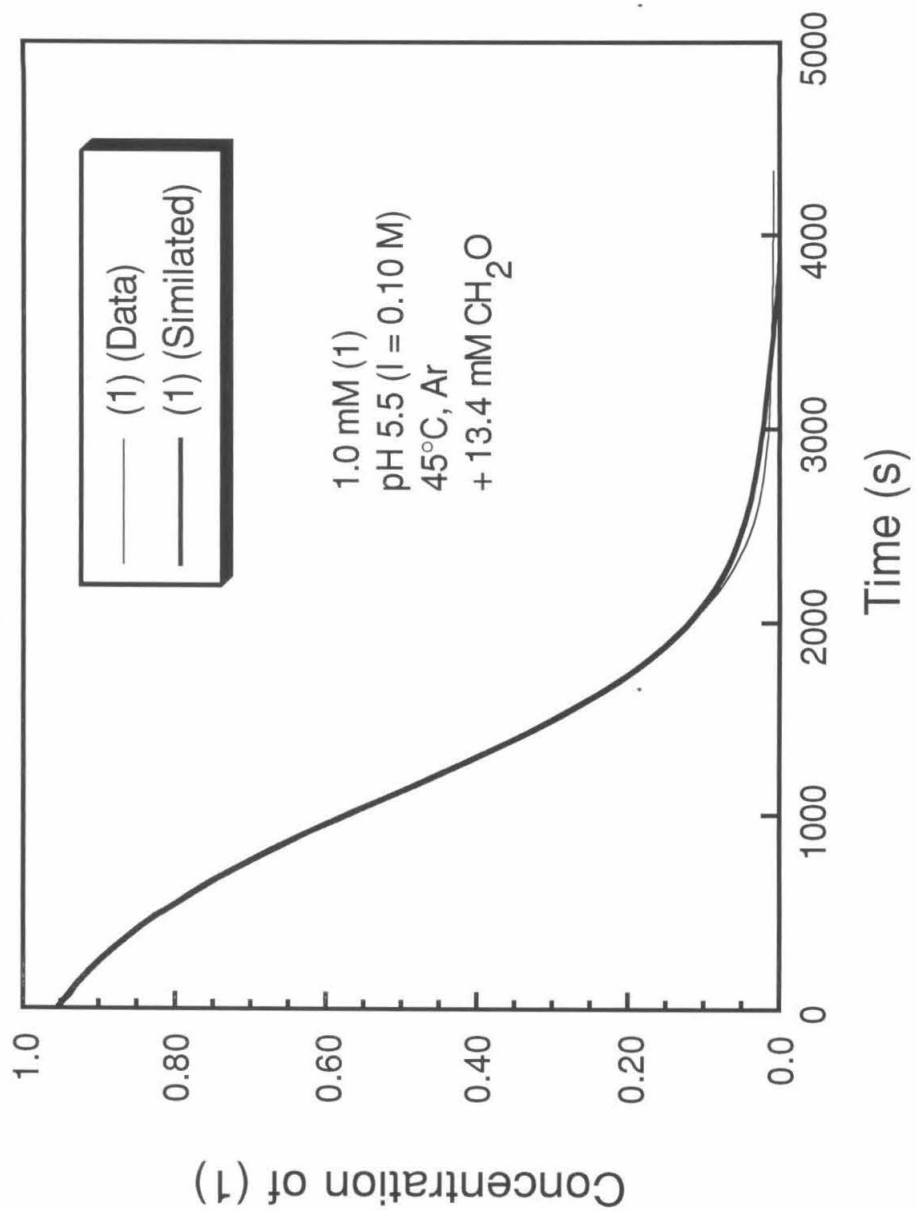

Equation 5.4. *Formaldehyde* dependent curve-fitting rate law.

$$\text{Rate} = \frac{[\text{HCHO}][\mathbf{1}]}{A[\text{HCHO}]+B} + \frac{[\mathbf{1}][(\mathbf{6})^+][\text{HCHO}]}{D+C[\text{HCHO}]+E[(\mathbf{6})^+]}$$

Both terms in the rate law are reminiscent of saturation kinetics in formaldehyde. The simplest mechanism for the first term requires only two steps (Figure 5.8). The constants in the first term of Equation 5.2 are easily related to the rate constants in the steady state rate law in Figure 5.8, allowing the microscopic rate constants for this mechanism to be calculated (Table 5.1).

Figure 5.8. Two step mechanism and corresponding steady state rate law for non-autocatalytic component of formaldehyde oxidation by **1**.

$$(\mathbf{1}) \underset{k_{-1}}{\overset{k_1}{\rightleftharpoons}} [\ ] \xrightarrow{k_2;\ +\ \text{HCHO}} [\ ] \xrightarrow[?]{\text{fast}} [\mathbf{6}]^+$$

$$\text{Rate}_1 = \frac{[\text{HCHO}][\mathbf{1}]}{A[\text{HCHO}]+B}$$

In spite of large errors, the values of k_1 and k_2/k_{-1} over the range of pH values are indicative of proton orders of 0 and 1 respectively. This result suggests intermediate deprotonation in the formaldehyde coordination step corresponding to k_2. Though values of k_1 are within experimental errors of each other, they exhibit a trend that could be symptomatic of systematic errors in curve fitting. The isotope effects are also tabulated but should be interpreted with caution due to the large errors and the suggestion of systematic error. However, the small values indicate that the primary isotope effect is near unity. It should be noted that a normal secondary kinetic isotope effect is expected to magnify the primary effect.

The second term of the curve-fitting rate law has a form similar to the steady-state rate law for a three step mechanism (Figure 5.9). The key to rewriting this chemical rate law

Table 5.1. Rate constants for proposed mechanism of non-autocatalytic reaction component.

Substrate	Solution pH	k_1 (10^{-4} s^{-1})	k_2/k_{-1} (M^{-1})
HCHO	5.55	1.45 (0.09)	1.2 (0.2)·10^2
HCHO	6.37	2.6 (0.2)	2.9 (0.3)·10^1
HCHO	7.17	5.3 (1.8)	5.6 (1.9)·10^0
DCDO	6.37	1.56 (0.12)	4.9 (5.2)·10^1

in the same form as the second term of Equation 5.4 is to find substitutions that would make the HCHO and $[\mathbf{6}]^+$ dependence appear in the three term denominator. Two mathematical possibilities exist for the chemical rate law expression, but only one of these is consistent with the reaction stoichiometry (Figure 5.10).

Figure 5.9. General three step mechanism and corresponding steady state rate law.

$$(\mathbf{1}) \underset{k_{-1}}{\overset{k_1}{\rightleftharpoons}} [\ ] \underset{k_{-2}}{\overset{k_2}{\rightleftharpoons}} [\ ] \xrightarrow{k_3} [\ ] \xrightarrow[?]{\text{fast}} [\mathbf{6}]^+$$

$$\text{Rate}_1 = \frac{k_1 k_2 k_3 [\mathbf{1}]}{k_{-1}k_{-2} + k_{-1}k_3 + k_2 k_3}$$

Figure 5.10. Three step mechanism and steady state rate law consistent with autocatalytic component of formaldehyde oxidation by **1**.

$$(\mathbf{1}) \xrightarrow[k_{-1};\ -[\mathbf{6}]^+]{k_1;\ +[\mathbf{6}]^+} [\ ]^+ \xrightarrow[k_{-2};\ -CH_2O;\ +[\mathbf{6}]^+]{k_2;\ +CH_2O;\ -[\mathbf{6}]^+} [\ ] \xrightarrow{k_3} [\ ] \xrightarrow[?]{\text{fast}} [\mathbf{6}]^+$$

$$\text{Rate}_2 = \frac{k_1 k_2 k_3 [\mathbf{1}][(\mathbf{6})^+][\text{HCHO}]}{k_{-1}k_{-2}[(\mathbf{6})^+] + k_{-1}k_3 + k_2 k_3 [\text{HCHO}]}$$

In this mechanism, this reaction consumes one equivalent of HCHO but no $[6]^+$ (assigned to k_1 and k_{-2}).

The rate constants and ratios of rate constants calculated from the rate law above have dubious value due to large errors and a number of extrapolation problems. Though these values are largely uninformative, the primary isotope effect again appears to be near unity, and a deprotonation is evident in the step corresponding to k_3 at pH≤6.4.

Table 5.2. Rate constants for proposed three step mechanism for autocatalytic reaction component.

Substrate	Solution pH	k_1 ($M^{-1}s^{-1}$)	k_2/k_{-1} (M^{-1})	k_3/k_{-2} (M)
HCHO	5.55	2.3 (0.1)	7.8 (5.6)·10^2	1.7 (1.2)·10^{-5}
HCHO	6.37	2.4 (0.2)	3.5 (0.5)·10^2	1.83 (0.17)·10^{-4}
HCHO	7.15	-128 (1946)*	-0.2 (2.8)*	9.8 (0.8)·10^{-4} §
DCDO	6.37	-4.2 (4.1)*	-4.7 (4.7)*	4.8 (0.6)·10^{-4} §

* Extrapolation errors made values inaccessible.

§ Values unreliable due to failure to extrapolate other constants.

However, the proposed mechanism does illustrate important features of this reaction. First, the Ru^{IV}-Ru^{IV} species **1** *itself* does not appear to react productively with HCHO. This is no surprise in light of the observed inertness of **1** toward ligand exchange (Chapter 4). The dimer must rearrange in order to react productively with HCHO. Second, the lack of a large kinetic deuterium isotope effect further supports the notion that dimer rearrangement and formaldehyde coordination are the slow steps in this reaction. In the initial reaction, the dimer likely undergoes a slow isomerism to an intermediate that reacts with HCHO (likely in its hydrated form). As product $[6]^+$ accumulates, it either assists this rearrangement or allows reaction by another pathway. Overall, the reaction of HCHO with **1** appears to be an inner-sphere reaction that requires activation of the relatively inert **1**.

Though further interpretation of these results would be very speculative, these results do make chemical sense in the context of dimer chemistry described in Chapters 2 and 4. The first pathway of the proposed mechanism involves a preequilibrium of **1** with an intermediate. This could be the Ru^{IV}-Ru^{IV} analog of the known equilibrium between the edge-sharing and face-sharing Ru^{III}-Ru^{III} dimers $[\mathbf{3}]^{2+}$ and $[\mathbf{4}]^{2+}$. Such a face sharing Ru^{IV}-Ru^{IV} dimer could be more likely to coordinate hydrated formaldehyde to form a Ru^{IV}-Ru^{IV} hydrated formaldehyde adduct (Figure 5.11) which requires only a deprotonation to establish the conjugated formate π-system which could facilitate electron transfer to the metal centers.

Figure 5.11. Possible Ru^{IV}-Ru^{IV} hydrated formaldehyde adduct intermediate.

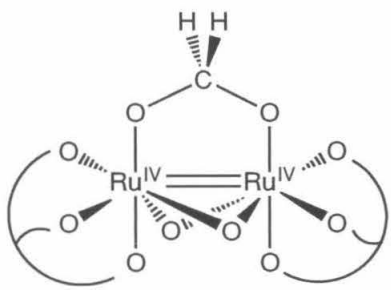

Similarly, the autocatalytic mechanism involves a preequilibrium of **1** with the product $[\mathbf{6}]^{+}$ that prepares the dimer for subsequent coordination of formaldehyde. Unfortunately, the nature of this interaction is unclear, and the intermediates are spectroscopically elusive. One possibility is that the $[\mathbf{6}]^{+}$ forms a dimer-dimer complex with **1** to form a face-sharing structure for the Ru^{IV}-Ru^{IV} pair (Figure 5.12) analogous to that illustrated in Figure 5.11 where the Ru^{III}-Ru^{III} dimer acts as a bridging ligand. The dimer $[\mathbf{6}]^{+}$ could then act as a leaving group upon coordination of hydrated formaldehyde.

The more familiar possibility for such a reaction would involve $[\mathbf{6}]^{+}$ dimer donating one or two electrons to **1** to induce lability to rearrangement or formaldehyde coordination. However, the steady state concentrations will be low which would require a remarkably fast

Figure 5.12. Possible Ru^{IV}_2-Ru^{III}_2 intermediate.

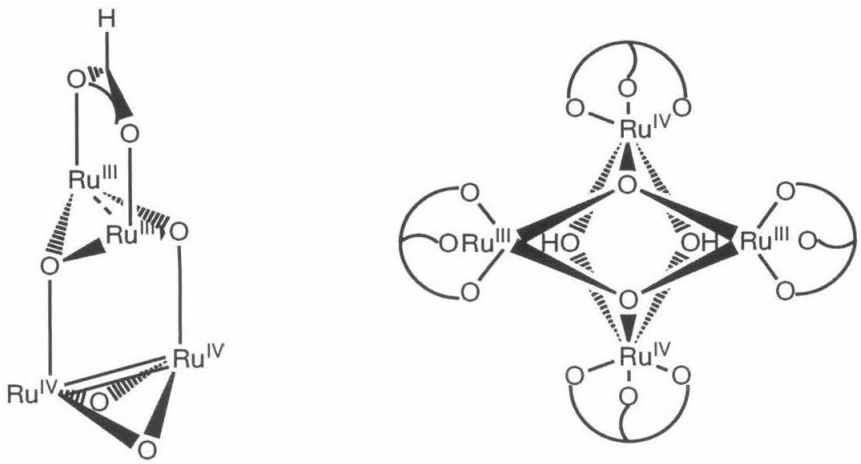

exchange reaction for the reaction to proceed as observed by this pathway. At pH 7, the Ru^{IV}-Ru^{IV}/Ru^{III}-Ru^{III} redox potential for the formate adduct is 200 mV above that of **1**. A steady state mole fraction of less than 0.1% of $[(L_{OMe})Ru^{IV}(\mu\text{-}O)_2(\mu\text{-}HCOO)Ru^{IV}(L_{OMe})]^+$ ($[\mathbf{7}]^+$) and $[(L_{OMe})(H_2O)Ru^{III}(\mu\text{-}OH)_2Ru^{III}(OH_2)(L_{OMe})]^{2+}$ ($[\mathbf{3}]^{2+}$) could form and remain undetected. The steady state concentrations of mixed valent Ru^{IV}-Ru^{III} intermediates would be significantly lower due to the electrochemical instability of these redox states relative to both their Ru^{III}-Ru^{III} and Ru^{IV}-Ru^{IV} states. This may require the ligand exchange to be faster than would be expected for octahedral d^4 and d^5 complexes. For example, in a typical reaction examined as part of this study, a steady state concentration of 1 μM of an intermediate would have to account for three ligand exchanges a second. Though this possibility cannot be excluded, it seems unlikely.

The ruthenium intermediates in equilibrium with **1** and $[\mathbf{6}]^+$ are elusive--no intermediates are evident by UV-vis spectroscopy. ESR was employed in an attempt to detect intermediates (Figure 5.13). **1** exhibited no ESR spectrum while $[\mathbf{6}]^+$ exhibited only a small ESR signal. ESR spectroscopy on an aqueous mixture of **1** and $[\mathbf{6}]^+$ exhibited no changes or additional

Figure 5.13. EPR spectra of $[H_21]^{2+}$ and $[6]^+$ and mixture in H_2O.

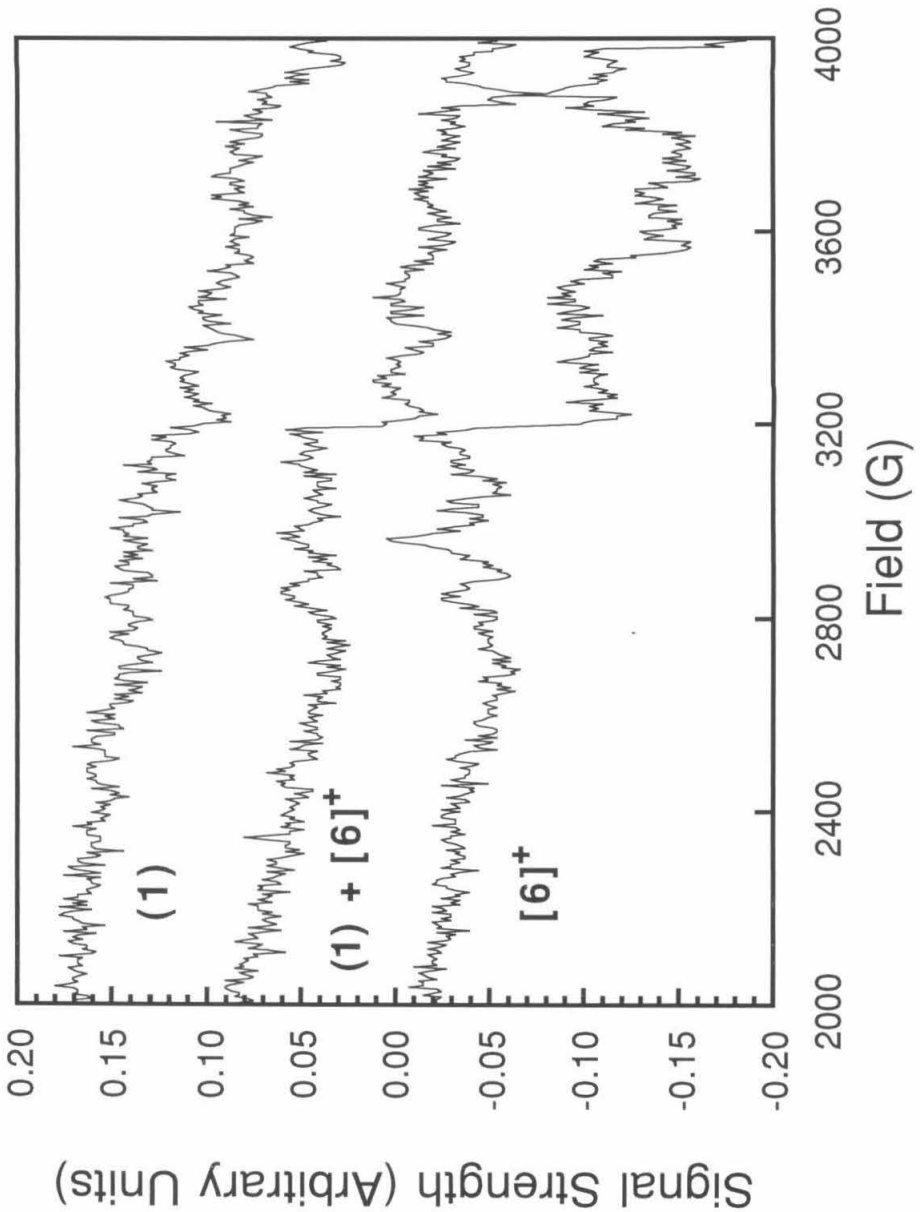

signals to the spectra of the individual solutions. Either the intermediate(s) are diamagnetic or are formed in concentrations below the detection limit of the spectrometer.

Addition of the diaquo Ru^{III}-Ru^{III} dimer $[3]^{2+}$ to a reaction mixture of between **1** and formaldehyde dramatically accelerates the reaction rate. This dimer appears to be a better catalyst for this reaction than $[6]^{+}$. Unfortunately, the identity of the catalytic species is not clear since this dimer reversibly rearranges under the reaction conditions to form $[(L_{OMe})Ru^{III}(\mu\text{-}OH)_3Ru^{III}(L_{OMe})]^{+}$ ($[4]^{+}$) (Figure 5.14).

Figure 5.14. Interconversion of $[3]^{2+}$ and $[4]^{2+}$.

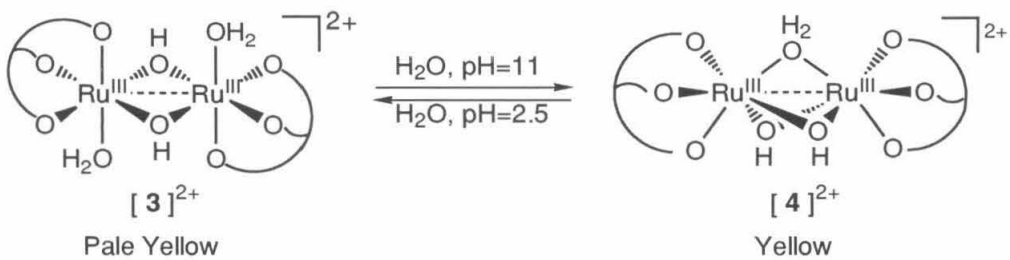

Nevertheless, the Ru^{IV}-Ru^{IV}/Ru^{III}-Ru^{III} redox potentials for both compounds are lower than that for the formate adduct; this would increase the concentrations of intermediates in an electron transfer step thus being consistent with the dramatic rate acceleration. The face sharing species, which is similar in structure to $[6]^{+}$ could also form dimer-dimer complexes with **1**. In principle, $[3]^{2+}$ could be promoting the reaction in much the same way as the $[6]^{+}$.

The mechanism appears general for the oxidation of substrates by **1**. As mentioned in Chapter 4, reactions of nearly all organic substrates (aldehydes, alcohols, and phosphines) in acetonitrile or water appear to have slow initial reaction rates followed by rapid rate acceleration. In the reaction of triphenylphosphine with **1**, the two products arise from an intermediate that appears to be the autocatalytic species (See Chapter 4). The similar

behavior of this reaction with that of the aqueous reaction suggests that the principle reaction features are independent of the solvent and vary only slightly with substrate.

The oxidation of ascorbic acid is the one exception to autocatalytic behavior. This reaction exhibits fast first order reactivity in both dimer and substrate at pH 7 (Figure 5.15). The mathematical relation that demonstrates first order kinetics between nearly equimolar amounts of **1** and ascorbic acid can be found in Appendix 5. Among the substrates examined with **1**, only ascorbic acid is known as a strong outer-sphere reducing agent for metal complexes.[6] The reaction between **1** and ascorbic acid proceeds by an outer sphere mechanism in contrast to the inner sphere oxidation of formaldehyde and other substrates.

Conclusion and Parting Speculation

The evidence above indicates that the oxidation of formaldehyde by **1** is an extraordinary reaction that circumvents the usual high barriers to oxidation. Though the actual means of substrate oxidation is not definitively established by the data presented here, the mechanism of substrate oxidation is likely unique.

This reactivity probably results from of the novel electronic properties of the dimer. First, the dimer possesses metal-metal coupling, evident by the diamagnetism of the dimer. This coupling probably strongly encourages the two electron events that dominate the bulk chemistry and electrochemistry of the dimer. Second, the coordination environment of substrate probably encourages the oxidation. If the mechanism proceeds through the intermediate illustrated in Figure 5.11, the oxidation could be imagined to occur by the flow of electrons from a C-H sigma bond through nonbonding oxygen p orbitals to the electrophilic metal centers. This reaction would likely be accompanied by deprotonation of the bound hydrated formaldehyde. The electrophilic metal centers draw electron density from the lone pairs of the hydrated formaldehyde oxygens, which draw electron density from the C-H bonds. The weakened C-H bonds are thus rendered more susceptible to proton abstraction. When proton abstraction occurs,

Figure 5.15. Indicative curve for ascorbic acid oxidation by **1**.

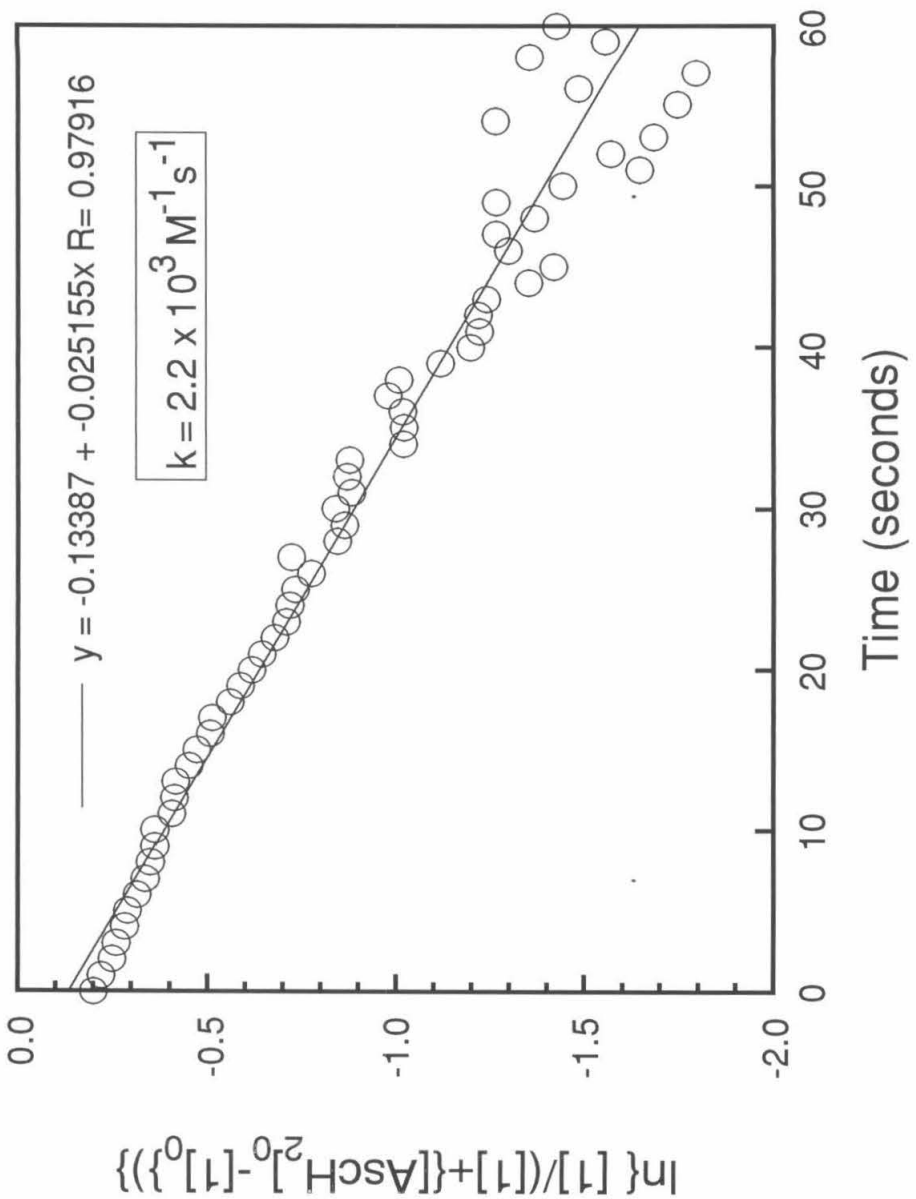

the delocalized system of formate would appear and electron density could flow from the breaking C-H bond through the formate π-system to the Ru^{IV}-Ru^{IV} core.

Experimental

General experimental considerations for bulk chemistry and electrochemistry were identical to those described in the Experimental section of Chapter 2.

Kinetic Measurements on Oxidation of Formaldehyde by (1). A stock solution was prepared of **1** (0.0949 g, 64.5 μmol, 1.291 mM) in nano-pure water (50.00 mL). A stock solution was also prepared of $[6]^+$ (0.0137 g, 10.0 μmol, 1.25 mM) in nano-pure water (10.00 mL). Stock buffer solutions were prepared by volumetrically dissolving the salts mixtures tabulated below in nano-pure water (100 mL).

Table 5.3. Salt composition of buffers used in kinetics.

These salts were volumetrically dissolved into water (100 mL) to prepare the corresponding buffers:

pH 5.55	$NaH_2PO_4 \cdot H_2O$ (5.025 g, 36.41 mmol)
	$Na_2HPO_4 \cdot 7H_2O$ (1.215 g, 4.53 mmol)
pH 6.37	$NaH_2PO_4 \cdot H_2O$ (2.410 g, 17.46 mmol)
	$Na_2HPO_4 \cdot 7H_2O$ (2.911 g, 10.86 mmol)
pH 7.15	$NaH_2PO_4 \cdot H_2O$ (0.669 g, 4.84 mmol)
	$Na_2HPO_4 \cdot 7H_2O$ (4.042 g, 15.05 mmol)

In a typical experiment, 2.00 mL of the **1** stock solution and 0.50 mL of a buffer stock solution were first combined in a UV-vis cuvette containing a stir bar. The cuvette was sealed with a thick septum, and the solution was sparged with moist argon. (The argon was previously sparged through buffer solution matching the sample in pH and ionic strength.) The sample was warmed with stirring to 45 °C in the spectrometer. The sample was removed, tapped to

dislodge gas bubbles, and replaced in the spectrometer for another five minutes. The formaldehyde (35%) was then injected into the sample. Data collection was begun ten seconds later.

A spectrum from 400 nm to 820 nm was collected for each time point to monitor for the possible appearance of intermediates. Approximately 73 data points were collected at equal durations over the bulk of the experiment (90 to 95% completion). A second, identical data collection was begun upon completion of the primary data set to measure the absorption at 100% completion.

This data were interpreted using the analytical wavelength 680 nm, the peak adsorption of **1**. The product $[\mathbf{6}]^+$ exhibits only a weak adsorption at 694 nm which posed no difficulty in data analysis. The initial dimer concentration of dimer was calculated from the initial absorptance quadratically extrapolated from the first three data points. (This extrapolation was performed by the TrueBasic program listed in Appendix 6.) Initial concentrations of formaldehyde were calculated from the volumes added to the reaction, and initial concentrations of $[\mathbf{6}]^+$ (in experiments involving deliberate addition of product) were calculated from stock solution concentration. The concentrations of **1** through the experiment were calculated from the absorptance data by standard means using the initial concentrations of **1** and $[\mathbf{6}]^+$ and the final absorptance. Concentrations of product $[\mathbf{6}]^+$ and formaldehyde were deduced from the reaction stoichiometry.

Raw absorption data were saved to DOS 6.0 text files and translated to Mac text files with the program Apple File Exchange. These files were edited in Microsoft Word 5.1a with the "replace" option to remove nonsense text characters that appeared at the beginning of each data sequence and to remove all extraneous spaces around commas. The edited text files were then read into KaleidaGraph where the 680 nm data was extracted and tabulated versus time. Concentrations of $[\mathbf{6}]^+$ and formaldehyde were then calculated as described above.

Curve fitting to the expression in Equation 5.1 was best accomplished by saving the KaleidaGraph data as a text file and using the program listed in Appendix 3. This program asks for the reaction stoichiometry and reaction orders for each species and returns the rate constants. These constants were confirmed by digital simulation of the data curves by the program listed in Appendix 4.

Curve fitting to the expression in Equation 5.2 was best accomplished within KaleidaGraph. The concentration data for **1** were converted to rate data using the "derivative" option in the "macros" menu. The curve fit was calculated using the "custom" KaleidaGraph's curve fitting routine with the expression below (C0 was substituted with the initial concentration of **1**). The routine returns $k_{1,obs}$ as m1, a as m2, and b as m3 along with the corresponding errors. Digital simulation from these constants was accomplished within KaleidaGraph by integrating rates calculated through this expression.

Equation 5.5. KaleidaGraph formula for custom fitting rate law.

```
(m0*m1) + (m0*(C0-m0)/(m2+m3*(C0-m0)))
;m1=0.001;m2=0.001;m3=0.001
```

The formaldehyde dependencies in each of the curve-fitting constants were determined by the standard means of searching for linearity among various plots of the constants against formaldehyde concentrations. The linear regressions in Figures 5.7, 5.8, and 5.9 below were calculated by standard means. These plots afforded the linear relations in Equations 5.6, 5.7, and 5.8. Linear relations to formaldehyde concentrations were found for all three constants of the curve-fitting rate law in Equation 5.2. The linear equations for k_{1obs} (Equation 5.6) and a (Equation 5.7) hold no surprises, but the linear relationship between b and 1/[HCHO] (Equation 5.8) has a negative intercept which is likely an artifact of curve fitting. If the intercept were a real effect, it could be a sign of another level of complexity in the rate law. Since all three rate constants contribute to the observed data curve, an error in one constant could propagate into the

Figure 5.16. Plot of $1/k_{1obs}$ vs. 1/[HCHO].

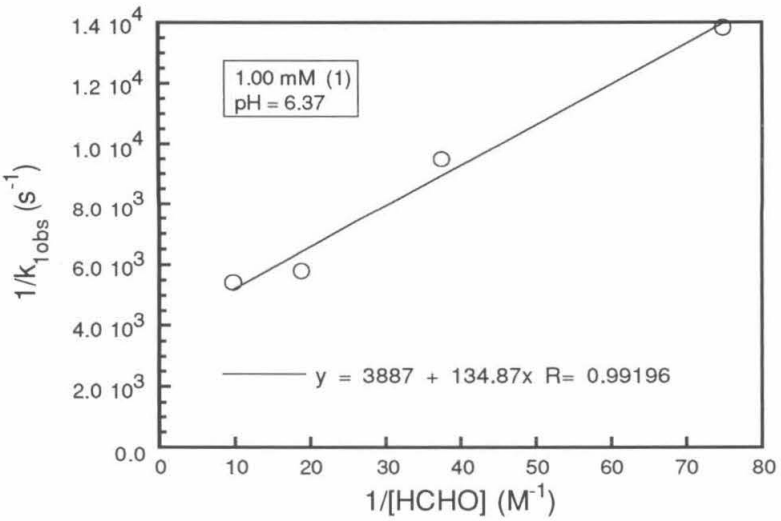

Figure 5.17. Plot of *a* vs. 1/[HCHO].

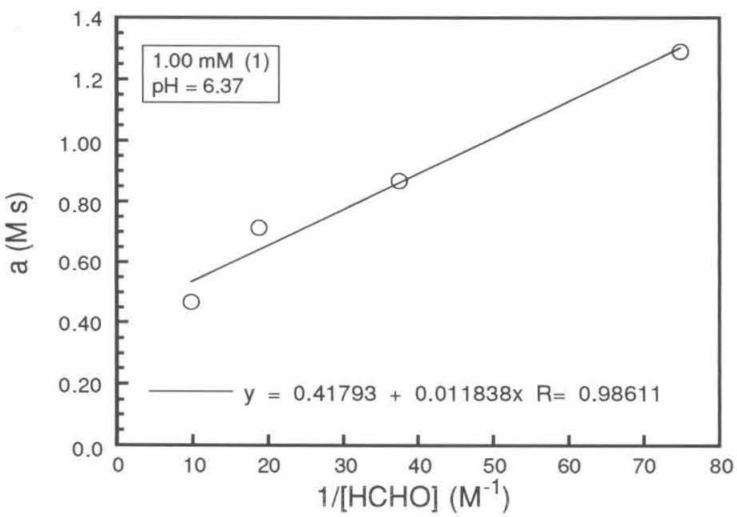

Figure 5.18. *Plot of b vs. 1/[HCHO].*

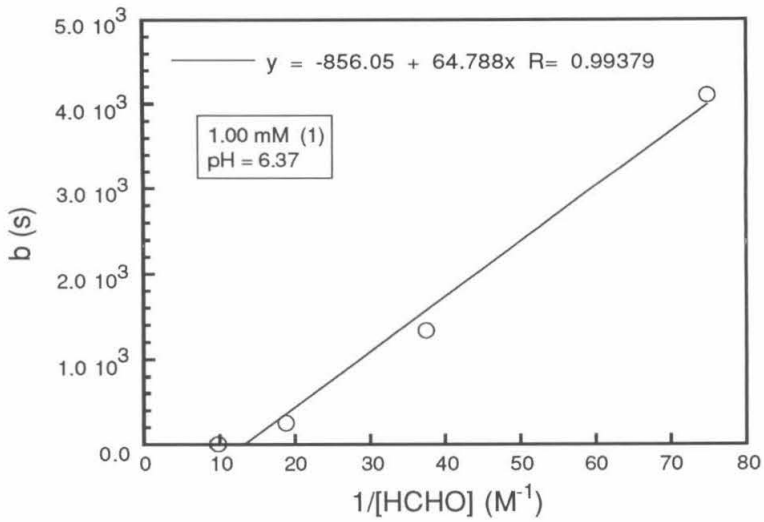

Equation 5.6. Formaldehyde dependence in k_{1obs}.

$$\frac{1}{k_{1,obs}} = A + \frac{B}{[HCHO]} \qquad k_{1,obs} = \frac{[HCHO]}{A[HCHO] + B}$$

Equation 5.7. Formaldehyde dependence in a.

$$a = C + \frac{D}{[HCHO]} \qquad a = \frac{C[HCHO] + D}{[HCHO]}$$

Equation 5.8. Formaldehyde dependence in b.

$$b = F + \frac{E}{[HCHO]}$$

Equation 5.9. Formaldehyde dependence in b neglecting negative intercept.

$$b = \frac{E}{[HCHO]}$$

others. The curve fitting routine could be incorporating such a subtle systematic error into the constants. Since the magnitude of this intercept is small compared to typical values of b and since this analysis is exploratory, the negative intercept of b was ignored (Equation 5.9). Equation 5.4 is the resulting formaldehyde dependent curve fitting rate law after the formaldehyde dependencies were substituted into the modified curve-fit rate law (Equation 5.2).

Equation 5.4. Formaldehyde dependent curve fitting rate law.

$$\text{Rate} = \frac{[\text{HCHO}][\mathbf{1}]}{A[\text{HCHO}]+B} + \frac{[\mathbf{1}][(\mathbf{6})^+][\text{HCHO}]}{D+C[\text{HCHO}]+E[(\mathbf{6})^+]}$$

Errors were propagated through the linear regressions by scatter plotting the mean, mean+sigma and mean-sigma values and then curve fitting to the custom equation "m0*m1+m2." This returned the slope as m1 and the intercept as m2 with their corresponding errors. Errors were propagated through the remainder of the analysis by standard means.

The rate constants and ratios k_1 and k_2/k_{-1} in Figure 5.8 were calculated from the curve fitting constants A and B in Equation 5.4 by the expressions in Equation 5.10.

Equation 5.10. Relationship between curve-fitting rate constants and chemical rate constants in non-autocatalytic reaction component.

$$k_1 = \frac{1}{A} \qquad \frac{k_2}{k_{-1}} = \frac{A}{B}$$

Analogously, the rate constants and ratios k_1, k_2/k_{-1}, and k_3/k_{-2} in Figure 5.9 were calculated from the curve fitting constants C, D, and E in Equation 5.4 by the expressions in Equation 5.11. The **1**, $[\mathbf{6}]^+$, and formaldehyde concentrations for the experiments reported are tabulated below with the corresponding curve fitting rate constants. The chemical rate constants calculated from these values are tabulated in Table 5.1 and 5.2.

Equation 5.11. *Relationship* between curve-fitting rate constants and chemical rate constants in autocatalytic reaction component.

$$k_1 = \frac{1}{C} \qquad \frac{k_2}{k_{-1}} = \frac{C}{D} \qquad \frac{k_3}{k_{-2}} = \frac{D}{E}$$

Kinetics of ascorbic acid oxidation by 1. Stock solutions were prepared of $[H_2\mathbf{1}](CF_3SO_3)_2$ (0.0219 g, 14.89 μmol, 1.489 mM) and ascorbic acid (0.0175 g, 99 μmol, 39.7 mM) in water (10.0 mL and 2.50 mL respectively). The buffer was prepared by dissolving $NaH_2PO_4{\cdot}H_2O$ (0.4964 g, 3.597 mmol, 35.97 mM) and $Na_2HPO_4{\cdot}7H_2O$ (0.5911 g, 2.205 mmol, 22.05 mM) into water (100.0 mL). Solutions of **1** (0.10 mL) and buffer (2.50 mL, pH 6.9, I=0.102 M) were mixed in a UV-vis cuvette and allowed to stir and thermally equilibrate to 25 °C in the spectrometer. An initial spectrum was collected, and data acquisition was initiated immediately upon injection of ascorbic acid solution (45 μL). Spectra from 400 to 820 nm were collected every second for 73 seconds. A final spectrum was collected 5 minutes later. Concentrations of **1** were calculated by standard means using the analytical wavelength 680 nm. First order behavior was demonstrated through the relation derived in Appendix 5. This is illustrated in Figure 5.15.

EPR spectroscopy of mixtures of 1 and [6]$^+$. Solutions of $[H_2\mathbf{1}](CF_3SO_3)_2$ (0.0949 g, 64.5 μmol, 1.291 mM) and $[\mathbf{6}][CF_3SO_3]$ (0.0137 g, 10.0 μmol, 1.25 mM) were prepared in water (50.0 mL and 10.0 mL respectively). A 1.0 mL sample of each solution was loaded into a 5 mm diameter magnetic spectroscopy tubes, flash frozen in liquid nitrogen, and examined by EPR spectroscopy. This was repeated for a 1:1 mixture of the two solutions. The digitized spectra are compared in Figure 5.13. EPR spectra were collected with a Varian E102 EPR spectrometer at 9.170 GHz over a field strength of 1000 to 5000 Gauss.

Table 5.4. Curve fitting rate constants for reaction of **1** with formaldehyde.

[1] (mM)	[HCHO] (mM)	pH	$k_{1,obs}$ (s^{-1} 10^{-6}) (error)	a (M s) (error)	b (s) (error)
0.951	102.5	7.15	177 (12)	0.556 (0.030)	-82 (45)
0.967	53.3	7.15	117.7 (5.1)	0.826 (0.035)	273 (53)
0.973	26.7	7.15	76.6 (3.7)	1.279 (0.080)	1331 (123)
1.038	13.4	7.15	36.4 (2.5)	3.31 (0.26)	2710 (307)
0.979	102.5	5.55	135 (16)	0.444 (0.023)	-96 (34)
0.947	53.3	5.55	129 (11)	0.437 (0.023)	175 (36)
0.939	26.7	5.55	106 (11)	0.474 (0.039)	669 (61)
0.977	13.4	5.55	90.3 (8.8)	0.475 (0.052)	2053 (86)
0.954	102.5	6.37	184.5 (9.0)	0.467 (0.017)	3 (26)
1.034	53.3	6.37	172.3 (6.0)	0.713 (0.029)	254 (40)
1.016	26.7	6.37	105.5 (5.2)	0.867 (0.058)	1334 (86)
1.009	13.4	6.37	72.3 (3.5)	1.29 (0.12)	4106 (192)

Table 5.5. Curve fitting rate constants for reaction of **1** with d_2-formaldehyde.

[1] (mM)	[DCDO] (mM)	pH	$k_{1,obs}$ (s^{-1} 10^{-6}) (error)	a (M s) (error)	b (s) (error)
0.995	99.2	6.37	147.7 (8.1)	0.560 (0.027)	255 (39)
1.016	48.5	6.37	99.7 (5.1)	0.701 (0.041)	1308 (63)
0.974	24.9	6.37	84.1 (3.5)	1.42 (0.13)	3301 (186)
1.029	12.5	6.37	60.1 (3.6)	3.97 (0.84)	7503 (1133)

References

1. Young, G. J.; Linden, H. R. *Fuel Cell Systems,* Advances in Chemistry Series 47; American Chemical Society: Washington, DC, 1965; pp 47, 53-57.

2. See references 11, 13-18 in Chapter 1.

3. Coicher, N.; Eldik, R. van, *Inorg. Chem.*, **1991**, *30*, 2375-2380. Moore, J. W.; Pearson, R. G. *Kinetics and Mechanism*; Wiley: New York, 1981; p 26.

4. Ghosh, M. C.; Gould, E. S. *Inorg. Chem.*, **1991**, *30*, 483-487. Moore, J. W.; Pearson, R. G. *Kinetics and Mechanism*; Wiley: New York, 1981; p 318.

5. Helzer, G. *Applied Linear Algebra with APL*; Little, Brown and Company: Boston, 1983; pp 86-92.

6. Khan, M. M. T.; Chatterjee, D.; Shukla, R. S. *J. Mol. Catal.*, **1991**, *69*, 33-39. Bansch, B.; Vaneldik, R.; Martinez, P. *Inorg. Chim. Acta*, **1992**, *201*, 75-82. Gangopadhyay, S.; Saha, S. K.; Ali, M.; Banerjee, P. *Internati. J. Chem. Kin*, **1991**, *23*, 105-112.

Appendices

Appendix 1

Atom Coordinates, Bond Distances, Bond Angles for X-ray Crystallographic Determination of $[(L_{OMe})(CH_3CN)Ru^{III}(\mu\text{-}OH)_2Ru^{III}(NCCH_3)(L_{OMe})][CF_3SO_3]_2$.

Table 1. Complete positional and isotropic thermal parameters for $[(L_{OMe})(CH_3CN)Ru^{III}(\mu\text{-}OH)_2Ru^{III}(NCCH_3)(L_{OMe})][CF_3SO_3]_2$ **[5]**$[CF_3SO_3]_2$.

	x, y, z and $U_{eq}{}^a \times 10^4$			
Atom	x	y	z	U_{eq} or B
Ru1	4726(.3)	1121(.2)	4504(.2)	218(1)
Co1	2671(.6)	3505(.4)	2071(.4)	333(1)
P1	2597(1)	1652(1)	2500(1)	297(2)
P2	2152(1)	3444(1)	3677(1)	316(2)
P3	5181(1)	3116(1)	2313(1)	298(2)
S1	1824(2)	1959(1)	7545(1)	574(3)
F1	1887(5)	489(4)	9427(3)	1162(14)
F2	−232(5)	790(5)	8710(3)	1332(16)
F3	407(6)	2056(4)	9305(3)	1431(16)
O1	2418(5)	983(3)	7207(3)	746(11)
O2	549(6)	2736(4)	6999(4)	1276(18)
O3	3004(6)	2460(5)	7816(5)	1516(20)
O4	3751(3)	816(2)	3294(2)	273(6)
O5	842(3)	1494(2)	2908(2)	432(8)
O6	2720(4)	1154(3)	1546(2)	503(8)
O7	2598(4)	4583(2)	3825(2)	459(8)
O8	319(3)	3576(2)	3965(2)	471(8)
O9	2921(3)	2403(2)	4537(2)	356(7)
O10	5939(3)	2559(3)	1439(2)	430(8)
O11	6064(4)	4220(2)	2007(2)	473(8)

Table 1. (Continued)

Atom	x	y	z	U_{eq} or B	
O12	5779(3)	2361(2)	3393(2)	311(6)	
O13	3389(3)	71(2)	5546(2)	270(7)	
N1	5666(4)	1554(3)	5616(2)	292(8)	
C1	930(7)	1307(6)	8819(4)	688(16)	
C2	523(7)	4269(5)	1402(5)	635(17)	
C3	2587(9)	5185(6)	1049(6)	846(23)	
C4	1463(11)	3830(5)	712(5)	808(22)	
C5	2805(8)	4384(8)	486(5)	911(28)	
C6	1187(8)	5093(5)	1584(5)	692(19)	
C7	6069(5)	1886(4)	6223(3)	356(10)	
C8	6601(7)	2286(7)	7029(5)	689(17)	
C9	454(6)	340(5)	3437(5)	579(15)	
C10	4146(8)	660(7)	1149(5)	719(17)	
C11	2533(12)	4688(6)	4852(6)	874(22)	
C12	−408(7)	2623(6)	4640(6)	712(18)	
C13	7576(6)	2079(6)	1417(5)	639(17)	
C14	6259(9)	4808(6)	2723(6)	728(18)	
H1	−443(62)	4015(43)	1696(39)	6.0	*
H2	926(68)	5475(48)	2013(43)	6.6	*
H3	3079(76)	5653(54)	1134(49)	8.0	*

Table 1. (Continued)

Atom	x	y	z	U_{eq} or B	
H4	3472(79)	4309(58)	152(51)	8.6	*
H5	1479(80)	3389(54)	462(49)	7.7	*
H6	7337(68)	2616(50)	6787(44)	6.5	*
H7	7342(66)	1578(46)	7466(41)	6.5	*
H8	5864(66)	2483(48)	7447(43)	6.5	*
H9	6410(72)	4263(49)	3359(44)	6.9	*
H10	6783(68)	5305(49)	2412(44)	6.9	*
H11	5238(68)	4958(48)	3111(45)	6.9	*
H12	8077(61)	2659(45)	921(41)	6.1	*
H13	8125(63)	2156(46)	1961(41)	6.1	*
H14	7778(65)	1371(45)	1629(43)	6.1	*
H15	−1223(67)	2608(51)	4361(45)	6.7	*
H16	−899(67)	2844(47)	5212(43)	6.7	*
H17	187(69)	2004(49)	4710(44)	6.7	*
H18	2443(86)	4173(56)	5297(51)	8.3	*
H19	1639(76)	5122(59)	4841(54)	8.3	*
H20	2984(78)	5276(56)	4863(49)	8.3	*
H21	−644(60)	490(41)	3756(36)	5.5	*
H22	641(58)	−101(43)	2923(38)	5.5	*
H23	1125(60)	−66(42)	3930(38)	5.5	*

Table 1. (Continued)

Atom	x	y	z	U_{eq} or B	
H24	4876(68)	330(48)	1670(43)	6.8	*
H25	4617(66)	1288(48)	624(43)	6.8	*
H26	3885(63)	6(46)	882(40)	6.8	*
H27	3308(46)	266(33)	5985(29)	1.7(10)	*

[a] $U_{eq} = \frac{1}{3} \sum_i \sum_j [U_{ij}(a_i^* a_j^*)(\vec{a}_i \cdot \vec{a}_j)]$

* Isotropic displacement parameter, B

Table 2. Bond distances for [5][CF_3SO_3]$_2$.

	Distance(Å)		Distance(Å)
Ru1 –Ru1	2.622	P2 –O9	1.514(3)
Ru1 –O4	2.054(2)	P3 –O10	1.586(3)
Ru1 –O9	2.021(3)	P3 –O11	1.593(3)
Ru1 –O12	2.043(3)	P3 –O12	1.528(3)
Ru1 –O13	2.013(3)	S1 –O1	1.416(4)
Ru1 –N1	2.009(3)	S1 –O2	1.406(5)
Ru1 –O13	2.001(3)	S1 –O3	1.403(6)
Co1 –P1	2.171(1)	S1 –C1	1.816(6)
Co1 –P2	2.152(1)	F1 –C1	1.286(7)
Co1 –P3	2.163(1)	F2 –C1	1.317(8)
Co1 –C2	2.061(6)	F3 –C1	1.292(8)
Co1 –C3	2.072(8)	O5 –C9	1.451(6)
Co1 –C4	2.070(8)	O6 –C10	1.416(8)
Co1 –C5	2.063(8)	O7 –C11	1.425(9)
Co1 –C6	2.078(6)	O8 –C12	1.438(7)
P1 –O4	1.518(3)	O10 –C13	1.435(7)
P1 –O5	1.590(3)	O11 –C14	1.410(8)
P1 –O6	1.579(3)	O13 –H27	0.70(4)
P2 –O7	1.587(3)	N1 –C7	1.123(5)
P2 –O8	1.590(3)	C2 –C4	1.362(10)

Table 2. (Continued)

	Distance(Å)		Distance(Å)
C2 –C6	1.339(9)	C11 –H19	0.86(7)
C2 –H1	0.95(5)	C11 –H20	0.88(7)
C3 –C5	1.402(11)	C12 –H15	0.83(6)
C3 –C6	1.358(10)	C12 –H16	0.94(6)
C3 –H3	0.81(7)	C12 –H17	0.82(6)
C4 –C5	1.406(11)	C13 –H12	0.95(6)
C4 –H5	0.72(7)	C13 –H13	0.94(6)
C5 –H4	0.71(7)	C13 –H14	0.81(6)
C6 –H2	0.85(6)	C14 –H9	0.90(6)
C7 –C8	1.459(8)	C14 –H10	0.81(6)
C8 –H6	0.80(6)	C14 –H11	1.01(6)
C8 –H7	1.02(6)		
C8 –H8	0.87(6)		
C9 –H21	1.02(5)		
C9 –H22	1.00(5)		
C9 –H23	0.88(5)		
C10 –H24	0.92(6)		
C10 –H25	0.99(6)		
C10 –H26	1.04(6)		
C11 –H18	0.73(7)		

Table 3. Bond angles for [5][CF_3SO_3]$_2$.

	Angle(°)		Angle(°)
O9 –Ru1 –O4	91.4(1)	C5 –Co1 –P1	116.2(2)
O12 –Ru1 –O4	87.5(1)	C6 –Co1 –P1	140.2(2)
O13 –Ru1 –O4	90.1(1)	P3 –Co1 –P2	92.3(0)
N1 –Ru1 –O4	175.4(1)	C2 –Co1 –P2	101.2(2)
O13 –Ru1 –O4	90.6(1)	C3 –Co1 –P2	113.2(2)
O12 –Ru1 –O9	87.1(1)	C4 –Co1 –P2	138.4(2)
O13 –Ru1 –O9	84.8(1)	C5 –Co1 –P2	152.4(2)
N1 –Ru1 –O9	85.9(1)	C6 –Co1 –P2	89.5(2)
O13 –Ru1 –O9	176.2(1)	C2 –Co1 –P3	161.1(2)
O13 –Ru1 –O12	171.4(1)	C3 –Co1 –P3	98.0(2)
N1 –Ru1 –O12	88.7(1)	C4 –Co1 –P3	129.3(2)
O13 –Ru1 –O12	89.8(1)	C5 –Co1 –P3	96.4(2)
N1 –Ru1 –O13	93.3(1)	C6 –Co1 –P3	130.6(2)
O13 –Ru1 –O13	98.4(1)	C3 –Co1 –C2	64.6(3)
O13 –Ru1 –N1	91.9(1)	C4 –Co1 –C2	38.5(3)
P2 –Co1 –P1	89.9(0)	C5 –Co1 –C2	65.7(3)
P3 –Co1 –P1	89.3(0)	C6 –Co1 –C2	37.8(2)
C2 –Co1 –P1	103.8(2)	C4 –Co1 –C3	65.5(3)
C3 –Co1 –P1	155.3(2)	C5 –Co1 –C3	39.6(3)
C4 –Co1 –P1	91.6(2)	C6 –Co1 –C3	38.2(3)

Table 3. (Continued)

	Angle(°)		Angle(°)
C5 –Co1 –C4	39.8(3)	O12 –P3 –O11	105.2(2)
C6 –Co1 –C4	64.0(3)	O2 –S1 –O1	117.0(3)
C6 –Co1 –C5	65.1(3)	O3 –S1 –O1	113.4(3)
O4 –P1 –Co1	118.6(1)	C1 –S1 –O1	102.8(3)
O5 –P1 –Co1	105.9(1)	O3 –S1 –O2	116.4(3)
O6 –P1 –Co1	114.9(1)	C1 –S1 –O2	102.3(3)
O5 –P1 –O4	109.8(1)	C1 –S1 –O3	101.6(3)
O6 –P1 –O4	105.6(2)	P1 –O4 –Ru1	127.7(1)
O6 –P1 –O5	100.4(2)	C9 –O5 –P1	120.2(3)
O7 –P2 –Co1	108.1(1)	C10 –O6 –P1	124.5(4)
O8 –P2 –Co1	113.3(1)	C11 –O7 –P2	119.0(4)
O9 –P2 –Co1	118.4(1)	C12 –O8 –P2	122.3(3)
O8 –P2 –O7	101.6(2)	P2 –O9 –Ru1	131.9(2)
O9 –P2 –O7	108.0(2)	C13 –O10 –P3	122.4(3)
O9 –P2 –O8	106.0(2)	C14 –O11 –P3	122.9(4)
O10 –P3 –Co1	106.4(1)	P3 –O12 –Ru1	128.2(2)
O11 –P3 –Co1	115.2(1)	Ru1 –O13 –Ru1	81.6(1)
O12 –P3 –Co1	118.8(1)	H27 –O13 –Ru1	105.1(33)
O11 –P3 –O10	99.1(2)	H27 –O13 –Ru1	116.4(33)
O12 –P3 –O10	110.4(2)	C7 –N1 –Ru1	173.0(3)

Table 3. (Continued)

	Angle(°)		Angle(°)
F1 –C1 –S1	112.5(4)	H5 –C4 –Co1	121.7(54)
F2 –C1 –S1	109.9(4)	C5 –C4 –C2	107.8(6)
F3 –C1 –S1	112.7(5)	H5 –C4 –C2	138.4(54)
F2 –C1 –F1	104.4(5)	H5 –C4 –C5	113.8(54)
F3 –C1 –F1	107.7(5)	C3 –C5 –Co1	70.5(4)
F3 –C1 –F2	109.3(5)	C4 –C5 –Co1	70.4(4)
C4 –C2 –Co1	71.1(4)	H4 –C5 –Co1	124.6(56)
C6 –C2 –Co1	71.8(4)	C4 –C5 –C3	105.9(7)
H1 –C2 –Co1	123.0(32)	H4 –C5 –C3	124.0(56)
C6 –C2 –C4	108.9(6)	H4 –C5 –C4	130.1(56)
H1 –C2 –C4	124.1(32)	C2 –C6 –Co1	70.5(4)
H1 –C2 –C6	127.0(32)	C3 –C6 –Co1	70.7(4)
C5 –C3 –Co1	69.8(4)	H2 –C6 –Co1	119.2(40)
C6 –C3 –Co1	71.1(4)	C3 –C6 –C2	109.9(6)
H3 –C3 –Co1	123.1(47)	H2 –C6 –C2	130.7(40)
C6 –C3 –C5	107.5(7)	H2 –C6 –C3	119.0(40)
H3 –C3 –C5	136.5(47)	C8 –C7 –N1	178.5(5)
H3 –C3 –C6	115.9(47)	H6 –C8 –C7	107.7(43)
C2 –C4 –Co1	70.4(4)	H7 –C8 –C7	103.9(32)
C5 –C4 –Co1	69.8(4)	H8 –C8 –C7	115.2(39)

Table 3. (Continued)

	Angle(°)		Angle(°)
H7 –C8 –H6	90.6(53)	H20 –C11 –H19	88.3(64)
H8 –C8 –H6	126.4(58)	H15 –C12 –O8	108.0(42)
H8 –C8 –H7	108.0(50)	H16 –C12 –O8	108.2(36)
H21 –C9 –O5	104.3(29)	H17 –C12 –O8	110.2(42)
H22 –C9 –O5	107.3(30)	H16 –C12 –H15	97.1(55)
H23 –C9 –O5	111.7(34)	H17 –C12 –H15	108.9(59)
H22 –C9 –H21	120.3(41)	H17 –C12 –H16	123.0(55)
H23 –C9 –H21	110.6(44)	H12 –C13 –O10	106.3(33)
H23 –C9 –H22	102.7(45)	H13 –C13 –O10	112.2(34)
H24 –C10 –O6	111.0(37)	H14 –C13 –O10	115.7(40)
H25 –C10 –O6	108.8(34)	H13 –C13 –H12	90.2(47)
H26 –C10 –O6	107.1(31)	H14 –C13 –H12	133.1(52)
H25 –C10 –H24	105.6(50)	H14 –C13 –H13	92.5(52)
H26 –C10 –H24	108.5(48)	H9 –C14 –O11	107.1(39)
H26 –C10 –H25	115.9(46)	H10 –C14 –O11	105.7(43)
H18 –C11 –O7	118.1(56)	H11 –C14 –O11	110.6(34)
H19 –C11 –O7	100.2(48)	H10 –C14 –H9	129.2(58)
H20 –C11 –O7	111.3(44)	H11 –C14 –H9	77.4(51)
H19 –C11 –H18	103.1(73)	H11 –C14 –H10	124.1(54)
H20 –C11 –H18	125.8(71)		

Appendix 2

Atom Coordinates, Bond Distances, Bond Angles for X-ray Crystallographic Determination of $[(L_{OMe})Ru^{III}(\mu\text{-}OH)_2(\mu\text{-}HCOO)Ru^{III}(L_{OMe})][CF_3SO_3]\cdot 2H_2O$.

Table 1. Complete positional and isotropic thermal parameters for $[(L_{OMe})Ru^{III}(\mu\text{-}OH)_2(\mu\text{-}HCOO)Ru^{III}(L_{OMe})][CF_3SO_3]\cdot 2H_2O$ **[6]**$[CF_3SO_3]$.

x, y, z and $U_{eq}{}^a \times 10^4$

Atom	x	y	z	U_{eq}
RuA	8187(.2)	1478(.1)	8675(.2)	135(1)
RuB	9706(.2)	1069(.1)	8444(.2)	137(1)
O1A	6805(2)	1195(1)	8562(2)	200(6)
O2A	7408(2)	1882(1)	7351(2)	204(6)
O3A	7952(2)	2172(1)	9349(2)	192(6)
O4A	9547(2)	1816(1)	8934(2)	194(6)
O5A	8838(2)	1094(1)	10008(2)	215(6)
O1B	11194(2)	1298(1)	8793(2)	212(6)
O2B	9282(2)	1399(1)	7071(2)	214(6)
O3B	10131(2)	299(1)	8137(2)	196(5)
O4B	8272(2)	782(1)	7989(2)	182(6)
O5B	10180(2)	731(1)	9808(2)	199(6)
C12	9636(3)	805(2)	10264(3)	217(9)
CoA	5614(.3)	2357(.2)	7847(.3)	189(1)
CoB	11122(.3)	800(.2)	6806(.3)	175(1)
P1A	5744(.7)	1451(.4)	7994(.7)	198(2)
P2A	6560(.7)	2316(.4)	7055(.7)	196(2)
P3A	6997(.7)	2521(.4)	9145(.7)	190(2)
P1B	11813(.7)	1204(.4)	8211(.7)	192(2)
P2B	9726(.7)	1293(.4)	6351(.6)	184(2)

Table 1. (Continued)

Atom	x	y	z	U_{eq}
P3B	10403(.7)	156(.4)	7303(.7)	210(2)
C1A	4027(3)	2315(2)	7084(4)	356(15)
C2A	4387(3)	2763(2)	6727(3)	360(11)
C3A	4883(3)	3138(2)	7498(4)	371(14)
C4A	4815(3)	2921(2)	8318(4)	362(12)
C5A	4290(3)	2413(2)	8066(4)	353(11)
C1B	11743(3)	1192(2)	5970(3)	259(8)
C2B	10992(3)	799(2)	5404(3)	262(9)
C3B	11306(3)	268(2)	5819(3)	285(9)
C4B	12260(3)	327(2)	6640(3)	294(9)
C5B	12531(3)	894(2)	6727(3)	291(10)
O6A	5052(2)	1232(1)	8509(2)	270(6)
O7A	5197(2)	1160(1)	6965(2)	329(7)
O8A	5807(2)	2229(1)	5947(2)	326(7)
O9A	7174(2)	2878(1)	7066(2)	347(7)
O10A	7263(2)	3166(1)	9145(2)	313(7)
O11A	6826(2)	2507(1)	10117(2)	283(6)
O6B	12811(2)	850(1)	8856(2)	308(7)
O7B	12345(2)	1793(1)	8203(2)	298(6)
O8B	8821(2)	1060(1)	5380(2)	322(7)

Table 1. (Continued)

Atom	x	y	z	U_{eq}
O9B	9956(2)	1879(1)	5973(2)	287(6)
O10B	9390(2)	−52(1)	6410(2)	357(6)
O11B	11009(2)	−423(1)	7590(2)	409(7)
C6A	5131(5)	639(2)	8763(5)	445(13)
C7A	5697(4)	820(3)	6518(4)	446(13)
C8A	6228(5)	2173(3)	5245(4)	516(18)
C9A	6690(6)	3385(3)	6559(6)	668(19)
C10A	8298(4)	3381(2)	9585(5)	430(14)
C11A	6728(4)	1977(2)	10515(4)	431(13)
C6B	13399(5)	1000(4)	9861(4)	617(20)
C7B	11792(4)	2306(2)	8058(5)	429(13)
C8B	7823(4)	895(3)	5297(4)	434(14)
C9B	9146(4)	2291(2)	5580(4)	419(13)
C10B	8637(4)	−390(3)	6559(4)	468(13)
C11B	11922(5)	−479(3)	8473(6)	653(18)
W1	9329(2)	2714(1)	7810(3)	571(9)
W2	8013(3)	−170(2)	8821(4)	638(14)
S1X	5043(.9)	766(.5)	2871(.9)	473(3)
O1X	4060(2)	648(2)	2119(2)	646(11)
O2X	5080(3)	1200(2)	3525(3)	777(11)

Table 1. (Continued)

Atom	x	y	z	U_{eq}
O3X	5667(3)	288(1)	3345(3)	603(10)
CX	5760(3)	1068(2)	2255(3)	203(10)
F1X	5788(2)	691(1)	1586(2)	739(9)
F2X	5303(3)	1517(1)	1753(2)	762(9)
F3X	6716(2)	1192(2)	2846(3)	941(12)

[a] $U_{eq} = \frac{1}{3} \sum_i \sum_j [U_{ij}(a_i^* a_j^*)(\vec{a}_i \cdot \vec{a}_j)]$

Table 2. Bond distances for [6][CF_3SO_3].

	Distance(Å)		Distance(Å)
RuA –O1A	2.032(2)	P3A –O11A	1.607(3)
RuA –O2A	2.079(2)	P1B –O6B	1.589(3)
RuA –O3A	2.052(2)	P1B –O7B	1.601(3)
RuA –O4A	1.988(3)	P2B –O8B	1.594(3)
RuA –O5A	2.056(2)	P2B –O9B	1.600(3)
RuA –O4B	1.995(3)	P3B –O10B	1.587(3)
RuB –O1B	2.042(2)	P3B –O11B	1.588(3)
RuB –O2B	2.073(2)	C1A –C2A	1.394(7)
RuB –O3B	2.051(2)	C1A –C5A	1.402(7)
RuB –O4B	1.989(3)	C1A –HC1A	0.83(5)
RuB –O5B	2.058(2)	C1A –CpA	1.185
RuB –O4A	1.985(3)	C2A –C3A	1.405(7)
CoA –CpA	1.709	C2A –HC2A	0.84(4)
CoB –CpB	1.699	C2A –CpA	1.195
CoA –C1A	2.068(5)	C3A –C4A	1.399(7)
CoA –C2A	2.093(5)	C3A –HC3A	0.92(5)
CoA –C3A	2.091(5)	C3A –CpA	1.188
CoA –C4A	2.086(5)	C4A –C5A	1.390(7)
CoA –C5A	2.071(5)	C4A –HC4A	0.84(5)
CoB –C1B	2.069(4)	C4A –CpA	1.189
CoB –C2B	2.070(4)	C5A –HC5A	0.82(5)
CoB –C3B	2.074(4)	C5A –CpA	1.190
CoB –C4B	2.088(4)	C1B –C2B	1.409(6)
CoB –C5B	2.090(5)	C1B –C5B	1.413(6)
O1A –P1A	1.520(3)	C1B –HC1B	0.90(3)
O2A –P2A	1.512(3)	C1B –CpB	1.200
O3A –P3A	1.517(3)	C2B –C3B	1.401(6)
O4A –HO4A	0.73(4)	C2B –HC2B	0.89(4)
O5A –C12	1.247(5)	C2B –CpB	1.197
O1B –P1B	1.520(3)	C3B –C4B	1.412(6)
O2B –P2B	1.512(3)	C3B –HC3B	0.88(4)
O3B –P3B	1.523(3)	C3B –CpB	1.194
O4B –HO4B	0.67(4)	C4B –C5B	1.398(6)
O5B –C12	1.263(5)	C4B –HC4B	0.86(4)
C12 –HC12	0.94(4)	C4B –CpB	1.199
P1A –O6A	1.597(3)	C5B –HC5B	0.85(5)
P1A –O7A	1.583(3)	C5B –CpB	1.194
P2A –O8A	1.583(3)	O6A –C6A	1.456(7)
P2A –O9A	1.600(3)	O7A –C7A	1.436(7)
P3A –O10A	1.584(3)	O8A –C8A	1.447(7)

Table 2. (Continued)

	Distance(Å)		Distance(Å)
O9A –C9A	1.441(9)	C10B –H0B2	0.99(7)
O10A –C10A	1.438(6)	C10B –H0B3	0.86(7)
O11A –C11A	1.436(6)	C11B –H1B1	0.92(7)
O6B –C6B	1.444(8)	C11B –H1B2	0.86(7)
O7B –C7B	1.423(7)	C11B –H1B3	0.87(6)
O8B –C8B	1.438(6)	W1 –H1W1	1.131
O9B –C9B	1.442(6)	W1 –H2W1	1.133
O10B –C10B	1.443(7)	W2 –H1W2	0.75(5)
O11B –C11B	1.427(8)	W2 –H2W2	0.81(6)
C6A –H6A1	0.91(5)	S1X –CX	1.816(4)
C6A –H6A2	0.88(6)	S1X –O1X	1.414(4)
C6A –H6A3	0.82(7)	S1X –O2X	1.423(4)
C7A –H7A1	0.89(6)	S1X –O3X	1.439(4)
C7A –H7A2	0.95(8)	CX –F1X	1.373(5)
C7A –H7A3	0.91(9)	CX –F2X	1.317(5)
C8A –H8A1	0.92(5)	CX –F3X	1.312(5)
C8A –H8A2	0.83(6)		
C8A –H8A3	0.82(8)		
C9A –H9A1	0.97(7)		
C9A –H9A2	0.96(10)		
C9A –H9A3	0.89(8)		
C10A –H0A1	0.93(7)		
C10A –H0A2	0.87(9)		
C10A –H0A3	0.96(7)		
C11A –H1A1	0.89(5)		
C11A –H1A2	0.90(6)		
C11A –H1A3	0.97(5)		
C6B –H6B1	0.98(6)		
C6B –H6B2	0.83(6)		
C6B –H6B3	0.89(8)		
C7B –H7B1	0.84(7)		
C7B –H7B2	0.89(5)		
C7B –H7B3	0.88(6)		
C8B –H8B1	0.89(6)		
C8B –H8B2	0.96(4)		
C8B –H8B3	0.93(5)		
C9B –H9B1	0.87(5)		
C9B –H9B2	0.88(6)		
C9B –H9B3	1.00(6)		
C10B –H0B1	0.99(6)		

Table 3. Angles distances for [6][CF_3SO_3].

	Angle(°)		Angle(°)
P1A –CoA –CpA	123.2	O1B –RuB –O3B	85.3(1)
P2A –CoA –CpA	128.1	O1B –RuB –O4B	173.1(1)
P3A –CoA –CpA	123.8	O1B –RuB –O5B	89.2(1)
P1A –CoA –P2A	88.1(0)	O1B –RuB –O4A	86.5(1)
P1A –CoA –P3A	94.7(0)	O2B –RuB –O3B	95.4(1)
P2A –CoA –P3A	88.4(0)	O2B –RuB –O4B	88.1(1)
CoA –P1A –O6A	109.4(1)	O2B –RuB –O5B	177.8(1)
CoA –P1A –O7A	110.4(1)	O2B –RuB –O4A	90.5(1)
CoA –P2A –O8A	107.4(1)	O3B –RuB –O4B	88.7(1)
CoA –P2A –O9A	115.4(1)	O3B –RuB –O5B	83.1(1)
CoA –P3A –O10A	107.6(1)	O3B –RuB –O4B	88.7(1)
CoA –P3A –O11A	113.6(1)	O4B –RuB –O5B	93.6(1)
P1B –CoB –CpB	122.9	O4B –RuB –O4A	99.8(1)
P2B –CoB –CpB	123.8	O5B –RuB –O4A	90.6(1)
P3B –CoB –CpB	125.9	RuA –O4A –RuB	79.8(1)
P1B –CoB –P2B	92.5(0)	RuA –O4B –RuB	79.5(1)
P1B –CoB –P3B	93.0(0)	RuA –O1A –P1A	128.2(1)
P2B –CoB –P3B	89.0(0)	RuA –O2A –P2A	129.5(1)
CoB –P1B –O6B	106.6(1)	RuA –O3A –P3A	132.0(1)
CoB –P1B –O7B	113.5(1)	RuB –O1B –P1B	128.1(1)
CoB –P2B –O8B	112.5(1)	RuB –O2B –P2B	129.9(1)
CoB –P2B –O9B	106.5(1)	RuB –O3B –P3B	127.0(1)
CoB –P3B –O10B	108.5(1)	RuA –O5A –C12	121.4(2)
CoB –P3B –O11B	115.2(1)	RuB –O5B –C12	119.3(2)
O1A –RuA –O2A	88.5(1)	O5B –C12 –O5A	127.4(4)
O1A –RuA –O3A	86.8(1)	HC12 –C12 –O5A	117.2(22)
O1A –RuA –O4A	172.3(1)	HC12 –C12 –O5B	115.4(22)
O1A –RuA –O5A	87.0(1)	O6A –P1A –O1A	105.7(1)
O1A –RuA –O4B	87.5(1)	O7A –P1A –O1A	109.9(1)
O2A –RuA –O3A	88.8(1)	O7A –P1A –O6A	101.4(1)
O2A –RuA –O4A	94.5(1)	O8A –P2A –O2A	108.8(1)
O2A –RuA –O5A	174.6(1)	O9A –P2A –O2A	101.6(1)
O2A –RuA –O4B	90.2(1)	O9A –P2A –O8A	104.0(2)
O3A –RuA –O4A	86.1(1)	O10A –P3A –O3A	109.7(1)
O3A –RuA –O5A	87.9(1)	O11A –P3A –O3A	106.4(1)
O3A –RuA –O4B	174.3(1)	O11A –P3A –O10A	98.8(1)
O4A –RuA –O5A	89.6(1)	O6B –P1B –O1B	108.3(1)
O4A –RuA –O4B	99.6(1)	O7B –P1B –O1B	106.0(1)
O5A –RuA –O4B	92.7(1)	O7B –P1B –O6B	99.5(1)
O1B –RuB –O2B	89.0(1)	O8B –P2B –O2B	107.8(1)

Table 3. (Continued)

	Angle(°)		Angle(°)
O9B –P2B –O2B	109.5(1)	CpB –C1B –HC1B	175.3
O9B –P2B –O8B	100.4(1)	C3B –C2B –C1B	108.1(4)
O10B –P3B –O3B	108.7(1)	HC2B –C2B –C1B	126.0(24)
O11B –P3B –O3B	105.7(2)	CpB –C2B –C1B	54.1
O11B –P3B –O10B	99.1(2)	HC2B –C2B –C3B	125.8(24)
C5A –C1A –C2A	108.5(4)	CpB –C2B –C3B	54.0
HC1A –C1A –C2A	122.7(33)	CpB –C2B –HC2B	178.6
CpA –C1A –C2A	54.5	C4B –C3B –C2B	108.2(4)
HC1A –C1A –C5A	128.9(33)	HC3B –C3B –C2B	125.0(27)
CpA –C1A –C5A	54.0	CpB –C3B –C2B	54.2
CpA –C1A –HC1A	176.7	HC3B –C3B –C4B	126.8(27)
C3A –C2A –C1A	107.4(4)	CpB –C3B –C4B	54.0
HC2A –C2A –C1A	131.7(28)	CpB –C3B –HC3B	177.7
CpA –C2A –C1A	53.8	C5B –C4B –C3B	107.8(4)
HC2A –C2A –C3A	120.9(28)	HC4B –C4B –C3B	123.5(24)
CpA –C2A –C3A	53.6	CpB –C4B –C3B	53.7
CpA –C2A –HC2A	174.1	HC4B –C4B –C5B	128.8(24)
C4A –C3A –C2A	108.1(4)	CpB –C4B –C5B	54.1
HC3A –C3A –C2A	128.4(30)	CpB –C4B –HC4B	177.0
CpA –C3A –C2A	54.1	C4B –C5B –C1B	108.4(4)
HC3A –C3A –C4A	123.3(30)	HC5B –C5B –C1B	127.5(34)
CpA –C3A –C4A	54.0	CpB –C5B –C1B	54.0
CpA –C3A –HC3A	175.5	HC5B –C5B –C4B	124.1(34)
C5A –C4A –C3A	108.2(4)	CpB –C5B –C4B	54.4
HC4A –C4A –C3A	127.7(32)	CpB –C5B –HC5B	178.5
CpA –C4A –C3A	53.9	C6A –O6A –P1A	117.0(3)
HC4A –C4A –C5A	124.1(32)	C7A –O7A –P1A	125.7(3)
CpA –C4A –C5A	54.3	C8A –O8A –P2A	119.6(3)
CpA –C4A –HC4A	176.7	C9A –O9A –P2A	124.0(4)
C4A –C5A –C1A	107.9(4)	C10A –O10A –P3A	123.1(3)
HC5A –C5A –C1A	127.0(32)	C11A –O11A –P3A	119.4(3)
CpA –C5A –C1A	53.7	C6B –O6B –P1B	119.2(3)
HC5A –C5A –C4A	125.2(32)	C7B –O7B –P1B	121.2(3)
CpA –C5A –C4A	54.2	C8B –O8B –P2B	124.1(3)
CpA –C5A –HC5A	178.6	C9B –O9B –P2B	119.4(3)
C5B –C1B –C2B	107.5(4)	C10B –O10B –P3B	120.7(3)
HC1B –C1B –C2B	127.8(21)	C11B –O11B –P3B	121.0(4)
CpB –C1B –C2B	53.9	H6A1 –C6A –O6A	107.5(33)
HC1B –C1B –C5B	124.5(21)	H6A2 –C6A –O6A	114.1(39)
CpB –C1B –C5B	53.6	H6A3 –C6A –O6A	106.0(49)

Table 3. (Continued)

			Angle(°)				Angle(°)
H6A2	-C6A	-H6A1	111.1(51)	H7B2	-C7B	-O7B	110.2(34)
H6A3	-C6A	-H6A1	101.6(58)	H7B3	-C7B	-O7B	121.5(39)
H6A3	-C6A	-H6A2	115.5(62)	H7B2	-C7B	-H7B1	100.5(60)
H7A1	-C7A	-O7A	115.2(41)	H7B3	-C7B	-H7B1	101.6(62)
H7A2	-C7A	-O7A	116.1(46)	H7B3	-C7B	-H7B2	110.0(52)
H7A3	-C7A	-O7A	100.7(55)	H8B1	-C8B	-O8B	104.9(35)
H7A2	-C7A	-H7A1	119.1(61)	H8B2	-C8B	-O8B	109.6(26)
H7A3	-C7A	-H7A1	115.1(69)	H8B3	-C8B	-O8B	106.3(30)
H7A3	-C7A	-H7A2	84.9(71)	H8B2	-C8B	-H8B1	117.9(44)
H8A1	-C8A	-O8A	111.8(30)	H8B3	-C8B	-H8B1	108.7(46)
H8A2	-C8A	-O8A	109.6(40)	H8B3	-C8B	-H8B2	108.8(39)
H8A3	-C8A	-O8A	100.0(55)	H9B1	-C9B	-O9B	111.1(33)
H8A2	-C8A	-H8A1	122.1(50)	H9B2	-C9B	-O9B	108.9(39)
H8A3	-C8A	-H8A1	104.1(62)	H9B3	-C9B	-O9B	111.8(34)
H8A3	-C8A	-H8A2	106.5(67)	H9B2	-C9B	-H9B1	114.7(51)
H9A1	-C9A	-O9A	107.7(42)	H9B3	-C9B	-H9B1	103.1(47)
H9A2	-C9A	-O9A	108.5(58)	H9B3	-C9B	-H9B2	107.1(52)
H9A3	-C9A	-O9A	103.5(51)	H0B1	-C10B	-O10B	110.5(35)
H9A2	-C9A	-H9A1	111.1(71)	H0B2	-C10B	-O10B	103.4(43)
H9A3	-C9A	-H9A1	115.9(66)	H0B3	-C10B	-O10B	108.7(45)
H9A3	-C9A	-H9A2	109.7(77)	H0B2	-C10B	-H0B1	101.5(55)
H0A1	-C10A	-O10A	110.5(45)	H0B3	-C10B	-H0B1	118.3(57)
H0A2	-C10A	-O10A	102.1(58)	H0B3	-C10B	-H0B2	113.4(62)
H0A3	-C10A	-O10A	106.5(39)	H1B1	-C11B	-O11B	105.5(46)
H0A2	-C10A	-H0A1	111.1(73)	H1B2	-C11B	-O11B	119.4(45)
H0A3	-C10A	-H0A1	117.5(59)	H1B3	-C11B	-O11B	117.9(39)
H0A3	-C10A	-H0A2	107.9(70)	H1B2	-C11B	-H1B1	105.5(65)
H1A1	-C11A	-O11A	109.5(34)	H1B3	-C11B	-H1B1	110.8(61)
H1A2	-C11A	-O11A	101.5(39)	H1B3	-C11B	-H1B2	97.1(60)
H1A3	-C11A	-O11A	111.2(27)	H2W1	-W1	-H1W1	104.2
H1A2	-C11A	-H1A1	112.1(51)	H2W2	-W2	-H1W2	110.6(59)
H1A3	-C11A	-H1A1	110.1(43)	O2X	-S1X	-O1X	116.0(2)
H1A3	-C11A	-H1A2	112.2(48)	O3X	-S1X	-O1X	116.1(2)
H6B1	-C6B	-O6B	104.2(37)	CX	-S1X	-O1X	104.3(2)
H6B2	-C6B	-O6B	118.1(42)	O3X	-S1X	-O2X	113.3(2)
H6B3	-C6B	-O6B	107.9(50)	CX	-S1X	-O2X	102.6(2)
H6B2	-C6B	-H6B1	110.6(56)	CX	-S1X	-O3X	101.9(2)
H6B3	-C6B	-H6B1	104.3(62)	F1X	-CX	-S1X	109.3(3)
H6B3	-C6B	-H6B2	110.7(65)	F2X	-CX	-S1X	111.8(3)
H7B1	-C7B	-O7B	110.8(49)	F3X	-CX	-S1X	113.0(3)

Table 3. (Continued)

	Angle(°)
F2X –CX –F1X	105.4(3)
F3X –CX –F1X	107.7(3)
F3X –CX –F2X	109.3(3)

Appendix 3

Program for curve fitting by matrix least squares.

This program was written in TrueBasic and used as listed below. This program calculates rate constants for a rate law defined in a separate file using concentration data in another file.

The data file is created from a KaleidaGraph file with time data in the first column and concentration data for each species listed in subsequent columns. The KaleidaGraph data was "exported" as a "text" file. This file was read into Microsoft Word where all tabulation characters were converted to carriage returns. The number of data points and then the column number for the observed species were added to the beginning of the file before this file was saved as a "text only" file.

The second file, a "text only" file, defines the rate law. The file used in this research simply consisted of the numbers listed below followed by carriage returns.

```
2          (the number of terms in the rate law)
3          (the number of species in rate law)
1          (reaction orders of species in first term of rate law)
0
0
1          (reaction orders of species in second term of rate law)
1
1
```

The program itself is listed below. REM (comment) statements describe the purpose of variables and routines within the program.

```
REM finding the data file
PRINT "data file name: ";
INPUT  dataf$
OPEN #1: name dataf$
INPUT #1:n
REM n is the number of data points collected
INPUT #1:crxt
REM reactant number corresponding to controlling data

REM finding chemsystem file
PRINT "system filename: ";
INPUT chemsys$
OPEN #2:name chemsys$
INPUT #2:nterm
REM number of terms in rate law
INPUT #2:rxts
REM number of reactants
```

```
REM general dimensioning
DIM x(100)
MAT redim x(n)
REM (time data)
DIM y(100)
MAT redim y(n)
REM (controlling data)
DIM ya(3)
REM (y matrix for calculating cubic)
DIM xa(3,3)
REM (x matrix for calculating cubic)
DIM aa(3)
REM (matrix for results of cubic)
DIM ua(100)
MAT redim ua(n)
REM (matrix for cubic coefficients)
DIM ub(100)
MAT redim ub(n)
REM (matrix for quadratic coefficients)
DIM uc(100)
MAT redim uc(n)
REM (matrix for linear coefficients)
DIM ud(100)
MAT redim ud(n)
REM (matrix for constant coefficients)
DIM mx(100,2)
MAT redim mx(n,nterm)
REM (x matrix for calculating rate constants)
DIM xm(2,100)
MAT redim xm(nterm,n)
REM (transpose of mx)
DIM r(100,5)
MAT redim r(n,rxts)
REM (reactant concentrations)
DIM p(10,10)
MAT redim p(nterm,rxts)
REM (rate law coefficients for term,reactant)
DIM kk(100)
MAT redim kk(nterm)
REM (rate constants)
DIM ia(100,100)
MAT redim ia(n,n)
REM (intermediate matrix for big calculation)
DIM ib(2,100)
MAT redim ib(xterm,n)
REM (intermediate matrix for big calculation)

REM reading remaining reaction parameters
FOR count=1 to nterm
  FOR countb=1 to rxts
    INPUT #2:p(count,countb)
  NEXT countb
NEXT count
```

```
REM reading data file
FOR count=1 to n
  INPUT #1:x(count)
  FOR countb=1 to rxts
    INPUT #1:r(count,countb)
  NEXT countb
NEXT count

REM transfering controlling concentration to rate buffer
FOR count=1 to n
  LET y(count)=r(count,crxt)
NEXT count

REM calculating quadratic of first point
FOR counta=1 to 3
  LET ya(counta)=y(counta)
  LET xat=x(counta)-x(1)
  LET xa(counta,3)=1
  LET xa(counta,2)=xat
  LET xa(counta,1)=xat*xat
NEXT counta
MAT xa=inv(xa)
MAT AA=XA*YA
LET ua(1)=aa(1)
LET ub(1)=aa(2)
LET uc(1)=aa(3)

REM calculating quadratic for middle points
FOR count=2 to n-1
  FOR counta=1 to 3
    LET ya(counta)=y(counta+count-2)
    LET xat=x(counta+count-2)-x(count)
    LET xa(counta,3)=1
    LET xa(counta,2)=xat
    LET xa(counta,1)=xat*xat
  NEXT counta
  MAT xa=inv(xa)
  MAT AA=XA*YA
  LET ua(count)=aa(1)
  LET ub(count)=aa(2)
  LET uc(count)=aa(3)
NEXT count

REM calculating quadratic for last point
FOR counta=1 to 3
  LET ya(counta)=y(counta+n-3)
  LET xat=x(counta+n-3)-x(n)
  LET xa(counta,3)=1
  LET xa(counta,2)=xat
  LET xa(counta,1)=xat*xat
NEXT counta
MAT XA=INV(XA)
MAT AA=XA*YA
LET ua(n)=aa(1)
```

```
LET ub(n)=aa(2)
LET uc(n)=aa(3)

REM calculating rate equation matrix
FOR count=1 to n
  FOR term=1 to nterm
    LET mx(count,term)=1
    FOR nn=1 to rxts
      IF p(term,nn)>0 then
        LET mx(count,term)=mx(count,term)*(r(count,nn)^p(term,nn))
      END IF
      IF p(term,nn)<0 then
        LET temp=-p(term,nn)
        LET temp=r(count,nn)^temp
        LET mx(count,term)=mx(count,term)/temp
      END IF
    NEXT nn
  NEXT term
NEXT count
MAT xm=trn(mx)
MAT ia=xm*mx
MAT  ia=inv(ia)
MAT ib=ia*xm
MAT kk=ib*ub
FOR term=1 to nterm
   PRINT "k(",term,") = ";kk(term)
NEXT term
PRINT  "DONE"
CLOSE #1
CLOSE #2

REM calculating error in fit based on rates.
LET err=0
FOR count=1 to n
  LET rate=0
  FOR countb=1 to nterm
    LET factr=1
    FOR countc=1 to rxts
      LET factr=factr*(r(count,countc)^p(countb,countc))
    NEXT countc
    LET factr=factr*kk(countb)
    LET rate=rate+factr
  NEXT countb
  LET drate=rate-ub(count)
  LET err=err+drate*drate
NEXT count
LET err=err^0.5
PRINT "the final root mean square error = ";
PRINT err
END
```

Appendix 4

Program for kinetic simulation.

This program calculates reaction rates from a simple rate law given in a separate file and rate constants entered by keyboard and calculates the concentration of each reaction species over the course of the reaction. This program finally generates a KaleidaGraph readable text file of concentrations for each reaction species.

The program requires one input file which defines of the rate law. The file used in the research in this thesis consisted of the following characters followed by carriage returns.

```
2          (the number of terms in the rate law)
3          (the number of species involved in rate law)
Ru4        (names of species in numerical order)
Ru3
ald
-1         (reaction stoichiometry of first species in first term)
1          (reaction order of first species in first term)
1          (reaction stoichiometry of second species in first term)
0          (reaction order of second species in first term)
-1         (reaction stoichiometry of third species in first term)
0          (reaction order of third species in first term)
-1         (analogous data for second term)
1
1
1
-1
1
```

The program itself is listed below.

```
PRINT "System File ";
INPUT chemfile$
OPEN #1:name chemfile$
INPUT #1:rxnnum
INPUT #1:cpdnum
DIM rate(1)
DIM rxnrate(1)
DIM cpd(1)
DIM delcpd(1)
DIM cpdcef(1,1)
DIM cpdpwr(1,1)
DIM cpdnam$(1)
MAT REDIM rate(rxnnum)
MAT REDIM rxnrate(rxnnum)
MAT REDIM cpd(cpdnum)
MAT REDIM delcpd(cpdnum)
MAT REDIM cpdcef(rxnnum,cpdnum)
MAT REDIM cpdpwr(rxnnum,cpdnum)
MAT REDIM cpdnam$(cpdnum)
FOR cpdcnt=1 to cpdnum
```

```
   INPUT #1:cpdnam$(cpdcnt)
NEXT cpdcnt
FOR rxncnt=1 to rxnnum
   FOR cpdcnt=1 to cpdnum
      INPUT #1:cpdcef(rxncnt,cpdcnt)
      INPUT #1:cpdpwr(rxncnt,cpdcnt)
   NEXT cpdcnt
NEXT rxncnt
CLOSE #1
FOR cpdcnt=1 to cpdnum
    PRINT "Concentration of ";cpdnam$(cpdcnt);" ";
    INPUT cpd(cpdcnt)
NEXT cpdcnt
PRINT "Total reaction time ";
INPUT tottim
PRINT "Time units ";
INPUT unttim
LET deltim=tottim/unttim
DIM rxnprof(1,1)
MAT REDIM rxnprof(cpdnum,unttim+1)
FOR cpdcnt=1 to cpdnum
   LET rxnprof(cpdcnt,1)=cpd(cpdcnt)
NEXT cpdcnt
FOR rxncnt=1 to rxnnum
    PRINT "Reaction rate of reaction ";rxncnt;" ";
    INPUT rate(rxncnt)
NEXT rxncnt
LET untcnt=1
DO while untcnt<unttim
  FOR rxncnt=1 to rxnnum
     LET ratetemp=1
     FOR cpdcnt=1 to cpdnum
        IF cpdpwr(rxncnt,cpdcnt)<>0 then
          LET ratetemp=ratetemp*(rxnprof(cpdcnt,untcnt)^cpdpwr(rxncnt,cpdcnt))
        END IF
     NEXT cpdcnt
      LET rxnrate(rxncnt)=ratetemp*rate(rxncnt)
  NEXT rxncnt
  FOR cpdcnt=1 to cpdnum
     LET delcpd(cpdcnt)=0
  NEXT cpdcnt
  FOR rxncnt=1 to rxnnum
     FOR cpdcnt=1 to cpdnum
        LET delcpd(cpdcnt)=delcpd(cpdcnt)+deltim*rxnrate(rxncnt)*cpdcef(rxncnt,cpdcnt)
     NEXT cpdcnt
  NEXT rxncnt
  FOR cpdcnt=1 to cpdnum
     LET rxnprof(cpdcnt,untcnt+1)=rxnprof(cpdcnt,untcnt)+delcpd(cpdcnt)
  NEXT cpdcnt
  LET untcnt=untcnt+1
LOOP
PRINT "Output file name ";
INPUT  filename$
OPEN #1:name filename$,create new,org text
```

```
FOR untcnt=1 to unttim
   LET timm=(untcnt-1)*deltim
   PRINT #1:timm;
   FOR cpdcnt=1 to cpdnum
      PRINT #1:",";rxnprof(cpdcnt,untcnt);
   NEXT cpdcnt
   PRINT #1:
NEXT untcnt
CLOSE #1
END
```

Appendix 5

Integration of second order rate expression without pseudofirst-order conditions.

The following derivation is for the rate behavior in the reaction below with approximately equal concentrations for both reactants.

$$A + B \xrightarrow{k} C$$

For simplicity, let $A = [A]$, $A_0 = [A]_{t=0}$, $B = [B]$, $B_0 = [B]_{t=0}$

$$\frac{dA}{dt} = -kAB$$

$$B = B_0 - (A_0 - A)$$

$$\frac{dA}{dt} = -kA\left[(B_0 - A_0) + A\right]$$

$$\frac{dA}{A\left[(B_0 - A_0) + A\right]} = -k\,dt$$

$$\frac{1}{A\left[(B_0 - A_0) + A\right]} = \frac{1}{A(B_0 - A_0)} - \frac{1}{\left[(B_0 - A_0) + A\right](B_0 - A_0)}$$

$$\int_{A_0}^{A} \frac{dA}{A(B_0 - A_0)} - \int_{A_0}^{A} \frac{dA}{\left[(B_0 - A_0) + A\right](B_0 - A_0)} = -\int_0^t k\,dt$$

$$\frac{1}{(B_0 - A_0)} \ln(A)\Big|_{A_0}^{A} - \frac{1}{(B_0 - A_0)} \ln\left[(B_0 - A_0) + A\right]\Big|_{A_0}^{A} = -kt\Big|_0^t$$

$$\frac{1}{(B_0 - A_0)} \ln \frac{AB_0}{A_0\left[(B_0 - A_0) + A\right]} = -kt$$

$$\ln \frac{A}{\left[(B_0 - A_0) + A\right]} = -(B_0 - A_0)kt + \ln \frac{A_0}{B_0}$$

In a plot of $\ln \dfrac{A}{\left[(B_0 - A_0) + A\right]}$ versus t (time):

$$\text{Slope} = -(B_0 - A_0)k$$

$$\text{Intercept} = \ln \frac{A_0}{B_0}$$

Appendix 6

Program for quadratic extrapolation.

The program listed below extrapolates by quadratic extrapolation the value of a function at a fourth point from three known points. Absorption data is entered as values of y for times entered as values of x. The program was written in TrueBasic.

```
DIM mx(3,3)
DIM x(3)
DIM y(3)
DIM a(3)
FOR count=1 to 3
   PRINT "enter x(";count;")=";
  INPUT x(count)
   PRINT "enter y(";count;")=";
  INPUT y(count)
  PRINT
NEXT count
FOR count=1 to 3
  FOR countb=1 to 3
    LET mx(count,countb)=x(count)^(3-countb)
  NEXT countb
NEXT count
MAT mx=inv(mx)
MAT a=mx*y
DO
  LET lp$="n"
   PRINT "extrapolate to what value";
  INPUT b
   LET c=a(1)*b*b+a(2)*b+a(3)
   PRINT "extrapolated y=";c
   LET slope=2*a(1)*b+a(2)
   PRINT "slope=";slope
  PRINT
   PRINT "another (y/n)?";
  INPUT lp$
LOOP while lp$="y" or lp$="y"
END
```